UNIVERSITY OF TRENTO - Italy

Department of Industrial Engineering

Doctoral School in Materials, Mechatronics and Systems Engineering

30th cycle

Ground Testing and In-Flight Performance of a Space Mechanism

Tutor
Prof. Daniele Bortoluzzi

PhD Candidate
Andrea Zambotti

Academic Year 2018/2019

Abstract

LISA Pathfinder is a mission designed for testing the key technologies of the future LISA mission, whose goal is the detection of gravitational waves through the measurement of the relative motion of dedicated proof masses.

In LISA Pathfinder, a critical task is the release of two *Test Masses* (TMs); each TM has to be injected into free fall by a dedicated *Grabbing Positioning and Release Mechanism* (GPRM). Despite the symmetrical design of the GPRM, during the release, as an effect of asymmetric impulses exchanged by the TM and the release tips of the GPRM, the TM can acquire a *residual momentum*. The release is successful if the residual momentum of the TM can be compensated by the force authority of the capacity control, which allows to centre the TM in its housing; as a consequence, a residual momentum of the TM higher than a maximum requirement can be critical for the mission.

In the *nominal release* configuration, which assumes a monodimensional dynamics of the mechanism along the axis of the release tips, the residual momentum can be produced by the asymmetry of pushing forces (due to relative time delays between the two tips) or by two unbalanced *adhesive pulls* on the two sides. In particular, the low repeatability of the adhesive pulls suggests their characterization through a dedicated on-ground experimental campaign.

The characterization of the adhesive pulls exchanged by the TM and the GPRM has been the focus of the on-ground experimental campaigns performed by the University of Trento since the early 2000s. The *Transferred Momentum Measurement Facility* (TMMF) has been developed: a mock-up of the TM release, which allows a high measurability of the adhesive pulls and guarantees the representativeness of the experiment, has been tested in order to estimate the properties of the adhesive force at the contact between the two bodies. The estimated parameters, applied to a model of the in-flight release, allowed to predict that the effect of the asymmetric adhesive pulls applied by the GPRM to the TM should not be critical for the residual momentum.

In this thesis we report the completion of the research on the effect of adhesion in the TM release of LISA Pathfinder, by means of additional on-ground experimental campaigns, and by comparing the predictions with the actual behaviour of the GPRM in the releases performed during the early stages of the LISA Pathfinder mission (2016).

Prior to the launch of the mission, the on-ground TMMF facility has been modified in 2015 in order to host a copy of the GPRM, thus increasing the rep-

resentativeness of the experiment w.r.t. the nominal release. The on-ground test campaign, consisting in several release tests, allowed to obtain a new (conservative) estimation of the effect of adhesion in the TM release of LISA Pathfinder.

The estimation of the adhesive effect, which yielded first a conservative prediction, has been then improved by investigating in detail the release dynamics of the TMMF. Thanks to a vibration mode-based model of the TMMF, the effect of the adhesive pull on the measured dynamics has been estimated with its uncertainty, thus yielding a more precise prediction for the in-flight case.

The launch of the LISA Pathfinder mission occurred on December 3, 2015, and prior to the beginning of the scientific operations the two TMs have been injected into free fall. Due to the criticalities observed in the releases, an additional *in-flight release test campaign* has been planned during the end-of-life activities (June 2017), by alternating several times grab and release of each TM. The in-flight release campaign yielded a statistical distribution of the residual momentum of the TM at the release, which we analysed in detail in order to characterize the actual in-flight GPRM performance. In particular, we focused on the deviation of the predictions (based on the assumption of nominal release) w.r.t. the in-flight observations, by looking for the motivations of the residual momentum measured in the in-flight case.

Note to the reader

The thesis is composed of an Introduction and of three main chapters, whose sequence reflects the evolution of the PhD research between November 2014 and November 2018. The chapters are thought to be read in the reported order; this holds especially for chapters 2 and 3, since in chapter 3 the data of the on-ground experimental campaign of chapter 2 are analysed in detail. The content of chapter 4, which discusses the in-flight experiments of LISA Pathfinder, is mostly independent of the contents of the previous ones.

The Introduction (chapter 1) should address the reader by presenting the context of the research. In particular, in the Introduction the problem of the release in LISA Pathfinder (section 1.1) is the main focus of all the work and should be therefore considered first. For a better comprehension of the goal of the on-ground experimental campaign, we suggest also section 1.2, which describes the on-ground campaigns prior to 2014.

The organization of each chapter should provide an overview of its content. At the beginning of each chapter, the aim of the work is initially declared and the research is summarized by reporting briefly the content of each section.

A similar approach has been adopted for the introduction of each section, with respect to the content of each subsection. We remind that a section is defined by two numbers (e.g. 2.5) and a subsection by three numbers (e.g. 2.5.1, but we will often write "section 2.5.1" for simplicity).

At the end of each chapter, we summarize the main conclusions in a dedicated section, by focusing on the lesson learnt.

In Conclusions and Future Developments (chapter 5) we summarize the content of the book by recalling the main results of the chapters and the criticalities occurred in the research, with an additional focus on the possible developments and further activities.

Many additional analyses, computations and tables that are not strictly necessary for the comprehension of the chapters are reported in the Appendix. The appendices A, B and C refer to chapters 2, 3 and 4 respectively.

Since in the description of the research many acronyms and definitions are introduced, a list of the most commons terms is reported.

At the end of the book the reader can find a comment on the original contributions of the research, the acknowledgements, a list of the PhD activities (including the scientific production), and the bibliography.

Contents

Preface **3**

Note to the reader **5**

1 Introduction **11**
1.1 Test Mass release in LISA Pathfinder 12
1.1.1 LISA and the detection of gravitational waves 12
1.1.2 LISA Pathfinder 13
1.1.3 The inertial sensor in LISA Pathfinder 14
1.1.4 The problem of the release into a geodesic 17
1.1.5 GPRM structure and release action 19
1.1.6 Dynamical model of the in-flight release 24
1.2 Experimental estimation of the adhesive impulse 32
1.2.1 Measurement of small impulses in aerospace applications . 32
1.2.2 The Transferred Momentum Measurement Facility 34
1.2.3 Prediction of the in-flight release momentum 36

2 On-ground GPRM testing **39**
2.1 Principle of the experiment 40
2.1.1 Differences with respect to the in-flight release 40
2.1.2 Release experiment 40
2.1.3 Dynamical model of the on-ground release 42
2.1.4 Information in the free flight velocity 44
2.1.5 Reproduction of the in-flight conditions 45
2.2 Experimental setup 47
2.2.1 Experimental architecture: overview 47
2.2.2 Environments: lab, clean booth and vacuum chamber . . . 48
2.2.3 The sensing device: TM and pendulum 49
2.2.4 Blocking and release system 52
2.2.5 Positioning and alignment system 55
2.2.6 Measurement systems 57
2.2.7 Camera 58
2.2.8 Vibration isolation 59
2.2.9 Pumping and vacuum system 60
2.2.10 Controllers 61
2.2.11 User interface 62

2.3 TM release in the TMMF 64
2.3.1 Experimental procedure 64
2.3.2 Test output 66
2.4 Experimental results 71
2.4.1 Release test campaign 71
2.4.2 Sensitivity to orientation 72
2.5 A conservative estimation for a nominal release 75
2.5.1 From on-ground results to in-flight estimation 76
2.5.2 Probability distribution 79
2.5.3 Comparison with previous predictions 81
2.6 Summary of the on-ground GPRM testing 82

3 Vibration mode-based impulse estimation 83
3.1 Information in the release signal 84
3.1.1 Time-displacement reference frame 84
3.1.2 Harmonics in the free flight signal 87
3.1.3 Determination of the free flight interval 88
3.2 Free flight signal and fit of the harmonics 91
3.2.1 Peaks in the free flight signal 92
3.2.2 Frequency - velocity diagram 93
3.2.3 Estimation of the harmonics in the free flight interval . . . 95
3.3 Dynamical model of TM vibrations 99
3.3.1 Description of the mass as a continuous vibrating system . 100
3.3.2 Estimation of modal parameters 101
3.4 Estimation of the adhesive impulse 107
3.4.1 Mode inputs and general solution 110
3.4.2 Comparison between model and measurement 115
3.4.3 Nominal solution 120
3.4.4 Effect of uncertainties: Monte Carlo simulation 124
3.4.5 Effect of a misalignment of the TM w.r.t. plunger and interferometer 130
3.4.6 Conclusions 130
3.5 Summary of the impulse estimation 132

4 In-flight TM release 135
4.1 GRS and nominal release 137
4.1.1 Reference frame 137
4.1.2 Nominal release procedure 138
4.1.3 Measurement and control system 143
4.2 Release operations in LISA Pathfinder 146
4.2.1 Releseas of February 2016 146
4.2.2 GPRM identification and release campaign 150
4.2.3 Identification tests 152
4.3 Release campaign and plunger release velocities 158
4.3.1 Test classifications and release strategies 159
4.3.2 Results: plunger release velocities 160
4.3.3 Capacitive control performance 164

4.4 Analysis of the in-flight release data . . . 167
4.4.1 Main instants of a single test data set . . . 168
4.4.2 Detection of the main instants in the data set . . . 168
4.4.3 Analysis of the pin release velocity . . . 172
4.5 Pin release velocities in the release campaign . . . 179
4.5.1 Momentum at the release and compliance with the requirements . . . 179
4.5.2 Dependence on the preload force . . . 182
4.5.3 Relation between reliability and momentum . . . 183
4.5.4 Kinetic energy after impacts . . . 185
4.5.5 Kinetic energy variation due to plunger retraction . . . 186
4.5.6 Velocity directions and deviation from the nominal pin release 188
4.6 Exclusion of the nominal release configuration . . . 191
4.6.1 Reference test . . . 192
4.6.2 Assumption: pin impulses on the landing area . . . 193
4.6.3 Centred pin contact . . . 196
4.6.4 Decentred pin contact . . . 202
4.6.5 Buckling instability of the plungers . . . 204
4.7 TM-plunger contact in the fast pin releases . . . 209
4.7.1 Possible motivations of TM-plunger contact at the pin release 209
4.7.2 Orthogonal impulse model . . . 210
4.7.3 Electrostatic effect . . . 216
4.7.4 Information of the orthogonal impulse model . . . 217
4.7.5 Representativeness of the reliable tests . . . 218
4.8 Slow pin releases . . . 224
4.8.1 Slow pin release: nominal case . . . 224
4.8.2 Pin release velocity in the slow pin releases . . . 226
4.8.3 Information in the slow pin releases . . . 232
4.8.4 Effect of plunger retraction . . . 234
4.9 Future development of the GPRM . . . 236
4.9.1 Possible motivations of the non-nominal behaviour of the GPRM . . . 236
4.9.2 Release strategies without modifications of the GPRM . . . 237
4.9.3 Modifications of the GPRM . . . 239
4.9.4 Experimental testing of the GPRM . . . 241
4.10 Summary of the in-flight release tests . . . 243

5 Conclusions and future perspectives 245

Appendix A On-ground GPRM testing 251
A.1 Alignment procedure . . . 251

Appendix B Vibration mode-based impulse estimation 253
B.1 Identification of the peaks . . . 253
B.1.1 Estimation of the amplitude of oscillation . . . 253
B.1.2 Probability density function and threshold . . . 255
B.2 Pattern recognition . . . 257

B.3 Fit of the free flight interval . . . 259
B.3.1 Fit model . . . 259
B.3.2 Steps of the iterative fit . . . 260
B.4 Analytical response of TM continuous model . . . 262
B.4.1 Modal projection of concentrated forces . . . 262
B.4.2 Modal projection of forces acting on the TM . . . 262
B.4.3 Initial mode deformation . . . 265
B.4.4 Pin force . . . 265
B.4.5 Needles force . . . 267
B.5 Monte Carlo simulation in a case with no adhesion . . . 268
B.6 Compliance with the measured phases . . . 269
B.6.1 Result for 1 test . . . 269
B.6.2 Results for 10 tests . . . 271

Appendix C In-flight TM release **275**
C.1 Reliability tests . . . 275
C.1.1 Reliability test based on pre-release noise . . . 275
C.1.2 Reliability test based on reference signals . . . 276
C.2 Motivations of the TM-plunger impulses . . . 280
C.2.1 Impact between plunger and TM . . . 281
C.2.2 Continuous push of the plunger . . . 282
C.3 Effect of pyramidal plunger on ϕ rotation . . . 285
C.4 Exclusion of stiffness asymmetry in the slow pin tests . . . 289
C.5 Capacitive forces between plunger and TM . . . 291
C.6 Results of the in-flight release campaign . . . 295

Acronyms and common terms **311**
Acronyms . . . 311
Common terms . . . 311

Original contributions **315**

Acknowledgements **317**

PhD activities **319**
Scientific Production . . . 319
Participation to Congresses, Schools and Workshops . . . 320
PhD Courses . . . 320
Teaching Activity . . . 320

Bibliography **323**

Chapter 1

Introduction

In this chapter the context of the research is discussed.

Section 1.1 is dedicated to the problem of the release in LISA Pathfinder mission. We describe the scientific motivations (section 1.1.1) and the principle and structure of the experiment (section 1.1.2). We move then to the main focus of this work, which is the release of the proof mass of the Gravitational Reference Sensor (1.1.3) into a geodesic. The motivations of the caging and release mechanism and the criticalities related to the release are discussed in section 1.1.4, with particular attention to the problem of adhesion; these considerations have been a basis for the design of the release mechanism 1.1.5. Based on the working principle of the release mechanism, a simple dynamical model of the release has been developed 1.1.6; this model will be often recalled in the chapters of this book as a reference model (and especially in chapter 4, where the performance of the release mechanism will be discussed); in this section, the main criticalities related to the estimation of the adhesive force at the release are reported, and the representativeness of the assumption of *nominal release* is commented.

In section 1.2 we resume the principles and the main results of the dedicated experimental campaign hosted at the University of Trento from the early 2000s. The estimation of small impulses, which is a common task in the scientific research and especially in the aerospace field (1.2.1), is the purpose of the Transferred Momentum Measurement Facility (section 1.2.2): the effect of the adhesive pull between a release tip and a proof mass has to be estimated in order to project the results to the in-flight case. The latest results up to 2015 are shown in section 1.2: the measurements of the facility are considered for a prediction of the performance of the release mechanism in LISA Pathfinder. The on-ground setup in its latest configuration will be described in chapter 2, together with its measurements and related predictions (also analyzed in chapter 3).

The contents of this chapter are mainly a summary of previous scientific works, reported in the bibliography.

1.1 Test Mass release in LISA Pathfinder

LISA is a scientific mission aimed at the detection of gravitational waves (section 1.1.1). The principle of the mission is the measurement (through laser interferometry) of the relative displacement between two free falling masses, in order to estimate the effect of gravitational waves on their relative acceleration. For the testing of the main technologies involved in LISA mission, the LISA Pathfinder spacecraft has been successfully launched in December 2015 (section 1.1.2).

A critical task in LISA Pathfinder is the release of the proof mass that constitutes the inertial sensor (section 1.1.3), which has to fluctuate freely in the spacecraft in order to follow a geodesic trajectory. The proof mass needs to be caged during the launch and released when the spacecraft is in orbit. The release mechanism can transfer to the mass a residual momentum that has to be maintained under a limit, according to the maximum control authority of the capacitive actuation on the proof mass; in particular, the adhesive bonds at the contact between mass and release tip can create a critical adhesive pull (section 1.1.4).

Based on these considerations, an appropriate release strategy has been established and a release mechanism (section 1.1.5) has been designed. The release mechanism guarantees the rupture of the adhesive bonds; however, effects of asymmetries can still arise with this configuration, as described in the model of section 1.1.6 (which contains a brief description of the adhesive forces at the contact). The estimation of the asymmetry effects due to adhesion will be first addressed in the description of the on-ground setup in section 1.2.

1.1.1 LISA and the detection of gravitational waves

The existence of gravitational waves (GW) is one of the main consequences of Einstein's general relativity [1]. According to general relativity [2], gravity manifests itself as massive objects bending the structure of spacetime [3]. The motion of massive bodies produces periodic perturbation of the spacetime, with sequential stretches and compressions: as a consequence, the distance between two particles is rhythmically increased and reduced as a gravitational wave propagates in the sorroundings [3]. This perturbations, which are generally tiny since gravity is a weak interaction, can be enhanced if they arise from intense gravitational field: this is the case for astrophysical objects like black holes, white dwarfs and neutron stars [3]. Gravitational waves could therefore provide a new window on the universe, enabling us to detect the effects of the earliest moments of the big bang and of the formation of black holes [1].

The detection of gravitational waves would therefore constitute a strong confirmation of Einstein's theory. An indirect proof of the existence was found in 1974 by Hulse and Taylor, which discovered a pulsar in a binary system [4]. Experiments for a direct observation date back to the 1960s, and were based on the measurements of small variations in the length of metal bars [3] [5].

In the last years, the most important experiments for the direct detection of gravitational waves are based on the laser interferometry, which increases the sensitivity to the effect of gravitational waves by measuring tiny variations in

the length of perpendicular arms (each with an extension of several kilometers). LIGO (Laser Interferometer Gravitational-Wave Observatory) observed in 2015 a transient gravitational wave signal, due to a binary black hole merger [6]. However, the bandwidth of GWs detectable through on ground setups is limited , because of the limited length of interferometers (few kilometres) and due to the unshieldable background of local gravitational noise [7].

LISA (Laser Interferometer Space Antenna), programmed for 2034, is a space observatory of gravitational waves, based on the interferometer principle [7]. It consists of a cluster of three spacecraft, disposed at the vertices of an equilateral triangle with sides of 50 millions of kilometres. Each spacecraft hosts two test masses: a single test mass is associated to a corresponding test mass on one of the two remaining spacecrafts, and a laser beam measures the distance between the two test masses. If each spacecraft is designed in order to isolate all the disturbances of the relative motion except the gravitational effects, the length of the arms of the interferometer are uniquely affected by gravitational phenomena. In such a condition, gravitational radiations can be detected over a broad band at low frequencies (0.1 mHz - 100 mHz), which are associated to many GW phenomena [8].

1.1.2 LISA Pathfinder

LISA Pathfinder (launched on December 3, 2015) is a mission dedicated to the testing of the key technologies to be hosted on the future LISA mission [9] [10]. The main goal of LISA Pathfinder is the experimental demonstration of the free fall of *test masses* (TMs) at the level required for LISA [11] [12]. It consists of a single spacecraft in which two cubic test masses are hosted (referred to as TM1 and TM2, as shown in figure 1.1): TM1 acts as an inertial sensor, driving the motion of the satellite through a μN-thruster actuation in order to keep TM1 centred in its *housing* w.r.t. the sensitive axis (x), while a capacitive control forces TM2 to stay centred in its housing as well. The relative motion of the two test masses is monitored through an interferometer, and therefore the relative acceleration $\Delta\ddot{x}$ is measured. If the non-gravitational disturbancies affecting the relative acceleration $\Delta\ddot{x}$ can be minimized or measured (including for instance the capacitive actuation acting on TM2), the differential acceleration Δg (i.e. the quote of the measurement free from spurious accelerations) can be estimated. The spacecraft is therefore designed in order to minimize external effects acting on the inertial sensors (pressure due to sunlight, charged particles of the solar wind and micrometeoroids) and any electrostatic actuation acting on the TMs has to be subtracted from $\Delta\ddot{x}$.

Any perturbation due to GWs would therefore correspond to an oscillation of the Δg signal. In order to guarantee the readability of such an effect, the signal to noise ratio has to be maximized. LISA Pathfinder does not have the sensitivity to detect GWs, due to the reduced length of the interferometer, but is sensitive to the differential acceleration [3]: the goal of the mission is the reduction of the Δg noise up to a level that allows a future detection in the LISA setup. The requirement for LISA corresponds to a maximum PSD (Power Spectrum Density) level of the Δg noise, as a function of the frequency; a corresponding requirement for LISA

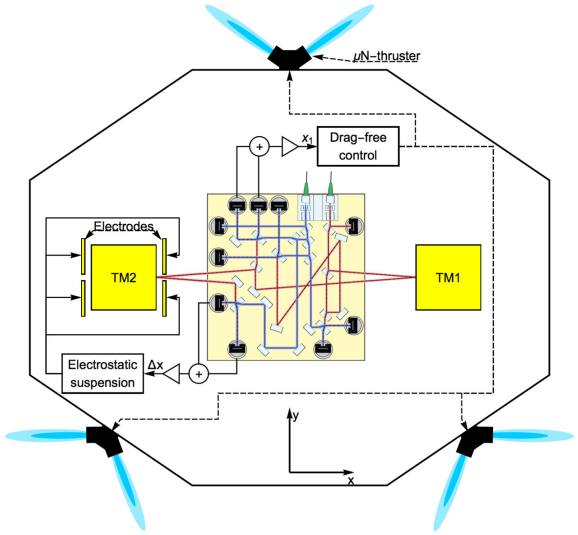

Figure 1.1: schematic of LISA Pathfinder spacecraft (from [11]). x_1 (TM1 dispacement along x axis) drives the μN-thruster control while Δx (measured through the laser interferometry) drives the electrostatic suspension of TM2.

Pathfinder has been established by taking into account the different structure of the experiment [11].

50 days after the launch and after having separated from its propulsion module, LISA Pathfinder reached the L1 Lagrange point of the Sun-Earth system; then, after the commissioning of the instrument, the *release* of the two TMS into free fall was performed in mid-February, in order to start the science operations on March 1, 2016. The release of the TMs into free fall is a critical issue (described in 1.1.4) and is the main focus of this thesis.

LISA Pathfinder demonstrated that the reference test masses can be put in free fall with a relative acceleration noise satisfying the requirements; the amplitude spectral density of the noise $S_{\Delta g}^{1/2}$ is below the LISA requirements by more than a factor 5 at the 1 mHz frequency limit, and of a factor 1.25 in the 0.5 mHz - 10 mHz bandwidth [11] [13] [14].

In addition, several dedicated experiments for the test of the LISA technologies were performed [15] [16] [17] [18].

1.1.3 The inertial sensor in LISA Pathfinder

Each of the two masses is hosted in the *Inertial Sensor Subsystem* (ISS), which is composed of a dedicated vacuum chamber, a capacitive sensor electrode housing (consisting of 18 electrodes, guard ring and housing structures), a caging system to secure the TM during launch and to release it in flight, a system for test mass charge management and diagnostic items [10] [19]. The ISS is represented in figure 1.2.

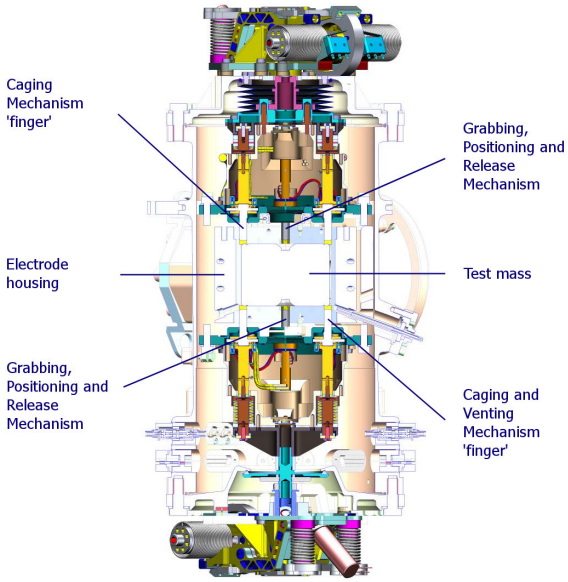

Figure 1.2: inertial sensor in LISA Pathfinder, showing the main mechanical and electrical components involved in this work (courtesy of ESA). In the picture, the TM is caged by the Caging and Vent Mechanism (CVM) and grabbed by the Grabbing Positioning and Release Mechanism (GPRM).

We distinguish in the following the two main components of the ISS which we will refer to in this work: the reference sensor and the caging and release system.

Gravitational Reference Sensor and Test Mass

The test mass and the sorrounding capacitive sensor constitutes the *Gravitational Reference Sensor* (GRS) [10]. The GRS, mainly developed by the University of Trento and its consortium, is the core payload on the spacecraft [20].

The test masses (TMs) are the main bodies involved in the experiment. Each TM consists a gold coated 46 mm cube, made of a AuPt, low magnetic susceptibility alloy, with a mass of approximately 1.928 kg and high density to minimize the displacement caused by disturbances [21] [22] [18] [23]. The masses are separated from the walls of the sensor by gaps of $2.9 \div 4$ mm [18], which mitigate the effect of forces produced by charge patches located on the surfaces of housing and TM [24]. Each TM differs from a perfect cube because of indentations designed for the contact with the caging and release mechanisms.

Each TM is hosted inside a sensing *electrode housing* (EH), a hollow molybdenum structure hosting gold-coated sapphire electrodes [25], as shown in figure 1.3. The electrodes of the GRS can act alternatively as a capacitive measurement system or as a capacitive actuator (which can exert an electrostatic force of tens of fN on the TM [10], with a maximum force authority of $5 \cdot 10^{-7}$ N [26]). To achieve

actuation, a voltage difference is established across electrode and proofmass [27]. The main properties of the GRS as a measurement system will be discussed in section section 4.3.3, in the context of the measured motions of the TMs at the release).

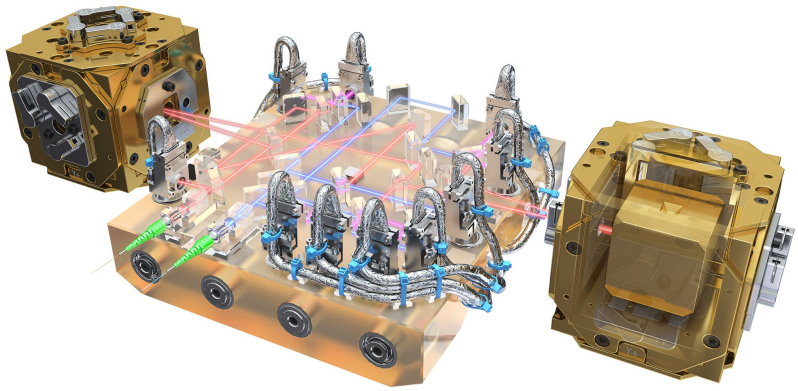

Figure 1.3: LISA Technology Package core assembly without the vacuum enclosure (courtesy of ESA). The picture shows the *optical bench* between the two TMs. The right TM is shown here in free fall inside its housing; the indentations on the TM are shown.

Caging and release system

The caging and release system, which has to secure the TM during the launch and to release it into free fall before the scientific operations, is the sum of two mechanical subsystems: the *Caging and Vent Mechanism* (CVM) and the *Grabbing Positioning and Release Mechanism* (GPRM), both shown in figure 1.2 and in figure 1.4.

The CVM consists in a paraffin actuator system which allows 8 fingers to grasp the 8 corners of the TM [28]. The *caging* task of the CVM is to secure the TM during the launch, by providing a 3000 N holding force [10] [29], without damaging the TM surface. The CVM is also designed to grab, position, centre and release the TM in orbit, whenever needed [29]. The *venting* function of the CVM is performed by a integrated vacuum valve, opened at the same time when the bottom fingers are retracted, in order to vent the ISH to free space [28].

The GPRM is the mechanism designed for the transition from the caged configuration of the TM to the free fall. It is composed of two fingers (*plungers*), aligned with the z direction, which grab the TM on two opposite sides (with a proper geometrical coupling by means of indentations on the TM surfaces, as shown in figure

1.6). The GPRM must also be able to re-grab the TM in case the TM is out of control of the capacitive control: the small gaps between TM and housing prevent the body from high rotations and allows therefore the plungers to reach the TM indentations in any configuration [30]. Furthermore, the TM can be discharged while held by the grabbing fingers [31], which are also used to inject a bias voltage in order to have capacitive readings of the TM position and attitude. The GPRM is not operating in the science mode.

Before describing the GPRM structure (section 1.1.5), we discuss briefly the problem of the release, in order to highlight the requirements needed for such a mechanism.

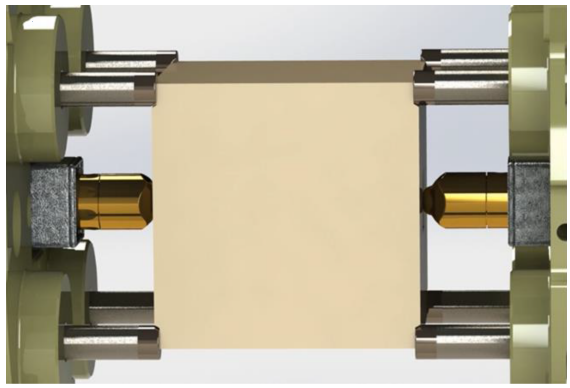

Figure 1.4: caging and release system with CVM fingers and GPRM plungers (frame of a 3D animation created by Carlo Zanoni; solid models courtesy of Airbus Defence and Space, RUAG, ESA, University of Trento).

1.1.4 The problem of the release into a geodesic

As described in section 1.1.3, the gravitational sensor is hosted in an housing with large gaps in order to reduce the effect of charge patches. This choice has three main drawbacks [24]: the TM surface and the sorrounding surfaces must be at least gold coated, in order to limit the effects of charge patches that can create noise in the force signal; the capacitive force authority is reduced due to large gaps; finally, the TM has to be heavily constrained during launch. In order to avoid serious damages to the TM during the launch (due to impacts between TM and housing), the TM cannot be left free to shake in the available gaps and a caging mechanism must be considered [32]: this function is performed during the launch by the CVM.

Once the spacecraft orbit is commissioned, the transition between the caged configuration of the TM during the launch (with a caging force range of kN) and the free fall of the TM in orbit (with a capacitive control force of fN) must be performed by dedicated release mechanisms. The release phase (whose analysis is the main focus of this work) is a critical issue in LISA Pathfinder mission [33].

Residual momentum and effect of adhesion

According to the electrostatic control force authority, a maximum *release momentum* (i.e. momentum of the TM injected into free fall) is established [34]: as a consequence, the momentum transferred by the holding mechanism at the release must be lower than the limit, producing velocities lower than 5 μm/s for translations and 100 μrad/s for rotations [24]. If the momentum at the release exceeds the limits, the control system is unable to capture and center the TM [35]. In an optimal (ideal) condition, the symmetry of the GPRM and the synchrony of the motion of the release fingers should guarantee a release of the TM with no residual momentum, thus allowing the electrostatic control to mantain the TM centred in its housing. However, the presence of *adhesive forces* at the TM-pin contact surface could have an important effect on the TM momentum at the release, such as on the synchronization of the sides of the mechanism.

For a mechanical manipulator, when the order of magnitude of the adhesive forces is comparable with the one of the holding forces of the mechanism, the adhesive effects can not be neglected [36] [37] [38]. This is particularly critical for space mechanisms, since environmental conditions (vacuum, temperature) can enhance the adhesive effects [39] by inhibiting the formation of oxide and enhancing the cold welding [26] [40]; moreover, the interaction forces between contacting bodies are not obscured by gravity field, surface contaminants caused by exposure to the atmosphere, or by acoustic noise propagated by the air [41]. The adhesive interaction between holding tips and TM converts into momentum: both the strength and the elongation of the bonds (enhanced by the presence of the gold coating) contribute to integrate impulse to the released mass [42].

The design of the release mechanism must therefore be robust w.r.t. the adhesive effect. In a case where the capacitive force authority for the position and attitude control is lower than (or comparable to) the adhesive force between the constraint and the body, the separation may be performed through a quick retraction of the caging device, relying on the body's inertia to break the adhesive bonds arising at the contacts [26] [36].

A proper design can also reduce the adhesive forces at the two sides of the TM. The adhesion force depends on the materials of the two surfaces staying in contact, on the contact area and on the contact force. The material of the surfaces is fixed because of electrostatical consideration [13]; as a consequence, the contact surfaces and forces must be minimized, in order to reduce the strength of adhesion [24].

That's why the caging function and the release function are performed through different devices. The caging function is performed during the launch by the CVM. The CVM exerts high forces on the TM: as a consequence, it needs a proper geometrical coupling with the TM through (relatively) extended indentations and is characterized by a slow dynamics. The release function is performed by two small tips of dental gold alloy [43] hosted in the plungers of the GPRM (*pins*), which are characterized by a small dimension with little contact surface, quick dynamics (thanks to their low inertia) and the possibility of applying lower forces compared to the CVM.

Injection into free fall: handover to plungers, handover to pins, release

The transition between the caged configuration during the launch and the release in orbit is composed of three different steps, summarized in figure 1.6 (which refers to the sketch of figure 1.5).

The TM is handed over to the GPRM (*handover to plungers*): the two plungers of the GPRM grab the test mass on the two opposite z sides (as shown in figure 1.2), allowing the CVM mechanism to retract. The GPRM preload at the grabbing is reduced (up to few N) in order to preserve from strong cold welding and fretting phenomena [43], and centers the TM in the housing. The geometrical coupling between the plungers and the TM is designed in order to maintain the nominal orientation of the TM w.r.t. the housing.

The preload is further reduced and the TM is engaged by two small tips (*pins*), which are extracted from the plungers and move along the plunger axis (z axis) while the plungers retract in order to control the holding force. This procedure is called *handover to pins* [44]. In the *nominal* configuration, i.e. with perfectly aligned mechanisms and no rotations (of the TM w.r.t. the housing and the plungers), this procedure guarantees a unique contact of the TM with the pins (with a small preload force in the order of $0.1 \div 1$ N to avoid damages of the gold-platinum surfaces [30]), and a gap of more than 10μm between TM and plungers.

Finally, the *release* is performed through the quick retraction of the pins (by means of the voltage fall of their piezo mechanisms); few tenths of second after the pin release, also the plungers are retracted and the TM can move freely and unconstrained. The capacitive actuation can be eventually activated in order to keep the TM centre in the housing.

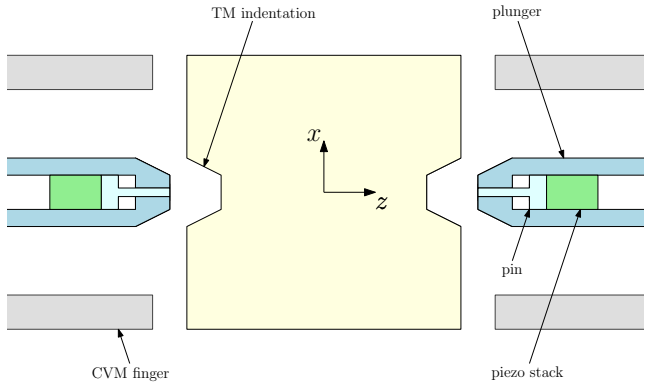

Figure 1.5: simplified sketch of caging and release system components.

1.1.5 GPRM structure and release action

We describe here the structure of the GPRM, whose on-ground and in-flight testing is the main focus of this work. The GPRM, developed by Thales Alenia Space and RUAG, has been designed by taking into account the problems described in section

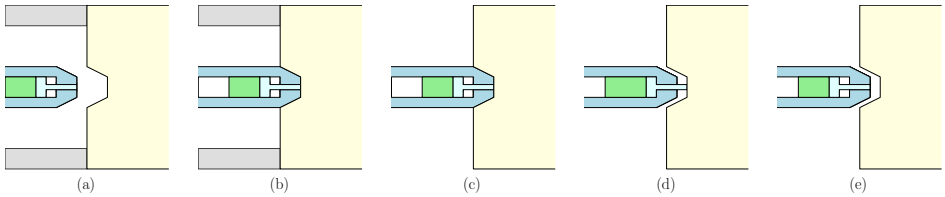

Figure 1.6: steps of the injection into free fall (only one side is shown thans to the symmetry of the system). a) TM caged by the CVM. b) TM grabbed by the plungers. c) CVM retraction. d) Pin extraction with synchronous retraction of the plunger. e) pin release.

1.1.4 and to perform the release according to the described strategy of figure 1.6.

Grabbing finger and actuation unit

The GPRM is hosted in the intertial sensor as shown in figure 1.7. It consists of 2 main sub-assemblies: the *actuator unit* (hosted out of the housing) and the *grabbing finger* (plunger), containing all the elements that are moving [45]. As shown in figure 1.7, the grabbing finger, which has a travel range of 17 mm, can enter the housing and grab the TM through a proper geometrical coupling with the TM, consisting in a recess (indentation) at the centre of each Z face of the TM. If the TM is grabbed by the two plungers, the synchronous motion of the plungers (one extended and one retracted) can centre the TM over a range of ± 0.5 mm along z axis [30].

In figure 1.8 the components of the GPRM are shown. The grabbing finger is fixed in the lateral direction by a spring preloaded guiding system composed of sliders on one side and rollers on the opposite sides [45]; the motion of the grabbing finger along the z axis occurs thanks to an actuator consisting in a piezo electric "feet" walk [30]. As shown in the picture, close to the endstop bracket of the GPRM a force sensor beam and a strain gauge are hosted, for the feedback of the TM-plunger contact force and of the z extension of the plunger.

The grabbing finger is made of titanium; on the front part, a gold-platinum cap is fixed [46], in order to satisfy the electrostatic requirements for the bodies inside the inertial sensor. The two plungers (Z+ and Z-), whose external diameter is 10 mm, are identical except for the shape of the plunger end, as shown in figure 1.9: the Z+ plunger has a conical shape in order to avoid rotational torsion forces on the TM, while the Z- plunger has a pyramidal shape for the rotational positioning of the TM.

For the release in orbit, the TM shall be positioned in the centre with accuracy smaller than 100 μm in all axes and a rotational accuracy smaller than 1600 μrad about all axes; these limits have been tested and verified through dedicated on-ground test campaigns [31].

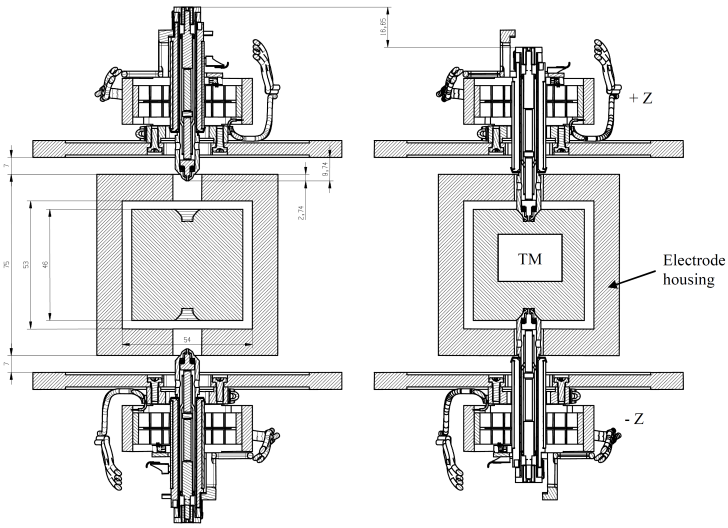

Figure 1.7: retracted and grabbed positions of the Z+ and Z- grabbing fingers (courtesy of ESA [30]).

Release tip and piezo actuation

The main task of the plunger is the positioning and the release of the TM. As discussed in section 1.1.4, the positioning prior to the release is performed by the two plungers, but the release is performed by two *pins* that grab the TM through the handover to pins, as sketched in figure 1.6.

The position of the release tips (pins) inside the plunger is shown in figures 1.8 and 1.10. The release tip is a small body (0.4 g [47]) made of dental gold alloy [24] with a small cylindrical end (diameter 0.8 μm, curvature radius 10 mm). The release tip is rigidly attached to a *piezo stack* actuator (3x3x18mm) and the system is preloaded by means of washer springs.

The nominal relation between the voltage applied to the piezo and the piezo elongation is linear: the release tip is completely retracted if the voltage is 0 and extends of 18 μm if the voltage is 120 V. In a nominal configuration, the pin touches the TM after an initial extension of 4 μm; as a consequence, after the handover to pins the TM is held by the pin with a distance between the plunger shaped surfaces and the TM of approximately 14 μm in z direction (see section 4.1.2). The retraction of the release tip occurs when the voltage source is turned off and the piezo is short-circuited through a resistor: the instantaneous fall of the voltage make the compressed high-stiffness washer spring extend, allowing a quick retraction of the pin with the rupture of adhesive forces at the TM-pin contact. According to dedicated measurement tests, the retraction time is less than 0.2 ms [48] [49].

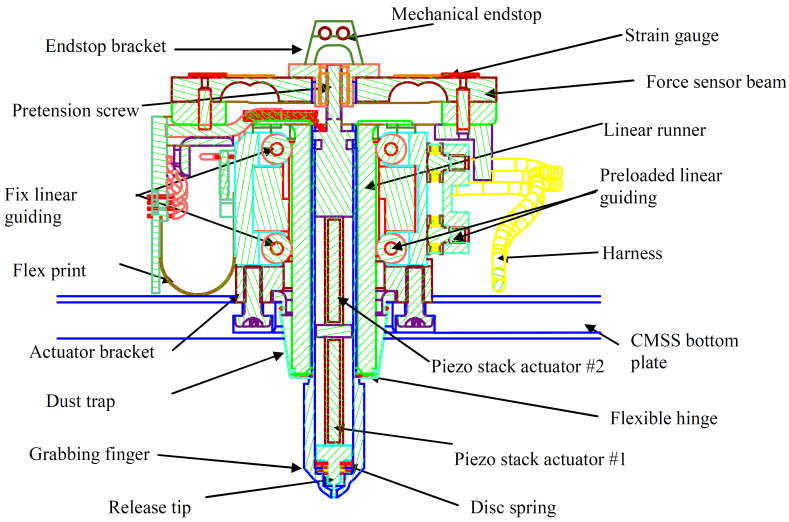

Figure 1.8: cut view of the GPRM with extended grabbing finger (courtesy of ESA [30]).

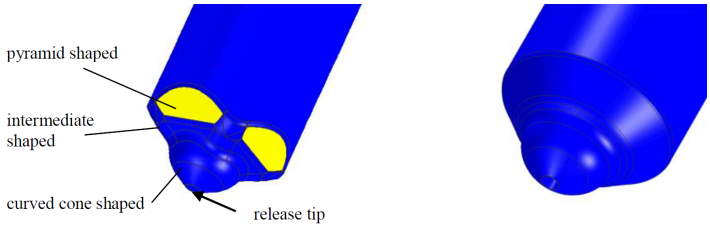

Figure 1.9: Z- plunger (left) and Z+ plunger (right). Courtesy of ESA [30].

Criticalities at the release

As previously described, the injection of the TM into free fall is performed through the quick pin retraction; nominally, the symmetric retraction of the pins should guarantee a TM release with no residual momentum. However, some problems that lead to an unexpected TM residual momentum could occur.

If we consider a *nominal* situation in which the TM is uniquely in contact with the pins before the release, the criticality of the release is the result of two effects [50]. First of all, the mechanical action could be not really symmetrical on both sides, thus leading to a *net pushing impulse* given by the combination of preload force and delay of one of the two sides of the release mechanism. Second, on each TM-pin contact the rupture of the adhesive bonds creates an adhesive impulse according to a force-elongation profile ([43]). The adhesive forces at the TM-pin contact have a limited repeatability: the strength of the adhesive bonds is affected by the surface topography at the microscopic scale, which is not controlled by the

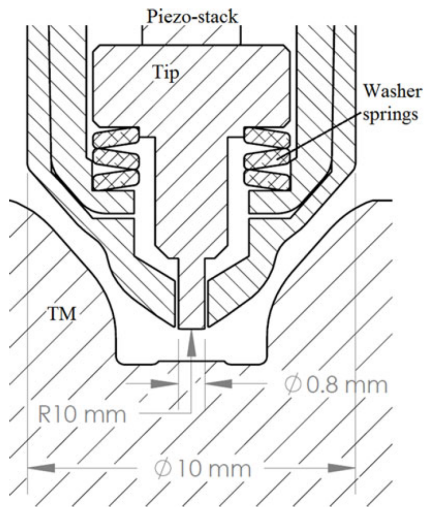

Figure 1.10: lumped model of the piezo actuator (from [24]).

conventional machining processes [51]. If the two adhesive effects differ on the two sides of the TM, the *net pulling impulse* can increase the residual momentum at the release [51]. These *asymmetry effects*, which be explained through a specific model in section 1.1.6, can contribute to a TM residual momentum along z direction. The analysis of these asymmetry effects (and especially the adhesive effect) and their possible criticality on the in-flight release is the focus of the first two chapters (2 and 3) of this thesis.

The asymmetry effects are the only problems that can arise if the TM is held uniquely by the pins before the release. In case of an excessive relative rotation between TM and plungers (therefore in a *non-nominal* case), the TM could be in contact also with the plungers (and not only with the pins) at the release: in particular, when the maximum allowed tilt angle (rotation about x or y axis) is exceeded, the pyramidal shape of the plungers can remain in contact with the indentation of the test mass also after the handover to pins, thus making not possible a nominal release [52]. In the early stages of the GPRM design, the problem of a contact after the handover to pins was excluded thanks to the design tolerances [44]. However, a TM-plunger contact could occur also if the plunger has an unexpected lateral or axial motion, and some analyses of the plunger motion has highlighted a critical lateral motion of the plunger when its motion is inverted [53] [54]. As a result of this lateral motion, with the final configuration (slider-roller) the risk of residual TM-plunger contact after the handover to pins was considered "moderate"; in addition, the risk of re-contact after the retraction of the plunger was considered "high" [55]. Moreover, we will see in chapter 4, where the in-flight release data will be analyzed, that the contact between TM and plunger at the release cannot be excluded.

1.1.6 Dynamical model of the in-flight release

In the following, we discuss a model for the in-flight release. This model takes into account a profile of adhesive force and the possible asymmetry of the motion of the two pins. Notably, the model of the release considers a *nominal release* condition.

The model will be considered in chapter 2 as a reference for the description of the on ground GPRM testing and for the prediction of the in-flight release based on the experimental results. It will be recalled also in chapter 4, in order to analyse the in-flight results and discuss the possible deviations from the nominal condition.

Nominal release and its representativeness

We mean with *nominal release* a TM release having the following properties (a further definition will be given in section 4.1.2):

1. after the handover to pins and the application of the target preload, the TM is in contact with the GPRM only by means of the pins, which touch the mass at the center of the landing area. Therefore, no additional contact occurs between the plungers and the TM.

2. the TM is aligned with respect to the housing before the release, centred at the zero reference position and with negligible inclinations of its surfaces with respect to the housing.

3. the plungers and the pins are perfectly aligned with the TM, i.e. the plungers axes and the centers of the landing areas of the TM lie on the z axis.

4. at the release, performed through the retraction of the pins, the forces exchanged by TM and pin are perfectly aligned with z axis, and no contact between the TM and the plungers occurs.

For instance, the sketch of figure 1.6 refers to a nominal release. In this condition, the resulting motion of the TM after the pin release (and before any contact with plungers or housing) will be uniquely along z axis. Therefore we can reduce the problem to a mono-dimensional dynamics if the hypothesis of nominal release is assumed.

The nominal release is assumed in this thesis (especially for chapters 2 and 3,) since we will focus on the independent effect of adhesion on the final in-flight velocity. In other words, we want our model to predict the effect of adhesion in absence of other effects (even more important), like a possible contact between plunger and TM on the indentation surface (at the release or immediately after the release). We follow the approach of the previous TMMF campaigns (see section 1.2 and [56]) where the results of the on-ground testing have been always considered for a prediction based on the nominal case. The task of the Industrial Engineering Department of the University of Trento was indeed the estimation of the effect of adhesion in the release, and not a complete prediction of the in-flight release velocity (which requires the consideration of all the possible contribution to the in-flight momentum, also non-nominal).

The nominal release corresponds obviously to an *ideal* case, whose representativeness has to be discussed. With reference to the previous list, we comment each assumption:

1. as commented in section 1.1.5, the contact between TM and plunger after the handover to pins and before the release was excluded by the tolerances of the design, but if we consider the critical lateral motion of the plunger (observed in tests performed on the GPRM) such a contact cannot be excluded. In this condition, transversal impulses (along x and y directions) could be applied from the plungers to the TM, leading to transversal motion, rotation and in general to a completely non-nominal behaviour.

2. the assumption of perfectly centred TM w.r.t. to the housing simply allows to consider that the TM is at the zero reference position (for both translations and rotations). Deviations of the initial position and attitude from the zero reference do not influence the dynamical model of the release, which focuses on the final release momentum.

3. the misalignment of the direction of retraction of the pin with respect to the orthogonal to the TM surface is neglected, for two reasons: first of all, the quantity is limited thanks to design requirements [56] (in section 4.6 we will consider a worst-case misalignment due to the geometry); second, it produces shear stress on adhesion patch that reduces the strength of adhesion and its criticality, thus making the assumption conservative [56].

4. the orthogonality of the force w.r.t. the TM surface is the result of the previous assumptions. The most critical assumption is the absence of contacts between TM and plunger after the release, since (as commented in section 1.1.5) the lateral motion of the plunger is very critical when the plunger retraction is commanded (few seconds after the pin release).

In conclusion, the nominal release is representative of the in-flight condition if we assume that no contact between TM and plunger occurs at the pin release and at the plunger retraction.

Force profiles

In figure 1.11 the force profiles on the two Z sides of the TM in the in-flight nominal configuration are shown. Before time 0, the TM is in equilibrium under the effect of the two opposite pushing forces whose value is f_0 on both sides. The nominal length of the extracted pins is 18 μm.

Once the release is commanded, the two pins retract very quickly from the extended length to 0. We can assume in principle that the two pins do not start their motion at the same time; this can be due to mechanical motivations or delays in the circuit. As a consequence, we can consider that at time 0 one of the two pins is retracted, while the other one starts with a *time delay* t_D.

We consider also that the two pins can have a different velocity during the retraction. Under the nominal preload (0.3 N), the Hertzian penetration of the pin in the landing area of the TM was estimated approximately equal to 0.1 μm [57];

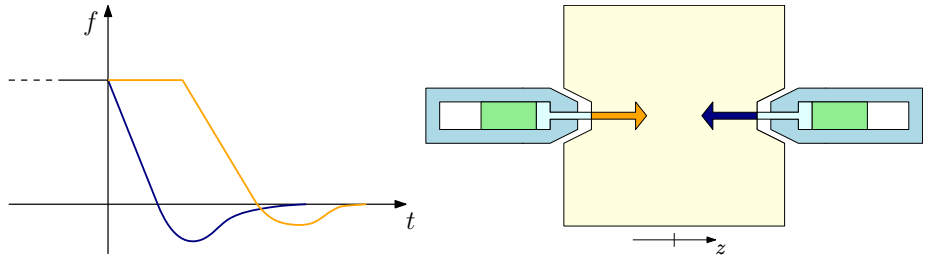

Figure 1.11: force profiles on the two sides of the TM during the release. The forces are considered positive if directed towards the centre of mass of the TM (i.e. they are defined as pushing forces). In the picture, the shapes of the curves are distorted and exaggerated in order to highlight the curve properties.

as a consequence, thanks to the rigid stiffness of the piezo actuation mechanism (section 1.1.5), we can assume that the preload is 0 when the pin has retracted of 0.1 μm; the null preload is reached for each pin in the *time-to-0-preload* (t_1 in the following).

Once the pushing force of the pin on the TM has reached the null value, the pin detaches from the mass. A further pin retraction produces an adhesive pull of the pin to the mass (negative force in the graph of figure 1.11). The force adhesive profile is generally unknown; in previous works [24], a reasonable force-elongation profile was assumed, due to the constant velocity of the pin retraction. At the complete rupture of the adhesive bonds, the pin detaches from the TM.

As a consequence, on each side of the TM the force applied by the pin is a *pushing force* (due to the preload) as long as the contact holds; it becomes a *pulling force* (due to adhesion) when the pin detaches from the landing area. The force profiles of the two pins are reported in figure 1.12.

Impulses applied on the TM and linear momentum

For each side of the TM, the impulse applied to the TM from time 0 is the integral of the described force profile, as shown in figure 1.12. The overall impulse applied to the TM during the release, which is the vector sum of the two opposite impulses, is equal to the variation of the TM linear momentum and therefore (since the TM is in equilibrium before the release) to the TM linear momentum after the release.

For the Z+ and Z- pins (figure 1.12), we have that their total impulses given to the TM (ι^+ and ι^- respectively) are given by the following equations:

$$\iota^+ = -\frac{1}{2} f_0 t_1^+ + \iota_{adh,z+} \tag{1.1}$$

$$\iota^- = f_0 t_D + \frac{1}{2} f_0 t_1^- - \iota_{adh,z-} \tag{1.2}$$

where t_1^+ and t_1^- are the two times-to-0-preload, $\iota_{adh,z+}$ and $\iota_{adh,z-}$ are the two adhesive impulses (integrals of the adhesive forces over the corresponding time

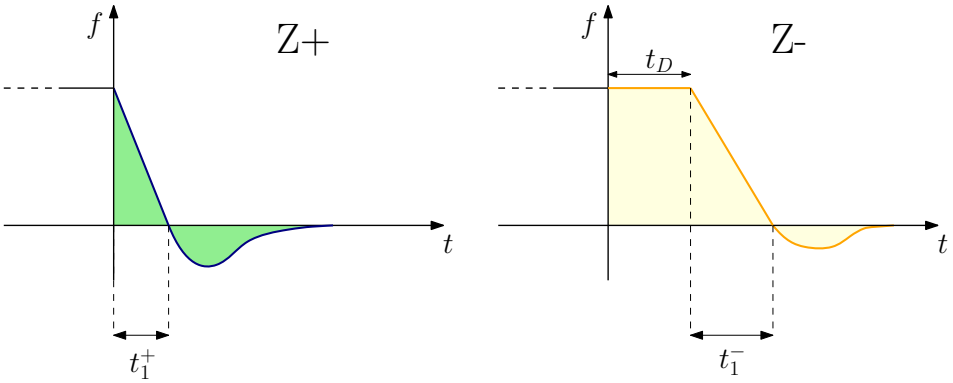

Figure 1.12: impulses associated to the two force profiles (left: Z+ pin, right: Z- pin). The areas in the positive force half-plane correspond to positive (pushing) impulses; the areas in the negative force half-plane correspond to (pulling) negative impulses.

period), and t_D is the delay of the Z- pin w.r.t. the Z+ pin. In the equations, we refer to figure 1.11 and the sign of each contribution is considered positive if directed towards the positive z axis.

Notice that, in order to write equation (1.2) for Z- pin, we have considered that the pin force remains constant for a time t_D after the retraction of the opposite pin. This is a reasonable simplification since we are assuming that t_D is much lower than the period of the TM-plunger system when considered as a mass-spring system; in other words, the duration of the elastical relaxation of a preloaded plunger ($\approx$ 3.5 ms, according to the estimation of section 4.2.3) is much higher than the duration of the phenomenon ($\approx$ 0.1 ms) [57]. This consideration allows to approximate the slow decrement of the pushing force of the plunger with a constant value while one pin has started its retraction and the other hasn't started the retraction yet (this motivates the constant force of the Z- profile for a time t_D in figure 1.11).

The total impulse given to the TM will be

$$\begin{aligned} Mv_{flight} &= \iota^+ + \iota^- && (1.3)\\ &= f_0 t_D + \frac{1}{2} f_0 (t_1^- - t_1^+) + \iota_{adh,z+} - \iota_{adh,z-} && (1.4) \end{aligned}$$

where M is the mass of the TM and v_{flight} is the residual z velocity after the release.

If we define

$$\begin{aligned} \Delta t_1 &= t_1^+ - t_1^- && (1.5)\\ \Delta \iota_{adh} &= \iota_{adh,z+} - \iota_{adh,z-} && (1.6) \end{aligned}$$

we get:

$$Mv_{flight} = f_0 t_D - \frac{1}{2} f_0 \Delta t_1 + \Delta \iota_{adh} \tag{1.7}$$

Equation (1.7) tells us that the TM momentum at the release is the result of the asymmetry the pin pushing forces (depending on parameters f_0, t_D and Δt) and the asymmetry of the adhesive pulls ($\Delta \iota_{adh}$).

Equation 1.7 is obtained by applying the equality between linear momentum and impulses on the TM, which is a correct solution for the computation of the release velocity (if the time profiles of the forces are known). A complete solution of the TM motion through differential equation can be computed, but it does not differ significantly from the one of equation 1.7 due to the large inertia of the TM and the low frequency of the plunger-TM oscillator (compared to the duration of the phenomenon). If we assume a delay of 200 μs between the pins (design limit for the delay), the duration of the phenomenon is $\approx$ 250 μs; if we assume a final TM velocity of 5 μm/s (the requirement), in a rough (worst-case) computation the TM moves of 5 μm/s $\cdot$ 250 μs $\approx$ 1 nm, which is a negligible displacement. The main simplification of equation 1.7 consists in considering the plunger push as constant; however, if we consider a high delay of the two pins (thus maximizing the deviation of the plunger push from a constant behaviour), the prediction of equation 1.7 differs of 0.15 % from the result of the differential equation.

We will often refer to equation 1.7 in the next chapters.

Estimation of v_{flight}

A probability distribution for v_{flight} in equation (1.7) can be estimated if the probability distributions of the parameters are known.

- The estimation of a probability distribution for the adhesive pull ι_{adh} (which is characterized by a low repeatability) is the goal of the on-ground testing (see section 1.2 and the estimations of chapter 2 and 3).

  The adhesive pull is the result of an *adhesive force* applied between the pin surface and the surface of the TM at the contact. When no penetration between the surfaces occurs, the adhesive force is attractive; the higher the penetration, the higher the (repulsive) Hertzian pressure, and the lower the total attractive force. When the Hertzian force overcomes the attractive force, the total force is repulsive.

  Adhesive models are applied to simple cases like the contact between a sphere and a flat surface [58]; depending on the geometry and the materials, different models are possible: the two main models are the JKR model [59] and the DMT model [60], which apply in different conditions [61]. In figure 1.13 left, the JKR model (which applies in pure elastic case) is shown, with P repulsive force and δ penetration between the surfaces. In a quasi-static case, if the distance between the two surfaces increases (i.e. the penetration δ is negative), the detachment can occur at point C (in case of *constant load*) or D (in case of *displacement control*). In the simple JKR model case, the $\delta - P$ diagram can be used in order to estimate the force-elongation profile produced (in a quasi-static case) when the two surfaces detach starting from

a null preload (figure 1.13 right); the integral of the adhesive force yields the adhesive impulse in this simple case.

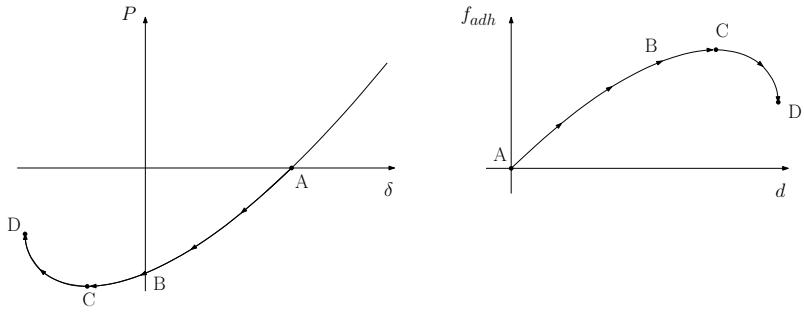

Figure 1.13: JKR chart (left, from [43]) and corresponding *force-elongation curve* for a quasi-static elongation (right). P is the repulsive force at the contact, while δ is the penetration between the surfaces. The adhesive force f_{adh} is defined as the opposite of the repulsive force P ($f_{adh} = -P$), while the elongation d is defined as the relative detachment of the bodies from the equilibrium position A, where an hypothetical load cell would measure a null contact force ($d = \delta_A - \delta$).

The model of figure 1.13 is useful in order to explain the generation of an adhesive pull in a simple case. However, in the reality the contact between the pin and the TM cannot be modeled simply as a contact between a sphere and a plane, and the elastic assumption is not representative, since a plastic deformation can occur with the target preload. A plastic deformation can increase the radius of each asperity (when considered as a sphere), thus increasing significantly the pull-off force w.r.t. the theoretical value [56]. Few works deal with an elastic-plastic and plastic contact regime [58]; in an elastic regime, a more realistic model the sum of many contacts [62], if the two surfaces are considered as a set of many asperities (with a statistical distribution of their heights). An example is reported in [43], showing the resulting adhesive force at the detachment, which can be fitted as a sum of exponentials. A direct (experimental) measurement of the adhesive force, described in [24], confirms that a sum of exponentials can effectively describe the adhesive force (sketched in figure 1.12) produced when the two surfaces detach with constant velocity [63]. These observations on the profile of the adhesive pull will be considered in chapter 3, when the magnitude of the adhesive pull (the integral) will be estimated.

Due to the high difficulty of the modelation, the estimation of the adhesive pull ι_{adh} (the integral of the adhesive force) must be performed experimentally. However, some properties of the adhesive pull are known. For each pin, the adhesive pulling impulse depends on the velocity of retraction of the tip at the detachment (v_{RT}) and adhesion binding energy (ΔU) according to the following equation [64] [65]:

$$\iota_{adh} = \frac{\Delta U}{v_{RT}} \tag{1.8}$$

As a consequence, for a given value of binding energy ΔU, the faster is the retraction of the pin, the lower is the adhesive pull. ΔU can be estimated once an estimation of ι_{adh} is given.

We know moreover a maximum time range for the duration of the adhesive pull. The *maximum* duration of the adhesive pull is expected to correspond to the maximum elongation of the adhesive bonds, which for the case of the TM release has been estimated 2 μm [51]. As a consequence, the maximum duration of the adhesive pull is equal to the *time-to-2-μm*, i.e. the time required for the pin to retract of 2 μm. For the pin of the GPRM, the time-to-2-μm has been estimated through the repeated measurement of the pin retraction profile (figure 1.14), performed by RUAG on flight models [51]. In figure 1.14, the different pin velocities correspond to a non-repeatability of the voltage drop commanded by the CCU (occurring in particular during the incipient motion). Based on these measurements (24 retraction tests), we get that the mean value of the time-to-2-μm is 40 μs while the standard deviation of the distribution is 5 μs (as a consequence, we can define the 37.5 - 41.7 interval as a 95% confidence interval for the mean value, if we assume a normal distribution for the time-to-2-μm).

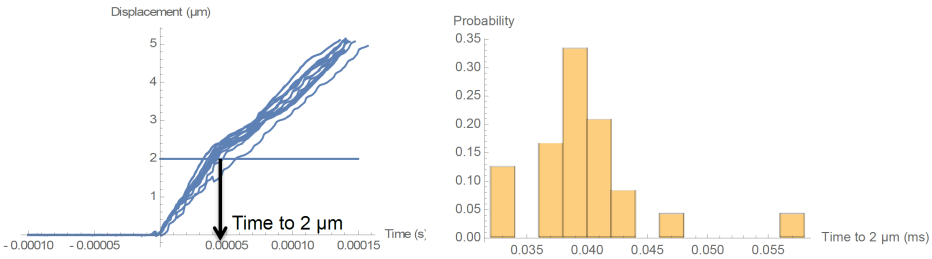

Figure 1.14: time-to-2-μm: measurement campaign performed by RUAG (left) and distribution (right). From [51]).

The main goal of the first part of this work (chapters 2 and 3) is the estimation of the *magnitude* of the adhesive pull ι_{adh} for the in-flight setup. By assuming that the two opposite pins are affected by the same probability distribution of ι_{adh}, if the probability distribution of ι_{adh} is known, then the probability distribution of $\Delta\iota_{adh}$ follows immediately. In alternative, since for the in-flight prediction we need to estimate $\Delta\iota_{adh}$, an experimental method that predicts $\Delta\iota_{adh}$ can do the job even without the knowledge of ι_{adh} (this approach will be discussed in chapter 2).

- the probability distribution of the time-to-0-preload t_1 has been estimated with the same method used for the time-to-2-μm. Based on the RUAG pin retraction tests (figure 1.14), and by assuming that the null preload is reached when the pin has retracted of 0.1 μm (pin penetration in the contact surface), we get a mean value of t_1 of 1.2 μs with a standard deviation of 0.4 μs. A probability distribution of Δt_1 follows immediately, by computing the

	time-to-0-preload	time-to-2-μm	time delay
expected range	0.8-1.6 μs	35-45 μs	0-30 μs

Table 1.1: expected ranges for the time intervals of the TM release dynamics. The ranges for time-to-0-preload and time-to-2-μm are considered as the $\pm\sigma$ interval (with σ standard deviation); the limit for the time delay correspond to the delay that produces a momentum out of the requirement (in the case of nominal preload).

probability distribution of the differences.

- the estimation of the time delay t_D is more difficult. Measurements performed at MAGNA have shown that the two drops (from 120 V to 0 V) of the two piezo stacks commanding the pin retractions have a fair synchronization but are characterized by a different slope (in particular during the incipient motion) [51]; as a consequence, the delay t_D could be neglected if we assume that it is due only to a delay of the two circuits. In the early stages of the design of the GPRM, a recommendation of a maximum time delay of 200 μs was given assuming a holding load of 20 mN [66], on the basis of a numerical simulation of the release dynamics; in order to obtain the same additional linear momentum with the nominal preload of 0.3 N, the requirement would be approximately 13 μs.

  Based on the same RUAG retraction tests of figure 1.14, a rough estimation of the delay of (30 μs) was given by measuring (for a single pin) the dispersion of the starting time of the pin, w.r.t. the triggered electric signal. According to equation 1.7, with the nominal preload a delay of 30 μs would produce a momentum out of the requirement (to be added to the other terms of equation 1.7). However, this estimation was not fully representative of the experiment, since (for instance) it did not take into account the influence of the mechanical preload.

  Due to its uncertainty, and according to the approach followed by previous TMMF predictions [26] [65], in the following we will consider the time delay t_D as a variable parameter. The estimation of the effect of adhesion is independent of the time delay t_D, but the time delay appears in equation 1.7 since it's a possible effect in a nominal (monodimensional release). In particular, according to the previous predictions of the adhesive effect (see section 1.2), the time-delay could be the most critical effect for the final release momentum.

In table 1.1, we summarize the expected ranges for the time parameters of the release.

1.2 Experimental estimation of the adhesive impulse

The criticality of the adhesive impulse in LISA Pathfinder (sections 1.1.4 and 1.1.5) has needed an accurate analysis of the adhesive force profile at the release. This task has been performed in the past years by the University of Trento through the *on-ground* reproduction of the release procedure with a dedicated *mock-up*. By applying an adhesive impulse to a sensing body, the properties of the impulsive force have been estimated through the measurement of the vibration produced; this is a typical example of *force reconstruction* (or *inverse problem*). The estimated properties of the adhesion at the contact surface have then be considered for a model of the *in-flight* case (through a model similar to the one of section 1.1.6), hence taking into account the differences between the real in-flight mechanism and the on-ground mock-up.

In order to estimate the effect of adhesion at the release, the experiment has been designed based on a *nominal release* condition. The goal of the research of the Industrial Engineering Department of the University of Trento is indeed the analysis of the adhesive pull applied to the TM and the prediction of its effect on the TM momentum in LISA Pathfinder. The final prediction can be then improved by taking into account other effects that can be summed to the adhesive one if we assume a nominal release (like the delay effect described in section 1.1.6). Moreover, the effect of adhesion can be critical for a non-nominal release as well; a non-nominal release (e.g. contact between TM and plunger) could be also the consequence of a too high momentum transferred by adhesion. As a consequence, the analysis of the adhesive effect in a nominal release is a necessary step for the on-ground testing of the release mechanism.

As commented in section 1.1.6, the risk of a non-nominal release is not negligible. However, this observation is based on analyses that have been performed much later than the design of the on-ground experiment. During the early design of the on-ground experiment, the properties of the release mechanism were not fully defined.

In section 1.2.1 the most common techniques for the force reconstruction of impulsive forces are discussed. In section 1.2.2 we discuss the main requirements and criticalities for the estimation of the release momentum in LISA Pathfinder, with a short description of the developed experimental setup (whose latest stage will be described in details in section 2.2); finally, in section 1.2.3 the latest results of the in-flight velocity estimation (prior to the testing of the GPRM described in chapter 2) are presented.

1.2.1 Measurement of small impulses in aerospace applications

The analyses and measurements of small impulses is a common issue in the aerospace field. An example is given by the release problem of the LISA Pathfinder GPRM and in general when small forces are exchanged by manipulators [37]. The most famous application is however the propulsion of microthrusters. Knowing the impulses imparted by thrusters to an orbiting satellite allows the control of its orbit

[67], by compensating the residual drag and electromagnetic radiation pressure [68].

The estimation of the thrusters propulsion is based on many experimental solutions. An indirect measurement can be performed from parameters like the ion current density [69]; another method is the measurement of a dynamical displacements produced on a sensing body on which the thruster is fastened [70].

The estimation of the small impulses from the measurement produced is an example of *inverse problem*, i.e. the reconstruction of the applied force based on the analysis of the output. Based on available classifications [71], direct methods are the ones trying to reconstruct the force by means of the input-output relation, in time or frequency domain, through an analytical model (generally linear). The most common direct methods, like deconvolution, require the complete knowledge of the output time history. Direct methods are generally ill-posed and require complex, application specific models or extensive curve fitting [72]. Ill-poseness problem can be solved by regularization, i.e. including additional information in the initial problem, like physical constraints [73].

Ideally, the effect of a quick impulse could be studied in the two limit cases of a force acting on a free mass or on a massless spring, in order to obtain a linear releation between output and input (acceleration and force respectively) [36]. Based on this observations, and by considering the dynamic response typical of a real on-ground system, a typical solution for the identification of small impulses is the adoption of a low-frequency oscillator: the transferred momentum converts into a easily measurable low-frequency oscillation, and an appropriate measurement system can record the acceleration of the system during the application of the force, thus yielding the force profile through Newton equation [36].

The pendulum is therefore a typical solution, in different forms (summarized in [74]): for instance, direct hanging pendulum [75] [76], double hanging pendulum [69], inverted pendulum [77], torsional pendulum [78].

According to the expected range of the impulse to be measured and to the duration τ of the impulsive force w.r.t. the period of oscillation of the pendulum T, many strategies are possible. When the duration of the impulse is much lower than the period of the system ($\tau \ll T$, i.e. the impulse behaves like an ideal one), the measurement of the maximum deflection is the most general approach [79]; this technique is used for impulses greater than 100 μNs [80]. Another possibility (when no other forces are present) is the application of filtering techniques to the displacement signal in order to estimate the adhesive force profile [67] [81] [42].

When the impulses to be detected are very small and characterized by low duration, the pendulum configuration requires bulky hardware in the vacuum chamber and several expedients to reduce mechanical vibrations and interferences [70]. In these cases, a possible solution consists in taking into account the mechanical noise by adding additional terms into a fitting function [82], in order to disentangle the contributions of force and vibrations.

Such a disentanglement occurs also if the system has an initial preload in the direction of the impulsive force, since the pushing force constitutes a systemic effect that has to be identified and subtracted from the output; this is the case for the Transfer Momentum Measurement Facility (section 1.2.2).

1.2.2 The Transferred Momentum Measurement Facility

The performance of the LISA Pathfinder release mechanism can be tested in two ways: directly (by testing the mechanism in its working condition) and indirectly. In the case of space mechanisms, the performance can be difficultly tested directly, since the space environmental conditions can be hardly reproduced with a ground setup. As a consequence, a mock-up of the mechanism can be designed in order to adapt the testing of the main mechanism criticalities to the on ground conditions. In this case, the on-ground measurements need to be interpreted by taking into account the possible differences between on-ground and in-flight setup.

Again, we remind that a *nominal release* is considered when the prediction of the in-flight release velocity is computed (see the considerations of section 1.1.6 and the introduction to section 1.2).

Principles and criticalities of the on-ground estimation

The principle of the estimation of the adhesive impulse is the application of an adhesive pull given to a *sensing body* by a *release tip* in a dedicated facility. The reproduction of the phenomenon must guarantee two main aspects: *measurability* and *representativeness* [36]. Measurability is related to the possibility of measure the phenomenon with accuracy and precision, while the experiment is representative of the phenomenon if it is able to reproduce the phenomenon with the same intensity of the in-flight case (considering therefore all the properties of the analyzed mechanism and the in-flight environmental conditions) [36].

For the representativeness of the experimental setup, the in-flight environmental conditions have to be reproduced: free-fall motion of the sensing body; reproduction of the surface properties at the contact between release tip; low pressure and absence of particles.

In order to apply a force reconstruction technique, the force impulse must be entirely converted into momentum of the sensing body [81]. Secondly, the momentum must be identified by the measurement of the resulting motion of the body, which is affected by noise sources and by the unavoidable constraining forces [83], which have therefore to be considered and eventually subtracted from the output. Consequently, the architecture of the experimental setup shall provide sufficient isolation from noise sources acting in the laboratory environment [81].

Moreover, the measurement accuracy must be reasonably smaller (at least two orders of magnitude) than the maximum allowed linear momentum of the LISA TM (i.e. fractions of μNs) [81]. In order to deal with the resolution of the instruments and with the limits of the lab environment, scale factors can also be introduced in the mock-up: for instance, the sensitivity of the measurement to the impulse can be increased by reducing the inertia of the sensing body.

Experimental setup

The Transferred Momentum Measurement Facility (TMMF) (figure 1.15), whose latest configuration is described in details in chapter 2, is an example of low-frequency oscillator for the estimation of an impulsive force. It is based on a simple-pendulum (which, as described in section 1.2.1, is a typical solution in similar cases)

excited by an adhesive pull performed by a release tip. Such a suspension system can minimize the risk of impulsive constraining forces in direction of the impulse to be measured [67], and can provide a good isolation from gravity and micro-seismic noise [83]:

- the oscillation period is far larger than the force action, therefore the impulse approximation may be applied: since the perturbation of the oscillator position during the force application is negligible, we can assume the equivalence between momentum variation and transferred impulse [36].

- the TM is weakly constrained along two DOF (Degree of Freedom), thus avoiding relevant shear stress on the horizontal direction [36]. A basic requirement of the on-ground experiment is indeed to prevent the rupture of adhesion induced by forces or torques acting along constrained degrees of freedom [83].

The measurement is performed through a micro-vibration interferometer, which is designed for displacements in the μm-nm range and guarantees an appropriate resolution. The representativeness of the system is guaranteed by reproducing the in-flight physical conditions:

- the system is hosted in a clean *vacuum chamber* in order to reproduce the absence of pressure and particles (which could in principle affect the system dynamics as well as the adhesive contact properties).

- materials and geometry at the contact between the tip and the pendulum are designed in order to reproduce the in-flight ones.

In order to increase the sensitivity of the system w.r.t. the input, the inertia of the pendulum is smaller ($\approx 1/20$) than the one of the in-flight TM.

Moreover, a *unilateral release* is performed, in order to avoid a cancelation of the effects on the two sides of the release system (as we expect in the in-flight model, see equation (1.7)) which would lead to a smaller momentum and to an indetermination of the impulse-momentum relation. Reducing the analysis of the system to a unilateral case is indeed possible thanks to the (nominal) symmetry of the in-flight release mechanism. As sketched in the zoom of figure 1.15, the unilateral release is performed thanks to static *needles* on the opposite side of the release tip; the needles material is chosen in order to avoid the formation of adhesive bonds at their contact with the test mass.

The adhesive impulse is therefore applied to the pendulum (the sensing body) through the release tip on one side. The reproduction of a controlled monodimensional motion of the release tip is critical and its evolution has passed through different steps. During the development of the TMMF, three constructive solutions have been experienced [36]. The first setups were composed of a double pendulum, with the adhesive tip suspended and actuated through a horizontal wire [84] [32] in order to minimize the effect exerted by the micro seismic noise. This solution, explored with two different actuation mechanisms for the tip [36], has then been modified due to two main reasons: the difficulty of the preload application and actuation, and the irregular tip motion, with shear and bending stresses. A

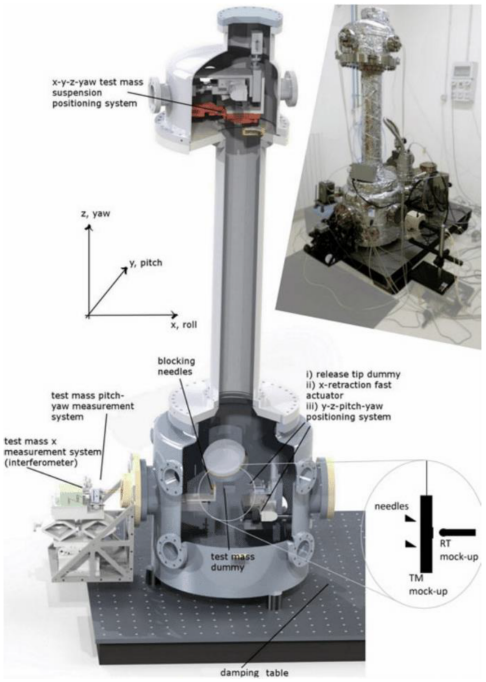

Figure 1.15: TMMF setup up to 2014 (from [51]).

misalignment of the tip w.r.t. the mass can indeed cause tangential forces which reduce the pull-off force, thus leading to an underestimation of the phenomenon [32], [85], [86], [67].

As a consequence, a rigid setup was chosen, with the advantage of constraining the phenomenon along the nominal horizontal direction [36]. The sensitivity to shear effects is explored by performing the release in different directions [87]. Due to the fact that the setup is stiffly connected to the vacuum chamber, the micro seismic noise disturbance has to be filtered through an active 6 DOF anti-vibration table.

The TMMF representativeness has been constantly updated based on the modifications to the design of the GPRM. For instance, as the target preload of the in-flight release increased (from 0.02 N to 0.3 N), the contact preload in the TMMF increased as well. The geometry of the surfaces in contact (TM and release tip) has also followed the design of the mechanisms hosted in the satellite.

1.2.3 Prediction of the in-flight release momentum

The on-ground experimental campaigns performed at the University of Trento have estimated the effect of adhesion in the in-flight release at many different steps of the evolution of the TMMF.

Results can be found in [88], [89], [24], [87], [50], [35], [26]. In all these cases,

the predicted release velocity due to the adhesive effect has been estimated lower than the requirements, thus leading to the conclusion that adhesion should be (with a high probability) not critical for the release.

Here we present briefly the latest result (up to 2014), as an example of a typical approach for the estimation of the in-flight adhesive forces based on the on-ground TMMF experimental campaign.

The prediction of the in-flight velocity described in [24] consists of the following steps:

1. a lumped model for the piezo actuator of the GPRM (pin mechanism, see section 1.1.5) has been developed (see also [90]), and its parameter identified by fitting the displacement signal of the piezo in a release campaign of the pin with no loads and no contact applied to the tip. The optimization has been constrained in order to obtain feasible parameters [26] for the pin release mechanism.

2. as discussed in section 1.1.6, the adhesion force-elongation function is assumed to be described by an exponential function that is defined parametrically by three constants X_1, X_2, X_3 [87]:

$$f_{adh} = X_1 e^{-\left(\frac{\Delta x}{X_2}\right)^{X_3}} \Delta x \tag{1.9}$$

   where Δx is the elongation of the adhesive bond. The parameters of the force adhesive profiles have been estimated through a dedicated test campaign of the TMMF, thanks to the differentiation of the displacement signal in order to get the acceleration of the test mass (and so the applied force), which has been then filtered w.r.t. the additional effect of the needles push in order to get the net adhesive contribution. Since the adhesive parameters can be considered independent of the quickness of retraction of the tip [81], the force-elongation function can be transferred from the on ground system to the in-flight environment [24].

3. thanks to the parameter identifications of steps 1 and 2, a complete lumped model of the release phenomenon has been developed, by taking into account the piezo parameters and the adhesive force-elongation function with their estimated probability distributions; moreover, the dispersion of some geometrical parameters (like the pin radius) and the asymmetry effects (like a delay of the two pin retractions) have been taken into account.

Thanks to a Monte Carlo simulation [24] [87] [50] [26], a total of 100000 simulations have been run, with the final in-flight release velocity of the TM as output. The results are shown in figure 1.16. More than 99% of the simulations are below 1.50 μm/s, therefore under the requirement (5 μm/s).

A confirmation of these predictions can be obtained by testing directly the GPRM inside the TMMF: one side of the GPRM replaces the release tip of figure 1.15, in order to reduce the differences between the in-flight mechanism and the on-ground setup, thus avoiding the necessity of "projecting" the experimental results from one release mechanism to another and making the prediction more robust

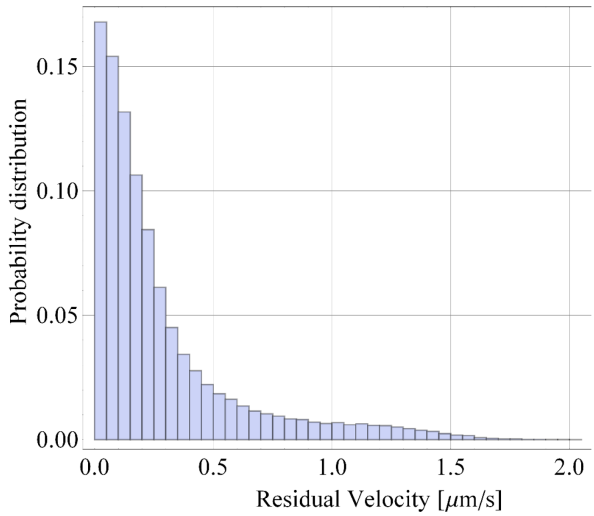

Figure 1.16: results of the Montecarlo simulation for the prediction of the in-flight release (from [50]).

w.r.t. any difference between the modelation of the piezo mechanism and its actual behaviour. This new setup will be described in chapter 2 (with the related predicted release momentum discussed in section 2.5).

Chapter 2

On-ground GPRM testing

As discussed in section 1.2.2, the goal of the Transferred Momentum Measurement Facility (TMMF) is the estimation of the linear momentum transferred by the release tip of the Grabbing Positioning and Release Mechanism (GPRM, section 1.1.5) in LISA Pathfinder in a nominal release: in particular, the TMMF analyses the criticality of the adhesive forces between release tip and test mass at the release.

In this chapter the latest TMMF setup, designed for the GPRM testing, is described. The TMMF setup has been updated by installing one side of the GPRM inside the vacuum chamber; the GPRM replaces therefore the release tip commanded by the piezo actuator of section 1.2.2.

The working principle of the new experimental and the goal of the experiment are discussed in section 2.1. A dynamical model of the system is reported, in order to highlight similarities and differences with respect to the in-flight case. This section should address the reader by summarizing the main features of the on-ground GPRM testing.

The complete experimental setup is then described in section 2.2. An experimental procedure for the release of a test mass in the new condition is established (section 2.3): the test mass is initially blocked and after the pin release it acquires velocity up to a steady state condition characterized by constant velocity (*free flight velocity*).

According to the model presented in section 2.1, this final velocity is due to the sum of two main contributions: adhesive impulse and push of the needles. The test campaign yields hence a set of release data (section 2.4), collected by several repetition of the release test, which allow statistical considerations on the role of adhesion on the free flight velocity. By taking into account the dynamical model, a conservative prediction of the in-flight release velocity is finally discussed (section 2.5); the detailed analysis of the release signal, with a more precise estimation of the adhesive pull, will be described in 3.

In section 2.6 we summarize the results, highlighting the most important conclusions, criticalities of the experimental campaign and suggestions for future analyses.

Part of this chapter has been published in [51] and [65].

2.1 Principle of the experiment

In the *on-ground* experiment, the release procedure of LISA Pathfinder is reproduced through a dedicated mock-up. A *test mass* is released through the pin retraction of one side of the GPRM, starting from a blocked condition. The output of the experiment is the measurement of the test mass displacement, which is then analyzed in order to extract information on the impulse applied to the test mass at the release. The experiment, hosted in a dedicated vacuum chamber, is designed in order to reproduce the environmental conditions of the in-flight release.

In section 2.1.1 we remark the main differences between on-ground and in-flight experimental setup; these differences have to be taken into account in order to predict the behaviour of the in-flight mechanism from the results of the on-ground one. In section 2.1.2 we summarize the experiment and the role of its main components; a dynamical model for the experiment (similarly to the *in-flight* one of section 1.1.6) is reported in section 2.1.3. Based on the dynamical model, we anticipate in section 2.1.4 the method of the estimation of the in-flight velocity (discussed in detail at the end of this chapter in section 2.5). Finally, in section 2.1.5 we discuss the conditions that allow the experiment to be representative of the investigated phenomenon.

2.1.1 Differences with respect to the in-flight release

The on-ground experiment differs from the *in-flight* one (section 1.1) for two main aspects:

- the release is *unilateral*. It is performed by a single side of the GPRM (Z-), while on the opposite side no actuation is commanded. As a consequence, the on-ground release reproduces a unilateral in-flight release, which represents a worst case if the aim is the minimization of the residual momentum: in this condition there is indeed no possible cancelation of the opposite forces (see equation (1.7)).

- the test mass differs from the in-flight case. The test mass of the on-ground setup is approximately 20 times lighter than the nominal test mass of the GRS of LISA Pathfinder. This choice has two main advantages. First, the measurement of the transferred momentum is easier, since a momentum transferred to a lighter mass implies a higher velocity, therefore the sensitivity of the measurement system is increased. Second advantage (although not originally considered in the development of the setup), the test mass geometry, similar to the one of a thin plate, allows micro-vibrations of the test mass (about 1000 orders of magnitude lower than the measured displacement of its centre of mass); this allows to extract information on the transferred momentum by means of a modal analysis (discussed in chapter 3).

2.1.2 Release experiment

In this chapter, for better readability, we will refer with the acronym *TM* to the on-ground test mass, similarly to the inertial sensor of the LISA Pathfinder

satellite. This could create some ambiguity; however, the context will help the reader understand which body is associated to the acronym.

The TM is one of the three main components of the experimental setup. It is suspended by means of a hanging pendulum and positioned between the two remaining devices: the Z- GPRM on one side (which we will refer to simply as *GPRM* in this chapter) and three *blocking needles* on the opposite side. In the nominal configuration, the three devices are aligned along the z axis, as sketched in figure 2.1. Figure 2.2 reports a photo of the three devices after the installation inside the vacuum chamber.

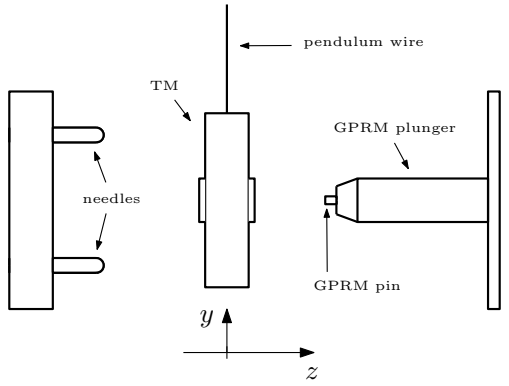

Figure 2.1: scheme of the three devices involved in the experiment. A single wire connects the TM to the top of the vacuum chamber; the rotations (pitch and yaw) of the TM w.r.t. the hanging point are monitored by the optical lever.

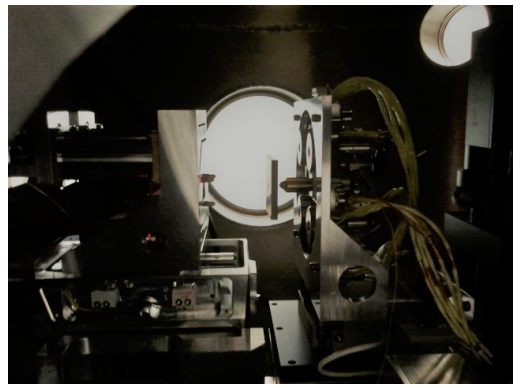

Figure 2.2: photo of the three devices involved in the experiment after the installation inside the vacuum chamber. In the picture, the needles are located on the left of the TM; the GPRM plunger on the right. The thin suspension wire of the TM is not visible in the picture.

The experimental procedure consists of the following steps, represented in figure

2.3 and which we will refer to in the chapter.

1. *free TM* (figure 2.3 a). The TM oscillates freely between needles and GPRM along z axis.

2. *blocked TM* (figure 2.3 b). Needles and GPRM approach to the TM until the TM is grabbed by the needles on one side and by the GPRM pin on the other side. The nominal preload of the in-flight case (0.3 N) is applied in order to hold firmly the TM; as a consequence, the needles are compressed.

3. *TM release* (figure 2.3 c). It is the phenomenon to be monitored and measured. The GPRM pin retracts very quickly (less than 0.2 ms), transferring a momentum to the TM through the adhesive pull, and making the TM free on its side (positive z). Being the TM free on one side, the needles (compressed in the blocked configuration) convert their elastic potential energy into kinetic energy of the TM, hence transferring further momentum to the TM.

4. *free flight velocity* (figure 2.3 d). At the complete relaxation of the needles, the TM detaches and is free on both sides; the needles are designed in order to give no adhesive pull to the TM at the detachment. The final velocity of the TM, which depends of the overall momentum transferred by pin and needles during the release, is called *free flight velocity*.

2.1.3 Dynamical model of the on-ground release

The measurement of the TM z displacement during the TM release allows to estimate the contribution of the adhesive pull of the pin to the final free flight velocity, by means of a dynamical model. This is an example of *inverse problem* (section 1.2.1), i.e. the estimation of an input force from the output motion of the sensing body.

Similarly to the in-flight case (section 1.1.6), we develop for the on-ground experiment a dynamical model. The model allows to emphasize differences and similarities between the TMMF release and the in-flight release, thus leading to the elaboration of the TMMF results for the prediction of the in-flight residual velocity (section 2.5).

The force time history (force profile) of the TMMF one-sided release is shown in figure 2.4. The pin retraction occurs only on one side: as a consequence, while the force profile of the pin side is similar to the in-flight case (figure 1.11), on the opposite side the needles push the mass as a preloaded spring (figure 2.3).

The total duration of the pin force profile (t_2 in the picture) is approximately 10 times lower than the duration of the needles push (t_3): ≈ 40 μs versus ≈ 400 μs [51]. As a consequence, we can consider that the pin transfers momentum to the TM in the early stage of the needles push; at the detachment of the pin, TM and needles system can be described as a mass-spring system with an initial preload and an initial velocity.

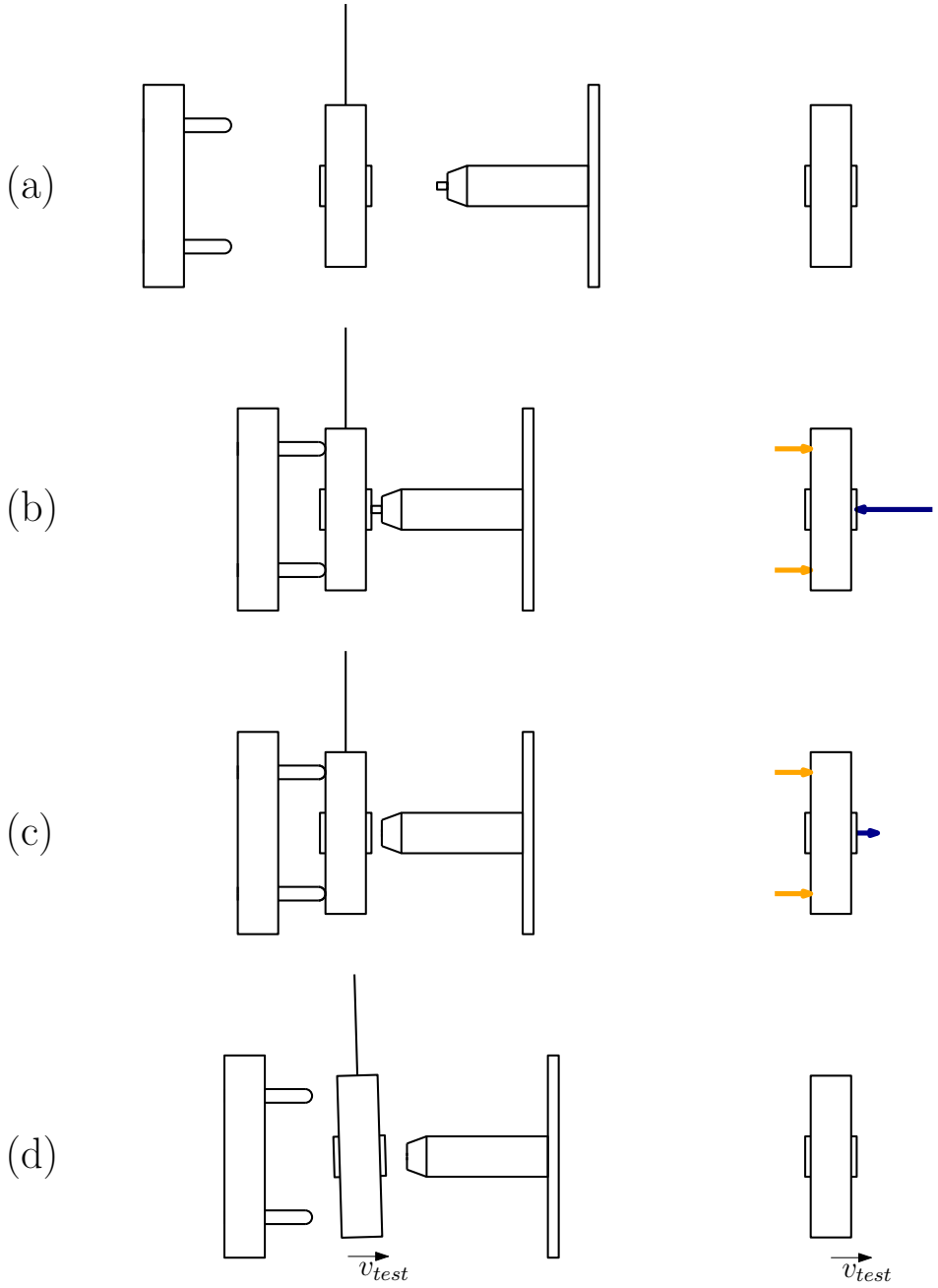

Figure 2.3: steps of the experiments. The mechanism configuration is shown on the left; the forces acting on the TM on the right. Starting from the free TM configuration (a), needles and GPRM approach to the TM until the blocking condition is reached at the target preload (b): the forces on the opposite sides are in equilibrium. At the release (c) the pin is retracted: the adhesive pull of the pin and the needles push make the TM accelerate in z direction, up to the detachment (d). The final *free flight velocity* at the detachment v_{test} depends on total impulse applied to the TM after the pin release.

In this case, an energetic approach allows an easy computation of the final TM momentum. The initial kinetic energy K_i at the detachment of the pin is:

$$K_i = \frac{1}{2}k_n\Delta_x^2 + \frac{1}{2}mv_0^2 \tag{2.1}$$

where m is the mass of the TM, f_0 the preload, k_n the stiffness of the needles, Δx is the initial compression of the needles (depending on the stiffness and the preload force) and v_0 is the initial velocity given by the momentum transferred by the pin force:

$$\Delta x = \frac{f_0}{k_n} \tag{2.2}$$

$$mv_0 = -\frac{1}{2}f_0 \cdot t_1 + \iota_{adh} \tag{2.3}$$

The final kinetic energy K_f at the release of the TM (detachment between TM and needles) is

$$K_f = \frac{1}{2}mv_{test}^2 \tag{2.4}$$

where v_{test} is the free flight velocity. By equating K_i and Kf we get

$$\frac{1}{2}k_n(\Delta x)^2 + \frac{1}{2}mv_0^2 = \frac{1}{2}mv_{test}^2 \tag{2.5}$$

and therefore, if we focus on the final momentum of the TM mv_{test}, we get

$$mv_{test} = \sqrt{mk_n(\Delta x)^2 + m^2v_0^2} \tag{2.6}$$

We can see that the final linear momentum (defined in the following as p) is the square root of the quadratic sum (i.e. "pythagorean sum") of the momentum due to the preloaded needles (q) and the momentum due to the pin force (ι, with the same notation used in section 1.1.6). We can indeed define:

$$p = mv_{test} \tag{2.7}$$

$$q = \sqrt{mk_n}\Delta x = \sqrt{\frac{m}{k_n}}f_0 \tag{2.8}$$

$$\iota = mv_0 = -\frac{1}{2}f_0 \cdot t_1 + \iota_{adh} \tag{2.9}$$

thus obtaining the easy formula:

$$p = \sqrt{q^2 + \iota^2} \tag{2.10}$$

2.1.4 Information in the free flight velocity

As equation (2.10) describes, the final free flight velocity of a test depends on the adhesive pull ι_{adh} and more generally on the impulse applied by the pin ι; however, it is mainly affected by the pushing impulse of the needles q. As a consequence, the information of the adhesive impulse must be extracted from the free flight velocity, by "filtering" the effect of the needles.

We anticipate here the approach followed in this work, which is twofold:

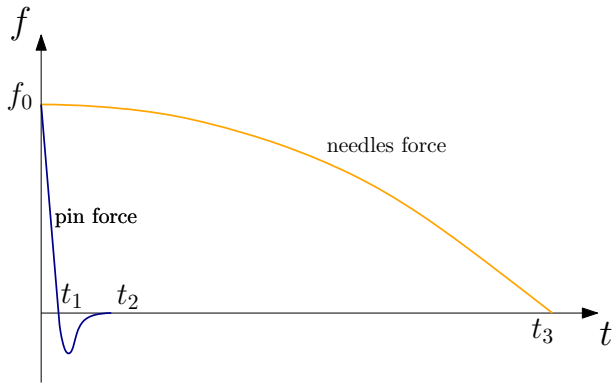

Figure 2.4: qualitative scheme of the force profiles of the TMMF release. The colours correspond to the ones of figure 2.3. At time t_1 is the force of the pin is zero, i.e. the pin switches from a *pushing* behaviour to a *pulling* behaviour. The detachment of the pin occurs at the end of the adhesive pull (time t_2). The detachment of the TM from the needles occurs at the end of the needles push (time t_3).

- if the goal is just the prediction of the contribution of adhesion to the in-flight release velocity, we need to estimate the *difference* between the impulses of the pins acting on the two sides of the in-flight TM (as explained by equation (1.7)). A *distribution of free flight velocities* (obtained by repeating several times the release at the same preload f_0) can yield a *conservative* (*worst-case*) distribution of the differences of the adhesive forces of equation (2.10) that does not require a precise knowledge of the needles contribution (although some assumptions on the needles contributions are needed). By means of proper assumptions, this TMMF result can be "projected" to the in-flight case. This approach, which yields a conservative estimation of the in-flight release velocity, is described in detail in section 2.5 at the end of this chapter.

- if we want instead a precise estimation of the adhesive impulse of equation 2.10, we need to investigate effects of the adesive pulls which are not "hidden" by the prevailing needles push. This will be done by analyzing the TM vibration as a thin plate in chapter 3 (the estimation of a distribution of adhesive impulses can be eventually considered for a new prediction of the in-flight release velocity through the model of equation (1.7)).

As discussed in the following section (2.1.5), both the approaches need the experiment to be representative of the in-flight conditions.

2.1.5 Reproduction of the in-flight conditions

As commented in the previous section (2.1.4), the forces exchanged by GPRM and TM in the TMMF are estimated in order to make predictions of the in-flight velocity.

This approach is based on the representativeness of the on-ground adhesive impulse w.r.t. the in-flight one: i.e., we are assuming that the quantity ι_{adh} appearing in the on-ground model of equation (2.10) has *the same probability distribution* of the ι_{adh} quantities of the in-flight model (equation (1.7)). This assumption is guaranteed by the TMMF experimental conditions, which reproduce the environmental conditions of the in-flight release:

- the GPRM hosted in the TMMF is a copy of the in-flight mechanism.
- the TM is designed in order to reproduce the surface properties of the in-flight case at the contact.
- the TM is suspended by a wire and isolated from the ground vibrations (through a micro-seismic active isolation), thus reproducing the free fall along the direction of the release (z axis).
- the experiment is hosted in a vacuum chamber, which guarantees a high cleanliness and a pressure representative of the in-flight condition ($\approx 10^{-7}$ mbar).
- the temperature (ambient temperature) is representative of the in-flight conditions.
- the TM and the devices are electrically grounded, thus guaranteed no difference of voltage between TM and GPRM and needles; electrostatic forces can arise between TM and GPRM only due to a possible triboelectrical effect, which is however representative of the in-flight condition (since it could also occur in-flight).

The detailed description of the experimental setup, which reproduces the one already described in section 1.2.2 with the additional integration of the GPRM, is the focus of section 2.2.

2.2 Experimental setup

In this section, the structure of the experimental with all its components (environments, devices, measurement systems) is described.

In section 2.2.1 we give an overview of the main systems of the experimental setup.

The lab environments are presented in section 2.2.1. We focus then on the description of the TM and its suspension system (section 2.2.3) and of GPRM and needles (section 2.2.4). The positioning system is described in section 2.2.5, the measurement systems in section 2.2.6, the visualization system in section 2.2.7. The environmental conditions are representative of the in-flight release thanks to the isolation from vibrations (2.2.8) and the pumps mantaining the low pressure 2.2.9. Finally, we focus on the controllers (section 2.2.10) and on the user interface (section 2.2.11).

2.2.1 Experimental architecture: overview

The experimental components (and their relations) are represented in the scheme of figure 2.5. They can be grouped in the following *systems*:

- *sensing system.* It is the TM pendulum, whose measured displacement is the output of the experiment.

- *blocking and release system.* It is composed of GPRM and blocking needles, since both contribute to hold the TM before the release and both transfer momentum to the TM at the release (as described in section 2.1.2). In order to approach to the mass during the blocking phase and apply the desired preload, they are mounted on linear runners, aligned with z axis, which will also be considered parts of the blocking and release system.

- *positioning and alignment system.* It is not directly involved in the experiment, but allows to regulate and align the system in order to get the desired configuration in the test. It is composed of 3 linear actuators and 1 angular actuator for the positioning of the pendulum hanging point; 3 linear actuators and 2 angular actuators for the alignment of the GPRM plunger; two angular actuators for the needles orientation.

- *measurement system.* It is composed of a laser interferometer, for the measurement of the linear displacement of the mass along the z axis, and an optical lever for the measurement of the orientation of the TM. Further measurements come from the feedback signals of some actuation devices: force and position of the plunger, ionic pump pressure.

- *visualization system.* A high-speed camera, connected to an electronic microscope, allows the visualization and the recording of the devices and of the experiment operations inside the vacuum chamber.

- *vibration isolation.* The experimental setup is assembled on an isolation platform.

- *pumping system.* In order to simulate the in-flight low pressure condition, three pumps (each designed for a specific pressure target), which have to be activated in sequence, work in order to mantain a low pressure in the vacuum chamber.
- *controllers.* The controllers of GPRM, needles actuator, positioning system, measurement system and pumping system connect the devices with the computers.
- *user interface.* It consists of three computers, that allow to manage the complete experimental procedure. The GPRM has its own dedicated computer.

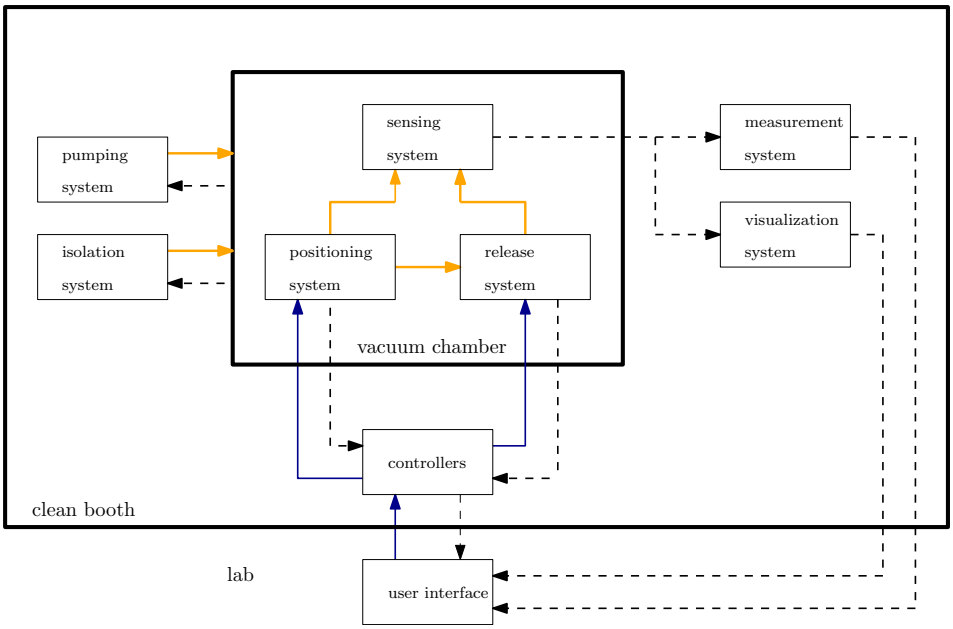

Figure 2.5: scheme of the experimental setup. The connections represent physical actions (red lines), commands (blue lines), feedbacks (dashed black lines).

2.2.2 Environments: lab, clean booth and vacuum chamber

Before starting with the description of the setup, it is useful to describe the organization of the laboratory that hosts the experiment, defining some terms we will refer to in the document. We distinguish among lab, clean booth and vacuum chamber.

The *lab* is the room where all the experimental setup is assembled. It is located at the Industrial Engineering Department of the University of Trento. The main components of the experimental setup are inside a clean booth, which is a separate and isolated environment in the room. Outside of the clean booth, but communicating with the internal devices, there are computers for the control of the devices

and the data acquisition and analysis, which are connected with dedicated data acquisition devices.

The *clean booth* (figure 2.6) is a separate environment located in the lab, designed for hosting space application devices. The clean booth is completely isolated from the rest of the lab in order to satisfy a high cleanliness requirement, which is mandatory for the maintenance and reliability of precise space mechanisms. This requirement is guaranteed thanks to the following expedients:

- environment isolation through metallic walls. The changing room located at the entrance of the clean booth allows to avoid any air flow between inside and outside.
- precautions against introduction of dust and filth. Wearing a special tracksuit is compulsory for all the operators that work inside the clean booth.
- high pressure w.r.t. the lab. This is done thanks to an air fan system.
- constant cleaning of devices and surfaces.

At the beginning of the test campaign, its ISO 14644-1 specification (depending on number and dimension of particles per air volume) was 6 for the entire clean booth.

As shown in figure 2.5, the clean booth hosts many device controllers, as well as the pumps for the vacuum maintenance in the vacuum chamber and measurement devices like interferometer and camera.

The *vacuum chamber* (shown in figure 2.6) is a separated hermetically closed environment inside the clean booth, reproducing a high vacuum condition, with low pressure and higher cleanliness. The pumps can lead up to a $2 \cdot 10^{-7}$mbar pressure level, which is then maintained by a ionic pump for the whole duration of the experiment.

As shown in figure 2.7, the release experiment is completely performed inside the vacuum chamber. Here the GPRM Z- device is hosted, together with TM pendulum, needles, and the associated actuation systems (figure 2.2). Three windows at three different sides of the vacuum chamber allow the laser beams of interferometer and optical lever to measure the motion of the TM, a lamp to illuminate the setup and a camera (mounted on a microscope) to visualize the experiment from the computers. Some COM ports are located on flanges in order to allow the communication between devices inside the vacuum chamber and their controllers.

2.2.3 The sensing device: TM and pendulum

As discussed in section 2.1, the TM is the main body involved in the experiment, since its motion yields information on the GPRM forces applied on it.

The TM can be described as a metallic parallelepiped, hung through a wire to the top of the vacuum chamber. As discussed in section 1.2, this is a classical solution for the on-ground simulation of the free fall of a body: the geometry of the system guarantees that, for small oscillation, the TM dynamics can be linearized and no gravitational effect has to be taken into account.

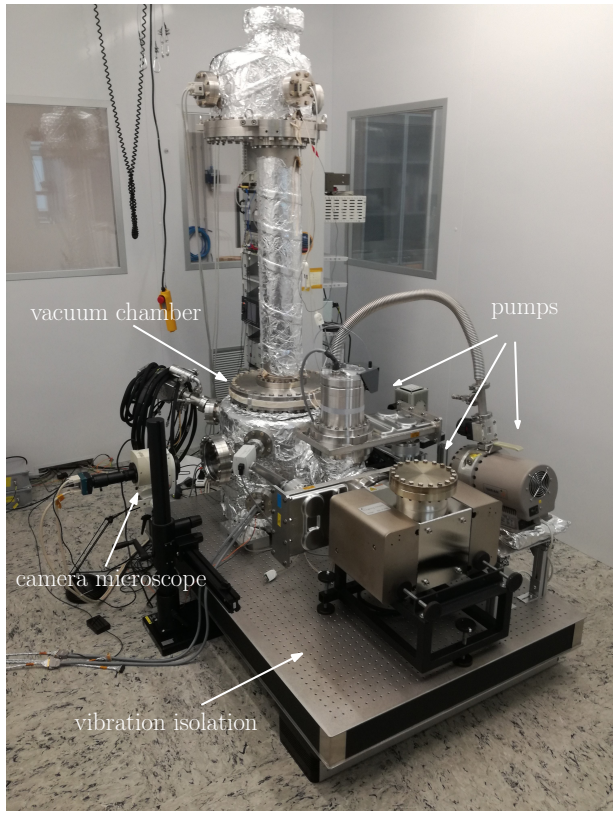

Figure 2.6: experimental setup hosted inside the clean booth.

The detailed geometry of the TM is shown in figure 2.8, while the material properties are reported in table 2.1. The main body (*frame*) is a 36x36x4 mm W-alloy parallelepiped, with a cylindrical hole in its centre where a gold cylinder (*insert*) is assembled by interference coupling.

The total mass ($\approx$ 88.5 g) can be approximated to the one of the frame. As a consequence, the frame of the TM is the main inertia involved in the dynamics of the system. The insert does not affect the dynamics of the TM if considered as a rigid body, but affects the vibration of the body when considered as a continuous mechanical system (thin plate), thus requiring a FEM simulation for the computation of the natural modes of vibration (see chapter 3).

The motivation for the gold coated insert at the centre of the mass is the reproduction of the in-flight contact between the gold coated mass of LISA Pathfinder and the GPRM pin.

As shown in figure 2.7, the TM is hung through a wire that is linked to its positioning system at the top of the vacuum chamber.

The high length of the wire (more than 1 m) w.r.t. the TM dimension and the small displacement of the TM in the experiment (few micrometers) allow to ap-

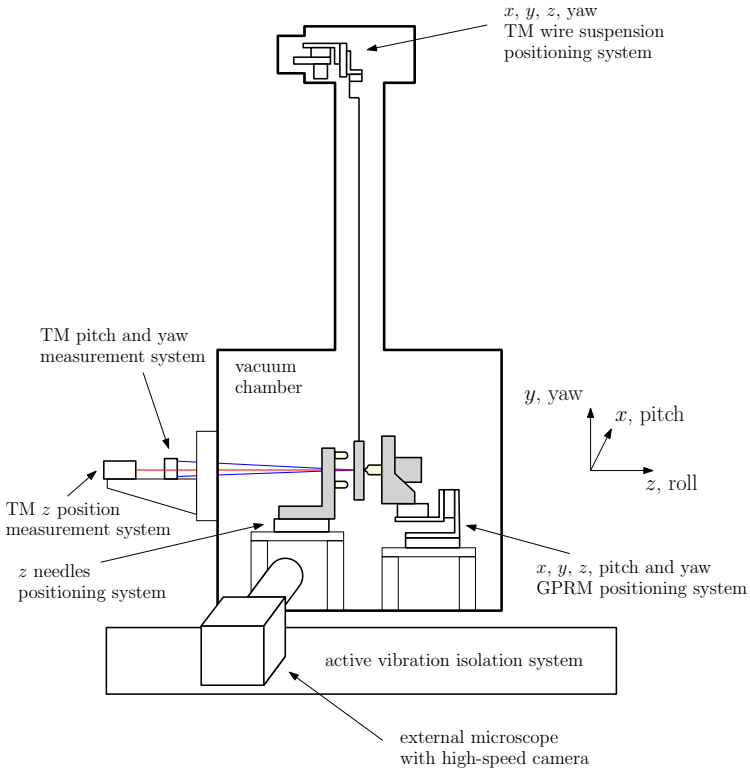

Figure 2.7: position of the experimental devices inside the vacuum chamber and reference frame. The laser beams of optical lever and interferometer pass through a dedicated view-port and through the triangular hole of the needles support.

proximate the TM free motion as a uniform linear motion. The natural frequency of oscillation of the pendulum (computed through the formula $\sqrt{g/l}$) is indeed lower than 0.5 Hz, thus corresponding to a period of oscillation of more than 2 seconds.

The release phenomenon has a low duration (few milliseconds) w.r.t. the period of the pendulum, so that the TM oscillates very close to the equilibrium with a negligible vertical displacement. Therefore, the horizontal motion z of the mass (which is the main output of the measurement system) is not significantly affected by the natural oscillation of the TM-wire pendulum system.

As a consequence, the TM can be considered as a free body along the z direction in the dynamical analysis of the experiment. We can indeed estimate the force due to gravity affecting the horizontal oscillation of the TM, which is

$$f_g = \frac{g}{l} \sin \epsilon \tag{2.11}$$

where ϵ is the angle of the pendulum w.r.t. the vertical axis of the lab. During the application of the adhesive pull, the TM moves in z of $\approx 0.1\mu$m, therefore the

	frame	insert
mass	87.08 g	1.23 g
material	W alloy	70Au30Pt
density ρ	17031.3 kg/m^3	19561.2 kg/m^3
Young modulus E	340 GPa	107 GPa
Poisson modulus ν	0.28	0.41

Table 2.1: material properties of TM frame and insert.

force due to gravity is approximately 10^{-6} N (at most) and, since the duration of the phenomenon is (at most) 100μs, the impulse due to gravity is (at most) $10^{-6}\text{N} \cdot 10^{-4}\text{s} = 10^{-10}\text{N s}$; this is more than 3 order of magnitudes lower than the expected range of the adhesive pull. A similar computation holds for the push of the needles, which follows the adhesive impulse: the maximum displacement of the TM is $\approx 1\mu$m (and therefore the gravitational force $\approx 10^{-5}$N, but the push of the needles is in the order of 0.1 N.

2.2.4 Blocking and release system

The blocking and release system is composed by both needles and GPRM, which are aligned with the z direction in the experiment, and are located on opposite sides of the TM (as shown in figures 2.1 and 2.2). Both needles and GPRM are assembled on linear runners, aligned with z axis.

Needles

The role of the needles is to constraint the mass on one side in the blocking phase, and to push the mass in the release phase (simulating therefore the behaviour of a static plunger on the opposite side of the active one).

The needles are shown in figure 2.9. Three equal horizontal needles, each with a round edge, are located on a L-shaped structure; they are positioned around the centre of the side facing the TM as an equilateral triangle (with side 26 mm), symmetric w.r.t yz plane, in order to guarantee a symmetric push to the TM.

The needles, with a limited contact surface and the presence of an conductive antiadhesive coating (CrN), are designed such that the adhesive phenomenon occurring at the needles-TM contact is negligible if compared with the one occurring between GPRM and insert. The negligibility of the adhesion between TM and needles has been proved experimentally in [24].

A hole (triangolar, in order to maximize its dimension) is placed inside the needles triangle in order to allow the measurement of the TM motion by the laser beams (emitted by the interferometer and the optical lever placed opposite to the TM w.r.t. the needles), as discussed in section 2.2.6.

The needles have the same length and their positioning and orientation system (described in section 2.2.5) allows a uniform push on the TM. The structure supporting the needles is assembled on a linear runner, located on a metallic structure

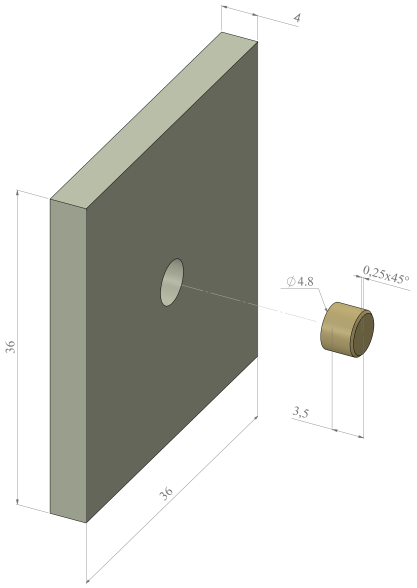

Figure 2.8: geometry of the test mass, with frame and cylindrical insert (courtesy of Nicolangelo Favia). Dimensions in mm.

which is fixed to the ground of the vacuum chamber. The high reliability and resolution of the linear runner allows to move the needles towards the TM with small motion steps of 0.1 μm.

GPRM

On the other side of the TM, a mock up of the Z- side of the in-flight GPRM is located. The properties of the GPRM have been described in section 1.1.5.

Its main component are a cylindrical finger (*plunger*), with a pyramid-shaped end, and another thin cylindrical tip (*pin*); they have the same symmetry axis, which in the experiment corresponds to the nominal z direction, and both can move along this axis. A detail of the plunger end with the (retracted) pin is shown in figure 2.10.

The pin (figure 2.10 right), which at its 0 displacement is completely retracted, can be nominally extracted out of the plunger by 18 μm. The pin motion is commanded by a piezo actuator: a full pin extraction corresponds to a voltage of 120 V given to the piezo. The extraction of the pin (i.e. the charge of the piezo) is performed in few seconds, while at the release the discharge of the piezo is instantaneous, thanks to the closure of the electrical circuit (see section 2.2.10): the inverse-step motion is the same of the nominal in-flight one (other retraction profiles are possible, see chapter 4). Thanks to the high stiffness of the connection between pin and piezo [24], we can assume that the pin displacement follows exactly the deformation of the piezo. The quick fall of the voltage (i.e. of the piezo charge)

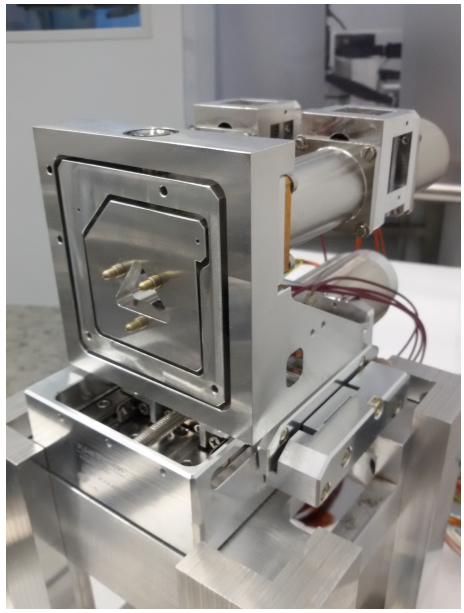

Figure 2.9: needles mounted on their linear positioner. The triangular hole in the centre allows the interferometer to measure the TM displacement.

makes therefore the pin retract with a very high speed, such that the rupture of adhesive bonds is guaranteed and the TM can move freely in the positive z direction after the pin retraction.

No feedback is available for the pin extraction: the GPRM controller deduces the pin extraction from the voltage applied to the piezo.

The plunger (figure 2.10 left) can move along its symmetry axis thanks to a stack actuator. Its displacement range is approximately 16000 μm w.r.t. a lower limit, and it can move with a maximum velocity of approximately 110 μm/s.

As reported in section 1.1.5, the plunger control system has a displacement feedback (strain gauge) and a force feedback (load cell). The strain gauge readout is not involved in any step of the experiment, while the force measurement has a fundamental role, since it allows to check if the desired preload is applied. The force signal has a constant offset of approximately 2.85 N and a force noise with standard deviation 0.02 N has been estimated when a constant force is measured by the load cell.

The plunger is not commanded during the on ground experiment. In the GRS of LISA Pathfinder, the plunger is commanded during the handover to plungers and the handover to pins in order to guarantee the nominal preload (see sections 1.1.4 and section 4.1.2), and it is retracted after the pin release in order to allow the free fall of the mass. In the on-ground setup, this role is assigned to a linear runner, on which the GPRM (with its positioners) is assembled (see section 2.2.5). The linear runner is similar to the one of the needles system, with a very precise resolution of the motion in the order of 0.1 μm.

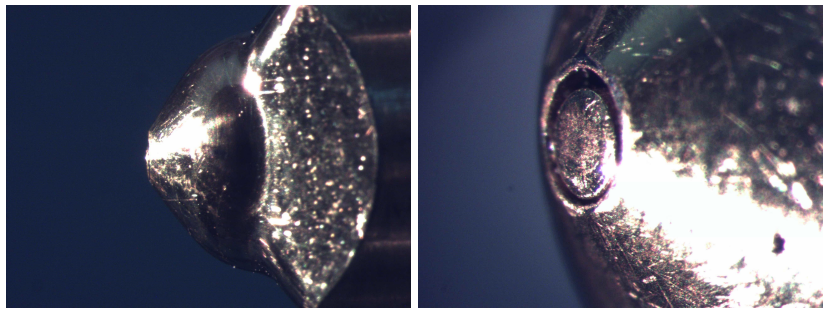

Figure 2.10: detail of plunger and pin. The plunger is pyramidal-shaped (left), since it corresponds to the Z- GPRM side. The pin can be extracted out of the plunger (right). The surfaces are gold-coated.

This choice is due mainly to three reasons. First, the linear runner has a higher reliability w.r.t. the plunger: in additional on-ground experiments, a significant and not repeatable difference between the commanded motion and the actual displacement of the plunger has been highlighted. Second, its maximum velocity is higher than the one of the plungers. Third, the motion of the linear runner can be controlled by the software governing the experiment, thus allowing an automatic motion of the linear runner when the TM is released (the linear runner starts its motion some ms after the end of the release phenomenon, thus not affecting the experiment).

2.2.5 Positioning and alignment system

The positioning system of the devices is not involved in the experiment, but it guarantees a correct alignment of the devices (TM, GPRM, needles) along the z axis before the release experiment. Their position inside the vacuum chamber is represented in figure 2.7.

TM positioning system

The TM positioning system is composed of three linear positioners and an angular positioner.

The x and y positioners allow to move the mass in the desired point of the xy plane, such that the needles axis (the centre of the equilateral triangle) is aligned with the TM insert and the needles push is uniform and symmetric. They can be also used for a tiny modification of the contact point between TM and insert in order to explore different adhesive conditions (see section 2.3).

The x and y positioners are also used to make the interferometer beam reach the centre of the insert. For instance, the x position is chosen by exploring the range of positions for which the readout maintains the maximum power (i.e. for which the interferometer beam bounces on the surface of the insert), since once the beam reaches the boundary of the insert the interferometer beam is no more reflected orthogonally. The x position will be the mean of the range, and its

uncertainty depends on the diameter of the laser spot. The interferometer points therefore the centre of the insert with an uncertanty of $\pm$ 100 μm (the radius of the insert is 4.8 mm).

The z positioner can be used (together with needles z linear runner and GPRM z linear runner) in order to shift the z nominal position of the mass in the final configuration.

The yaw angular positioner makes the TM surface orientation parallel with the needles contact plane, and aligns the TM with the interferometer, thus guaranteeing a good readout of the signal.

GPRM positioning system

The GPRM positioning system (figure 2.11) is composed of three linear motors and two angular motors.

The z positioner is the linear motor moving the GPRM along z, already described in section 2.2.4. The x and y positioners make the GPRM touch the mass exactly in the centre of the insert, thus positioning the pin along the reference z axis. This is possibile since the pin is aligned w.r.t. the interferometer (see appendix C.1), which points at the centre of the insert. Moreover, in y direction the position of the pin w.r.t. the insert is checked visually through the camera.

The angular motors, which control the TM pitch (*tilter*) and yaw (*goniometer*), are used in order to align the plunger with the z direction. They can also modify the plunger orientation in order to explore different release directions, thus looking for the maximum release direction and making the experiment "robust" with respect to little misalignments of the plunger axis (as explained in section 2.4.2).

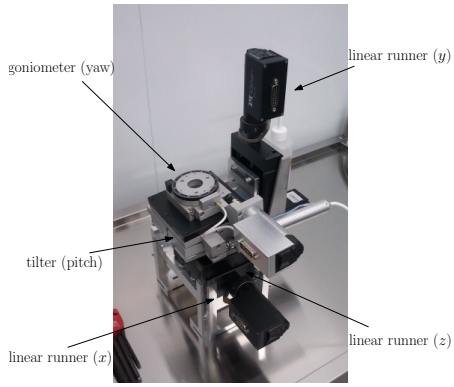

Figure 2.11: GPRM positioning system. The GPRM is mounted on the goniometer. The actuators are connected in series according to the following kinematic chain (from GPRM to ground): yaw, pitch, y, z, x.

Needles orientation system

The needles are connected to their L-shaped support (described in section 2.2.4) through angular positioners which can be commanded in order to modify their yaw and pitch orientation. Their main role is the correct alignment of the TM in the blocked configuration, by compensating unexpected inclinations of the TM surface read by the optical lever.

2.2.6 Measurement systems

The main output of the experiment is the TM z displacement, which is given by the laser interferometer. An optical lever measures the TM pitch and yaw. Both interferometer and optical lever are characterized by a sampling frequency of 200 kHz and can be synchronized. Other measurement systems are part of the feedback control system of some devices, like GPRM strain gauge and load cell (already described in section 2.2.4) and the pressure feedback of the pumps (section 2.2.9).

Interferometer

The laser interferometer is aligned with the z axis and measures the TM displacement at the release. It is also used for the alignment of the GPRM during the alignment procedure (see appendix A.1).

The interferometer device is mounted on a fixed structure connected to the isolation platform (figure 2.12), on which the vacuum chamber is assembled. The laser position and orientation can be regulated by a dedicated positioning system. The beam emitted by the interferometer passes through a window port and then through the triangular hole of the needles, such that the TM surface can be reached, as shown in figure 2.7. Beam direction and TM yaw are regulated in the alignment procedure (appendix C.1) in order to make the reflected beam reach the optical sensor of the interferometer.

If the TM is lifted up by its y positioner, the laser beam can point at the pin of the GPRM in order to measure its motion profile.

The control software of the interferometer measures the percentage of the signal power that returns to the device after bouncing on the mass. A reasonable threshold value for a reliable detection and measurement of TM displacement is 15%. During the release procedure, TM and laser beam are aligned such that a high reliability (more than 90 %) can be reached: the higher the percentage, the lower the interferometer noise in the measured signal.

6 gain levels are available for the interferometer; a low gain corresponds to a lower noise, but allows only the measurement of small ranges of displacement. Therefore, a low gain is set for operations requiring a high displacement of the TM (like alignment and blocking procedure); a high gain is set before the measurement of the release phenomenon, where the TM displacement to be observed for the capture of the event is lower than 2 μm. The noise properties at this gain level are discussed in chapter 3.

The interferometer is designed for the measurement of mechanical vibrations with a resolution in the subnanometer range, and for velocities lower than 1.5

m/s. The nominal wavelength of the laser beam is 632.8 nm, but a small variation ($\approx 1\%$) is possible if the environmental conditions change (e.g. temperature). The wavelength is an important parameter for the signal analysis, since a cyclic effect creates fictitious oscillation in the measured output (see section 3.2).

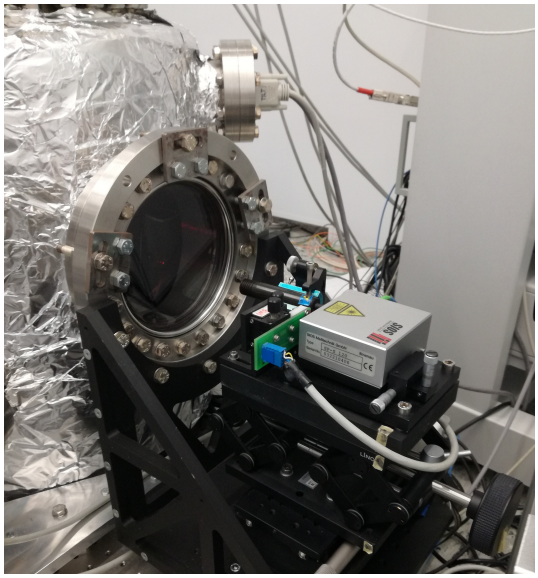

Figure 2.12: interferometer and optical lever.

Optical lever

The optical lever measures the TM pitch and yaw angles. The measurement of the TM orientation is necessary during the blocking phase, in order to guarantee the verticality of the TM surface in the blocked configuration. Moreover, through the optical lever the rotation of the TM at the release is checked.

The optical lever consists of two laser beam passing through the window port and reflecting on the TM surfaces; the position of the returning beams on the sensors yields information on the orientation of the surface. While the interferometer can measure also the motion of curve surfaces (like the pin contact surface) if a sufficient signal percentage is available, the optical lever requires the reflection on a smooth and flat surface in order to guarantee a reliable measurement signal.

2.2.7 Camera

A high-speed camera (see figure 2.6), connected to an electronic microscope, is used in order to visualize the devices of the release system (needles, TM and GPRM). The real-time visualization of the setup is important mainly for three reasons:

- the monitoring of the relative positions of the devices through the camera can avoid undesired contacts between them. During both alignment procedure

and experimental procedure, small displacements have to be commanded to the motors and the relative position has to be constantly checked, since unexpected contacts (e.g. between GPRM and test mass) have a negative influence on the system alignment and can be dangerous for the safety of the devices.

- a screenshot of the position of the devices can be useful for the alignment. By knowing the geometry of the devices, once a zoom level is chosen, a pixel-micrometer conversion factor can be computed and used in order to compute the motion that has to be commanded to the devices.

- it is important to record the setup during the release: since the interferometer measures the motion of the mass, the camera is the only feedback available for the behaviour of pin and plunger during the release. Thanks to the camera recordings, it is possible to prove that the detachment of the pin from the TM has effectively occurred during the experiment.

An example of camera frames is shown in picture 2.13. Frame dimension and frame rate are inversely proportional: the maximum rate (31466 frames per seconds) is obtained with the minimum dimension, i.e. 80x60 pixels (as in figure 2.21).

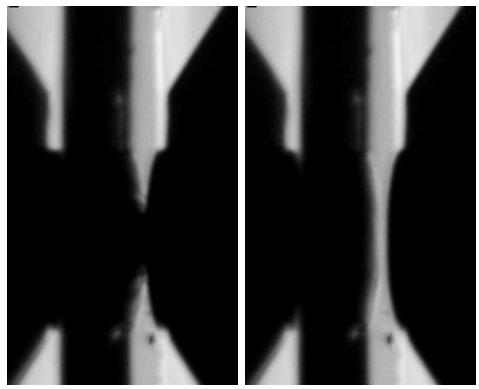

Figure 2.13: camera frames (160x264 pixels, 7311 fps). Left: pin extracted and in contact with the TM insert. Right: pin retracted.

2.2.8 Vibration isolation

Vacuum chamber, measurement system (interferometer and optical lever) and pumps are mounted on an active vibration isolation platform (see figure 2.6), based on piezoelectric actuators. The platform allows to reduce the effects of the ground vibration on the experiment output.

Since both release system and interferometer are rigidly connected to the vacuum chamber, the platform filters all the ground motion harmonics that can create

a relative displacement between interferometer and TM, thus avoiding the measuring of fictitious displacements by the interferometer; moreover, it guarantees that the blocking and release system does not transmit any vibration to the release mechanism during the experiment [36].

The vibrations due to the active pumps (which are not part of the ground noise) can introduce a noise in the signal, thus making the interferometer support oscillate. As a consequence, pumps have to be turned off for few seconds during the release procedure, as far as the pressure level does not increase significantly (see section 2.3.1).

2.2.9 Pumping and vacuum system

In order to simulate the environmental conditions of the in-flight setup, a high vacuum level has to be reached before the experiment. As a consquence, a pumping system, composed of three pumps, is placed close to the vacuum chamber.

Pumps

The pumps (shown in figure 2.6) are activated in sequence in order to reach the target pressure ($\approx 10^{-7}$ mbar) before every experimental campaign. Each pump has a dedicated port that can be opened when the pump has reached its steady state pumping rate and isolates the vacuum chamber when the pump is turned off.

Starting from the ambient pressure, a scroll pump is activated first; a turbomolecular pump leads then to the target pressure of about 10^{-7} mbar.

The vacuum condition is then mantained by a ionic pump, which remains active during all the operations. The ionic pump is turned off only for few seconds (10 sec. maximum) during the release event, in order to reduce the vibration on the platform (which affect the interferometer measurement, see section 2.3.1); in this time interval, the pressure can increase up to $3 \cdot 10^{-7}$ mbar.

Heating system for internal walls cleaning

Once the vacuum chamber is hermetically closed, and turbomolecular pump turned on, heating resistances are put on the external walls of the vacuum chamber and thus the internal temperature of the vacuum chamber increased, from an ambient temperature up to approximately 40 °C. This allows the outgassing of the internal walls, i.e. the detachment of particles which are consequently eliminated through the turbo pump. A Pt100 temperature sensor, placed close to the release setup in the vacuum chamber, monitors the temperature during the heating procedure, which can take several days. The heating bands are then removed during the test campaign, which is performed at the ambient temperature.

Pressure measurement

Two measurement systems for the vacuum chamber pressure are available: the ionic pump pressure feedback, which measures the pressure of the pump internal environment, and a pressure sensing device mounted on a flange of the vacuum

chamber. Since the second one is located closer to the TM, it yields the reference pressure that is registered during each release experiment.

2.2.10 Controllers

Controllers of several of the described system (positioners, interferometer and optical lever, pumps, GPRM) are placed in the clean booth or in dedicated places of the vacuum chamber. The properties of these devices will not be described here; we focus here only on the GPRM circuit, since it is representative of the in-flight setup and since a dedicated connection has been implemented for the on-ground test campaign.

GPRM circuit

The GPRM actuation and measurement circuit, shown in figure 2.14, consists of the following components:

- GPRM. Two cables connect the GPRM in the vacuum chamber with the external control devices: the actuation cable (P08) and the measurement cable (P06). Both cables are composed of 15 wires and connected to the external devices through dedicated 15 pins flanges (not all the connections are used). The pin map is shown in figure 2.15.

- external cables connecting the flange of the vacuum chamber with the control unit. The cables have been designed in order to install a voltage divider for the measurement of the stack bias (i.e. voltage of the pin actuation circuit); a real-time measurement of the voltage fall is indeed required for triggering the data acquisition.

- Caging Control Unit (CCU). It is the GPRM control unit and it converts the signals coming from the testing equipment (which hosts the GPRM computer and the power supply) into the corresponding analog signals required by the GPRM circuit. The CCU has to be kept in a controlled environment, therefore temperature and humidity levels of the clean booth are constantly monitored.

- voltage divider. Due to the high sampling ratio of the interferometer measurement, the acquisition window is limited in time and the measurement buffer has therefore to be triggered by the pin retraction, in order to capture the phenomenon. The measurement of the pin input voltage (stack bias) is the only feedback for the pin motion (extraction/retraction) that can be integrated with the software governing the experiment. The voltage divider allows the user to monitor the pin voltage in real time, by scaling the voltage down to a 5 V value, which is in the allowed measurement range of the acquisition system connected with the computers. As a consequence, the quick voltage fall measured by the computer (from 5 to 0 V) is synchronous with the 120 V voltage fall (and therefore with the pin retraction), allowing a dedicated software to trigger the acquisition according to the release event.

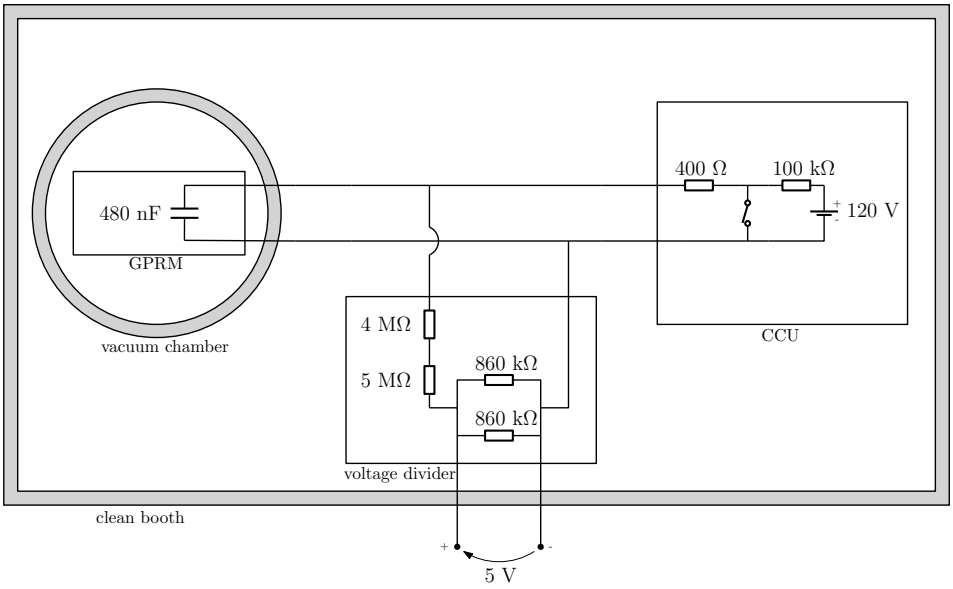

Figure 2.14: sketch of the pin actuation circuit (P08) in the on-ground testing. The charge of the piezo (pin extraction) and its discharge (pin retraction) are governed by the switch of the CCU circuit. The voltage divider allows the experimental software to monitor the voltage in the circuit.

2.2.11 User interface

The user interface is composed of three computers: computer 2 and 3 are dedicated to the whole experimental setup, including all the devices but the GPRM, which is controlled exclusively by a dedicated computer (computer 1) integrated in the Testing Equipment (TE). The controllers of the devices are connected to the computers (directly or through data acquisition devices).

The function of the computers in the experiment is summarized in figure 2.16.

Computer 1

This computer is connected with the GPRM testing equipment and allows the communication with the CCU. The main software governs the GPRM (plunger motion, pin extension and retraction) and yields information on force (from GPRM load cell), plunger position (from strain gauge) and pin extension (from the voltage applied to the piezo).

Computer 1 is part of the testing equipment (TE), which hosts also the power supply of the CCU and allows the communication between computer 1 and the CCU.

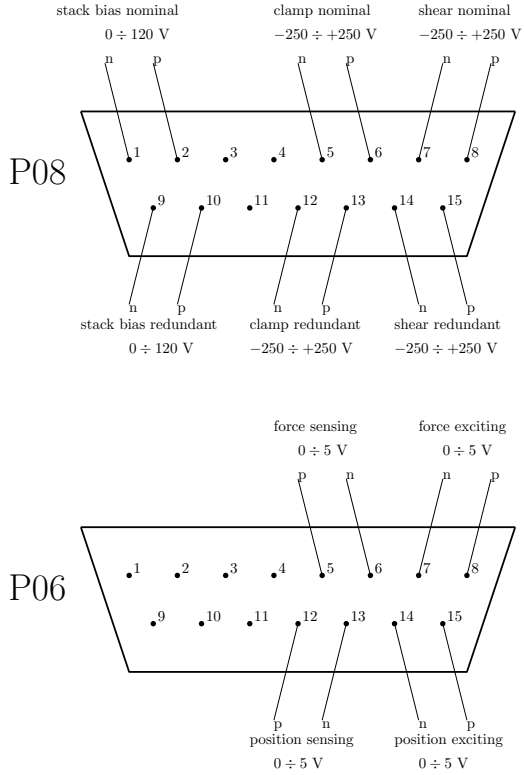

Figure 2.15: GPRM pin assignation. In the actuation cable (P08), the *stack bias* corresponds to the voltage of the piezo circuit of the pin, while *clamp* and *shear* to the plunger "piezo walk" positioning; the redundant circuit is a supply circuit alternative to the nominal one. The measurement cable (P06) is designed for load cell and strain gauge of the plunger.

Computer 2

Computer 2 commands the motion of the positioners for the alignment and release procedure, with a dedicated software based on the feedback of interferometer and optical lever. It acquires also the information of the pin voltage: when the pin retraction is commanded from computer 1, the fall of the voltage is detected and a trigger is sent to computer 3 for the data acquisition.

Computer 3

The main task of computer 3 is the measurement of the TM motion through interferometer and optical lever. During the experimental procedure, the software waits for the trigger sent by computer 2 in order to centre the acquisition buffer w.r.t. the release event. The synchronization allows also the recording of the camera frames.

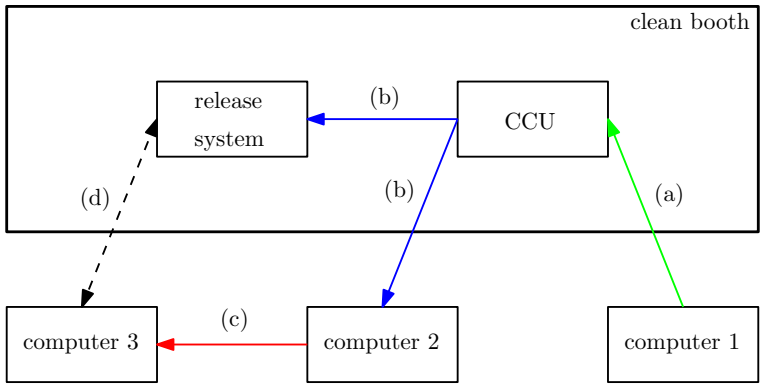

Figure 2.16: tasks of the computers in the experiment. Computer 1 sends the pin command to the CCU (a), which produces the voltage fall of the pin piezo circuit (b) in order to release the TM. The voltage fall is detected by computer 2, which sends a trigger (c) to computer 3, in order to centre the data acquisition (d) w.r.t. the release event.

2.3 TM release in the TMMF

In this section the steps of the experiment are described.

The three devices involved in the experiment (needles, TM and GPRM) are first aligned along z axis in order to constraint the release phenomenon in a unique direction (see appendix A.1). The details of the experimental procedure (already summarized anticipated in section 2.1.2) are reported, by distinguishing the *blocking procedure* and the *release procedure*.

The test outputs (TM displacement along z axis and camera frames) are discussed in section 2.3.2. The main test output is the z displacement measured by the interferometer, which will be analysed in detail in chapter 3.

2.3.1 Experimental procedure

As described in section 2.1.2. the experimental procedure is composed of a *blocking* procedure and a *release* procedure [91].

Blocking procedure

We report here the main steps of the blocking procedure, shown in figure 2.17:

- the blocking procedure starts in the free TM configuration (section 2.1), when the needles and the plunger (with the pin retracted) are approximately 1 mm far from the TM (figure 2.17 a).
- the TM oscillation is reduced thanks to the control loop of the TM positioners, and the needles are then gently approached (figure 2.17 b) to the TM until a contact can be deduced from the TM oscillation (perturbation of the

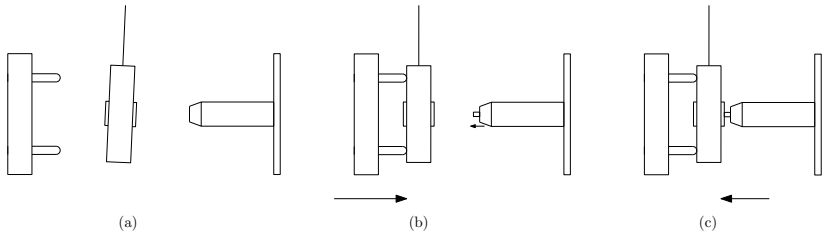

Figure 2.17: blocking procedure. Left: initial condition (free configuration), with TM oscillation. Centre: approach of the needles in order to stop the TM oscillation and pin extraction. Right: approach of the GPRM and application of the preload.

TM oscillation due to an impact). By repeating stabilization and needles approach, the full needles-TM contact is reached: this occurs when the TM does not show any oscillation and a displacement of 1 μm of the needles correspond to an equal motion of the TM along z axis.

- the CCU is then switched to operative mode and an extraction of the pin is commanded (figure 2.17 b). The full pin extension is read by computer 1 and by computer 2 through the voltage divider, and it is checked visually through the camera. Once the pin is extracted, the force value (f^A, which is the offset with zero preload) is registered.

- the plunger with the extracted pin is then approached to the TM, with a speed dependent on the distance from the TM: in order to avoid undesired impacts, the commanded motion steps and velocities are lowered when the camera shows that the pin is close to TM insert.

  The TM-pin contact (*incipient contact*, figure 2.17 c) is detected when a change in the orientation of TM surface (read by optical lever) is measured. The measured variation of the TM pitch has to be lower than a tolerance (approximately ± 30 μrad); a higher variation can occur if the needles are not aligned w.r.t. the TM vertical surface (in this case, the operation must be repeated after the correction of the needles orientation).

  The *blocked condition* is reached if a further displacement of the pin towards the mass does not change the orientation of the TM.

Once the TM is blocked, the preload is applied: the GPRM is pushed against the TM until a force level f^B is reached, such that the force increment is equal to the desired preload f_0:

$$f_0 = f^B - f^A \tag{2.12}$$

In order to reproduce the same conditions of the in-flight contact, the target value of f_0 is 0.3 N. The force increment ratio is approximately 0.1 N for a motion of 5 μm (due to the stiffness properties of the system): as a consequence, a displacement of 15 μm towards the mass is commanded. Although the reference for the preload force is always the output of the load cell, commanding the same displacement of the GPRM towards the mass for all the tests allows to improve the repeatability of

the preload force. The estimated standard deviation of f_0 (as defined in equation (2.12)) is approximately 0.02 N; the high relative uncertainty of f_0 is due to the low precision of the load cell in the preload range.

Release procedure

The release procedure is sketched in figure 2.18.

- once the mass is in the blocked configuration (figure 2.18 a), the preload applied and the signal level of the interferometer in the desired range (higher than 90%), the release procedure can be performed. The release software on computer 2 and laser and camera software on computer 3 are activated in "waiting mode" for the detection of the voltage fall due to the pin release.

  In order to minimize vibrations, the fans of the clean booth are switched off, as well as the ionic pump (for a maximum interval of 10 seconds before the release, in order to avoid a high increment of pressure). The laser modulator is also deactivated in order to decrease the interferometer signal noise.

- the GPRM pin release is then commanded from computer 1; the pin retracts quickly (figure 2.18 b) and the voltage fall is detected by computer 2 through the voltage divider, such that the trigger is sent to the camera software and to the laser software (as shown in figure 2.16); the two z positioners of the blocking system (needles and GPRM) are finally retracted, in order to minimize the number of impacts between the TM and the devices. After the recording of the desired number of data samples (2 seconds of acquisition), each measurement (interferometer, optical lever, camera) is automatically saved in the selected folder.

Fans and ionic pump are then turned on and CCU mode switched to standby mode.

The test procedure is concluded and a new test procedure can start from the repetition of the blocking procedure.

2.3.2 Test output

The main output of the test is the measurement of the z displacement of the TM during the release, which will be considered for the search of the direction of maximum impulse (see section 2.4.2) and for a first worst case prediction of the in-flight release velocity (section 2.5). The extraction of more detailed information from the release signal will be discussed in chapter 3. Another output is the camera recording: the camera frames are used to verify the pin detachment from the TM. The signal of the optical lever is considered in order to verify the variation of pitch and yaw signals during the release phenomenon. The variation in an observation window of 500 μs (which captures entirely the release phenomenon) is in the order of 10 μrad (less than 10^{-3} degrees) and therefore negligible.

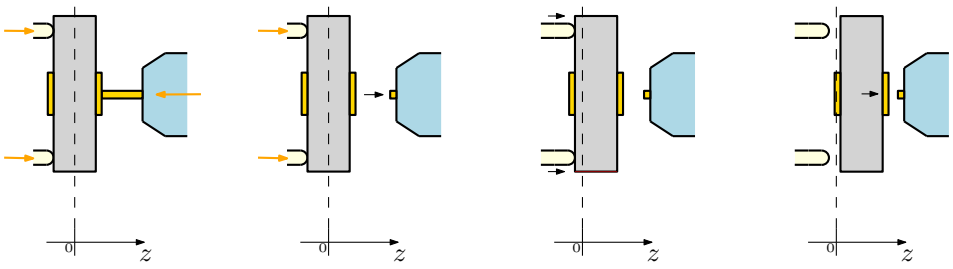

(a) (b) (c) (d)

Figure 2.18: release procedure and reference z axis. Black arrows correspond to motion of the devices, red arrows to applied loads. a) blocked configuration (the pin extension is exaggerated for sake of clarity), with the TM barycentre at the 0 position. b) pin retraction and push of the needles. c) extension of the needles and detachment. d) free flight of the TM.

Displacement signal

The sampling frequency of the interferometer signal is 200 kHz (i.e. one sample every 5 μs). According to the recording buffer settings, the interferometer software records 200k samples before the detection of the trigger and 200k after the detection, for a total number of samples corresponding to an observation window of 2 seconds. The samples distribution is chosen such that the phenomenon can be completely recorded, by taking into account its predicted duration and the possible delay between the pin release and the detection of the trigger by the measurement softwares.

The displacement data set is composed of two vectors, t (s) and z (μm), where z is the displacement of the $z-$ face of the TM insert (where the interferometer laser beam is reflected). The position of the insert does not coincide with the one of the TM centre of mass, due to the TM width and to mechanical vibrations of its structure that can lead to a relative displacement between them (although in the nanometre scale). This will be further discussed in chapter 3. For the purposes of this chapter, we will consider the TM as a rigid body; as a consequence, the difference between the two displacements is assumed to be constant and we can consider the measured position as the position of the barycentre (in other words, we are now considering the TM as a thin rigid plate with negligible width). The chosen reference for z axis is shown in figure 2.18: we consider that the position of the TM barycentre is $z = 0$ when the pin is retracted.

The release signal is shown in figure 2.19; a zoom of the TM acceleration (from blocked condition to free flight velocity) is shown in figure 2.20. The measured displacement signal shows a relevant variation of the TM position with respect to the blocked configuration (corresponding approximately to the 0 position). In the following, the main intervals and instants are distinguished and defined, and a reference frame given to the signal, such that the phenomenon starts in $z = 0$ at $t = 0$ (as shown in figure 2.20). These definitions will be further discussed in

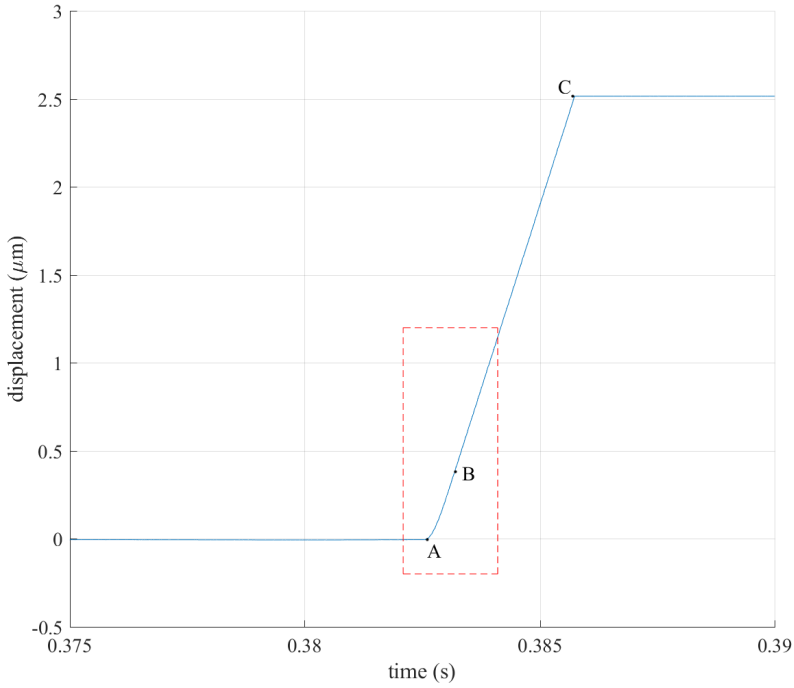

Figure 2.19: z output of the TMMF release (real data of a release test). The zoom of the red dashed rectangle corresponds to figure 2.20.

the next chapter (section 3.1): for the purposes of this chapter, only the free flight velocity (which is easily recognizable and measurable) has to be computed.

We define the following intervals and instants:

- *pre-release interval* (before point A in figure 2.19 and 2.20; figure 2.18 a). The mass is blocked and the pin is ready to be retracted. The noise in the signal decreases during this interval, until the ionic pump is completely switched off.

- *release instant* (point A in figure 2.19 and 2.20; figure 2.18 b). The mass moves w.r.t. to the blocked position. The *incipient motion sample* (i.e. the first sample with the mass considered in motion) is defined as the first sample exiting significantly the distribution of z signal in the pre-release (see section 3.1.1). As a consequence, the last sample before the incipient motion sample is the last sample with the mass in the blocked configuration, and will be referred to as *release sample*. In order to confer a reasonable t-z reference frame to the signal, the time axis is defined such that $t = 0$ for the release sample; the mean of the displacement distribution of few samples before the release instant (i.e. the mean position before the release) is considered as

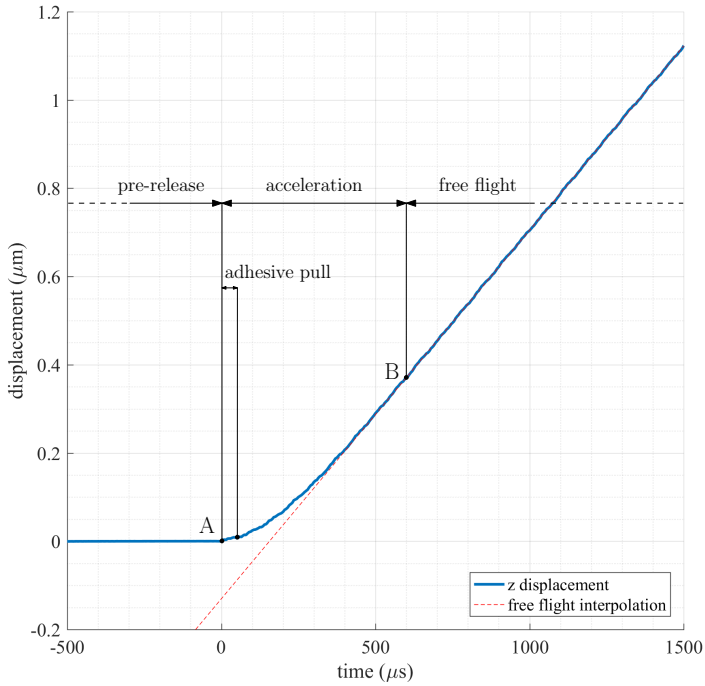

Figure 2.20: release z output (zoom) with the new reference frame. The red dashed line corresponds to the linear fit of the free flight velocity.

the 0 reference for z axis.

- *acceleration interval* (between A and B in figure 2.19 and 2.20). The mass moves due to the two forces applied: the adhesive pull and the push of the needles, both positive in z direction. Based on the results and analyses of the previous TMMF campaigns (reported in section 1.2.3), we expect that the contribution of adhesive pull for the TM displacement is much lower than the one of the needles push. Moreover, the expected duration of the adhesive pull is much lower ($\approx 1/10$) if compared to the duration of needles push; the adhesive pull is expected to be exhausted in a time range of 50 μs maximum, as shown in the figure (as explained in section 1.1.6, the maximum duration of the adhesive pull corresponds to the time required for the pin to move of a quantity corresponding to the maximum adhesive bond length). As a consequence, the needles push effect is prevailing for z displacement.

- *detachment instant* (point B in figure 2.19 and 2.20; figure 2.18 c). Since there is no mechanical joint between mass and needles, and adhesion between TM and needles can be neglected (see section 2.9), when the needles push is exhausted the mass detaches from the needles.

- *free flight interval* (from B to C in figure 2.19; figure 2.18 d). At the detachment, the mass starts moving freely with a uniform linear motion: the needles can be indeed modelled as a unilateral spring, and the equation of motion for such a mass-spring system is piecewise, since the spring forces the mass only when it is compressed. The slope of the TM motion in the t-z graph (red dashed line of figure 2.20) is therefore the *free flight velocity*, which is the main output for the purposes of this chapter.

- *signal saturation* (after C in figure 2.19). Before the release, the interferometer gain has been set in order to have a high measurement quality (low noise) during the release event; as a consequence, the measurement range is reduced. When the displacement exceed a maximum value, the signal is saturated and the constant threshold value is displaced.

The release phenomenon corresponds mainly to the acceleration phase, since in this interval the TM acquires momentum due to the adhesive pull. As it will be explained in chapter 3, important information is given by the pre-release interval and by the the free flight velocity interval.

In the pre-release interval we can define the 0 reference position and a reference noise spectrum (the pre-release noise).

We need to use the free flight signal in order to determine the detachment instant: the position of the detachment instant along t axis is unknown (and not quantifiable with the same method of the release sample), but it can be reasonably assumed that (when the slope of the signal is approximately constant) the mass is moving of uniform linear motion before the signal saturation. Therefore, if we interpolate the free flight signal with a linear regression close to the saturation and we plot the corresponding straight line (as shown in figure 2.20), we can estimate the detachment instant (the detailed estimation is discussed in section 3.1.3). Moreover, if we model the TM as a thin plate, a free motion of the mass allows to estimate the vibration of its first few modes with a high accuracy (which is not possible during the acceleration interval due to the prevalence of the effect of needles push). These issues will be discussed in chapter 3.

Camera recordings

The fast camera allows to record the release procedure with a sampling rate of 31466 frames per second, since the TM-pin contact surface can be monitored with a reduced number of pixel (80x60, as in figure 2.21). As shown in the figure, while the profiles of the two mechanisms can be difficultly seen in the contact condition, they can be easily distinguished when the pin retracts.

As already stated in section 2.2.7, the camera is used mainly during the blocking procedure to check the relative position between the components. However, thanks to the camera recordings it is possible to prove that the TM is free on the pin side during the interval acceleration (i.e. rupture of adhesive bond between pin and TM), as shown in figure 2.21 (as well as in figure 2.13).

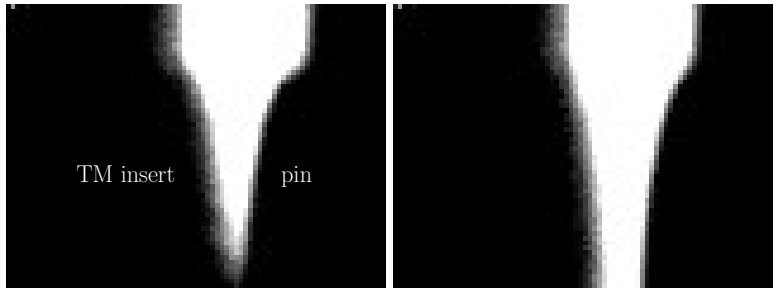

Figure 2.21: camera frames during release (31466 fps, 80x60 pixel). A detail of the profiles of TM insert and pin is shown. Left: contact between insert and pin. Right: pin release.

2.4 Experimental results

In this section, the experimental results are described.

The *release test campaign* consists of 120 release tests at the nominal preload with different plunger configurations. The goal of each release test is the measurement of the free flight velocity; the release test campaign yields therefore a statistics for the free flight velocity, which will be analysed in section 2.5.

The motivations of the release campaign are briefly discussed in section 2.4.1, while the results are commented in section 2.4.2.

2.4.1 Release test campaign

For a single release test, the free flight velocity can be easily estimated with high accuracy (uncertainty $\approx 0.1\%$) in the free flight interval, by means of a linear regression [92]. For instance, in the case of figure 2.20, the estimated free flight velocity is:

$$v_{test} = 835.0 \pm 0.91 \ \mu\text{m/s} \tag{2.13}$$

where the reported uncertainty is the standard deviation of the estimated slope.

If interpreted according to the model of section 2.1.3, the free flight velocity contains information on the adhesive pull (adhesive impulse). Unfortunately, the contribution of the needles push in equation (2.10) is much greater than the one of the adhesive impulse. As a consequence, a strategy for the "filtering" of the needles effect is required.

One possibility is a statistics of the free flight velocity by means of many repetitions of the test. This allows to compute a probability distribution of the differences of two opposite adhesive pulls in the in-flight case. This will be explained in the next section (2.5).

The repetition of the test through a dedicated *release test campaign* has also other motivations.

First, repeating the procedure can make predictions robust with respect to random disturbances. The main ones are due to effects that can also occur in the in-flight setup:

- non-repeatability of adhesion. The adhesion contact energy depends on many conditions that can be difficult to repeat from test to test: the creation of adhesive bonds between two surfaces has a low repeatability. Therefore also the adhesive pull, which depends on the number and the strength of adhesive bonds, can vary from test to test.

- uncertainty of the force. The load cell of the GPRM is affected by a high noise with respect to the nominal value (20 mN versus the nominal preload of 300 mN).

The test repetition is also motivated by the possibility of changing the test parameters:

- release direction. Although the pin and the TM have been aligned before the test, it is possible that in the "aligned" configuration the pin is not perfectly orthogonal with respect to the mass, which is the condition that should transfer (on average) the higher adhesive pull to the mass; a relative inclination different than the orthogonality could lead to spurious shear forces that limit the conversion of adhesion rupture into linear momentum [36]. It is also possible that this is not the case, namely the higher transferred momentum occurs with a not perfect orthogonality between pin and insert surface. As a consequence, exploring different release directions (i.e. yaw and pitch of the plunger) allows to find the system configuration corresponding to the direction of maximum transferred impulse.

- TM-pin contact zone. A repeated contact between TM and pin in the same zone of the insert surface can modify the TM surface w.r.t. its original state. Although the contact zone is difficulty repeated from test to test (due to random modifications of the TM position in the blocking phase), varying periodically the contact zone during a test campaign can average this effect. However, since the contact between TM and pin can be performed in a limited area, if a large number of tests has to be performed, groups of tests must necessarily be characterized by the same (nominal) contact zone.

The dependence of the tests with respect to release direction is investigated. By taking into account the nominal case, a preload force of 0.3 N (nominal preload) is applied and the test repeated for different pin orientations.

2.4.2 Sensitivity to orientation

In order to look for the direction of maximum impulse (i.e. the sensitivity to orientation), the test is repeated with different inclinations of the plunger (yaw and pitch, i.e. rotations about y and x axes).

The procedure needs an appropriate indicator for the impulse estimation. If the pin is not orthogonal w.r.t. the TM surface, shear forces arise at the contact, which can reduce the adhesive pulling impulse. The relative orientation affects also the needles push, since (in principle) a orthogonal preload maximized the needles compression. As a consequence, the parameter used for the maximum impulse is

the free flight velocity, which is maximized if the adhesive impulse and the needles push are maximized.

In order to state that the mean impulse associated to a release direction is statistically higher than the mean impulse of a different direction, 10 tests are repeated for every direction and, in order to compare two directions, the associated tests have to be compared by a hypothesis test . Two directions are assumed to produce the same mean velocity when the p-value of the test of hypothesis is larger than 50% [65]. This approach is similar to the one of previous configurations of the TMMF [87].

The aligned position is referenced as (0,0). A direction grid centered in (0,0) position is then designed: the grid resolution is 0.092° (according to the motion resoluton of the actuators) for each angular direction.

In table 2.2 an example of distribution for a single direction is reported; in table 2.3 we summarize the results for different directions, by reporting the mean velocity of each distribution. For a single direction, the uncertainty of every estimated velocity is significantly smaller compared to the standard deviation of the direction, confirming that the measurement precision is adequate. As shown in the table of figure 2.3, the maximum final velocities occur for two directions, namely (-0.3°, 0°) and (-0.3°,-0.092°), whose distributions are statistically consistent. The velocities along the surrounding directions are significantly smaller, such that the hypothesis test rejects the hypothesis of equal mean values [51]. The overall behavior of the release velocity is fairly regular and shows just an absolute maximum; since the absolute maximum is reached along two directions, we assume that the worst-case misalignment of the release tip direction spans of ±1.6 mrad (±0.092°) around each, covering the yaw interval between -0.392° and -0.208° and pitch interval between -0.184° and +0.092° [65].

		final velocity (µm/s)	fit uncertainty (µm/s)
test	1	828.1	0.73
	2	863.3	0.79
	3	886.1	0.84
	4	841.7	0.74
	5	790.8	0.61
	6	862.7	0.69
	7	884.8	0.79
	8	878.8	0.80
	9	842.5	0.72
	10	876.1	0.81
	mean	856	
	standard deviation	30	

Table 2.2: estimated free flight velocities for one release direction (yaw -0.3°, pitch +0.092°).

As a consequence, for the prediction of the in-flight velocity of the next section (2.5), 12 directions (black rectangle in figure 2.3) are chosen; the whole test

		yaw (°) -0.6	-0.392	-0.3	-0.208	0	+0.3
pitch (°)	+0.3					772 ± 33	
	+0.092		848 ± 26	856 ± 30	839 ± 28		
	0	820 ± 27	807 ± 36	873 ± 36	843 ± 39	847 ± 33	847 ± 37
	-0.092		837 ± 34	874 ± 18	847 ± 25		
	-0.0184		839 ± 23	838 ± 28	859 ± 39		
	-0.3					808 ± 39	

Table 2.3: mean final velocity (μm/s) of each release direction and standard deviation of the distribution (10 tests for each direction) . Neighbor numbers in equal colour are statistically consistent; the maximum corresponds to the two directions in red color. The black rectangle contains the 12 directions of the release campaign. Numbers in gray color have been measured while searching the direction of maximum with a a larger yaw step (0.3°).

campaign data set corresponds therefore to 120 tests.

In figure 2.22 the statistical distribution of the release velocities of the 120 tests is shown. The global mean velocity of the complete set of tests is 846.4 μm/s, with a standard deviation of 34.5 μm/s.

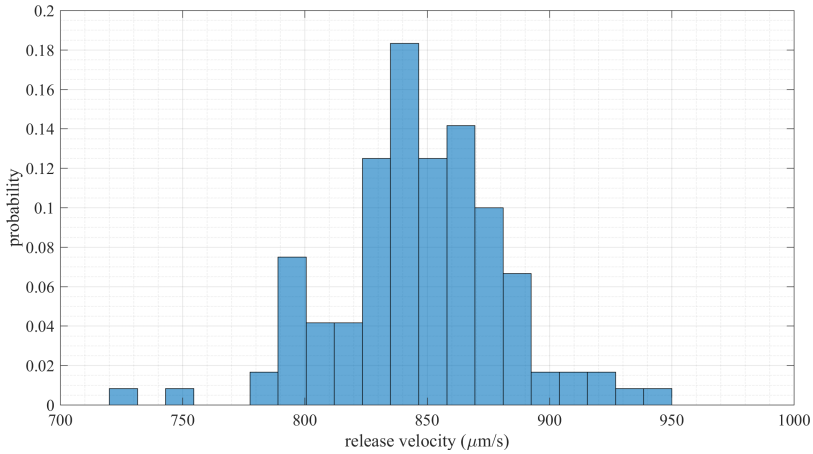

Figure 2.22: probability distribution of the release velocity in the release test campaign.

2.5 A conservative estimation for a nominal release

As discussed in section 2.1, the presence of two opposite GPRM (Z+ and Z-) in the satellite and the difference between the masses makes the TMMF not fully representative of the in-flight case.

The final linear momentum (i.e. free flight velocity) of the TM in the ground testing is due to needles push and GPRM adhesive pull, which are in the setup two unilateral effects (i.e. they have the same direction): therefore, we say that the on-ground test corresponds to a *one-sided release*. In a nominal in-flight case (see section 1.1.6), the final momentum is also due to a pushing force and an adhesive pull, but each contribution is the difference of two opposite (and in general different) contributions, each one due to one of the two plungers of the GPRM: we say indeed that the in-flight case is a *two-sided release*.

Moreover, given an external impulse due to an adhesive effect, the lower mass of the TM in the ground setup produces a higher velocity when compared to the in-flight case. As a consequence, for the prediction of the in-flight velocity the free flight linear momentum $p = mv_{test}$ measured by the TMMF has to be considered, and not the free flight velocity v_{test}.

In the following the TMMF results are interpreted by means of the on ground release model (equation (2.10)), and the measured probability distribution of the adhesive impulse is applied to the in-flight release model (section 1.1.6) for the prediction of the contribution of adhesion to the in-flight release velocity: this is possible since, despite the differences between the two system, the same adhesive contribution appears in both models.

In section 2.5.1 we summarize the principle of the estimation of the in-flight release velocity: the estimation is based on the output of the TMMF (free flight velocity) by taking into account the differences between on-ground setup and in-flight hardware (summarized by their dynamical models).

We consider then the data of section 2.4 in order to obtain a probability distribution of the in-flight release velocity; this is described in section 2.5.2. Notably, we are not considering in our predictions the effect of the time delay between the two pins (see section 1.1.6), since it cannot be estimated by the TMMF tests: in other words, we focus on the effect of the adhesive pull on the in-flight velocities (although we know that other effects can occur).

Finally, in section 2.5.3 we compare the results with the previous TMMF predictions.

It has to be mentioned that the prediction of the in-flight velocity is based on the assumption of nominal release (see section 1.1.6), i.e. release occurring along the nominal direction z with perfectly aligned devices (the nominal release configuration will be further defined in section 4.1.2). Moreover, since the final goal in this stage is the analysis of the criticality of the TM release in LISA Pathfinder w.r.t. the requirements, we are allowed to consider a *conservative* estimation of the effect of adhesion on the in-flight velocity; a more precise estimation of the contribution of adhesion will be discussed in chapter 3.

2.5.1 From on-ground results to in-flight estimation

In the following we describe the projection of the on-ground results to the in-flight case, by taking into account their dynamical models. In particular, we define a worst-case estimation of the percentage of the in-flight momentum that depends on the force applied by the pin (including adhesion); this allows to get a simple equation (equation (2.26)) that describes the probability distribution of the in-flight velocity based on the TMMF results.

Prediction of the in-flight velocity probability distribution

We recall here the equation that describes the in-flight release momentum in the nominal configuration (equation (1.7)), which has been defined in section 1.1.6 as the difference of the two momenta given by the pins:

$$M\ v_{flight} = \iota_{push} + \iota_{pull} = f_0 t_D - \frac{f_0\ \Delta t_1}{2} + \Delta\iota_{adh} \tag{2.14}$$

where M is the mass of the in-flight TM (1.928 kg), v_{flight} the in-flight release velocity, f_0 the preload, t_D the delay between the motion of the two pins, Δt_1 is related to the difference of the velocities of the two pin retractions, $\Delta\iota_{adh}$ is the difference of the adhesive impulses on the two sides.

As discussed in section 1.1.6, a probability distribution of the in-flight release velocity v_{flight} at the nominal 0.3 N preload can be estimated if all the contributions are known with their probability distribution.

The goal of the TMMF is the estimation of $\Delta\iota_{adh}$. If a probability distribution related to a single adhesive impulse is available (in the TMMF, $\iota_{adh,z-}$), by considering no systemic difference between the two sides of the GPRM we can easily compute the probability distribution of the difference between two impulses.

For the effect of Δt_1, a probability distribution (from measurement performed by RUAG) has been presented in section 1.1.6.

As discussed in the same section, the properties of the electrical circuit of the GPRM allow to consider that the command of retraction is given to the two opposite pins with a fair synchronization; based on this information, we would consider $t_D = 0$. However, this effect is strongly affected by the environmental and operating conditions and manifacturing details (including those of the flight electronics), therefore systematic differences between the flight and tested units cannot be excluded [51]. On the basis of this observations, we do not consider the time delay t_D in our predictions, but at the end of this section we will briefly comment the possible additional effect of t_D on the predictions.

We consider hence the following model for the in-flight prediction:

$$M\ v_{flight} = -\frac{f_0\ \Delta t_1}{2} + \Delta\iota_{adh} \tag{2.15}$$

As for section 2.1.3, we can define the momentum of each pin with the letter ι:

$$\iota^+ = -1/2 f_0 t_1^+ + \iota_{adh,z+} \tag{2.16}$$

$$\iota^- = 1/2 f_0 t_1^+ - \iota_{adh,z-} \tag{2.17}$$

such that

$$M\ v_{flight} = \Delta\iota \tag{2.18}$$

As a consequence, if a distribution for $\Delta\iota$ is known, a distribution for the in-flight release momentum can be estimated.

Conservative estimation of v_{flight}

We recall here the equation for the TMMF release momentum (equation (2.10)):

$$p = \sqrt{q^2 + \iota^2} \tag{2.19}$$

where p is the free flight momentum (mv_{test}), q is the momentum due to the needles push and ι the momentum due to the pin force. q and ι are defined in equations (2.8) and (2.9): ι takes into account both the effects of t_1 and ι_{adh}.

As described in section 2.4, a distribution is available for the TMMF free flight velocity v_{test}; the probability distribution is shown in figure 2.22, and the probability distribution of $p = mv_{test}$ follows immediately.

Based on the distribution of p, we want to estimate a conservative distribution of $\Delta\iota$, in order to compute equation (2.18).

If we assume a normal distribution of ι, then the distribution $\Delta\iota$ depends uniquely on the standard deviation σ_ι, since in the differences the mean value μ_ι disappears. As a consequence, if we are able to prove that, being p defined as in equation (2.19), the dispersion of p is higher than the one of ι, then Δp is an upper bound for $\Delta\iota$.

We discuss in the following the general relation between the dispersion of p and the dispersions of q and ι of equation (2.19).

Let's assume two normal distributions a (mean $\mu_a > 0$, variance σ_a^2) and b (mean $\mu_b > 0$, variance σ_b^2). Let's consider that $\sigma_a \leq \sigma_b$, i.e. b is defined as the more dispersed distribution. Let's consider their Pythagorean addition c :

$$c = \sqrt{a^2 + b^2} \tag{2.20}$$

It can be proved that in this case, if we define with $\widehat{\sigma_c}$ the estimator for the standard deviation of c, we get:

$$\sigma_a \leq \widehat{\sigma_c} \leq \sigma_b \tag{2.21}$$

which means that the value $\widehat{\sigma_c}$ is bounded by the two values σ_a, σ_b.

An analytical proof of equation (2.21) is not possible without a numerical integration; it can be easily proved for small values of the uncertainties through the error propagation. However, a numerical Montecarlo simulation (that makes the quantities μ_a, μ_b, σ_a, σ_b span of many orders of magnitude) has proved that the equation (2.21) holds for any combination of the parameters.

The same simulation has proved that, if a and b are positively correlated, then the equation is no more verified but the following relation still holds:

$$\sigma_a \leq \widehat{\sigma_c} \tag{2.22}$$

As a consequence, (2.22) holds independently of the (positive) correlation between a and b, thus revealing that the estimator for the standard deviation of the Pythagorean sum c is an upper bound for the standard deviation of the less dispersed distribution (a). Being the distribution of c not normal, the Montecarlo simulation has proved also the following:

$$\sigma_{\Delta_a} \leq \widehat{\sigma_{\Delta_c}} \tag{2.23}$$

i.e. the dispersion of Δ_c is an upper bound for the dispersion of Δ_a.

Based on this analysis, we can say that, in equation (2.19), if q (push of the needles) is more dispersed than ι (pin impulse), then the dispersion of p is higher than the one of ι and (as a consequence) Δp is a conservative estimation of $\Delta\iota$.

The assumption that q has the highest variability can be suggested by its estimation. According to the definition of equation (2.8), we have:

$$q = \sqrt{\frac{m}{k}} f_0 \tag{2.24}$$

As described in section 2.3.1, we consider that along the release campaign the preload force can have a variation described by a normal distribution with standard deviation 0.02 N. The accurate estimation of k_n (equivalent stiffness of the needles) is very unprecise and seems to be subjected to mechanical effects, like a play of the joint between the needles and their positioner that could make vary k_n significantly. Moreover, in the estimation of k_n a possible correlation with the preload force is suspected. These observations result from the analysis of the compression of the needles during the application of the preload (which has a low reliability due to the drift of the interferometer readout) and from the early stage of the analyses of the signal, when the acceleration phase of figure 2.20 has been fitted to the motion of a preloaded oscillator in order to extract information on the structural parameters (this strategy has been then substituted by the analyses of chapter 3).

However, from the analyses we get a range for the k_n stiffness which can vary from approximately 500 kN/m to 1000 kN/m. For values of k_n in this range, the dispersion of q in equation (2.24) can be estimated by simply considering the variability of the force of 0.02 N. The result is that, according to the estimations, q has always a higher variability w.r.t. p, although of the same order of magnitude. According to the statistical considerations summarized in equation (2.21), this means that σ_ι will be the less dispersed distribution, with a lower variability w.r.t. σ_p.

Moreover, we can consider that, if a correlation between q and ι exists, it is a positive correlation, since the quantity that affects both q and ι is the preload f_0: the higher f_0, the higher the needles push (due to the higher compression, see equation (2.8)), and the higher the adhesive impulse [88]. As previously commented (equation (2.22)), the positive correlation does not influence the fact that p is more dispersed than ι, if we assume that q has a higher variability w.r.t. p.

In conclusion, based on the assumption that the main contribution to the dispersion of the free flight momentum p is due to the needles push q, we have that Δp is a conservative estimation of $\Delta\iota$. By considering equation (2.18), we get the following conservative estimation for the distribution of the in-flight momentum:

$$Mv_{flight} = \Delta p \tag{2.25}$$

and since $p = m \cdot v_{test}$, we get the follwing estimation for v_{flight}:

$$v_{flight} = \frac{m}{M} \Delta v_{test} \tag{2.26}$$

Equation (2.26) is used to predict the probability distribution of the in-flight release velocities from the difference distribution of the TMMF release velocities. The second term of the equation highlights the fundamental difference between the TMMF (on-ground setup) and the GRS (in-flight hardware): the TMMF release velocities are considered in order to give a difference distribution (due to the unilateral release of the TMMF) and the ratio of the masses rescales the result (due to the lighter mass in the TMMF).

We stress the fact that equation (2.26) is a conservative estimation only under the assumption of higher dispersion for the needles push q w.r.t. the pin impulse ι. In chapter 3, where a more precise estimation of the adhesive impulse distribution is presented, we will show the compliance of this assumption with the experimental results.

2.5.2 Probability distribution

The probability distribution of the TMMF free flight velocity v_{test} has been shown in figure 2.22. In figure 2.23 left the corresponding distribution of the rescaled release velocities $\frac{m}{M} v_{test}$ of the TMMF is shown; from this distribution, the rescaled difference distribution $\frac{m}{M} \Delta v_{test}$ appearing in equation 2.26 can be computed (figure 2.23 right).

The distribution of figure 2.23 describes the conservative prediction for the in-flight release velocity according to equation 2.26. The mean is 0 while the standard deviation is 2.2 μm/s. The large majority of the distribution (96.5 %) is inside the requirements (5 μm/s).

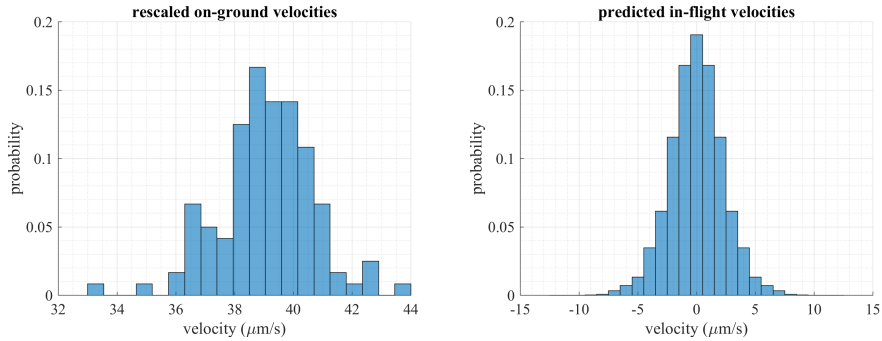

Figure 2.23: probability distributions: rescaled release velocities ($\frac{m}{M} v_{test}$, left) and statistical distribution of the differences ($\frac{m}{M} \Delta v_{test}$, right), which corresponds to the conservative prediction of the in-flight velocity in absence of time delay between the pin retractions.

Contribution of adhesion in the estimation

The estimation of figure 2.23 estimates the effect of the asymmetry between the pin forces on the in-flight velocity. However, as discussed in sections 1.1.6 and 2.1.3, the pin force is composed on both adhesive pull and pushing force due to the falling preload. As a consequence, we would like to decouple the two effects in order to obtain an estimation for the contribution of adhesion. This estimation will however be conservative, due to the statistical properties discussed in section 2.5.1.

A first approach is based on the estimation of the effect of Δt_1 in equation (2.15).

Δt_1 is the difference of the two *times-to-0-preload*. As discussed in section 1.1.6, an estimation of the time-to-0-preload is available:

$$t_1 = 1.2 \pm 0.4 \ \mu\text{s} \tag{2.27}$$

where the reported uncertainty corresponds to the standard deviation.

As a consequence, a worst case contribution of Δt_1 in equation 2.15 could be given by a very high value of t_1 for one pin and a very low value for the opposite one: for instance, $t_1^+ = 2.4$ μs and $t_1^- = 0.0$ μs (i.e. two opposite 3 σ variation with respect to the mean value). We would get in this case

$$\frac{1}{2} f_0 (t_1^+ - t_1^-) = 0.36 \text{ kg } \mu\text{m/s} \tag{2.28}$$

which would correspond to a contribution to the final in-flight velocity of approximately 0.18 μm/s (or -0.18 μm/s if we invert the two time values), a very small value with respect to the range spanned by the in-flight prediction (which is approximately -5$\div$5 μm/s).

As a consequence, in equation (2.15) the effect of t_1 on the final TM velocity can be neglected: we can therefore say that in our conservative assumption the distribution of the in-flight prediction (figure 2.23 right) is all due to the effect of the opposite adhesive pulls.

Effect of the delay t_D

For the estimation of the in-flight velocity, the effect of the delay t_D of equation (2.14) has been not considered. As discussed in section 1.1.6, in the early stage of the design of the GPRM, a maximum delay t_D of 200 μs was recommended. In [65] the delay t_D has been considered as a parameter that can modify the estimation of figure 2.23. We know (as commented in section 1.1.6) a delay of 30 μs can produce a momentum out of the requirement, if not balanced by a opposite adhesive pull; in particular, a possible delay of 80 μs could make the probability distribution of the in-flight velocity exit completely the requirement, with the large majority of the predicted velocities higher than 5 μm/s [65].

As a consequence, the time delay t_D can constitute a critical parameter for the in-flight dynamics of the TM injection into the geodesic trajectory [65].

2.5.3 Comparison with previous predictions

The estimation of the in-flight release velocity of figure 2.23 shows the non-criticality of adhesion for the in-flight release of LISA Pathfinder: the release velocity is lower than the limit (5 μm/s) with a large probability.

The estimation is more critical if compared to the ones of earlier stages of the TMMF development (see section 1.2.3). For instance, the probability distribution of figure 1.16 shows a release velocity lower than 1.50 μm/s in 99 % of the cases [24].

This difference is mainly due to the conservative estimation described in this section. The Montecarlo simulation described in section 2.5.1 has proved that the dispersion of $p = mv_{test}$ (the free flight momentum of the TMMF) is close to the dispersion of q if $q >> \iota$. As a consequence, if the adhesive impulse is comparable to the previous TMMF results (which has to be proved in the next chapter) and the free flight velocity is dominated by the needles push, we are attributing all the dispersion of the needles push (due for instance to a low repeatability of the preload force f_0) to the pin impulse distribution.

This was not the case for the previous predictions: the low velocities of the release tips replacing the GPRM in the previous stages allowed to estimate precisely the adhesive force profile through a differentiation of the displacement signal and the disentanglement of the needles push. In the last TMMF configuration described in this section, the very quick retraction of the GPRM pin did not allow the application of this strategy, leading to the discussed conservative method.

However, being the assumption of this section conservative and based on the reasonable assumption that the needles push is more dispersed than the pin impulse (mainly because of the variability of the applied preload), we can state that the latest stage of the TMMF assures that the contribution of adhesion is not critical in a nominal in-flight release.

2.6 Summary of the on-ground GPRM testing

In this chapter the latest stage of the Transferred Momentum Measurement Facility (TMMF) has been discussed. The general structure of the TMMF in its last configuration has been described (section 2.2). In particular, we have focused on the integration of one side of the Grabbing Positioning and Release Mechanism (GPRM) of LISA Pathfinder in the vacuum chamber, which aimed to increase the representativeness of the on-ground experiment w.r.t. the in-flight case: this modification required a dedicated measurement circuit and a new experimental procedure (section 2.3).

The output of the release test is the free flight velocity of the test mass (TM) produced by the adhesive pull and the push of the blocking needles (according to the model of section 2.1). Being the effect of the blocking needles prevailing w.r.t. the adhesive pull, a proper strategy for the estimation of the in-flight release momentum due to adhesion was needed.

This has been realized by collecting a probability distribution of the TMMF free flight velocity, with a setup orientation that maximized the final momentum of the TM (section 2.4). The statistics has been considered for a conservative estimation of the in-flight release velocity, based on the assumption that in the TMMF the contribution of the needles push is more dispersed than the one of the pin force (due mainly to the reliability of the preload force); the hypothesis has been motivated by experimental observations (and it will be definitively proved in chapter 3). In this case the variability of the free flight velocity in the TMMF, scaled by a factor equal to the ratio between the TMMF mass and the in-flight TM, is an upper bound of the variability of the in-flight velocity (section 2.5).

The resulting probability distribution of the in-flight release velocity (in absence of time delay between the pin retractions) is characterized by 96 % of the distribution inside the requirements. This confirms that, in absence of other important mechanical effects (like asynchrony of the pins), the effect of the opposite adhesive pulls is not critical for the residual momentum of the TM in LISA Pathfinder.

Being the estimation of the adhesive effect conservative, a more precise estimation (not worst-case) will be discussed in chapter 3.

Chapter 3

Vibration mode-based impulse estimation

In this chapter a more detailed analysis of the output of the TMMF experiment is described, and an estimation of the properties of the adhesive impulse, based on a dynamical vibrational model of the TM, is proposed.

In chapter 2, the effect of adhesion on the in-flight release velocity has been estimated (based only on the on-ground free flight velocities) by equating the dispersion of the free flight velocities with the dispersion of the pin impulses, leading to a conservative prediction of the effect of adhesion in the in-flight release.

The analysis of the release signal (i.e. z displacement of the TM at the release), which is the focus of this chapter, can yield more information. The properties of the release signal are commented in detail in section 3.1. The analysis of the signal leads to a new strategy for the estimation of the adhesive pull, based on the analysis of the harmonics contained in the *free flight signal* (i.e. displacement of the TM after the detachment from the needles). In the free flight signal, we notice the presence of harmonics created by the release operation (section 3.2); the repeatability of these harmonics along the whole test campaign suggests the presence of mechanical vibrations of the TM due to the release phenomenon. The TM can be indeed modelled as a thin vibrating plate (section 3.3), with its modal parameters (modal masses, mode shapes); therefore, by means of a linear modal decomposition a dynamical model can be developed, in order to predict the effect of the forces at the release (adhesive impulse, needles push, initial deformation) on the vibrations of the TM.

The experimental data of chapter 2 are finally fitted through the dynamical model of the TM vibrations in order to extract information on the adhesive impulse (section 3.4); this allows a more precise (not worst-case) estimation of the adhesive impulse magnitude.

In section 3.5 we summarize the main results, by commenting the compliance between the estimated impulse properties and the requirements of LISA Pathfinder mission, the comparison with previous predictions, and the main criticalities occurred in the data analysis.

3.1 Information in the release signal

In chapter 2 information on the effect of adhesive pull have been extracted from the final release velocity (free flight velocity), by applying a simple 1 DOF model in order to relate the free flight velocity with the parameters of the model, which included the adhesive pull.

This approach is based on a single datum: the final release velocity. The main advantage of this approach is the high precision of the release velocity estimation, since a simple linear fit of the free flight phase can yield a velocity value with a low uncertainty (see section 2.4.1).

On the other hand, predicting the contribution of the adhesive impulse by taking into account only the final release velocity implies neglecting other information that the measured release signal can yield; moreover, we have seen that only a worst-case assumption can be made on the basis of the final slope of the signal.

Further information can be extracted from the release signal. In particular, we will focus on the *modal informations of the free flight signal*. The free flight signal is the superposition of a linear behaviour (whose slope is the *free flight velocity*) and many oscillations with zero average. It is possible to see that the amplitude and the phase of some of these oscillations are well repeatable along the test campaign data set: this suggests that the oscillations are not random phenomena (like noise) but are strictly related with the repeatability of the release phenomenon. If information on the mechanical oscillation of the TM as a thin plate can be extracted from the free flight signal with a high accuracy, a modal decomposition allows to study the effect of the adhesive pull on the modes.

In this section, we will describe the signal in order to understand what kind of information can be deduced from its analysis. First of all (section 3.1.1), a reasonable and convenient time-displacement reference frame has to be established for the release signal (this was not necessary in the work of chapter 2 for the estimation of the free flight velocity). In section 3.1.2 we analyse for the first time the harmonics of the release signal, and in section 3.1.3 we describe how to distinguish the acceleration phase of the TM from the free flight interval (already defined in section 2.3.2); these preliminary operations will lead to the analysis of the free flight harmonics in section 3.2.

3.1.1 Time-displacement reference frame

As described in section 2.3.2, an appropriate reference frame has to be given to the release signal before its analysis. In particular, the 0 time reference must correspond to the beginning of the release phenomenon, while the 0 displacement reference must correspond to the (equilibrium) position of the TM before the release (this was the case for figure 2.20).

In figure 3.1 an example of release signal is shown. The sampling frequency is 200 kHz. As discussed in section 2.3.2, we consider the release signal composed by three intervals: *pre-release interval*, *acceleration interval* and *free flight interval*. In figure 3.2 a detail of the choice of the new reference frame is shown.

As already described in chapter 2, the recording settings of the experimental

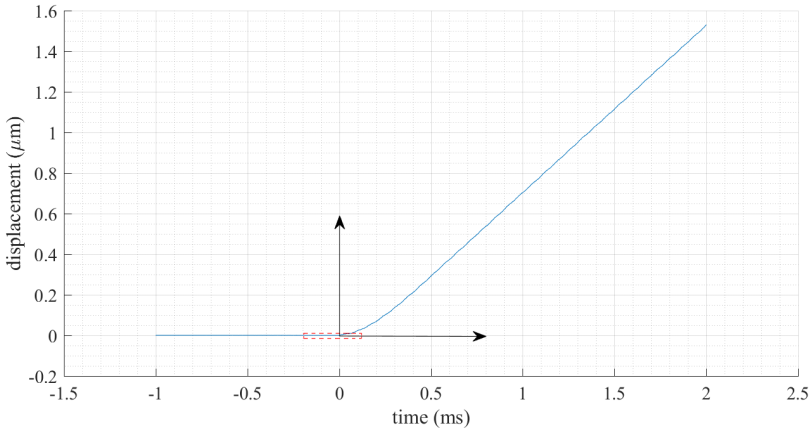

Figure 3.1: release signal and new reference frame. The red dashed rectangle corresponds to the zoom of figure 3.2.

procedure have been tuned in order to capture completely the release phenomenon within the 2 seconds of recording. As a consequence, we know that at the beginning of the acquisition the mass is blocked and at the end of the acquisition the mass has already moved.

By looking at the signal, we can immediately divide it into two parts: a first one during which the mass is blocked (negative time values in figure 3.1), and a second one with a significant growth of the displacement value (positive time values in the same figure).

It is possible to see that the signal remains quite constant in the first part. A more detailed analysis of the signal shows small oscillations (due to signal noise and vibrations) and a slow drift (due to the interferometer). However, the signal remains in a strict displacement band for a long time; the pin release corresponds to a change in the system equilibrium, which leads the displacement signal to exit this band.

As a consequence, we consider the 0 reference of the time axis as the last sample before we can detect a significant change in the signal value: the system is considered blocked at the 0 sample (which we will refer to as *release sample*) and in motion in the next sample (*incipient motion sample*). The iterative method for the detection of the release instant behaves as follows, starting from the beginning of the acquisition (see figure 3.2):

1. for an observation window of 20 samples $(z_{n-19}, z_{n-18}, ..., z_n)$, the mean value of the z signal $\mu_{z,n}$ and the standard deviation $\sigma_{z,n}$ are computed.

2. the first sample not included in the observation window (z_{n+1}) is analyzed. Two situations are possible:

   - if it exits the $\pm 5\sigma_z$ interval, i.e.

$$|z_{n+1} - \mu_{z,n}| > 5\sigma_{z,n} \tag{3.1}$$

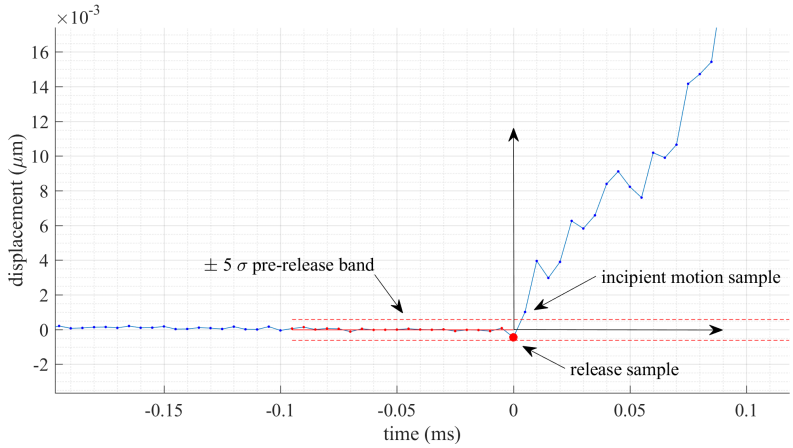

Figure 3.2: detail of the choice of the reference frame for t and z axes (zoom of figure 3.1). The red point is the *release sample* (zero reference for the time); the red segment corresponds to the mean of the 20 last samples before the release instant (zero reference for the displacement); the dashed lines correspond to the $\pm 5\sigma$ uncertainty band.

then we consider that the z_{n+1} sample corresponds to a motion of the TM (incipient motion sample). In this case, the previous sample z_n is the release sample, and the reference frame is established as follows:

$$t' = t - t(z_n)$$
$$z' = z - \mu_{z,n}$$

where (t, z) is the original reference frame, (t', z') is the new reference frame, $t(z_{n+1})$ is the time corresponding to the z_n sample.

- if the condition of equation (3.1) is not satisfied, the observation window shifts of one sample and the process is repeated starting from point 1.

A small number of samples for the observation window has been chosen in order to deal with the shift of the signal (which has a monotonically decreasing behaviour). The 5σ threshold has been chosen in order to have a detection of the incipient motion sample robust w.r.t. noise and signal drift.

The determination of the zero reference for displacement is performed only for sake of clarity in the description of the signal; the dynamical model developed in this chapter for the estimation of the impulse will be independent of the zero reference for displacement, which is therefore an arbitrary choice in order to make the TM start its motion from a null displacement.

Much more important is the determination of the start of the release phenomenon. It has to be noticed that the method necessarily chooses a sample for the 0 time reference (release sample): this does not guarantee that the phenomenon starts *exactly* at the chosen release sample. Figure 3.3 shows some possible interpretations of the system motion. Since we have estimated that the system is not

moving in 0 and is moving in the next sample, the phenomenon will start likely *between* the two instants. However, we cannot exclude also that the real start of the phenomenon occurs before time 0.

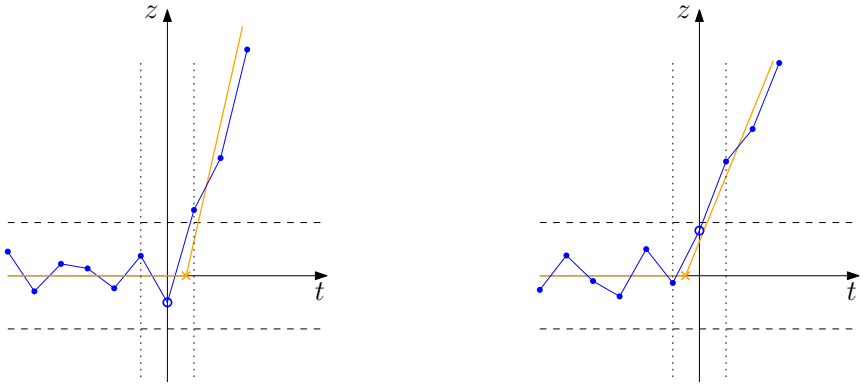

Figure 3.3: interpretation of the TM z motion and distinction between *release sample* (blue circle) and *release instant* (orange cross). Release instant subsequent to the release sample (on the left) and release instant previous to the release sample (on the right). The TM motion has been simplified here with a straight line (red line).

As a consequence, in section 3.4, where the uncertainty of the beginning of the release event, these observations will be taken into account in order to choose an appropriate uncertainty for the release instant.

3.1.2 Harmonics in the free flight signal

For a single test, the spectrum of the free flight signal can be analysed after subtracting the linear interpolation of the free flight velocity (de-trended signal), as shown in figure 3.4.

In figure 3.5 the prerelease signal and the free flight signal are compared, together with their spectra. The spectrum is computed through a discrete FFT on 200 samples: this number corresponds to the maximum number of free flight samples that can be extracted from all the tests (at the end of the free flight interval the signal is saturated, see figure 2.19 in section 2.3.2).

In the following, we comment the spectra by anticipating some considerations that will be discussed later in this chapter.

In the FFT spectrum of the free flight signal, some relevant amplitude peaks are shown. Most of them do not appear in the prerelease noise, suggesting that they are caused by the release phenomenon, or due to the motion of the mass. The main harmonic appearing in the pre-release spectrum is a peak at the 68 kHz frequency, which occurs also in the free flight spectrum (although with a smaller amplitude w.r.t. other peaks).

Many of the harmonics of the free flight spectrum can be identified: this means that they can be attributed to some mechanical effects (free vibration of the TM

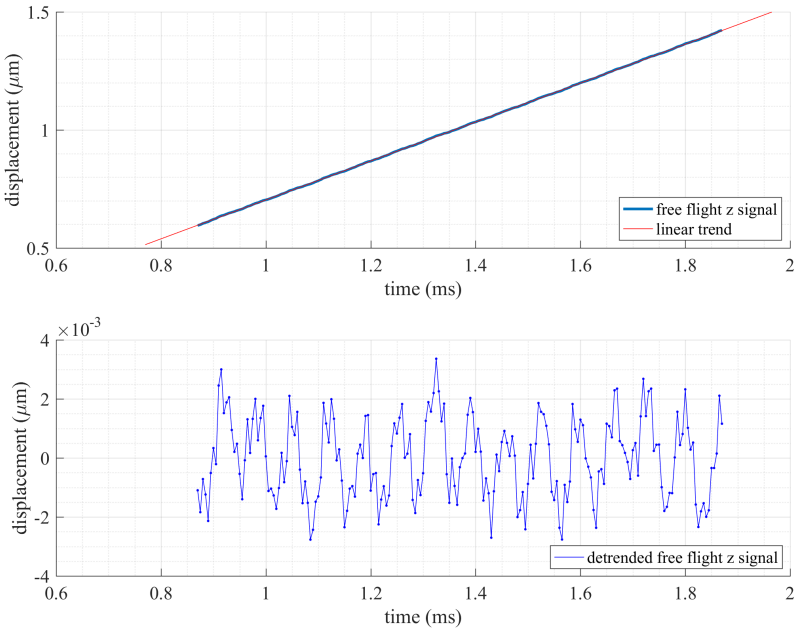

Figure 3.4: free flight signal and detrended free flight signal.

as a thin plate) or noise due to cyclic error of the interferometer (see section 3.2.2).

A model that takes into account the identified harmonics can be used for a fit of the signal in order to estimate their amplitude and phase with a good accuracy. In particular, once the mechanical harmonics corresponding to the free vibration of the TM as a thin plate are identified, the modal decomposition applied to a model of the TM as a thin plate can yield predicted values of these harmonics, which will depend on the parameters of the forces applied to the TM (including the adhesive force); the comparison between predicted and measured amplitude of the set of harmonics allows an estimation of the input properties.

3.1.3 Determination of the free flight interval

Before analysing the harmonics of the free flight interval (which, according to figure 3.5, can yield information on the release phenomenon), an estimation for the *detachment instant* (the beginning of the free flight phase, see section 2.3.2) has to be computed, such that the computation of the free flight velocity and the spectrum analysis are performed in a time range when the TM has effectively detached from the needles.

A possible strategy consists in the fit of the signal with the model of the TM-needles system as a unilateral mass-spring system . The model equation depends on the parameter ω (frequency of the mass-spring system) or (alternatively) on

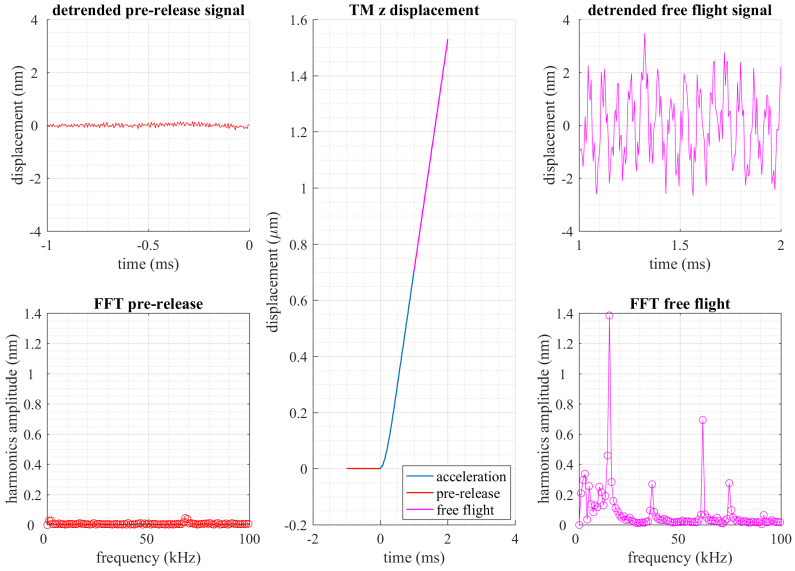

Figure 3.5: comparison between prerelease FFT spectrum and free flight FFT spectrum. Due to the sampling ratio of 200 kHz, the spectrum is defined from 0 to the Nyquist frequency (100 kHz).

the parameter T, which is the estimated detachment time; therefore, the fit of the signal can yield an estimation of parameter T with its uncertainty. The problem related with this strategy is that it is dependent on the choice of the dynamical model.

Here an alternative strategy is described (which was first presented in [93]). For each signal, the derivative can be computed (3.7). The derivative suggests that before the signal saturation the TM is in a free flight condition, with a constant velocity and the superposition of the derivatives of the harmonics described in section 3.1.2.

The velocity of the complete release signal is first of all filtered through a moving average, in order to make the analysis independent on the effect of the high frequency harmonics: the number of points N of the moving average is chosen as a function of the sampling frequency f_s and the chosen cut off frequency f_c:

$$N = 2\frac{f_s}{f_{cut}} \tag{3.2}$$

In figure 3.6 we show the FFT spectrum of the velocity of the complete release signal (not de-trended) during the TM motion (i.e. acceleration phase and free flight signal). It is possible to see that the main peak is located at the 0 frequency, corresponding to the rigid motion of the TM. Some important peaks are located from 10 kHz frequency on. Hence, f_{cut} can be chosen equal to 10 kHz: this is

an arbitrary choice based on the observation of the spectrum, but suffices for the purposes of a good estimation of the free flight instant. As a consequence, $N = 40$.

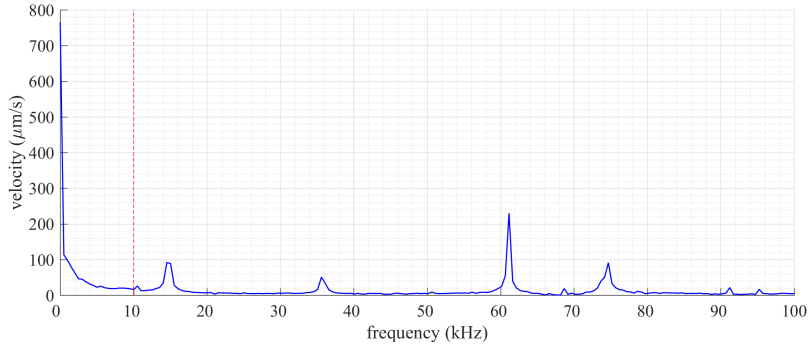

Figure 3.6: FFT of the TM velocity after the release (acceleration interval and free flight interval).

The resulting filtered velocity signal is then analyzed as follows: the mean velocity is computed for 100 samples close to the end of the signal (where we assume that the TM barycentre is moving with uniform linear motion), and 40 samples far from the last sample: this allows to consider only samples where the moving average has been computed with the maximum number of points. The mean velocity μ_v and the standard deviation of the signal σ_v is computed, as shown in figure 3.7. The free flight velocity instant is considered as the first sample that, after having exceeded the value $\mu_v + 1.5\sigma_v$, re-enters the band $\mu_v \pm 1.5\sigma_v$. This choice follows from statistical considerations that allow a robust estimation for the detachment instant [93], i.e. we can consider that, at the detachment instant, the signal is in the free flight phase with a very high probability.

The estimated value of T (detachment instant) is used for the identification of a robust free-flight interval, but can also yield an estimation of the natural frequency of the needles-TM system, whose order of magnitude is important for the dynamical model that will estimate the impulse properties (see 3.3). A rough estimation of the free flight instant suffices for the purposes of this chapter: by considering all the performed release test of the TMMF, we get $T = 600 \div 1000$ μs. Since (according to the TMMF release model, see section 2.1.3) this corresponds to a quarter of period of the TM-needles 1 DOF system, we get a natural frequency of approximately $250 \div 400$ Hz.

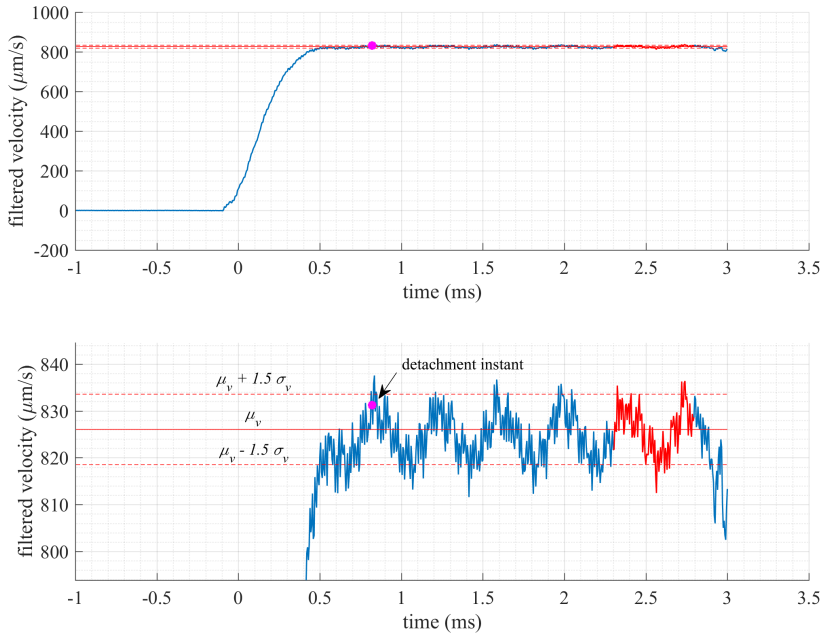

Figure 3.7: filtered velocity and free flight velocity band (red lines), computed from the red distribution at the end of the signal. The purple sample is the considered detachment instant.

3.2 Free flight signal and fit of the harmonics

In this section the content of the free flight signal (which can be described as a superposition of a straight line and some harmonics) is discussed. The analysis of the free flight signal and the estimation of the parameters of its harmonics yields the experimental data for the impulse estimation (sections 3.3 and 3.4).

In section 3.2.1 we comment a typical free flight spectrum (i.e. spectrum of the free flight signal), highlighting the main harmonics (peaks) appearing in the signal and their properties. Since many harmonics (peaks) appear in a free flight spectrum, we want to individualize the peaks associated to real oscillation: this is done through a statistical test based on a threshold.

Once the oscillations appearing in the signal are identified, in section 3.2.2 we discuss the set of identified peaks of the complete release campaign; the plot of the identified frequencies versus the free flight velocity allows to distinguish between *time harmonics* and *space harmonics*. These considerations will be the basis of the fit of section 3.2.3, where the properties of each harmonic (and amplitude in particular) are estimated.

3.2.1 Peaks in the free flight signal

For each of the 120 tests of the release campaign described in section 2.4.1, the spectrum of the de-trended free flight signal (figure 3.5) can be computed. By comparing the spectra of different tests, it is possible to notice a good repeatability of many harmonics from test to test. Moreover, we notice peaks whose frequency does not change through the set of test, and a frequency range (especially below 10 kHz) where the position of the peaks is less repeatable from test to test.

We remind that for these oscillations the velocity of the oscillation (product of amplitudes and frequency) is approximately 4 orders of magnitude lower than the limit of the interferometer (1.5 μm/s, see section 2.2.6), therefore the measurement is adequate.

Figure 3.8 shows an example for two tests with different free flight velocity. For some frequencies, a peak is shown for both tests (for instance, the peak close to 15 kHz appears in the two spectra with similar amplitude and at the same frequency; same for 35 kHz and 61 kHz). It is possible to see that for lower frequencies the position of some peaks can change: in particular, it is higher for the test with higher velocities. This behaviour is verified for many comparisons between tests spectra and suggests a dependence of the peak frequencies on the release velocities.

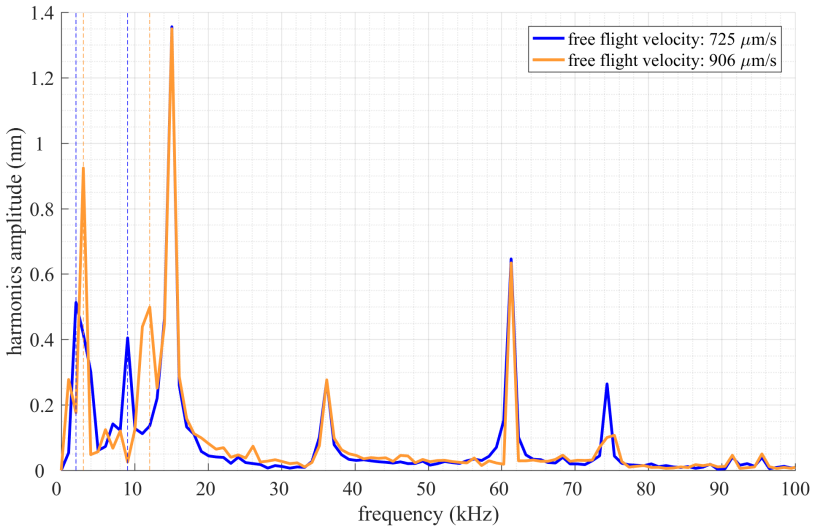

Figure 3.8: comparison between the free flight spectrum of two test with different free flight velocities: 725 μm/s (blue) and 906 μm/s (orange). The data are unfiltered. In the the 0-10 kHz range, peaks at different frequencies are shown (highlighted with dashed lines); out of the range, the frequency of the observed peaks is repeated among the tests.

In order to investigate the relation between peak frequency and free flight velocity, a method for the identification of the peaks has to be established. We see

indeed that many peaks appear in the FFT spectrum, but the low resolution of the FFT and the possibility of fictitious peaks do not allow to consider all the local maxima as real oscillation. As a consequence, an approach based on an *optimal filter* is adopted, and a threshold is chosen, such that only the spectrum peaks whose amplitude is higher than the threshold are considered. This is discussed in appendix B.1.

3.2.2 Frequency - velocity diagram

For each test and for each value of frequency ω, an hypothesis test based on an optimal filter (appendix B.1) allows to detect if a real oscillation at that frequency can be distinguished from the noise.

The frequencies of the detected peaks (i.e. the harmonics for which the null hypothesis of appendix B.1 is rejected) are plotted versus the free flight velocity of the test. The result is a frequency-velocity diagram (figure 3.9).

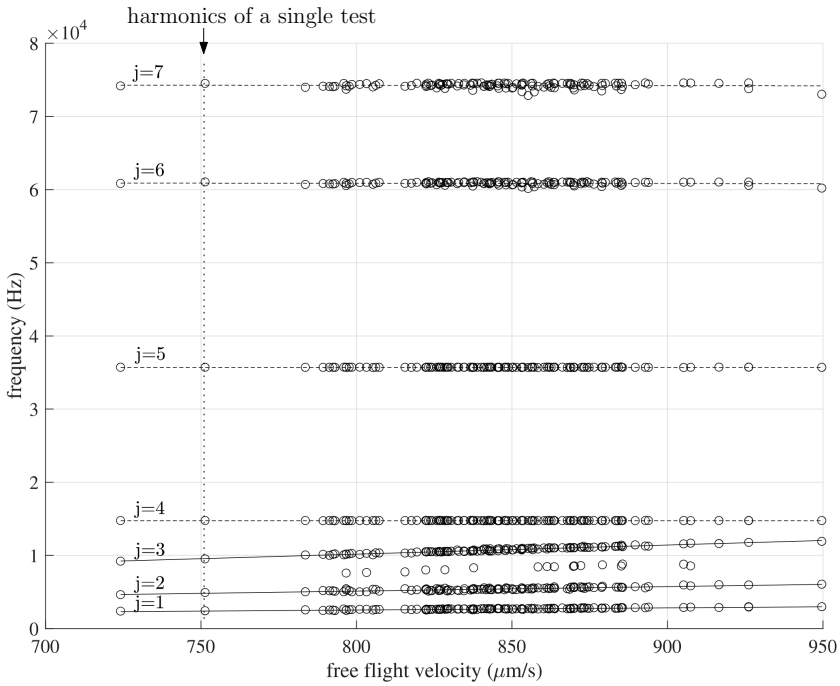

Figure 3.9: frequency - velocity chart. The detected harmonics (real oscillations) of a single test are plotted at the test free flight velocity. The patterns of time harmonics (constant frequency) correspond to the dashed lines while the pattern of space harmonics (linearly increasing frequency) correspond to continuous lines. The indices associated to each pattern are referred to table 3.1.

It is therefore possible to distinguish different sets on the graph: the detected frequencies may be grouped in *patterns*, some of which show a linear behaviour of

the frequency with respect to the free flight velocity, while in the other cases the frequency remains constant. Thanks to a pattern recognition algorithm (described in appendix B.2), it's possible to identify and analyse the patterns of points. Each pattern is composed of points of the graph 3.9 lying in the neighbourhood of a straight line. Two different kinds of patterns can be seen:

- a pattern whose points lie on a horizontal line (zero slope) defines a *time harmonic*. This corresponds to a harmonic detectable in the majority of the tests, whose frequency does not change w.r.t. the free flight velocity, and it can be associated to a mechanical oscillation, or a noise of the signal with constant frequency (related for instance to a vibration of the structure hosting the interferometer). Some of these patterns show harmonics with a repeatable phase, thus suggesting the presence of a mechanical harmonic, with a repeatability of the phase due to the repeatability of the mechanical release procedure.

- a pattern whose points lie on a straight line with slope different than 0 defines a *space harmonic*. All the space harmonics lie on straight line whose slope is the inverse of a submultiple of the interferometer wavelength, thus suggesting that these space harmonics are caused by the cyclic error phenomenon [94] [95], which generates a fictitious oscillation according to the relation:

$$z_s(z_t) = B\cos(2\pi\frac{n}{\lambda}z_t + \psi) \tag{3.3}$$

  where z_s is the oscillation associated to the cyclic error, z_t the true displacement of the TM, B the amplitude and ψ the phase of the generated oscillation. If we approximate the measured displacement with the motion of the centre of mass of the TM, i.e. $z_t \approx v \cdot t$, with v free flight velocity, we have indeed:

$$z_s(z_t) \approx B\cos(2\pi\frac{n}{\lambda}vt + \psi) \tag{3.4}$$

  Therefore the fictitious time frequency recognized for the z_s signal is:

$$f = \frac{n}{\lambda}v \Leftrightarrow \frac{f}{v} = \frac{n}{\lambda} \tag{3.5}$$

  Equation (3.5) can be used in order to associate each recognized velocity-dependent pattern to an integer n; this is done by considering the nominal wavelength of the interferometer $\lambda \approx 0.633$ μm (see appendix B.2).

  According to the interferometer specifications (see 2.2.6), the wavelength can vary inside a range because of environmental parameters: as a consequence, the λ parameter could slightly change from test to test. It's possible to improve the estimation the λ parameter for each test, by taking into account the relation (3.5) for all the space harmonics of the test and finding a unique value λ of the test through a least square solution.

- some points of the chart of figure 3.9 do not belong to any of the two described behaviours (time or space harmonics); it was not possible to associate them to a specific phenomenon, or simply they occur sporadically among the set

pattern j	classification	frequency of detection
1	n=2	100%
2	n=4	95.83%
3	n=8	100%
4	14745 Hz	100%
5	35689 Hz	100%
6	60849 kHz	100%
7	74234 kHz	97.50%

Table 3.1: recognized patterns and frequency of detection along the 120 tests of the release campaign.

of tests (thus making not possible the recognition of an associated pattern). For instance, some tests show peaks on the plot of figure 3.9 close to the line corresponding to a space harmonic with n=6 (between the straight lines $j = 2$ and $j = 3$), but the majority of the tests do not show them.

The results of the pattern recognition (appendix B.2), already shown in figure 3.9, are reported in table 3.1. A pattern index j has been associated to each recognized pattern. For each pattern, a corresponding peak is detected in more than 95% of the tests. According to the pattern index, harmonics 1, 2, 3 are *space harmonics*, while harmonics 4, 5, 6, 7 are *time harmonics*.

Space harmonics, which are compatible with the cyclic error of the interferometer, are fictitious oscillations due to the laser properties, which do not give any information about the motion of the system. Due to their high amplitude value, however, they will be taken into account for the fit of the signal of section 3.2.3, in order to increase the accuracy of the fit. Time harmonics contain the main information needed for the estimation of the impulse. Some of them will be associated to mechanical vibration modes of the mass, once the correspondence of the frequency is proved through a FEM model (see section 3.3.2).

3.2.3 Estimation of the harmonics in the free flight interval

The main properties (amplitude and phase) of the harmonics of table 3.1 can be estimated thanks to a fit of the free flight signal. An estimation of the harmonics properties (frequency, amplitude and phase) is used for the comparison of predicted and measured amplitude of the TM vibrations, in order to estimate the adhesive impulse properties (section 3.4). Although few harmonics need to be estimated for this purpose, including many harmonics in the fitting model can increase the precision of the estimation (i.e. the uncertainty of the parameters decreases). This is done by considering in the model all the harmonics that are related to one of the previously describe patterns (time harmonics or space harmonics).

The signal to be fitted is the free flight interval defined between two instants of the free flight signals, i.e. between 1 ms and 2 ms after the pin release (as shown in figure 3.5); the instants are chosen such that the detachment has certainly occurred

before the interval (according to the estimation of section 3.1.3), and the signal saturation occurs after the interval.

Fit model and fit algorithm are described in detail in appendix B.3. For each test, the fit considers all the space or time harmonics that appear in the z release signal of that test (according to figure 3.9): the resulting non-linear model is a superposition of all these harmonics (with the space harmonics defined as a function of the motion and therefore of the mechanical time harmonics). The fit, which considers the parameters computed through a FFT of the signal as first guesses, is a progressive fit since it increases the model complexity at each iteration (this is done in order to work close to the minima of the least squares function to be minimized). For each time harmonic 3 quantities are estimated (frequency, amplitude, phase), while for each space harmonic 2 parameters are estimated (amplitude, phase), according to the definition of equation (3.3). As a consequence, the fit model is composed of several parameters: for instance, the fit model of a test having all the harmonics listed in table 3.1 (3 space harmonics, 4 time harmonics) will contain $3 \cdot 4 + 2 \cdot 3 = 18$ parameters (20 if we detrend the signal by adding the linear interpolation to the fit).

After the last step of the iteration, the parameters of time and space harmonics are estimated with a covariance matrix which yields the standard deviations of the fit parameters and the covariances:

$$\mathrm{Cov}_{\mathrm{fit}} = \begin{bmatrix} \sigma_{11}^2 & \sigma_{12}^2 & \dots & \sigma_{1n}^2 \\ \sigma_{21}^2 & \sigma_{22}^2 & \dots & \sigma_{2n}^2 \\ \dots & \dots & \dots & \dots \\ \sigma_{n1}^2 & \sigma_{n2}^2 & \dots & \sigma_{nn}^2 \end{bmatrix} \tag{3.6}$$

where σ_{ij}^2 is the estimated covariance between the parameters i and j in the estimation, and n the number of the fitted parameters.

The comparison between the detrended signal and the detrended model is shown in figure 3.10 for a single test. The root mean square error (RMS) of the fit shown in the figure is approximately 10^{-6} μm, versus an oscillation of approximately $4 \cdot 10^{-3}$ μm peak-to-peak (mainly due to the prevailing 15 kHz oscillation, as shown in the spectrum of figure 3.8).

In figure 3.11 the comparison between the pre-release noise and the fit residuals is shown for the same test: in the interval between the two signals (corresponding to the acceleration interval due to the push of the needles) no signal is plot, since the model of the free flight cannot be extended backwards up to the 0 sample. The fit residuals are comparable with the pre-release noise in terms of order of magnitude, although the fit residuals have a higher amplitude. The residuals contain indeed some residual harmonic components, mainly due to the laser wavelength space harmonic corresponding to the integer $n = 6$, which was not recognized by the pattern recognition algorithm for this test and therefore not considered in the model.

The number of the parameters of the complete model (20) is quite high if compared to the number of samples in the data set (200). The number of samples in the data set is limited by the free flight duration: the signal saturation occurs few milliseconds after the release, while the first sample of the free flight phase is taken some samples after the detachment sample (free flight instant, see section

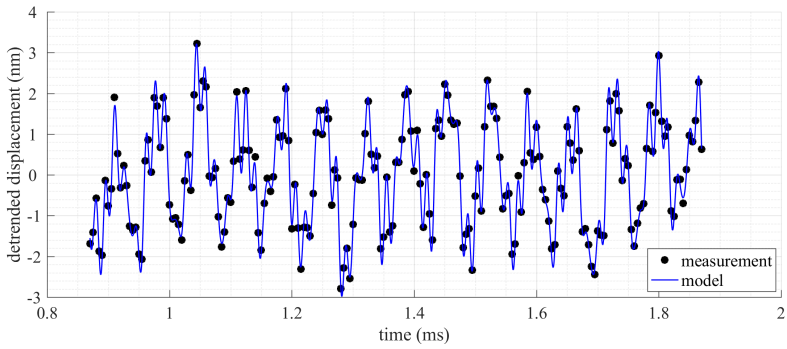

Figure 3.10: fit of the free flight interval: comparison between detrended data samples and model. Example for a single test.

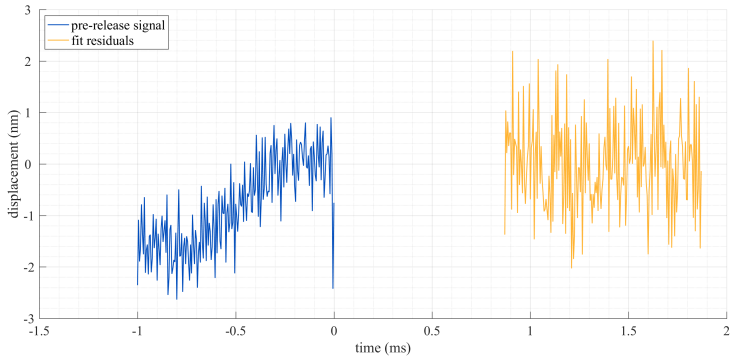

Figure 3.11: comparison between pre-release signal (blue) and free flight fit residuals (orange). Example for a single test.

3.1.3), for robustness w.r.t. the uncertainty on the position of the detachment sample (moreover, for sake of uniformity we consider always the 200 samples from $t = 1$ ms and $t = 2$ ms, which always belong to the free flight interval).

However, since all the fitted components are harmonics at different frequencies, the orthogonality of the harmonics allows the fit procedure to avoid ill-conditioning problems.

The precision of the estimation of amplitude and phase of the harmonics is particularly important for the 15 kHz and 35 kHz harmonics (4 and 5 of table 3.1), which are necessary for the impulse properties estimation (see section 3.4). In figure 3.12 the precision of estimation of the 15 kHz oscillation w.r.t. the number of fit parameters is shown (for a single test). It's possible to see that the precision of estimation increases significantly (1 order of magnitude) as the number of parameters increases. Although the decrement of the uncertainty is a natural consequence of the increment of the number of fit parameters, we accept

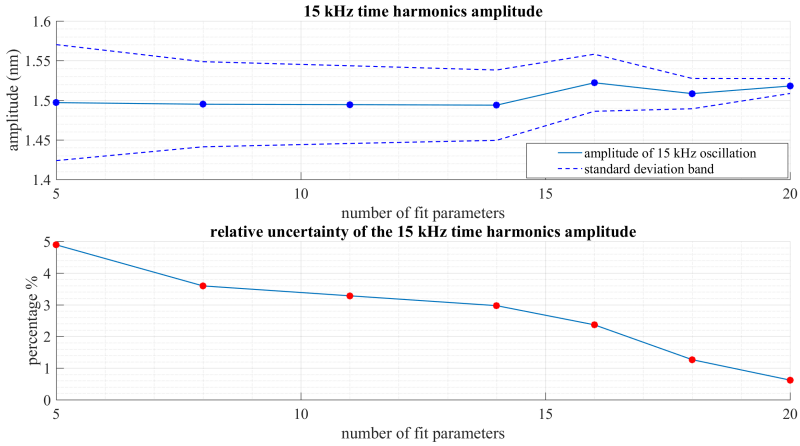

Figure 3.12: estimation of the amplitude of the 15 kHz oscillation: evolution of estimation and uncertainty (standard deviation) w.r.t. the increment of the fit parameters. Top: amplitude and its standard deviation. Bottom: ratio between standard deviation of the amplitude and its nominal value (relative uncertainty).

the estimation for two reasons: the harmonics considered in the model are real oscillations created by the release phenomenon (since they do not appear in the pre-release signal and satisfy the test of appendix B.1); except for the linear trend, the model is only composed of harmonics at different frequencies, which are orthogonal one to each other. The computation of the Pearson correlation coefficients of the fitted parameters (based on the covariance matrix of the fit) shows indeed that the parameters of different harmonics are generally uncorrelated (this will be further discussed in section 3.4 for the 15 kHz and 35 kHz harmonics).

If we are interested only in the 15 kHz and 35 kHz harmonics, other methods are possible: for example, we could fit only the two considered harmonics, thus simplifying the fit model. The progressive fit explained in appendix B.3 allows a lower uncertainty by taking into account all the considered harmonics: in table 3.2 we show the comparison between the estimations of the amplitudes of the two harmonics through two different methods.

15 kHz harmonics	progressive fit	simple fit
frequency (Hz)	14748 ± 3	14740 ± 27
amplitude (nm)	1.518 ± 0.009	1.497 ± 0.073
phase (rad)	-3.009 ± 0.031	-2.942 ± 0.241
35 kHz harmonics	progressive fit	simple fit
frequency (Hz)	35681 ± 17	35675 ± 227
amplitude (nm)	0.301 ± 0.009	0.308 ± 0.128
phase (rad)	-2.660 ± 0.151	-2.640 ± 1.997

Table 3.2: estimation of the parameters of 15 kHz and 35 kHz harmonics: comparison between different methods (example for one test). The simple fit corresponds to a fit of the single harmonics in the detrended signal. The reported uncertainties correspond to the estimated standard deviations resulting from the fit.

3.3 Dynamical model of TM vibrations

In the free flight signal *time harmonics* (independent on free flight velocity) have been identified. If some of them correspond to structural vibrations of the TM, this allows to conclude that the TM is not behaving like a rigid body (although an approximation for high displacement values is possible) and that the release has an important effect on the TM vibrations, since they are relevant in the signal after the release and do not appear in the pre-release signal.

The TM dimensions (with the plate width approximately 10 times lower than the other two dimensions, see figure 2.8) allow indeed to model the moving body as a vibrating continous body: dynamical differential equations can be written not only for the rigid motion of the TM (i.e. translation of the barycentre), but also for the amplitude of the vibration of the centre plane around the undeformed configuration.

Moreover, the vibration of a thin plate is a classical mechanical problem characterized by a linear solution, thus allowing the *modal decomposition* of the equations of motion [96] [97]. If the modal parameters of the vibrating body are known, it is possible to project the initial configuration of the TM and the external forces in the space of the modal coordinates; the amplitude of oscillation of the modes can then be predicted and these information used in order to estimate the effect of the adhesive impulse on the amplitude of oscillation of the modes, by comparing the measured amplitudes (estimated by the fit of section 3.2) with the model predictions.

The description of the TM as a linear vibrating system is discussed in section 3.3.1. The parameters appearing in the modal description have then to be estimated by a FEM analysis (section 3.3.2), which also must prove the correspondence between TM vibration and the estimated oscillations of the free flight.

3.3.1 Description of the mass as a continuous vibrating system

The displacement of the points of the TM centre plane along the horizontal direction (z) is defined as $w(x, y, t)$, where x, y are here the coordinates of the point on the centre plane, which is orthogonal to the direction of the motion of the TM (figure 3.13). It's important to notice that, if we define with $z(t)$ the displacement of the insert (at which the interferometer laser beam is pointed), we have

$$z(t) = w(0, 0, t) \tag{3.7}$$

Equation (3.7) does not take into account the fact that the interferometer could point not exactly at the TM centre; in section 3.4.5, we will comment the effect of a possible misalignment of the interferometer w.r.t. to the TM centre, based on the uncertainty estimated during the positioning of the TM (see section 2.2.5).

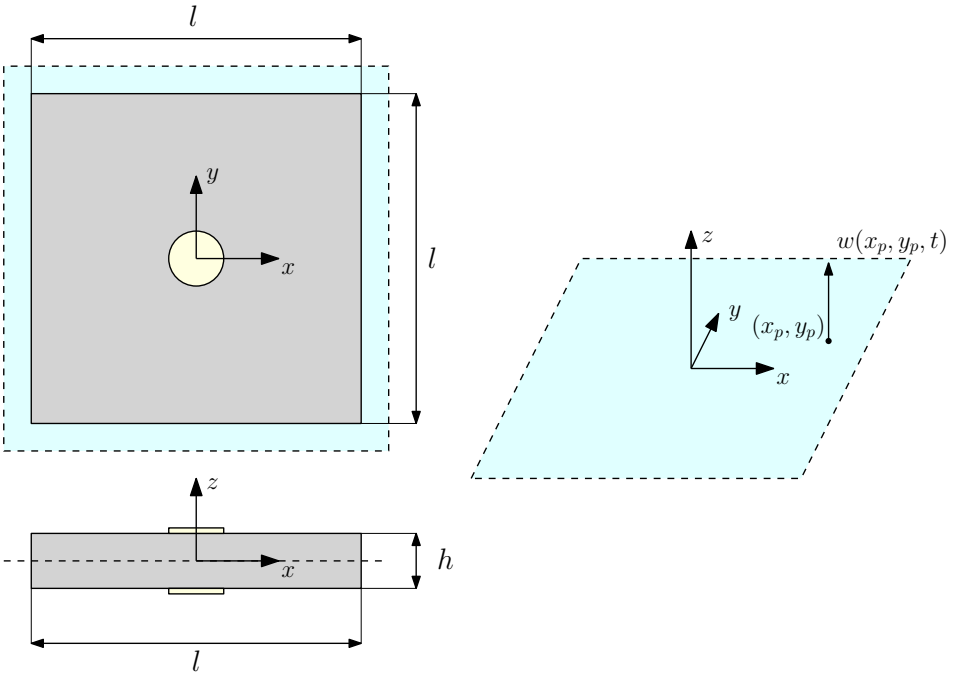

Figure 3.13: TM centre plane: reference frame and lateral displacement w of a point (x_p, y_p).

By modeling the TM as a vibrating system, if we consider that no significant damping is acting on the system (a reasonable hypothesis since the oscillations are small compared to the TM dimension) we can write the usual modal decomposition of the displacement:

$$w(x, y, t) = \sum_{n=0}^{\infty} W_n(x, y) q_n(t) \tag{3.8}$$

where $W_n(x, y)$ is the n-th mode shape ($[W_n] = 1$), and $q_n(t)$ is the n-th modal coordinate ($[q_n] = \mathrm{m}$).

The general differential equation for the j-th modal coordinate is:

$$\begin{cases} \ddot{q}_j(t) + \omega_j^2 q_j(t) &= \frac{1}{b_j} Q_j(t) \\ q_j(0) &= q_{j0} \\ \dot{q}_j(0) &= \dot{q}_{j0} \end{cases} \tag{3.9}$$

where ω_j is the angular frequency of the mode ($[\omega_j] = \frac{\mathrm{rad}}{\mathrm{s}}$), $Q_j(t)$ is the modal force ($[Q_j] = \mathrm{N}$), b_j is the modal mass ($[b_j] = \mathrm{kg}$), q_{j0} and $\dot{q}_{j0}$ are the initial conditions of the modal coordinate.

For each mode, modal forces and mass can be computed if the corresponding mode shape $W_j(x, y)$ is available:

$$b_j = \int_A \rho(x, y)\ W_j^2(x, y)\ dx\ dy \tag{3.10}$$

$$Q_j = \int_A f(x, y, t)\ W_j(x, y)\ dx\ dy \tag{3.11}$$

where A defines the centre plane of the TM (considered as subset of the cartesian plane xy), $\rho(x, y)$ is the density per unit area ($[\rho] = \frac{\mathrm{kg}}{\mathrm{m}^2}$), $f(x, y, t)$ is the distributed external force on the xy plane ($[f] = \mathrm{N}$).

It is possible to see that, if angular frequencies, mode shapes and modal masses are available, external forces and initial conditions can be projected in the mode space, in order to obtain the response for each q_j modal coordinate through the differential equation (3.9) and therefore (by applying (3.8) and (3.7)) the displacement of the insert $z(t)$.

Due to the discrete sampling and depending on the sampling frequency, we have information on the amplitude of oscillation of a limited number of modes; as a consequence, we will consider only these modes for the analysis of the data. Analytical models for the computation of the modal properties of the TM vibration are available in the literature; but these models consider usually uniform plates with negligible thickness, while in our case the thickness is not negligible and the insert at the centre of the TM is an important discontinuity (of geometry and material). Therefore, a FEM model is used for the computation of the mode shapes, as discussed in section 3.3.2.

3.3.2 Estimation of modal parameters

As explained in the previous paragraph, the goal of the FEM analysis is the estimation of the properties of the TM as a vibrating plate:

1. we want to compute the natural frequencies of the TM, and (if possible) to associate some of them to the frequencies recognized in the free flight spectrum (reported in table 3.1, whose amplitudes of oscillation have been

computed through the progressive fit of section 3.2.3). We expect this association to hold for the mode shapes with a peak at the insert position, since (being the interfometer laser beam pointed at the insert) the measurement output sensitivity is increased for these modes.

2. for those modes, the modal shapes have to be computed through the FEM analysis, thus yielding the modal masses through a discretization of equation (3.10).

The test mass, whose geometry and material properties have been described in section 2.2.3, is composed of a tungsten alloy frame with a gold-platinum cylindrical insert at its center. It cannot be modeled through a simple analytical model of a squared plate because of the gold-platinum insert at its center, which forms a discontinuity of material and width. Moreover, the coupling between insert and the TM is not a pure interference coupling (the addition of a small tungsten wire between insert and TM frame was required). As a consequence, also a realistic FEM modeling of the TM would be very complicated and would need in any case some assumptions in order to simplify the model.

That's the reason for a simplified model where frame and insert are considered with their own width and material properties, but imposing the continuity between frame and insert: frame and insert are considered rigidly connected. This choice takes into account the material discontinuity but allows an easier FEM computation, allowing to model the TM as a unique body. A possible negative consequence of this choice is the overestimation of some natural frequencies of the TM (due to the higher stiffness of the assumed constraint between frame and insert), especially the ones with higher deformation gradient (as it will result from the comparison between the frequencies estimated through the FEM analysis and the time harmonics recognized in the signal).

Modes of vibration of a square plate

Before discussing the results of the FEM model, the frequency comparison between FEM and signal and the computation of the modal masses, it's useful to remind the main equations governing the vibration of a rectangular plate. In the following, we refer mainly to [98] (the topic is presented in details also in [96] and [97]).

A rectangular plate can be defined as a *thin plate* if the ratio between the plate width and the other two dimensions are lower than $\frac{1}{9} - \frac{1}{10}$: if this is the case, the longitudinal internal forces and the shear forces of the materials can be neglected and only the lateral (flexional) forces can be considered. As a further assumption, the material has a linear elastic behaviour and is considered homogeneous and isotropic.

These assumptions allow to simplify the mathematical description of the problem and allow to obtain analytical solutions for the deformation $w(x, y, t)$ of the centre plane of the plate (figure 3.13).

Under these assumptions, the equation of motion is given by

$$D\nabla^4 w(x, y, t) + \rho \frac{\partial w(x, y, t)}{\partial t^2} = 0 \tag{3.12}$$

where ρ is the material density per unit area and D is the flexional rigidity, which is defined as follows:

$$D = \frac{Eh^3}{12(1-\nu^2)} \tag{3.13}$$

where E is the Young modulus, h is the plate width and ν is the Poisson modulus. For a linear regime (i.e. small displacements w.r.t. the plate dimension), the separation between time and space solutions can be assumed:

$$w(x,y,t) = W(x,y) \cdot T(t) \tag{3.14}$$

where $W(x,y)$ is the spatial deformation of the plate and $T(t)$ its time dependence. The form of (3.14) can be put into equation (3.12) and yields:

$$\frac{\partial^2 T(t)}{\partial t^2} + \omega^2 T(t) = 0 \tag{3.15}$$

$$D\nabla^4 W(x,y) - \rho\omega^2 W(x,y) = 0 \tag{3.16}$$

The solution of equations (3.15) and (3.16) can be computed as a solution for different *modes of vibration* thanks to the expansion theorem of the modal analysis:

$$w(x,y,t) = \sum_{m=0}^{\infty}\sum_{n=0}^{\infty} W_{mn}(x,y) \cdot T_{mn}(t) \tag{3.17}$$

where each choice of the indeces m and n determines a mode of vibration of the system.

For a square plate with different constraint conditions, many solutions are available in the literature. According to the solution of [98], the first five modes of a *free* uniform tungsten square plate with the dimensions of the TM frame are the ones reported in figure 3.14.

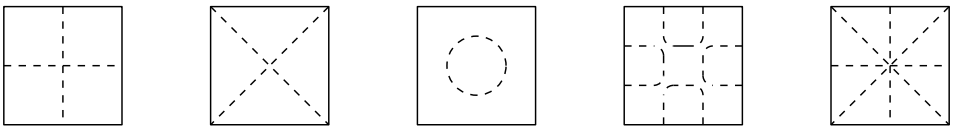

Figure 3.14: first five modes of vibration of a square plate, according to [98]. The dashed lines represent the node lines (points of the plane with null displacement).

It is possible to see that some of the modes of figure 3.14 (a, b and e) are characterized by a zero of the mode shape in the centre of the square; as a consequence, the TM centre (at which interferometer is pointed) would not show any vibration at those frequencies. The FEM model is adopted in order to estimate the properties of the modes that have a peak of the mode shape at the TM centre (c and d in figure 3.14): if this modes are excited by the release phenomenon, their vibration should be part of the measured motion of the TM centre.

It's important to remark that in modal analysis, if no boundary conditions are imposed to a system, the mode "at lowest frequency" is actually the rigid motion

	FEM frequency	spectrum frequency	difference
mode 1	14847 Hz	14745 Hz	0.69 %
mode 2	35888 Hz	35689 Hz	0.56 %
mode 3	64955 Hz	60849 Hz	6.75 %

Table 3.3: Comparison between the frequencies of the modes with peak at the centre and the recognized time harmonics with closer frequency (from table 3.1).

of the system (corresponding to a mode where the ω^2 value is 0 in the solution of (3.9)). As a consequence, for the free TM we have to consider also the *zero mode* (rigid motion), which is not reported in the solutions of figure 3.14 and whose behaviour is given by the non-deformed TM moving of uniform linear motion (i.e. $w(x, y, t) = vt + b$).

FEM model and results

A detailed model of the TM has been considered for a FEM analysis (a complete description can be found in [93]). As anticipated, the model considers the discontinuity of width and material for the insert, but assumes that the insert is rigidly attached to the frame. The FEM analysis has been performed through ANSYS, with ten-nodes *solid187* element for the mesh definition. The mesh has been built with the constraint of a discretization of the centre plane of the TM: this means that a subset of the mesh nodes lie on the centre plane with a uniform disposition, which will allow the computation of the displacement of the centre plane.

Once defined the FEM model, the mode shapes can be computed. As observed in the previous paragraph, we are interested in the mode shapes having a peak at the insert position. In figures 3.15 and 3.16 the first three mode shapes of this kind are shown; in table 3.3 the frequencies of the modes computed through the FEM are compared with the closer frequencies detected in the release signal (according to 3.1).

A high correspondence between FEM and measurements can be noticed for the first two modes. The third considered mode shows a significant deviation between FEM prediction and measurement. This is due to the higher gradient of deformation of the corresponding mode shapes (as shown in figures 3.15 and 3.16) close to the insert, which can enhance the influence of the model assumption related to the insert-frame connection.

As a consequence, thanks to the high correspondence between FEM and measurement, we can associate the 15 kHz and 35 kHz time harmonics detected in the spectrum of the release signal to their corresponding FEM mode shapes, which can be used for computing the mode masses of these two modes. In the following, we will refer to these two frequencies as *mode 1* and *mode 2* (as reported in table 3.3).

We neglect the information of the 60 kHz time harmonics, due to the too high deviation from the closer FEM frequency (*mode 3*). Neglecting 60 kHz harmonics could involve a loss of information; however, the linearity of the model and the orthogonality of the modes allow that the information extracted from 15 kHz and

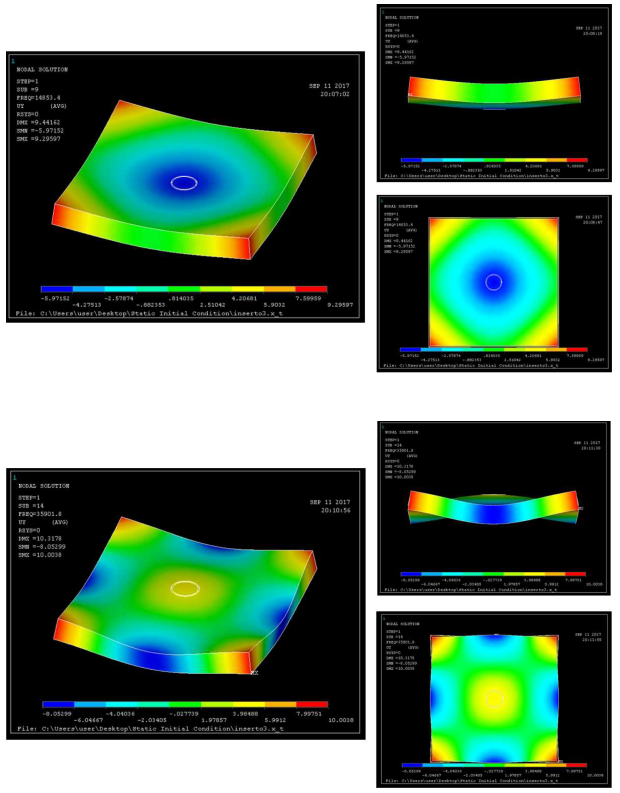

Figure 3.15: first and second mode with peak at the centre (FEM frequency: 14847 Hz and 35888 Hz). From [93] (ANSYS elaboration).

35 kHz modes is independent of the other modes. A linear model can indeed be considered in our case, since the measured oscillations ($\approx$ 1nm) are much lower than the TM dimensions (about 7 orders of magnitude).

Computation of modal masses

Thanks to the discretization of the centre plane (which constitutes a subset of the mesh nodes) in the FEM model, equation (3.10) can be discretized in order to compute the modal mass of each mode.

The mode shapes are evaluated for the nodes of the centre plane, with the normalization shown in figure 3.17: each mode shape is normalized w.r.t. the maximum displacement (reached at the vertices). According to the classical modal decomposition described in section 3.3.1, it can be easily proved that the normalization of the mode shapes is arbitrary; the modal parameters (modal mass, modal forces, modal coordinates) depend on the chosen normalization, but the computation of the physical displacement as the sum of the scaled modal displacements (equation (3.8)) remains unaffected .

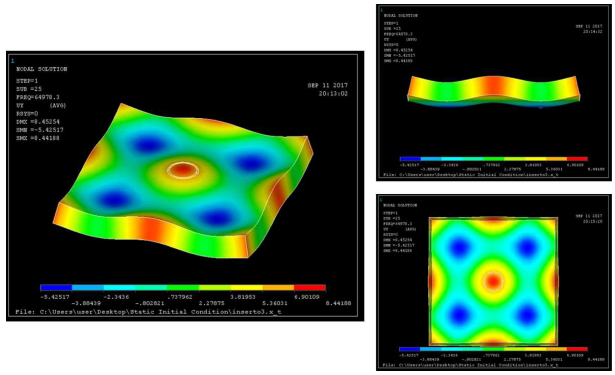

Figure 3.16: third mode with peak at the centre (FEM frequency: 64955 Hz). From [93] (ANSYS elaboration).

The centre plane is divided into triangular area elements. With reference to figure 3.18, for each mode shape and for each area element the displacement w_c of the element barycentre (x_c, y_c) can be computed as follows:

$$w_c = \frac{w_1 + w_2 + w_3}{3} \tag{3.18}$$

where w_1, w_2 and w_3 are the lateral displacements (i.e. along z axis) of the vertices of the area element for the considered mode shape.

Once the displacement of each area element of the centre plane is computed, the modal mass of the j-th mode can be computed as follows:

$$b_j = \rho_a \sum_{i=1}^{N_a} AiW_{i,j}^2 + \rho_b \sum_{k=1}^{N_b} AkW_{k,j}^2 \tag{3.19}$$

where ρ_a and ρ_b are the area densities (of frame and insert respectively), N_a and N_b the number of area elements for the centre plane, A_i and A_k the areas of i-th and k-th area element of the centre plane, $W_{i,j}$ and $W_{k,j}$ the displacement of i-th and k-th area element of the centre plane for the j-th mode shape.

The results are reported in table 3.4, compared with the corresponding analytical values predicted by [98] (for two different Poisson's coefficient close to the Poisson's coefficient of the TM frame) which are related to a more simple geometry (uniform plate with no discontinuity of material and geometry).

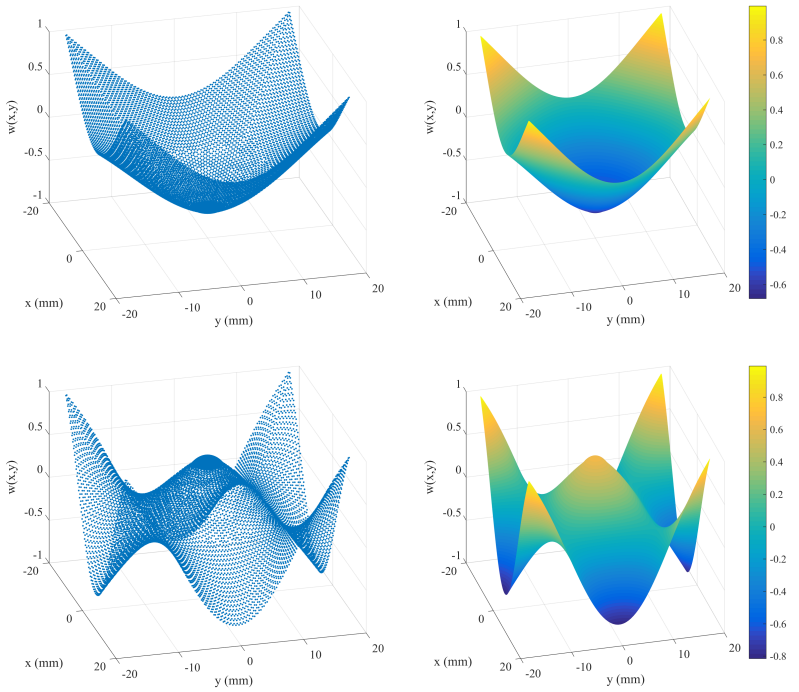

Figure 3.17: mode shapes: displacement of the centre plane. Top: mode 1 (15 kHz). Bottom: mode 2 (35 kHz). For each mode, the left picture shows the nodes of the centre plane, while the right one highlights the displacement through the colour scale.

3.4 Estimation of the adhesive impulse

In section 3.2, the estimation of the properties of the harmonics appearing in the free flight has been described. In section 3.3, the TM has been modeled as a free vibrating body, whose parameters have been estimated through a FEM analysis. In particular, it has been shown that an accurate modelation of the TM through a FEM model allows to associate two of the harmonics in the free flight to corresponding modes of the TM vibration, thanks to the high correspondence between predicted and measured frequencies.

As a consequence, by adopting the dynamical model with its estimated FEM parameters, we can compute the response of the two considered modes to the inputs applied at the release (by considering the equations of section 3.3.1) and compare them with the measured amplitudes of the corresponding harmonics in the free flight: if the chosen inputs depend on parameters, the optimal *input parameters* that fit the measured output can be estimated. Our goal is indeed the accurate estimation of the adhesive pulling impulse given by the tip to the TM at the insert-tip contact.

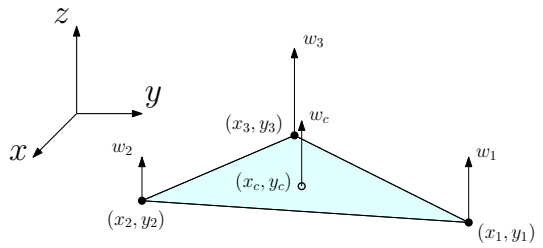

Figure 3.18: area element of the centre-plane and displacement.

FEM frequency	FEM modal mass	analytical modal mass ($\nu = 0.225$)	analytical modal mass ($\nu = 0.343$)
14847 Hz	11.691 g	10.782 g	10.944 g
35888 Hz	10.117 g	9.834 g	9.882 g

Table 3.4: modal masses of the three modes with peak at the centre. The modal masses refer to mode shapes normalized w.r.t. the maximum displacement of the centre plane.

The modes are mainly excited by the initial condition of deformation (due to the preload) and by the adhesive force. The adhesive force is unknown. A set of reasonable adhesive force profiles, based on previous experiments and observations, can be estabilshed; however, the *adhesive impulse magnitude* ι (i.e. the area of the adhesive force profile) has to be determined. Moreover, since the periods of oscillation of the modes are comparable with the expected duration of the adhesive force, the assumption of ideal impulse is not possible and the *duration of the adhesive pull* τ has to be taken into account as a second parameter. As described in section 1.1.6, the estimated maximum duration of the adhesive pull of the GPRM is indeed given by the time-to-2-μm which is approximately 40 μs, while the periods of the two considered modes are approximately 67 μs (15 kHz mode) and 28 μs (35 kHz mode).

Notice that, for a given force profile, if the force impulse and the force duration are determined, the force behaviour is completely determined.

As shown in figure 3.19, the strategy consists therefore in imposing the equality between predicted and measured oscillations for the two modes, thus obtaining two (nonlinear) equations; since for each mode the predicted oscillation depends on the two force profile parameters (adhesive impulse and duration), they can be (in general) uniquely determined. The uncertainty of the prediction depends on the uncertainty of the parameters appearing in the equation.

Considering two modes is the minimal choice for the resolution of such a problem. Extending the problem to a larger number of modes would lead to a least square problem, therefore to a non-exact solution, but with a higher reliability w.r.t. the available information. However, as discussed in section 3.3, the only two modes having a reliable information on the modal parameters are the ones whose

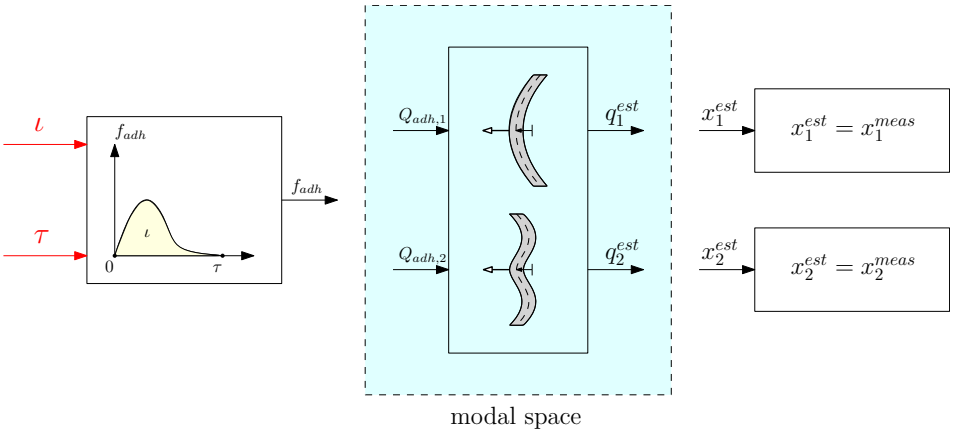

Figure 3.19: force reconstruction. Given a force profile, the adhesive force impulse (ι) and the force duration (τ) have to be chosen in order to give the equality between estimated and measured oscillations of the two chosen frequencies (through the projection of the force in the modal space). In the figure, for mode 1 $Q_{adh,1}$ is the modal projection of the adhesive force, q_1^{est} is the response of the mode predicted by the model, x_1^{est} is the physical oscillation at the frequency of the mode and x_1^{meas} is the measured physical oscillation (same for mode 2).

frequency is predicted by the FEM model.

The method we are following is a typical *inverse problem* (see 1.2.1), consisting in the determination of the input (the force) from the measured output (the oscillation). In particular, the estimation of the impulse applied to continuous vibrating systems is a common problem. They are generally simply supported systems, and both monodimensional [100] or bidimensional [73] [99] systems are analysed; this analysis is also applied to more comple vibrating systems (like turbines [101]). The most common approach is the measurement of the plate vibration through strain gauges. A typical problem consists in the estimation of the impulse amplitude and its location. The impulse is often considered as an ideal impulse (Dirac delta) [102]: this is a reasonable hypothesis if the impulse duration is much lower than the period of the considered modes.

When the impulse is not ideal, the most common approaches discussed in the literature are based on the availability of the output during the application of the force; our case is different due to the non-availability of this output when the force is applied. When the adhesive force is applied, the oscillation of the modes is indeed not known, because of the prevalence in the signal of the translation due to the needles push; that's why we have considered the free flight signal, where the (free) oscillations of the modes can be precisely estimated. Moreover, the approach here presented allows to consider a modal analysis of a moving plate, and is based on the measurement of a single point of the vibrating plate (although this depends on assumptions on the force acting on the plate).

Our goal is the prediction of the amplitude of the oscillations and the mini-

mization of their deviations from the measurement (similarly to [102]). A kind of mode selection (see [100]) is applied, since only few modes are recognizable in the signal, anyway allowing a unique solution for the determination of the force parameters (impulse amplitude and duration) in the expected range.

In section 3.4.1 we describe the analytical solution for the vibrations of the modes: the inputs acting on the TM are described and applied to the dynamical model of section 3.3.

In section 3.4.2 the analytical solutions for the amplitudes of oscillation are compared to the measurement, in order to estimate the impulse parameters ι and τ.

We analyse finally the results, by focusing first on a single test and extending then the computation to a set of 10 tests; we choose 10 tests corresponding to one of the two release direction of maximum impulse described in section 2.4.2, therefore highly representative of the whole campaign. The nominal result is discussed in section 3.4.3. The uncertainties of the estimated parameter ι and τ are given in section 3.4.4, by means of a Monte Carlo estimation that takes into account the uncertainties of the parameters appearing in the nominal estimation. In section 3.4.6 we comment the results of the impulse estimation.

3.4.1 Mode inputs and general solution

In figure 3.20 the release procedure is shown, highlighting the effects of the blocking systems on the TM deformation.

The TM has no deformation during its free oscillation before the release. The blocking action of tip and needles confer to the TM elastic potential energy. The quick pin retraction corresponds to the decrease of the preload force on the right side, with a final adhesive pull (similarly to the 1 DOF case described in 2.1.3). The mass is therefore free on its right side and the initial deformation converts into kinetic energy of vibration; the fall of the preload force applied to the TM by the needles is another force applied to the body. When the TM is finally detached from the needles, it vibrates as a continuous system, with a vibration amplitude for each mode of the TM.

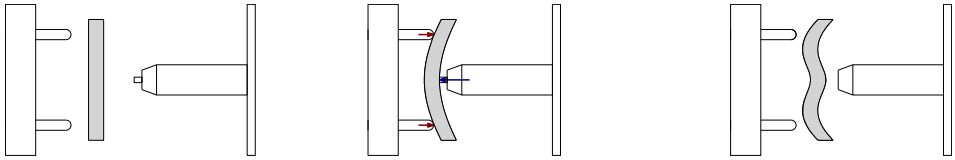

Figure 3.20: effect of the release procedure on the TM. Undeformed TM (left), initial deformation of the TM in the blocked condition (centre), free vibration of the TM (right).

As a consequence, the final steady state condition, corresponding to the free flight vibration of the TM, is the result of three different effects:

- initial deformation, which depends on the preload force f_0 and on the structural parameters of the body.

- force applied by the needles to the TM, which depends on the preload force f_0 and on the structural properties of the needles.

- force applied by the pin, which is composed by a falling pushing force followed by an adhesive pull (figure 2.4). The falling pushing force depends on the preload force f_0 and of the time-to-0-preload t_1 (see section 1.1.6), while the adhesive pull depends on ι and τ (the parameters to be estimated).

The considered effects correspond to inputs for the modes of the TM. The initial deformation can be decomposed in its modal components, thus leading to an initial condition q_0 for each mode. The forces acting on the TM can be as well decomposed into modal forces. As a consequence, the differential equation (3.9) can be written for each of the two considered modes; the solution evaluated for $t \to \infty$ yields the final amplitude of oscillation of the modes, which will depend on the adhesive force parameters.

Thanks to the assumption of linearity for the vibrations of the TM, we can consider the three contributions independently before summing their effect.

In the following, we report the modal projections of initial deformation, pin force and needles force. The detailed computations are reported in appendix B.4.

Initial mode deformation

The deformation of the TM in the blocking configuration is due to the opposite and equilibrated action of needles and pin (as shown in figure 3.20). The deformation corresponds for each modal coordinate q_j to an initial displacement q_{j0}:

$$q_{j0} = (-\alpha_j + \eta_j)\frac{f_0}{b_j \omega_j^2} \tag{3.20}$$

where f_0 is the preload force (0.3 N), b_j the modal mass of the j-th mode, ω_j the natural angular frequency of the j-th mode; α_j is the evaluation of the j-th mode shape at the origin of the TM centre plane (where the pin force is applied), while η_j is the mean of the evaluation of the j-th mode shape at the application points of the needles (the values are reported in table 3.5).

For a harmonic oscillator with no initial velocity, the initial displacement creates a cosine oscillation:

$$q_{j0} \cos \omega_j t \tag{3.21}$$

Since for each j (according to table 3.5) α_j is positive and η_j is negative, the initial condition is negative. This will lead to a response to the initial condition as a negative cosine:

mode	η_j	α_j
$j = 1$	-0.0423	0.6813
$j = 2$	-0.2521	0.6496

Table 3.5: η and α coefficients for the two modes.

The values η_j and α_j are nominal reference values. They could have a variability if the relative position between TM and needles or TM and plunger varies. In section 3.4.5, we will comment the effect of a possible misalignment of the plunger (i.e. a variation of α_j) on the final results (the variability of η_j does not affect the result due to the negligible effect of the plungers commented in section 3.4.3).

Projection of pin force

The pin force profile has already been described in section 2.1.3: the blocking force on the pin side decreases very quickly as the pin starts its retraction. When there is no more penetration of the tip into the mass surface (i.e. zero contact force), the further motion of the pin gives an adhesive pull to the mass.

In figure 3.21 a typical pin force profile is shown. We consider here the force positive if directed towards positive values of z (as a consequence, the adhesive force will be positive). The force starts from the negative value $f(0) = -f_0$ (where f_0 is the preload in the blocking condition), and it reaches the zero value at a time t_1. From time t_1 on, and for a duration τ, the adhesive pulling force $f_{adh}(t - t_1)$ is acting, with $f_{adh}(t)$ adhesive profile. The force of the pin $f(t)$ has the following piece-wise definition:

$$f(t) = \begin{cases} f_r & 0 \leq t \leq t_1 \\ f_{adh}(t - t_1) & t_1 \leq t \leq t_1 + \tau \\ 0 & t_1 + \tau \leq t \end{cases} \tag{3.22}$$

where f_r (ramp force) is given by the fall of the preload on the pin side:

$$f_r(t) = -f_0 \left(1 - \frac{t}{t_1}\right) \tag{3.23}$$

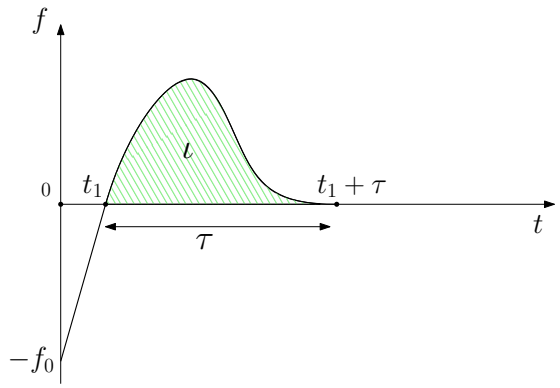

Figure 3.21: pin force profile. The coloured area corresponds to the adhesive impulse.

The adhesive force profile $f_{adh}(t)$ is unknown. Based on models for adhesion (section 1.1.6) and previous observations (section 1.2.3), we can consider a set

of possible pulling forces. Three examples of pulling forces are shown in figure 3.22: they are characterized by simple analytical expressions that allow closed analytical solutions. Force 1 (squared sine) approximates the expected adhesive profile at time τ (expiring force with null derivative), while force 2 (sine) gives a good approximation for time 0 (constant derivative, due to the continuation of the previous ramp of force). A good approximation would be given by a modulation of this two forces, but it would not lead to a easy analytical solution. Force 3 is less realistic if compared to the other forces; however, these three different forces will be considered in order to verify that the final response is not significantly influenced by the chosen force profile. The amplitude of the three forces is a function of the impulse ι, and is defined such that the integral of each force from 0 to τ is equal to ι. The adhesive profiles are therefore defined between $t = 0$ and $t = \tau$ as follows:

$$f_{adh,1}(t) = 2\frac{\iota}{\tau}\sin^2\frac{\pi}{\tau}t \tag{3.24}$$

$$f_{adh,2}(t) = \frac{\pi}{2}\frac{\iota}{\tau}\sin\frac{\pi}{\tau}t \tag{3.25}$$

$$f_{adh,3}(t) = \frac{\iota}{\tau} \tag{3.26}$$

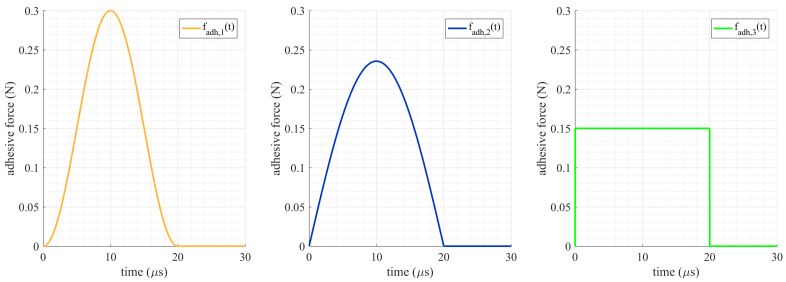

Figure 3.22: example of the different adhesive profiles (example for $\iota = 3$ kg μm/s and $\tau = 20$ μs).

After the input force have expired, for each mode a modal oscillation $q_j^r(t)$ corresponds to the response to the ramp force $f_r(t)$ and a modal oscillation q_j^{adh} corresponds to the response to the adhesive force $f_{adh}(t)$. Their analytical expressions are the following (for the purposes of section 3.4.2, we distinguish cosine and

sine components in the harmonics):

$$q_j^r(t) = \frac{\alpha_j f_0}{b_j \omega_j^2} \frac{1}{\omega_j t_1} [\cos\omega_j t(\omega_j t_1 - \sin\omega_j t_1) + \sin\omega_j t(\cos\omega_j t_1 - 1)] \quad (3.27)$$

$$q_j^{adh,1}(t) = \frac{\alpha_j \iota}{b_j \omega_j^2 \tau} \frac{4\pi^2}{4\pi^2 - \omega_j^2 \tau^2} [\cos\omega_j t(\cos\omega_j \tau - 1) + \sin\omega_j t(\sin\omega_j \tau)] \quad (3.28)$$

$$q_j^{adh,2}(t) = \frac{\alpha_j \iota}{2 b_j \omega_j} \frac{\pi^2}{\pi^2 - \omega_j^2 \tau^2} [\cos\omega_j t(-\sin\omega_j \tau) + \sin\omega_j t(\cos\omega_j \tau + 1)] \quad (3.29)$$

$$q_j^{adh,3}(t) = \frac{\alpha_j \iota}{b_j \omega_j^2 \tau} [\cos\omega_j t(\cos\omega_j \tau - 1) + \sin\omega_j t(\sin\omega_j \tau)] \quad (3.30)$$

Needles force

By means of a 1 DOF approximation, we can consider that the needles act on the TM as a preloaded spring (as discussed in section 2.1.3). The period of the TM-needles system (more than 2 ms, according to section 3.1.3) is very high if compared with the period of oscillations of the two modes. As a consequence, since the blocking force on the pin side disappears very quickly, we can approximate the needles push with a cosine:

$$p(t) = \begin{cases} f_0 \cos\frac{\pi t}{2T} & t \leq T \\ 0 & T \leq t \end{cases} \quad (3.31)$$

where T is the time for the detachment of the TM from the needles (estimated in section 3.1.3), as shown in figure 3.23.

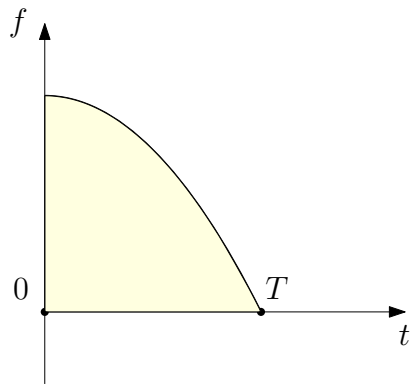

Figure 3.23: needles force profile.

The force of equation (3.23) is a simple approximation; however, different profiles would not differ too much from the one of equation (3.23), and we will prove in the following that the overall effect of the needles is negligible.

The force $p(t)$ of the needles is associated, for each j-th mode, to a modal oscillation $q_j^p(t)$ after the detachment (we highlight here the cosine and sine components

of the harmonic):

$$q_j^p(t) = 2\eta_j \frac{f_0 T}{b_j \omega_j} \frac{1}{\pi^2 - 4\omega_j^2 T^2} \left[\cos\omega_j t(2\omega_j T - \pi \sin\omega_j T) + \sin\omega_j t(\pi \cos\omega_j T)\right] \tag{3.32}$$

Complete response

The total response is given by the sum of the responses:

$$q_j(t) = q_{j0} \cos\omega_j t + q_j^r(t) + q_j^{adh}(t - t_1) + q_j^p(t) \tag{3.33}$$

where q_{j0}, $q_j^r(t)$, $q_j^p(t)$ are defined by equations (3.20), (3.27) and (3.32) respectively, while $q_j^{adh}(t)$ is one of the responses (3.28), (3.29) and (3.30) (according to the chosen adhesive force profile).

3.4.2 Comparison between model and measurement

The model of section 3.3, whose general solution has been discussed in section 3.4.1, allows to estimate a response of the system to some inputs, if the *model parameters* (structural parameters like frequencies, modal masses and mode shapes evaluations) are given. The goal of this section is to fit the model to the experimental measurements, in order to estimate the input parameters.

In the following, a method for the graphical representation of the problem is proposed. The chosen method allows an easy visualization of the problem and a comfortable handling of the oscillation components appearing in equation (3.33).

Phasor of a harmonic oscillation

In order to compute the sum of the harmonics with a method that allows to visualize the contribution of each of them, we associate a *phasor* to each oscillation.

According to the most common complex notation for phasors, we can write for an harmonic oscillation $r(t)$

$$r(t) = A\cos(\omega t + \phi) = \mathrm{Re}(Ae^{i(\omega t + \phi)}) \tag{3.34}$$

where

$$e^{i\omega t} = \cos\omega t + i \sin\omega t \tag{3.35}$$

As a consequence, for a generic modal oscillation written as the sum of cosine and sine terms, we have

$$\begin{aligned} q(t) &= A\cos\omega t + B\sin\omega t && (3.36)\\ &= \mathrm{Re}(Ae^{i\omega t}) + \mathrm{Re}(Be^{i(\omega t - \frac{\pi}{2})}) && (3.37)\\ &= \mathrm{Re}(Ae^{i\omega t} + Be^{i\omega t}e^{-i\frac{\pi}{2}}) && (3.38)\\ &= \mathrm{Re}((A - iB)e^{i\omega t}) && (3.39) \end{aligned}$$

where the corresponding complex phasor rotating in the complex plane with velocity ω is therefore

$$A - iB \tag{3.40}$$

If we sum together more harmonics having the same angular frequency, we get

$$\sum_{k=1}^{N} q_k(t) = \sum_{k=1}^{N} A_k \cos\omega t + B_k \sin\omega t \tag{3.41}$$

$$= \sum_{k=1}^{N} \mathrm{Re}((A_k - iB_k)e^{i\omega t}) \tag{3.42}$$

$$= \mathrm{Re}\left(\sum_{k=1}^{N}(A_k - iB_k)e^{i\omega t}\right) \tag{3.43}$$

$$= \mathrm{Re}\left(\left(\sum_{k=1}^{N}(A_k - iB_k)\right)e^{i\omega t}\right) \tag{3.44}$$

As a consequence, the sum of the harmonics is represented by a phasor whose (real and complex) coefficients are given by the sum of the respective coefficients of the phasors of the harmonics.

Phasor diagram for the oscillation of the modes

As equation (3.33) describes, in the free flight of the TM each mode is the sum of many harmonics having the same angular frequency. We can apply therefore the form of equation (3.44). Based on equations (3.20), (3.27), (3.28), (3.29), (3.30), (3.32), we write a complex phasor for each harmonics appearing in equation (3.33):

$$M_{j0} = (-\alpha_j + \eta_j)\frac{f_0}{b_j\omega_j^2}\left[1 - i\cdot 0\right] \tag{3.45}$$

$$M_j^r = \frac{\alpha_j f_0}{b_j\omega_j^2}\frac{1}{\omega_j t_1}\left[(\omega_j t_1 - \sin\omega_j t_1) - i(\cos\omega_j t_1 - 1)\right) \tag{3.46}$$

$$M_j^{adh,1}(t) = \frac{\alpha_j \iota}{b_j\omega_j^2\tau}\frac{4\pi^2}{4\pi^2 - \omega^2\tau^2}\left[(\cos\omega_j\tau - 1) - i(\sin\omega_j\tau)\right] \tag{3.47}$$

$$M_j^{adh,2}(t) = \frac{\alpha_j \iota}{2b_j\omega_j}\frac{\pi^2}{\pi^2 - \omega^2\tau^2}\left[(-\sin\omega_j\tau) - i(\cos\omega_j\tau + 1)\right] \tag{3.48}$$

$$M_j^{adh,3}(t) = \frac{\alpha_j \iota}{b_j\omega_j^2\tau}\left[(\cos\omega_j\tau - 1) - i(\sin\omega_j\tau)\right] \tag{3.49}$$

$$M_j^{p}(t) = \frac{2\eta_j f_0 T}{b_j\omega_j}\frac{1}{\pi^2 - 4\omega_j^2 T^2}\left[(2\omega_j T - \pi\sin\omega_j T) - i(\pi\cos\omega_j T)\right] \tag{3.50}$$

such that the the oscillation of mode j predicted by the model is:

$$q_j(t) = \mathrm{Re}\left(M_j e^{i\omega t}\right) \tag{3.51}$$

where

$$M_j = M_{j0} + M_j^r + M_j^{adh} + M_j^p \tag{3.52}$$

Equation (3.52) can be slightly modified in order to collect the whole contribution of the needles (which we will prove negligible). In order to have a unique

	description	unit	estimation
α_j	mode shape at insert position	1	estimated by FEM model
η_j	mean mode shape at needles position	1	estimated by FEM model
ω_j	mode natural angular frequency	rad/s	estimated by FEM model
b_j	modal mass	kg	estimated by FEM model
f_0	preload force	N	measured by load cell
T	needles push duration	s	estimated by signal analysis
t_1	fall time of pin preload	s	variable parameter
τ	adhesive impulse duration	s	input parameter
ι	adhesive impulse magnitude	kg m/s	input parameter

Table 3.6: physical quantities appearing in the mode phasor M_j.

term depending on η_j (mode shape evaluation at the needles' position), the sum of the two phasors M_{j0} and M_j^p can be rewritten as follows (according to equations 3.45 and 3.50):

$$M_{j0} + M_j^p = -\alpha_j \frac{f_0}{b_j \omega_j^2} + \eta_j \frac{f_0}{b_j \omega_j^2} + M_j^p = \widetilde{M}_{j0} + \widetilde{M}_j^p \tag{3.53}$$

where

$$\widetilde{M}_{j0} = -\alpha_j \frac{f_0}{b_j \omega_j^2} \tag{3.54}$$

$$\widetilde{M}_j^p = \eta_j \frac{f_0}{b_j \omega_j^2} + M_j^p \tag{3.55}$$

we have therefore that $\widetilde{M}_{j0}$ is the effect of the initial displacement of the mode due exclusively to the pin force, while $\widetilde{M}_j^p$ is the complete effect of the needles (effect of the initial displacement of the mode due exclusively to the needles force and needles push during the acceleration phase).

With this new definition, we can write:

$$M_j = \widetilde{M}_{j0} + M_j^r + M_j^{adh} + \widetilde{M}_j^p \tag{3.56}$$

In table 3.6 all the quantities appearing in the equation (3.56) are described, by distinguishing model parameters and input parameters (unknowns).

In figure 3.24 an example of mode phasor is shown.

Comparison with measured amplitude

We go now from modal coordinates to physical coordinates, in order to compare the model of equation 3.52 with the measured amplitudes.

As discussed in section 3.3.1, in the free flight interval we measure the motion $z(t) = w(0, 0, t)$ of the insert (with $w(x, y, t)$ displacement of the TM mean plane).

We define

$$z_j(t) = w_j(0, 0, t) \tag{3.57}$$

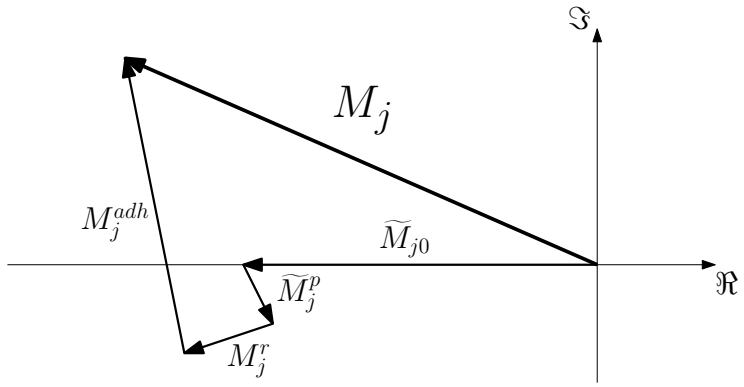

Figure 3.24: mode phasor in the complex plane.

which means that $z_j(t)$ corresponds to the spectrum component of $w(0,0,t)$ at the frequency ω_j.

We have therefore

$$z_j(t) = A_j \cos(\omega_j t + \phi_j) = \mathrm{Re}\left(A_j e^{i(\omega_j t+\phi_j)}\right) = \mathrm{Re}\left(A_j e^{i\phi_j} e^{i\omega_j t}\right) \tag{3.58}$$

where A_j (constant real value) is the amplitude of the physical oscillation of the insert having frequency ω_j and ϕ_j is the phase of the oscillation, both estimated by the fit (section 3.2.3). The complex phasor of the measured oscillation $z_j(t)$ is hence:

$$A_j e^{i\phi_j} = A_j(\cos\phi_j + i\sin\phi_j) \tag{3.59}$$

$A_j e^{i\phi_j}$ is therefore a measured quantity estimated by the fit of the free flight signal.

The relation between physical oscillation and modal oscillation follows immediately by combining equations (3.8) and (3.57): since we are focusing on the free flight interval, where the signal $w(0,0,t)$ corresponds uniquely to free vibrations of the TM, a physical oscillation having frequency ω_j is related to the modal oscillation q_j according to the equation

$$z_j(t) = w_j(0,0,t) = W_j(0,0)q_j(t) = \alpha_j q_j(t) \tag{3.60}$$

As a consequence, according to equations (3.58) and equations (3.51) we can write the corresponding of equation (3.60) for the phasor diagram:

$$A_j e^{i\phi_j} = \alpha_j M_j(\iota,\tau,t_1) \tag{3.61}$$

In equation (3.61), $A_j e^{i\phi_j}$ only depends on measurements, while $\alpha_j M_j$ depends on parameters and unknowns (as reported in table 3.6). In particular, two important unknowns correspond to the adhesive force profile properties: ι and τ. We can therefore find an estimation of the parameters by imposing the equality of equation (3.61) between measurement and model, for each of the two considered modes.

We have hence the following system of two equations in three unknowns:

$$A_1 e^{i\phi_1} = \alpha_1 M_1(\iota,\tau,t_1) \tag{3.62}$$

$$A_2 e^{i\phi_2} = \alpha_2 M_2(\iota,\tau,t_1) \tag{3.63}$$

In order to reduce the number of unknowns, we can solve the problem with different choices of the parameter t_1. As discussed in 1.1.6, the estimation of t_1 yields a limited range $(0 \div 2\ \mu)$. As a consequence, a small set of n values $t_1^1, t_1^2, ..., t_1^n$ can be chosen and the system solved in the two desired unknowns ι and τ:

$$A_1 e^{i\phi_1} = \alpha_1 M_1(\iota, \tau) \tag{3.64}$$

$$A_2 e^{i\phi_2} = \alpha_2 M_2(\iota, \tau) \tag{3.65}$$

for each value t_1^i, $i = 1, ..., n$.

Measured phasors ($A_j e^{i\phi_j}$) and predicted phasors ($\alpha_j M_j(\iota, \tau)$) have to be equals in terms of amplitude and phase. We can impose the equality of the amplitudes: this is indeed a necessary condition for the final solution; moreover, imposing the equality of the amplitudes allows to get a unique solution; further, the measured amplitudes are more reliable than the measured phases, which are affected by the uncertainty of the beginning of the event (see section 3.1.1). However, in section 3.4.6 we will comment also a possible approach for the analysis of the correspondence of the phases (described in appendix B.6).

In figure (3.25) the equality of the amplitudes is shown. We represent the vector $\alpha_j M_j$ of predicted amplitude as the sum of the components of equation (3.52) (as shown in figure 3.24), each scaled by the factor α_j. We can represent the measured amplitude as a circle with radius A_j . For the equality of the amplitudes, we want the predicted phasor to end exactly on the circle; according to equations (3.64) and (3.65), this corresponds to solving the following system of equations:

$$A_1 = |\alpha_1 M_1(\iota, \tau)| \tag{3.66}$$

$$A_2 = |\alpha_2 M_2(\iota, \tau)| \tag{3.67}$$

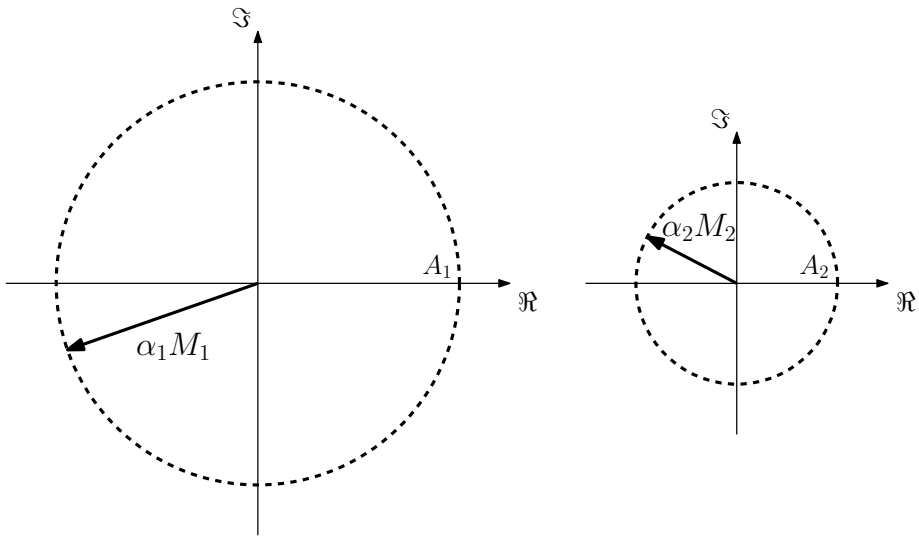

Figure 3.25: correspondence between measured amplitude and model amplitude.

The system of two equations in two unknowns can be solved numerically for each test. Depending on the parameters, the solution can be unique or we can have multiple solutions: this will be discussed in the next paragraph (section 3.4.3).

It's important to notice that in equations (3.66) and (3.67), some parameters are affected by uncertainties. The *random errors* are related to the uncertainties of the parameters of each test: amplitudes A_2 and A_3 (measured through the fit) and preload force f_0 (measured by the load cell) can change from test to test and are estimated with a measurement uncertainty. For the modal parameters (frequency ω_j, mode shape parameters α_j and η_j, and modal mass b_j) we assume the nominal values computed in section 3.3.2; errors in their computation can be considered as *systematic errors*, since these are structural parameters that remain constant along the test campaign.

Another possible source of error is a wrong estimation of α_1 and α_2 due to the misalignment of the interferometer w.r.t. the TM centre. The effect of a variability of these coefficients will be commented in section 3.4.5.

3.4.3 Nominal solution

Given the parameters of table 3.6 and chosen a value t_1, the system composed of equations (3.66) and (3.67) can be solved in the two unknowns ι and τ (see figure 3.27 and the comments at the beginning of 3.4.4).

Result for one test

In figure 3.26 the solution for a single test with nominal values of amplitudes A_1 and A_2, nominal force f_0 (300 mN) and the expected value for time t_1 (1.2 μs) is shown. Parameters and estimations for ι and τ are reported in table 3.7. The uncertainty of each measured amplitude is considered as an uncertainty of the corresponding radius: each circular sector corresponds to the $\pm 3\sigma$ region for the amplitude (where σ is the standard deviation estimated by the fit).

For each mode, the four different contributions of equation (3.52), scaled by the factor α_j, are highlighted (a phasor for each contribution).

The nominal solution of equations (3.66) and (3.67) corresponds to the parameters of the adhesive force (ι,τ) that make the phasor sum touch the circle of the measured amplitudes.

We can observe the following facts:

- the majority of the model output at the nominal solution (i.e. of the phasor sum $\alpha_j M_j$) is due to the response to the initial condition. This means that the modal response is mainly due to the initial deformation of the mass. For each mode, the value $\alpha_j \widetilde{M}_{j0}$ is indeed very close to the amplitude A_j.

- the response due to the initial condition (phasor $\alpha_j \widetilde{M}_{j0}$) is in general lower, in terms of amplitude, than the measured amplitude, even if we consider its 3σ uncertainty band (which would contain 99 % of the estimated distribution of the amplitude if it is considered normal). In this condition, the "missing" amplitude may be attributed to the effect of dynamical forces acting on the TM, i.e. needles (phasor $\alpha_j \widetilde{M}_j^p$) and pin force (sum of phasors $\alpha_j M_j^{adh}$ and

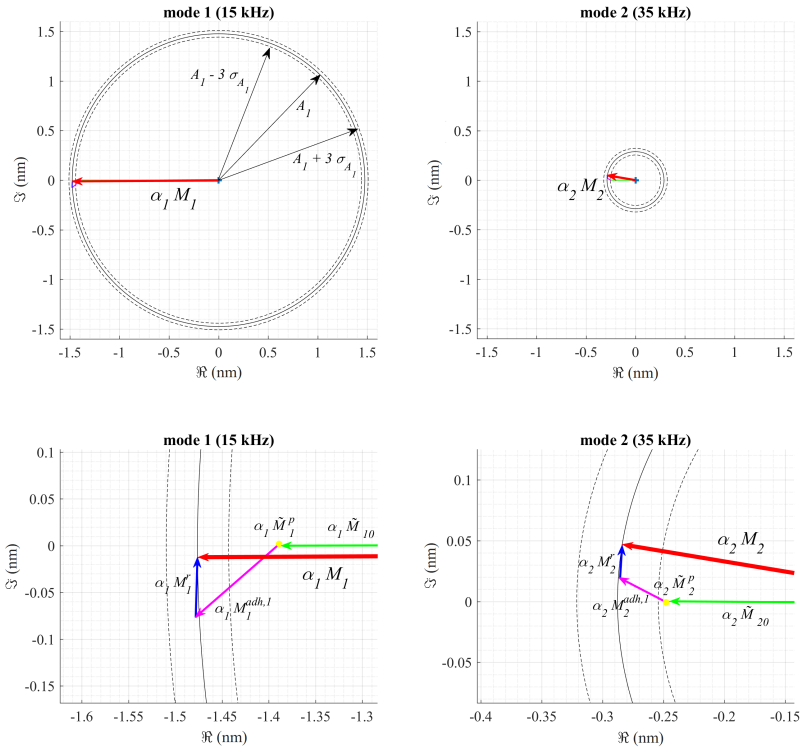

Figure 3.26: example of nominal solution. Top: correspondence between amplitude of the model $\alpha_j M_j$ and the measured amplitude A_j ($j = 1, 2$). Bottom: zoom with the total phasor (red) as sum of the phasors, according to equation (3.56). The contribution of the needles $\alpha_j \widetilde{M}_j^p$ is too small to be represented as an arrow (yellow point). The test parameters and estimated impulse magnitude and durations are reported in table 3.7.

$\alpha_j M_j^r$). However, the initial condition phasor $\alpha_j \widetilde{M}_{j0}$ is proportional to the preload, which could be in principle underestimated (this will be analysed in section 3.4.4).

- the effect of the pin force due to the preload fall ($\alpha_j M_j^r$) does not affect significantly the amplitude if compared to the effect of the adhesive force $\alpha_j M_j^{adh}$.

- it can be seen that the total effect of the needles $\alpha_j \widetilde{M}_j^p$ (defined in equation 3.55) is much lower than the effect of the initial deformation, and in general it is also lower than the effect of the pin force. This is due to the fact that the needles push is a low frequency input w.r.t. each mode: the response of the system to such a slow force decrement is similar to a step response, which

force profile	$f_{adh,1}$ (squared sine)
t_1	1 μs
T	500 μs
A_1	1.476 nm $\pm$ 0.011 nm
A_2	0.288 nm $\pm$ 0.011 nm
f_0	0.300 N $\pm$ 0.020 N
ι	0.2895 kg μm/s
τ	16.26 μs

Table 3.7: nominal solution of figure 3.26: parameters and estimated values of ι and τ.

is mainly compensated by the response to the initial deformation due to the needles (i.e. there is a compensation of the two phasors of equation 3.55). It can be shown that modifications of the parameters appearing in the needles phasor (preload f_0, push duration T, or shape of the force, e.g. by adding an initial slope to the needles force profile) does not significantly change the effect of the needles. This consideration allows to neglect the contribution of the needles.

- the estimated adhesive impulse ι is quite low if compared with the linear momentum requirement of the TM of LISA Pathfinder (section 1.1.4): in a worst case with no opposite impulse on the other side of the test mass (whose weight is 2 kg), the velocity created by such an adhesive impulse in the in-flight case would be approximately 0.15 μm/s, i.e. 30 times lower than the requirement.

- the estimated impulse duration is inside the expected range: the time-to-2-μm of the pin motion, estimated as a maximum duration of the adhesive pull, is approximately 40 μs (see section 1.1.6). If we sum t_1 and τ, we get a time of detachment $t_1 + \tau$ (see figure 3.21 lower than 20 μs.

The example of figure 3.26 corresponds to a solution with a precise choice for the values of t_1 and for the adhesive force profile. Table 3.8 compares the results with different choices of the two parameters. It can be seen that the results have a low variation along the two set of parameters, suggesting that an uncertainty of these parameters inside the expected range does not affect significantly the final prediction. We notice that in general the amplitude of the impulse is ≈ 0.3 kg μm/s and the duration is ≈ 15 μs, which (according to the definition of the forces of equation 3.24, 3.25, 3.26) corresponds to a peak of the force of

$$\max f_{adh} \approx \frac{\iota}{\tau} \approx 0.02\text{N} \tag{3.68}$$

In the following we will refer uniquely to a model with the nominal value $t_1 = 1.2$ μs and adhesive force profile 1 (squared sine, see figure 3.22).

The nominal case of figure 3.26 has an exact solution inside the expected range of τ (as well as the cases with different models of tabel 3.8). In figure 3.27 the

	adhesive profile 1	adhesive profile 2	adhesive profile 3
$t_1 = 0.2$ μs	$\iota = 0.29$	$\iota = 0.30$	$\iota = 0.34$
	$\tau = 17$	$\tau = 16$	$\tau = 14$
$t_1 = 1.2$ μs	$\iota = 0.29$	$\iota = 0.30$	$\iota = 0.33$
	$\tau = 16$	$\tau = 15$	$\tau = 14$
$t_1 = 2.2$ μs	$\iota = 0.29$	$\iota = 0.30$	$\iota = 0.33$
	$\tau = 15$	$\tau = 14$	$\tau = 13$

Table 3.8: nominal solution with different models (for the same case of figure 3.26 and table 3.7). Impulses ι in kg μm/s, durations τ in μs.

spaces of the solutions of equations (3.66) and (3.67) are shown. The solution of the system corresponds to the intersection of the two curves.

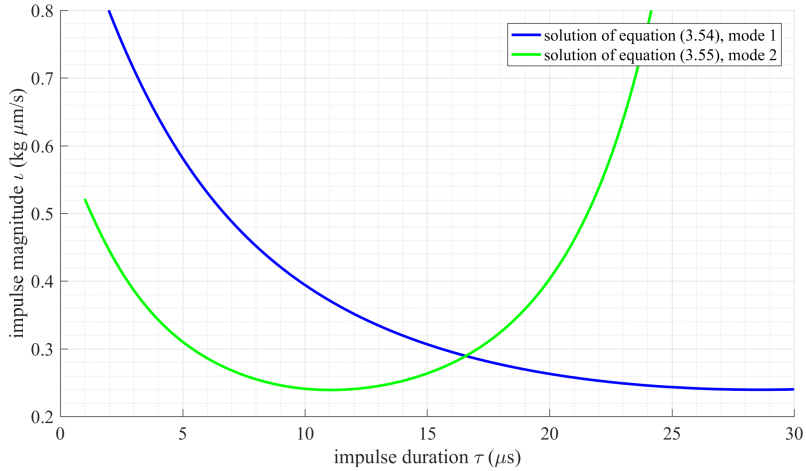

Figure 3.27: space of the solutions of equations (3.66) and (3.67) for the considered release test. The two solutions intersect in a unique point, for $\iota = 0.29$ kg μm/s, $\tau = 16.26$ μs.

However, if the parameters affecting the equations vary according to their uncertainties, the solution can change; in some cases, an exact solution could not be available, corresponding to a missing interception of the curves of figure 3.27: this occurs especially if we consider that the real preload has been higher than the nominal value, making the phasor $\alpha_j \widetilde{M}_{j0}$ of figure 3.26 exit the circular sector and exceed the amplitude circle.

test	1	2	3	4	5	6	7	8	9	10
ι (kg μm/s)	0.29	0.29	0.25	0.17	0.25	0.17	0.22	0.33	0.36	0.22
τ (μs)	17	17	14	13	18	9	15	17	20	14

Table 3.9: estimation of magnitude and duration of the adhesive impulse: nominal results for the 10 release tests.

	mean	standard deviation
f_0	0.3 N	0.02 N
A_1	1.476 nm	0.011 nm
A_2	0.288 nm	0.011 nm

Table 3.10: mean and standard deviations of the distributions of parameters f_0, A_1, A_2 in the case of figure 3.26 and table 3.7.

Results for 10 tests

In table 3.9 we report the nominal results for 10 release tests performed with the same orientation of the plunger (one of the maximum impulse directions of section 2.4.2). The maximum impulse and duration (belonging to the same test) are 0.36 kg μm/s and 20 μs respectively.

3.4.4 Effect of uncertainties: Monte Carlo simulation

As anticipated in a previous paragraph, some of the parameters of equations (3.66) and (3.67) are affected by uncertainties. Therefore, the dependence of the solution of the equation on the uncertainty parameters has to be investigated.

Result for one test

We analyze in the following the uncertainties related to the case of figure 3.26 and table 3.7), for which we computed the nominal solution.

The chosen method for the computation of the uncertainties is a Monte Carlo simulation. We establish three normal distributions for preload and measured amplitudes, according to their nominal values and standard deviations given by the load cell (for preload) and by the signal fit (for amplitudes). The system is then solved for each possible triple of values, and a corresponding distribution of the input parameters ι and τ is computed.

In figure 3.28 the three distributions of the model parameters f_0, A_1 and A_2 are shown. Each distribution is randomly extracted from a normal distribution characterized by mean and standard deviation of table 3.10 (we are considering normal probability density functions for f_0, A_1 and A_2). Having each distribution 50 values randomly generated from a gaussian distribution, the Monte Carlo simulation is based on a set of different 50^3=125000 triples of parameters f_0, A_1 and A_2.

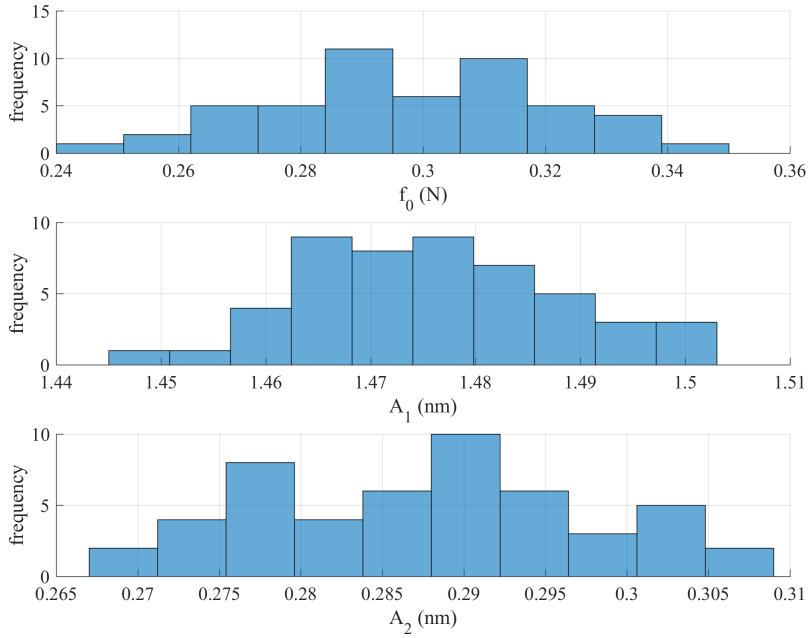

Figure 3.28: distributions of preload f_0 and amplitudes A_1 and A_2 for the Monte Carlo simulation (case of figure 3.26 and table 3.7). Each distribution is generated randomly by a normal distribution characterized by mean and standard deviation as reported in table 3.10

.

For the amplitudes, we consider gaussian distributions with the standard deviation estimated by the fit of section 3.2.3. In table 3.11 the covariance matrix (equation (3.6)) resulting from the fit of section 3.2.3 is reported; the squared standard deviations are located on the diagonal of the matrix. Given two generic parameters x and y, the normalized covariance can be computed according to the Pearson coefficient $\rho_{x,y}$:

$$\rho_{x,y} = \frac{\mathrm{cov}(x,y)}{\sigma_x \sigma_y} \tag{3.69}$$

The normalized covariance matrix is reported in table 3.12 (according to equation (3.69), the values on the diagonal are equal to 1 since $\sigma_x = \sqrt{\mathrm{cov}(x,x)}$). Being the values outside the diagonal lower than 2 %, we can consider the estimations of parameters A_1 and A_2 uncorrelated.

The distribution of the preload has been estimated by analyzing the fluctuation of the GPRM load cell measurement. Being amplitudes and preload estimated through different measurement systems, we consider the distributions of force and amplitudes estimations uncorrelated as well.

	A_1 (μm)	ϕ_1 (rad)	A_2 (μm)	ϕ_2 (rad)
A_1 (μm)	$1.08 \cdot 10^{-10}$			
ϕ_1 (rad)	$-6.09 \cdot 10^{-9}$	$1.24 \cdot 10^{-3}$		
A_2 (μm)	$-2.03 \cdot 10^{-13}$	$-3.04 \cdot 10^{-9}$	$1.09 \cdot 10^{-10}$	
ϕ_2 (rad)	$2.37 \cdot 10^{-10}$	$1.18 \cdot 10^{-4}$	$-2.58 \cdot 10^{-10}$	$3.05 \cdot 10^{-2}$

Table 3.11: covariance matrix of the fit for amplitudes and phases of modes 1 and 2, in the case of figure 3.26 and table 3.7.

	A_1 (μm)	ϕ_1 (rad)	A_2 (μm)	ϕ_2 (rad)
A_1 (μm)	1			
ϕ_1 (rad)	$-1.66 \cdot 10^{-2}$	1		
A_2 (μm)	$-1.87 \cdot 10^{-3}$	$-8.27 \cdot 10^{-3}$	1	
ϕ_2 (rad)	$1.30 \cdot 10^{-4}$	$1.92 \cdot 10^{-2}$	$-1.41 \cdot 10^{-4}$	1

Table 3.12: normalization of table 3.11 through Pearson coefficient.

For each triple (f_0, A_1, A_2) of the Monte Carlo simulation, the solution of equations (3.66) and (3.67), in the unknowns ι and τ, is computed. The function to be minimized is defined as follows:

$$g(\iota, \tau) = e_1^2(\iota, \tau) + e_2^2(\iota, \tau)$$

where e_1 and e_2 are the residuals of equations (3.66) and (3.67):

$$\begin{aligned} e_1 &= A_1 - |\alpha_1 M_1(\iota, \tau, f_0)| \\ e_2 &= A_2 - |\alpha_2 M_2(\iota, \tau, f_0)| \end{aligned}$$

where A_1, A_2 are the measured amplitudes and $|\alpha_1 M_1(\iota, \tau, f_0)|$ and $|\alpha_2 M_2(\iota, \tau, f_0)|$ are the amplitudes given by the model (we have included here the dependence on f_0 in order to highlight the most important parameters of the simulation). The minimum of function $g(\iota, \tau)$ in equation (3.4.4) is searched by means of a Levenberg-Marquardt algorithm. In order to make the research robust w.r.t. local minima, for each iteration the algorithm is applied multiple times, with the initial guess (ι^0, τ^0) varying in the following range:

$$\begin{aligned} \iota^0 &= -4 \div 4 \text{ kg} \cdot \mu\text{m/s} \\ \tau^0 &= -100 \div 100 \ \mu\text{s} \end{aligned}$$

In principle, we allow for each iteration negative values of τ. Some iterations minimize the residuals with a negative τ: this means that the input parameters of the Monte Carlo simulation need a negative value of τ (which has no physical sense) in order to be compliant with the model. Solutions with negative τ or with τ higher than 100 μs (which is the expected duration of the complete pin retraction) are discarded.

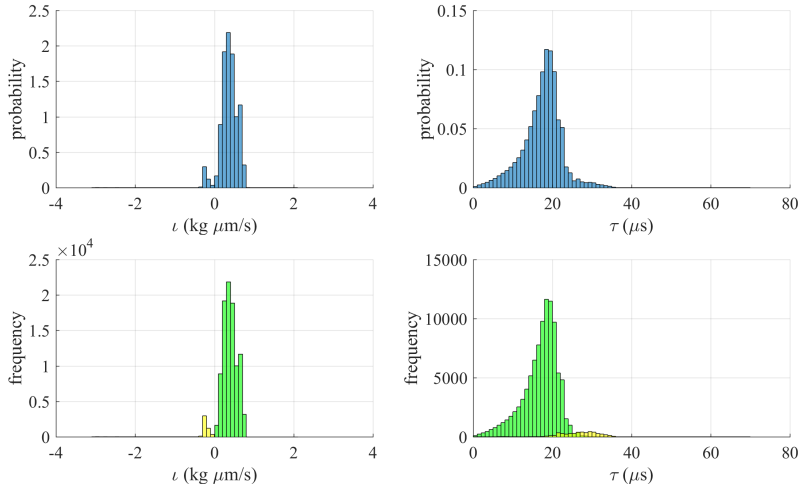

Figure 3.29: Monte Carlo simulation: feasible solutions (i.e. $\tau > 0$). Complete probability distributions of ι and τ (blue histograms) and distributions for each sign of the estimated impulse (green histograms for $\iota > 0$, yellow histograms for $\iota < 0$).

We maintain the iterations that yield a negative value of ι, since they have a physical explanation (a push of the pin instead of an adhesive pull), and are an unavoidable result of the algorithm as discussed in section B.5.

On 125000 runs, more than 124000 have an exact solution (which means that the residuals e_1 and e_2 are lower than 10^{-6}nm); the discarded solutions are characterized by high values of τ (higher than 100 μm). The non-exact solutions can be due to a combination of the parameters of the simulation (f_0, A_1, A_2) that are not compatible with the model (in the considered range of ι and τ parameters).

Approximately 80% of the iterations yield feasible solutions (i.e. exact solutions with positive τ lower than 100 μs). They are shown in figure 3.29; in the same figure, the solutions with positive ι (76.3% of the solutions) and negative ι (3.7%) are reported with different histograms. The statistical properties of the distributions of figure 3.29 are reported in table 3.13. Some outliers with negative values of impulse have been neglected; this choice is conservative, since these outliers (which have a high absolute value) would make the average of the complete distribution decrease.

We observe that the solutions corresponding to $\iota > 0$ have a value of ι between 0 and 1 kg μm/s) and show a value of τ which is inside the expected range (lower than 40 μs). Such a value of impulse in the in-flight case would not be critical: a critical adhesive impulse in the in-flight case would be indeed approximately 10 kg μm/s, corresponding to the test mass of approximately 2 kg moving with the limit velocity of 5 μm/s. The maximum value of the estimated impulse distribution is therefore less than 1/10 of the requirement.

	complete distribution: ι (kg um/s)	complete distribution: τ (us)
mean	0.367	17.4
standard deviation	0.216	4.9
quartiles	0.244 0.372 0.499	15.0 18.1 20.2

Table 3.13: statistical properties of the distributions of figure 3.29. The statistical properties for the complete distribution are reported (i.e. including positive and negative values of ι).

The solutions with negative ι do not correspond to adhesive pulls; they allow to obtain an exact solution for special choices of the parameters f_0, A_1 and A_2 (for instance, if the $\alpha_2\widetilde{M}_{20}$ phasor exceeds the amplitude circle, the equality between total phasor and amplitude can be obtained by reverting the sign of the adhesive phasor $\alpha_2 M_2^{adh}$).

In appendix B.5, we prove that the existence of solutions with negative values of impulses is related to the low value of the nominal impulse, by showing that in a fictitious case with no adhesion the algorithm would yield approximately 50% of the feasible solutions with $\iota < 0$ and 50% of the solutions with $\iota > 0$. This computation suggests that the negative part of the distribution must be maintained if we want to compute a mean of the distribution: if we compute the mean of the whole distribution (and not only of the distribution with positive impulse), in the fictitious case of appendix B.5 we would get indeed a mean impulse very close to 0, as expected.

In figure 3.30 the sensitivity analysis for the test is reported: the Monte Carlo simulation has been performed by varying the parameters (f_0, A_1, A_2) one at a time (with a normal distribution of 10000 samples). The result shows that the variability of impulse ι is mainly due to the preload force; moreover, the variability of the preload force can lead to negative values of impulses, and also to solutions with negative τ (with no physical meaning). The variability of the amplitudes leads to feasible solutions (i.e. with positive ι and τ) and affects mainly the duration of the impulse, while its effect is limited on the impulse magnitude.

Results for 10 tests

In figure 3.31 the results of the Monte Carlo simulations for the chosen set of 10 tests are reported.

We can see that the distributions of ι and τ are quite repeatable from test to test: this is also shown by the fact that the variability of the impulse ι in a single test is higher than the uncertainty of the nominal results of table 3.9 (the same holds for the duration τ).

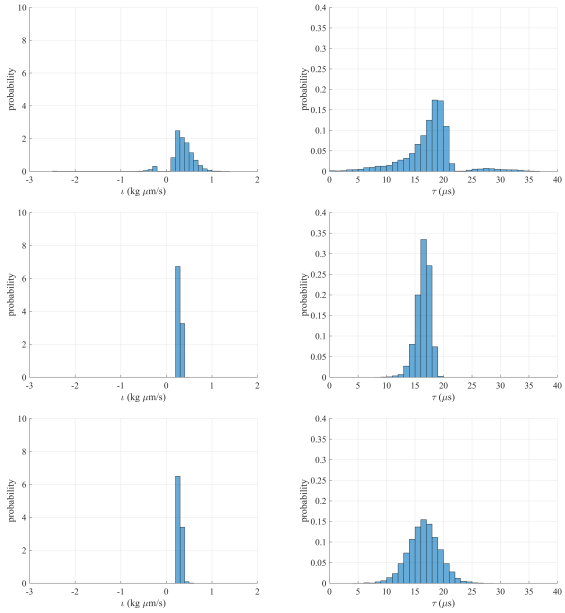

Figure 3.30: Monte Carlo simulation: probability distributions obtained by varying the parameters one at a time (top: f_0, centre: A_1, bottom: A_2).

We notice that for each test the maximum impulse ι of the distribution is ≈ 1 kg μm/s; moreover, for the cases with $\iota > 0$ (adhesive impulses) we get a duration τ always lower than 25 μm/s (and therefore in the expected range given by the time-to-2-μm, which is 40 μm/s).

Proof of the assumption of chapter 2

Regarding the conservative estimation of section 2.5 of the previous chapter, the results commented in this section prove that the dispersion of the momentum transferred by the pin (ι in equation (2.19)) to the TMMF is much lower than the dispersion of the final momentum p, which can therefore be considered as dominated by the variability of the needles push q.

We have indeed that, if we base on equation (2.9), the dispersion of the adhesive pull (which takes into account both the variability of the mean values of the Montecarlo simulations and the uncertainty of each estimation) is approximately 0.3 kg μm/s. The dispersion of t_1 is approximately 0.4 μs. As a consequence, the dispersion of ι will be lower than

$$\sigma_\iota < \sqrt{(\frac{f_0}{2}\sigma_{t_1})^2 + \sigma^2_{\iota_{adh}}} \approx 0.3 \text{ kg } \mu\text{m/s} \tag{3.70}$$

(considering also the variability of the preload force does not change significantly the result). This quantity is approximately 10 times lower than the standard deviation of the distribution of the TMMF free flight momentum p (≈ 3 kg μm/s).

3.4.5 Effect of a misalignment of the TM w.r.t. plunger and interferometer

The results of this section have been based on the assumption of a constant and precise value (for each mode) of α_j and η_j (see table 3.5). As commented, these values depend on the misalignment of the TM w.r.t. plunger, needles and interferometer. In particular:

- the value of η_j, defined as the mean value of the mode shape at the needles position, can change if the needles move w.r.t. the nominal position considered for the evaluation of the coefficient. However, the variability of η_j is not investigated due to the negligibility of the needles push.

- the value of α_j appears in the model two times. It represents both the sensitivity of the mode shape to the exciting pin force (equations (3.45) $\div$ (3.50)) and the sensitivity of the measured amplitude to the mode ((3.61)).

As commented in section 2.2.5 and in appendix C.1, the laser points at the plunger, and then the TM is positioned. As a consequence, the misalignment of the interferometer can be considered (at least as order of magnitude) the same of the laser. We recall that we can consider the laser pointing at the centre of the insert with an uncertainty of $\pm$ 100 μm.

In this range, both the mode shapes have a relative variation of the value α_j in the order of 10^{-4}. As reported in table 3.10, the ratio between uncertainty (standard deviation) and nominal value is $\approx 10^{-1}$ for the force and $\approx 10^{-2}$ for the amplitudes. This means that considering (for forces and amplitudes) the additional uncertainties due to α_j would not affect significantly the result. In other words, we can consider that the uncertainties of table 3.10 take into account also a possible variability of α_j.

The low variability of α_j is due to the fact that the mode shapes have a maximum at the centre, which is associated to a low gradient of the mode shape.

With a similar analysis we can show that, as long as the laser points on the insert (whose radius is 2.4 μm), it is not possible to detect mode shapes that show a zero at the centre (modes (a), (b), (e) of figure 3.14). For instance, for the mode (a) of the figure, a dynamical simulation shows that (with the values of the impulse magnitude and duration computed in this section) if the laser spot and the plunger are located at the diameter of the insert we would get a measured amplitude of $\approx 10^{-6}$ nm; for mode (e) we would get 10^{-3} nm, which is a value not detectable by computing the spectrum of the signal. As a consequence, the low dimension of the insert does not allow to measure these mode shapes (however, we remark than the measurement of other mode shapes is not necessary for the computation of the results).

3.4.6 Conclusions

In sections 3.4.3 and 3.4.4 we have considered an estimation of the adhesive impulse based on equations (3.66) and (3.67), thus imposing the equality between the amplitudes of the measurement and of the dynamical model. This approach allowed to get an estimation of the impulse magnitude ι; the methods has been

applied with a Monte Carlo simulation in order to get an uncertainty interval for the parameter. We have also seen that the estimation of the model parameter τ is inside the expected range (even if we consider its uncertainty), thus confirming the feasibility of the results.

In appendix B.6 we discuss the equality of both amplitudes and phases of the phasors, thus considering the complete equations 3.64 and 3.65. We prove that the nominal solution of the model (section 3.4.3), based on the matching of the amplitude between model and measurement, is 2σ-compliant w.r.t. the measured phases of both the modes; this is done by taking into account the uncertainty of the start of the event (which, as discussed in section 3.1.1, may not coincide with the time $t = 0$ of the signal).

Comparison with previous predictions

For each of the tests of figure 3.31, the probability distribution of the estimated impulse allows to determine a *range* rather than a precise value: we can see that the dispersion of the distribution is comparable with the mean value. Due to the high uncertainty w.r.t. the mean value and due to the low number of available distributions (due to the high computation time of the Monte Carlo simulations), a precise probability distribution of the effect of adhesion on the in-flight release velocity (like the one reported in [24]) cannot be determined.

However, the adhesive impulse given by one pin to the TM can be considered lower than 1 kg μm/s, thus confirming that adhesion is not critical for the in-flight velocity of the TM of LISA Pathfinder. In a worst-case, we can indeed consider that in the in-flight release (whose model is described in section 1.1.6) only one adhesive pull is acting on the TM, without the cancelation of the opposite adhesive impulse. In this situation, an adhesive pull of 1 kg μm/s would produce a velocity of the TM of approximately 0.5 μm/s (since the mass of the TM is 2 kg in the satellite); this velocity is 10 times lower than the requirement for a linear DOF.

Compared to the worst-case estimation of section 2.5, we obtain an estimation of the effect of the adhesive impulse that is closer to previous predictions (see section 1.2.3). In [24], the effect of adhesion (difference of the adhesive pulls) gives a in-flight velocity lower than 0.5 μm/s in 85 % of the cases (the distribution is entirely contained in the interval $0 \div 1.50$ μm/s). A similar result is shown in [26]: the probability distribution of the release velocity is entirely contained in the range $0 \div 0.5$ μm/s).

The estimated magnitude of the adhesive impulse (≈ 0.3 kg μm/s in mean) is similar to the correspondent result of [88] (≈ 0.8 kg μm/s in mean) in terms of order of magnitude (this last result was however obtained with a slower tip, which increases the adhesive pull as explained by equation 1.8).

3.5 Summary of the impulse estimation

In this section the data of the TMMF releases of chapter 3 have been analyzed in detail in order to extract information on the adhesive pull given by the GPRM pin to the TM in the on-ground setup.

The analysis of the signal in the free flight interval (section 3.1) led to the identification of some harmonics created by the release event. The harmonics of the free flight signal (section 3.2), corresponding to oscillations of the insert of the TM w.r.t. its centre of mass, have been recognized and classified in order to distinguish the real time harmonics from fictitious oscillations due to disturbances of the interferometer (space harmonics).

In particular, two of the time harmonics of the signal (whose frequencies are approximately 15 kHz and 35 kHz) have been identified as *modes of oscillation* of the TM vibrating as a thin plate (section 3.3). Based on the modal parameters of the TM estimated through a FEM analysis, the dynamical model of the TM at the release has been improved by considering the effect of the pin adhesive pull on the vibration of the modes.

In order to estimate the magnitude of the adhesive impulse, the model has been then fitted to the measured oscillations of the two modes, based on the equality of the measured amplitudes (section 3.4). The method yields an exact solution for the estimation of magnitude and duration of the impulse; the uncertainties of the parameters appearing in the model have been taken into account, in order to yield an uncertainty interval for the estimations.

The results, which show the consistence between the estimated duration of the impulse and the expectations, confirm that in LISA Pathfinder the contribution of adhesion to the residual release velocity of the TM is not critical; according to the estimations, the adhesive impulse given by a single pin to the TM in the TMMF is at most 1/10 of the requirement.

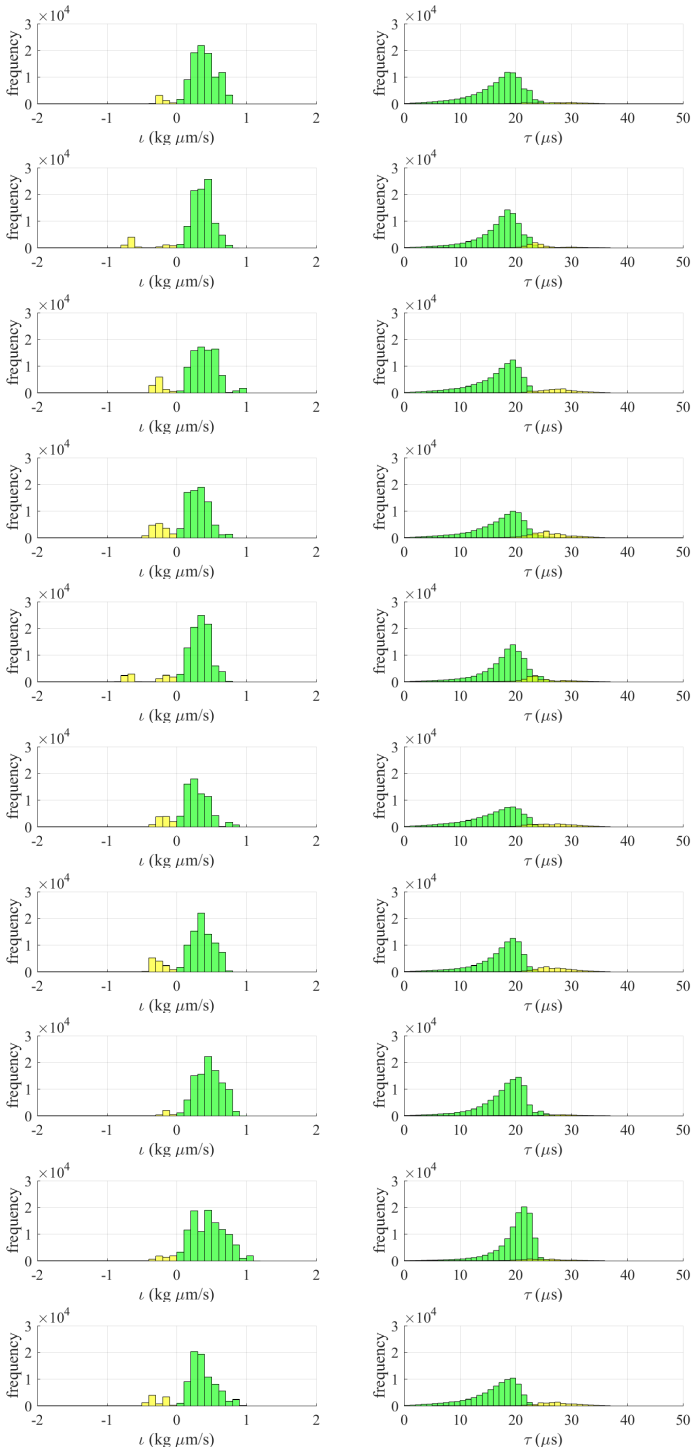

Figure 3.31: Monte Carlo simulation: feasible solutions (i.e. $\tau > 0$) for the set of 10 tests. The green histograms are the distributions of ι and τ for $\iota > 0$, the yellow histograms are the distributions of ι and τ for $\iota < 0$.

Chapter 4

In-flight TM release

In this chapter the in-flight releases of LISA Pathfinder mission are discussed. The release data are described and interpreted by means of simple dynamical models, in order analyze the release dynamics of the in-flight case and compare the actual behaviour of the *Grabbing Positioning and Release Mechanism* (GPRM) with the expectations of a nominal model and the requirements. In particular, the purpose of these analyses is twofold: investigating the motivations of the residual velocity of the TM at the release and (if possible) the role of adhesion.

The topics are proposed in cronological sequence, in order to highlight the steps of the research.

We describe first the structure of the *Gravitational Reference Sensor* (GRS) and the *nominal release* in section 4.1. The nominal release is the release procedure chosen for the injection into free fall of the *test mass* (TM); it has been the reference case for all the predictions of the TM residual momentum discussed in the previous chapters.

The releases of February 2016 are presented and analysed in section 4.2. These releases, which are performed through the nominal procedure and allow the test mass (TM) to move freely in the housing before the science phase, show a behaviour far different than the nominal one, with a kinetic energy distributed along all the degrees of freedom and velocities out of the requirements.

The GPRM behaviour is therefore further studied through the dedicated *release campaign* of June and July 2017, by repeating the release procedure with different strategies. In particular, two important instants of the release procedure are distinguished and analysed separately. As described in section 1.1.4, in a *nominal* configuration the TM is set into free fall through the quick retraction of the pins (*pin release*); after a pair of seconds, the plungers retract in order to allow a free motion of the TM. If the release velocity is lower than the requirements, no impact should occur between TM and plunger between the two instants; as a consequence, the velocity of the TM measured after the pin release (*pin release velocity*) should be therefore equal to the velocity of the TM measured after the plunger retraction (*plunger release velocity*). We say that *pin release velocity* and *plunger release velocity* should coincide (see section 4.1.2 for their definition). In section 4.3 the *plunger release velocities* are discussed: in general, we measure re-

lease momenta completely out of the requirements (except for specific cases), with high rotations. As a consequence, in order to understand the reasons of this non-nominal behaviour, and thanks to the specific signal analysis of section 4.4, also the *pin release velocities* are analyzed in section 4.5. For each test, the comparison of the two velocities can yield information on the behaviour of the mechanism: while in some cases the release momentum is out of the requirement after the pin release, in other cases the critical increment of momentum is related to the motion of the plunger.

For the tests characterized by critical velocities after the pin release, we want to understand the motivations of the high release momenta. We find that the tests with higher *pin release velocity* cannot be explained with a nominal TM-pin contact (section 4.6) and therefore an important contact between TM and plunger at the pin release must be considered (section 4.7).

In order to extract information on the effect of adhesion, we analyse a specific group of tests characterized by the prevailing effect of adhesion in a nominal situation (section 4.8).

Finally, based on the analyses some hints for the future development of the GPRM are given in section 4.9.

In section 4.10 we summarize the results of this chapter, highlighting the main information obtained from the in-flight tests of the GPRM.

It has to be remarked that the data analysis of this chapter is only a preliminary analysis of the LISA Pathfinder data; the main purpose of the work is a general description of the in-flight dynamics investigation of research directions for the future activity. The future developments of the research, which are mainly based on correlation analyses, analysed of the system geometry and dynamical simulations, will be briefly discussed in the Conclusions (chapter 5).

4.1 GRS and nominal release

In this section the properties of the GRS (*Gravitational Reference Sensor*) and the *nominal release* of LISA Pathfinder are discussed.

As a reference for this chapter, we describe first the reference frame in section 4.1.1.

In section 4.1.2 we recall the nominal release procedure. Here we describe also the general response of the TM to the release procedure: the important distinction between *pin release velocity* and *plunger release velocity* will be introduced. The *nominal configuration* of TM and plunger at the release is also described.

In this chapter, we focus mainly on the *release signals* of the TM, i.e. the measurement of the TM position and attitude at the release. The signals are given by the capacitive measurement (section 4.1.3); the electrodes used for the capacitive measurement can be used also for the capacitive control, whose properties yield the specifications (requirements) for the TM momentum at the release.

4.1.1 Reference frame

As discussed in section 1.1.3, the GRS is the part of the satellite hosting the TM, its blocking and release system and its measurement and actuation system.

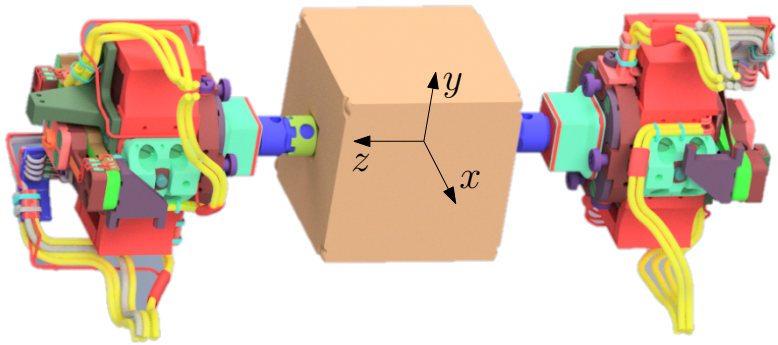

Figure 4.1: 3D view of the TM grabbed by the plungers (3D model courtesy of Carlo Gavazzi Space - OHB Italia SpA).

In figure 4.1 the reference frame is represented w.r.t. the TM grabbed by the plungers; in figure 4.2 the reference frame is represented w.r.t. the position of the electrodes on the housing [103]. The plungers are aligned along z axis; in a nominal release, plungers and TM should move only along z axis (monodimensional motion). The properties of TM and plungers have been described in sections 1.1.5 and 2.2.4; due to their shape, the plungers are also called *conical plunger* (Z+) and *pyramidal plunger* (Z-). As represented in figure 4.2, the angles of rotation are θ (about x axis), η (about y axis) and ϕ about z axis.

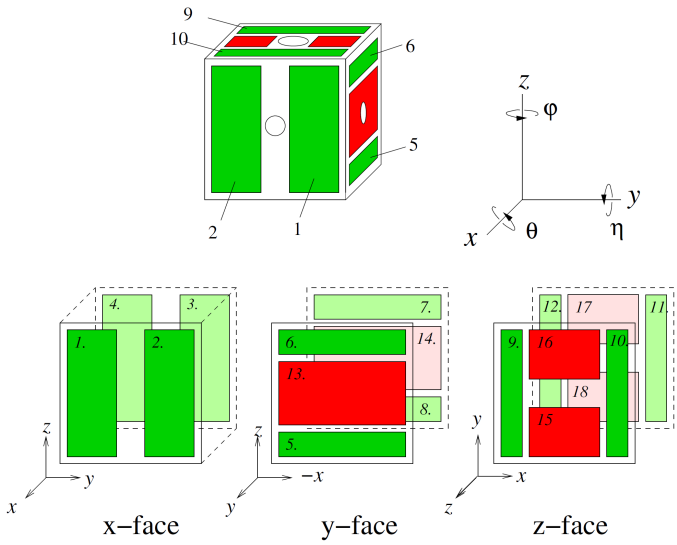

Figure 4.2: reference frame of the GRS, and position of the electrodes on the housing (from [103]). Sensing/actuation electrodes (from 1 to 12) are marked green; injection electrodes (from 13 to 18) are marked red.

4.1.2 Nominal release procedure

As anticipated in section 1.1.4 (see figure 1.6), the *nominal release procedure* consists of the following operations:

1. *TM handover to plungers.* The TM is initially blocked by the CVM (Caging and Vent Mechanism, section 1.1.3) with a high preload ($\approx$ 2000 N), and the plungers are extended until they touch the TM on the indentations of the TM surface. Once the TM is firmly grabbed by the plunger, the CVM is retracted.

2. *preload reduction.* The first step to reach the target 0.3 N preload at the release is the reduction of the blocking force of the plungers. This is done by retracting the plunger of small displacement steps: according to the GPRM stiffness (see section 4.2.3), the preload fall is approximately 0.2 N for 1 μm of retraction.

3. *TM handover to pins.* This operation leads to the nominal condition before the release, with the pins extracted of 18 μm (nominal length) holding the mass at the desired preload. The pins are extracted while the plungers are simultaneously retracted in order to maintain the target preload as the pins touch the TM.

4. *pin release*. The pin release is commanded and the quick voltage fall makes the pin release retract completely (see section 1.1.5). In the nominal situation, the TM should move freely after the pin retraction, with a residual momentum due to the effects described in section 1.1.6 (i.e. asymmetry of pushing forces and adhesive forces).

5. *plunger retraction*. Few seconds after the pin release, the plungers are retracted at a high speed (≈ 110 μm/s), such that the TM is let free to move inside the housing. In a nominal situation, if the residual velocity of the TM is inside the requirements, the plunger retraction avoids any impact between TM and plungers.

6. *ISFEE bias turned on*. The ISFEE plunger bias (which, as discussed in section 4.1.3, allows a better reliability of the measurement) reduces the readability of the control force, therefore it is not active during the pin release; some seconds after the pin release, it is switched on in order to measure the TM motion with a high reliability. As a consequence, the TM linear velocities and rotations are measured with a good accuracy only after the plunger retraction: however, since no impact between TM and plunger occurs in the nominal situation (i.e. when the residual velocity inside the requirements), this velocity should correspond to the velocity conferred to the TM after the pin release.

7. *actuation*. The electrostatic actuation is activated in order to control the TM attitude, and move the TM position to the zero of the reference frame.

General response of the TM at the release: pin release velocity, plunger release velocity

In figure 4.3 the general response of the TM to the release procedure is sketched. The situation represents the most general case, with a high residual momentum at the release and an impact of the TM with the plungers; the described case will serve as a reference in the rest of this chapter.

The TM, initially held by the pin (a), acquires a residual momentum after the pin retraction (b). For each DOF, we define the velocity after the release performed by the pin ($\vec{v}_1$ in the picture) as *pin release velocity* (and the associated momentum as *pin release momentum*). In general, we refer with those terms both to translational and rotational DOF. In a nominal situation, as the one summarized in section 1.1.6, this velocity should be uniquely directed along z axis, as an effect of adhesion and asymmetric motion of the pins.

The plungers retract with a high velocity approximately 2 seconds after the pin release. If the pin release momentum is high and out of the limits, the TM can have an impact with the plungers (c) before the plungers have retracted. Theoretically, we can have multiple impacts before the retraction of the plungers; moreover, an impact between the two bodies could also be due to an unexpected motion of the plunger when the plunger is retracted. When the plungers finally are retracting, we define the velocity of the TM ($\vec{v}_2$ in the picture) as *plunger release velocity* (and the associated momentum as *plunger release momentum*).

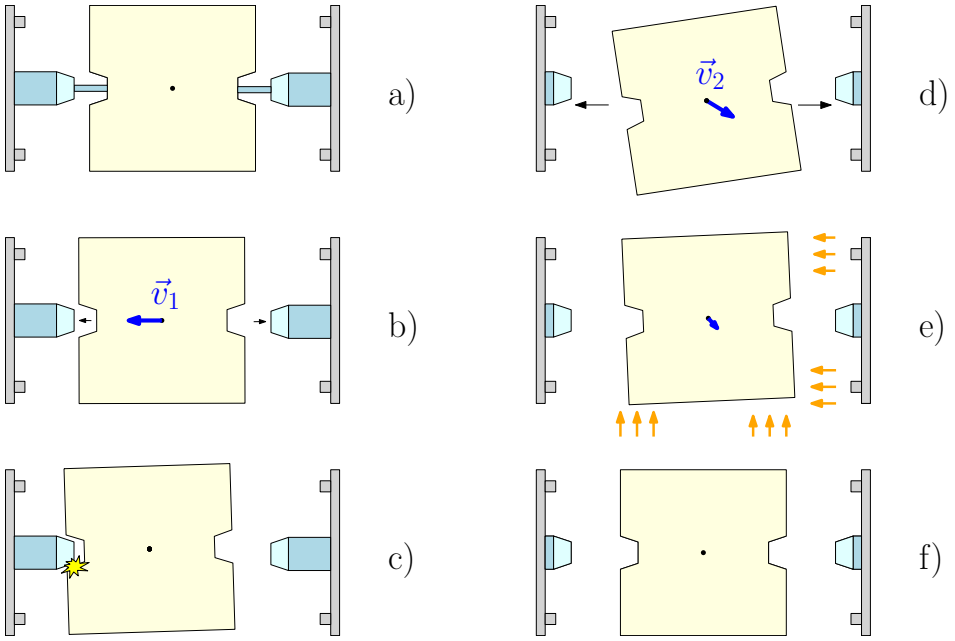

Figure 4.3: steps of the release procedure in a general situation. a) TM held by the pins. b) pin retraction and residual velocity $\vec{v}_1$ (*pin release velocity*). c) impact of the TM against one plunger and variation of the momentum. d) velocity of the TM at the retraction of the plungers $\vec{v}_2$ (*plunger release velocity*). e) effect of capacitive control: electrostatic forces acting on the TM. f) TM centred in the housing.

After the plunger retraction, the action of the electrodes on the TM (e) centres the TM in the housing (f). Since it is activated after the plunger retraction, the capacitive control has therefore to face the plunger release momentum.

We remark here the difference between the two velocities. Measuring the pin release momentum (also called *initial release momentum*) is important since it can yield information of the role of the adhesive pull at the release, thus allowing to compare the predictions of chapter 2 and 3 with the in-flight observations. Measuring the plunger release momentum (*final release momentum*) can give information on the effect of the plungers on the final momentum that has to be controlled by the electrodes.

The plunger release momentum can indeed differ w.r.t. the pin release momentum as a consequence of the following effects, both due to a relative TM-plunger contact (figure 4.3 c):

- impacts of the TM against the plunger when the plungers are not in motion (i.e. impacts due to the TM momentum);
- impacts of the plungers against the TM when the retraction of the plungers is commanded (i.e. impacts due to the plunger motion) or when the plungers

vibrate as a consequence of the pin release phenomenon (i.e. impacts due to the plunger vibration).

Theoretically, an impact with the plungers should decrease the momentum of the TM due to the loss of kinetic energy, thus yielding $|\vec{v}_2| < |\vec{v}_1|$ (if we focus on translations); this would imply a *passive* role of the plungers on the final release velocity. In the other case, i.e. $|\vec{v}_2| > |\vec{v}_1|$, we would observe an *active* role of the plunger: this is the case if (for instance) the plunger vibrate laterally at their retraction (with a "kick" given to the TM).

The separate estimation of the two velocities is therefore very useful for the investigation of the mechanical behaviour of the GPRM.

Nominal configuration at the release

In figure 4.4 the profiles of plunger and TM at the pin release is shown. The contact between TM and plunger occurs at the *coupling surface* of the indentation when the TM is grabbed by the plunger, while it occurs at the *landing area* when the TM is held by the pins.

In figure 4.5 the *nominal configuration* of TM, pin and plunger at the release is sketched, according to the system geometry. In the nominal configuration, after the handover to pins, the TM is in contact uniquely with the pin at the landing area (figure 4.5 centre). As shown in the figure, at the pin extraction the contact occurs after the pin has moved of 4 μm. As a consequence, since the commanded motion of the pin is 18 μm, the further extraction of 14 μm creates a corresponding detachment at the coupling surface of 14 μm. After the pin retraction, the minimum distance is reached at the coupling surface (as shown also in figure 4.4).

As a consequence, in the nominal case with the TM moving only along z axis due to the residual momentum, the TM should impact with one plunger after a motion of approximately 14 μm. In the nominal configuration, this is avoided by the retraction of the plunger, commanded approximately 2 seconds after the pin release (such that a TM with residual velocity lower than 5 μm/s should not impact with the plungers).

Effect of capacitive forces between plunger and TM

In the nominal case, the TM acquires at the release an initial velocity due to the effects described in section 1.1.6 (asymmetry effects of adhesion and pin delay). If a difference of voltage between the plunger and the TM exists, this could lead to *capacitive forces* between the plungers and the TM, similarly to the electrostatic attractive forces between two plates of an ideal capacitor.

In [104], the capacitances between the TM and the plungers are computed, through both semi-analytical model and FEM computation (a similar analysis is performed in [105]). The capacitances are considered for a simulation of the capacitive effect (influence of capacitive forces) after the release, by simulating an initial velocity of the TM of 5 μm/s (the requirement) and a constant different of voltage that varies in an expected range (0-2 V).

The results show that in a very worst case (2 V), the capacitive forces can be not negligible if the TM is close to the TM; however, the retraction of the plunger

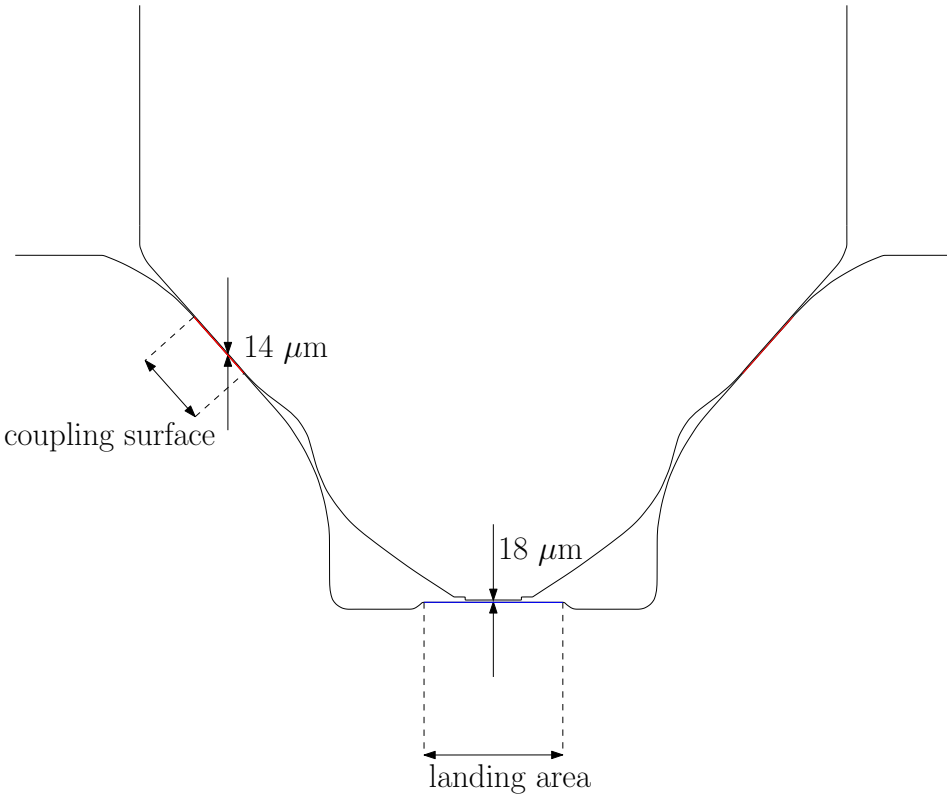

Figure 4.4: profiles of plunger and TM after the pin retraction (according to CAD geometry). The coupling surface (red) and the landing area (blue) are shown. After the pin release, the minimal distance between the bodies is at the coupling surface.

reduces this effect. This leads to an additional velocity of the TM of less than 15% in a very worst case; this additional velocity is acquired by the TM after 5-10 seconds. As a consequence, if the system behaviour is nominal and the z velocity is lower than the requirement, the capacitive forces should not affect significantly the final TM momentum, indipendently of the source of the difference of potential.

If we assume that the difference of voltage is due to a constant charge of the TM (due for instance to the *triboelettrification* effect that could occur at the detachment between TM and pins), the capacitive effect is even lower, since when the TM-plunger distance decreases, the difference of voltage decreases. This scenario is described in C.5 through a simplified monodimensional model, which takes into account the capacitances estimated by the FEM. The model confirms that if the release occurs nominally, the distortion of the TM velocity is negligible.

The capacitive effect is however not negligible if the TM is very close to the plunger (this can occur in a non-nominal situation), as a consequence of the capacitance asymptote for a relative distance close to zero. In the case of constant

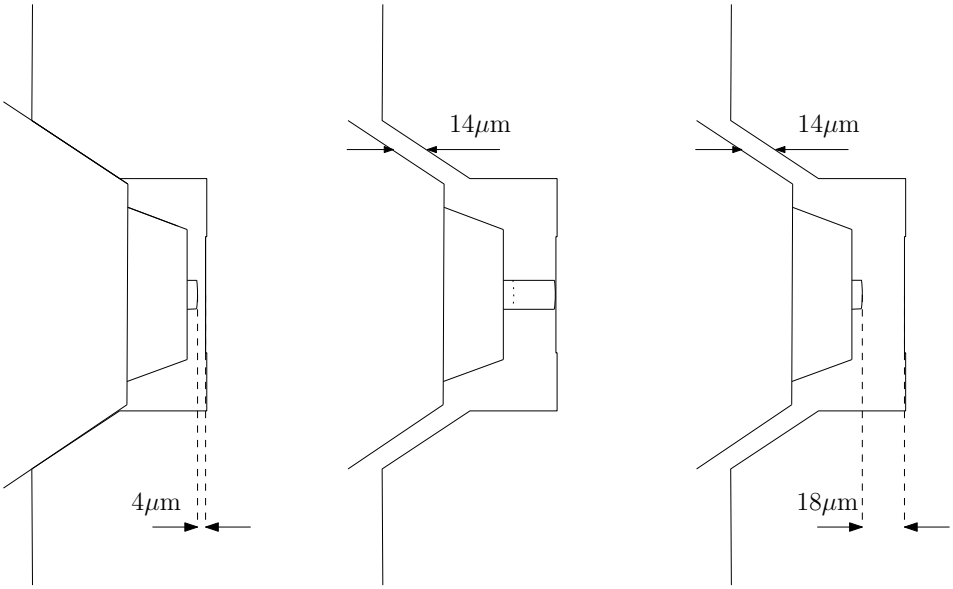

Figure 4.5: evolution of the distances between TM and plunger in a nominal configuration. Left: TM blocked by the plungers, with the pin at a 4 μm distance from the landing area. Centre: the pin is extracted of 18 μm. Right: pin retraction.

difference of potential between TM and plungers, we would get infinite forces as the TM touches the plungers. In the case of constant TM charge, the velocity produced by the electrostatic effect could significantly affect the release velocity only when the velocity produced by the TM-plunger contact is much lower than the requirement.

4.1.3 Measurement and control system

The capacitive sensor is a common solution for the inertial sensor on satellites [106]. As described in 1.1.2, the capacitive measurement of the TM attitude has a fundamental role in the science phase of the mission, since the drag-free thruster control [107] has to fly in formation with the first proof mass (TM1), such that the two bodies follow a pure geodesic [108]; in addition, the second test mass (TM2) must follow the spacecraft, in order to be centred w.r.t. its housing. This strategy allows the measurement of the relative acceleration Δg through the laser interferometry. Due to its criticality in the science phase, the capacitive system is designed in order to work with high precision.

Capacitive measurement

The capacitive measurement is based on the electrodes of figure 4.2. The electrodes are mounted externally to the metallic housing that contains the TM. Two kinds of electrodes are shown: *sensing/actuation* electrodes and injection *electrodes*. As

shown in the picture, the sensing electrodes, whose task is the measurement of the 6 DOF, are positioned symmetrically in each direction (2 for each face of the housing); this is a fundamental requirement for a precise measurement of the TM attitude [109].

The role of the sensing electrodes is the measurement of each degree of freedom through the relative variation of the capacitance between housing and TM [110]. The measurement principle can be simply represented in a monodimensional approximation: we consider the electrode and the opposite face of the TM as two infinite parallel plates. The situation for a single direction (z) is sketched in figure 4.6, assuming no rotation of the TM in the plane. The injection electrode (capacitance C_0 w.r.t. the TM), the TM and the two sensing electrodes (capacitances C_1 and C_2 w.r.t. the TM) constitute a circuit, which is excited by the injection electrode through a voltage V_{in} oscillating at high frequency. The currents exiting the sensing electrodes feed a electronic amplification circuit which yields an output V_{out}; since the motion of the TM (z in the figure) affects the two capacities C_1 and C_2, the output V_{out} can be related with the motion of the TM [110]. The measurement of the rotation of the TM about an axis can be detected with a similar scheme thanks to the two electrodes hosted on each face of the housing, as shown in figure 4.2. For instance, the two electrodes of each x face are positioned in order to be sensitive to a rotation about z axis: if $\phi \neq 0$, they have indeed different capacities w.r.t. the TM.

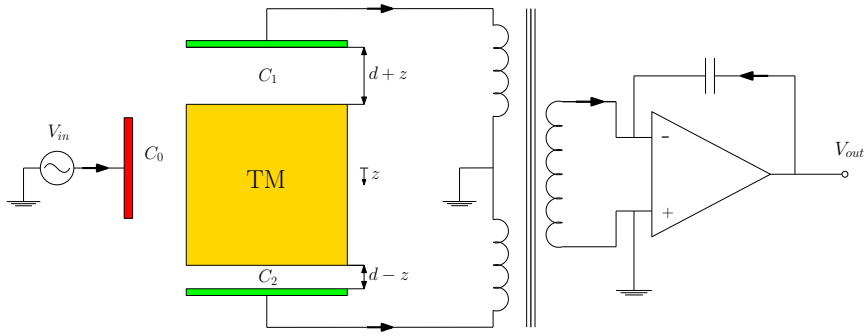

Figure 4.6: simplified model of the circuit for the capacitive measurement of one DOF (z displacement) [110]. The represented position of the electrodes does not reflect the real position (represented in figure 4.2).

An accurate relation between output voltage and TM motion must take into account many effects, like the effect of non-parallel plates [110] and of the boundary effects of finite plates [111].

Capacitive measurement at the TM release

The capacitive measurement is designed and calibrated for a high performance during the science phase. In the science phase of LISA Pathfinder, both TMs are kept in the centre of the housing (by the drag-free thruster control, for TM1, or

by the capacitive actuation, for TM2), with completely retracted plungers; this allows a simple linear relation between measurement of one DOF and the output voltage [110]. This is not the case for the TM release. As shown in figure 4.4, in the nominal release configuration, when the pin release has occurred and before the plunger retraction, the plungers are very close to the TM (≈ 14 μm) and can therefore modify the total capacitances C_1 and C_2: a plunger very close to the TM makes the capacitances increase; moreover, if the TM moves towards one plunger after the pin release, one of the two capacitances can tend to infinity [104], thus distorting significantly the signal [105].

The problem of the relative capacitance between plungers and TM can be avoided by turning on the *ISFEE plunger bias*: before the release, the same voltage of the TM is applied to the plungers. This minimizes electrostatic forces between plungers and TM, as well as the signal distortion.

The capacitive measurement has a sampling frequency of 10 Hz. This sampling frequency, which was designed for the low dynamics of the TM during the science phase, is a poor sampling if we focus on the release phenomenon, which occurs nominally in the order of 10^{-3} seconds. As a consequence, during the analysis of the in-flight release signal we will have to deal with the problem related to the low sampling (see section 4.4).

Capacitive control

As discussed in 1.1.3, the same electrodes used for sensing can be used for the actuation of the TM, by establishing a voltage difference across electrode and proof mass. The actuation scheme of LISA Pathfinder is described in [103].

The capacitive control of the TM, whose main task in the science phase is making TM2 follow the spacecraft, is important in the TM release since it allows to centre the TM in the housing, especially in the case of a high release momentum. Due to the limited capacitive authority, which is designed for a quasi-static process [110], a too high release momentum can lead to the failure of the position control after the release.

We recall in table 4.1 the requirements for the final momentum of the TM at the release:

DOF	**limit**
translations x, y, z	5 μm/s
rotations θ, η, ϕ	100 μrad/s

Table 4.1: requirements for the TM momentum at the release, w.r.t. the maximum authority of the capacitive control.

For each DOF, a velocity is *compliant* if its modulus is lower than the corresponding limit.

Since in this chapter we focus on the mechanical aspects of the release, we will analyze the actuation performance only from the point of view of the release momentum (section 4.3.3).

4.2 Release operations in LISA Pathfinder

In this section a brief summary of the in-flight release experiments is presented.

For a single release procedure, the main output is the motion of the TM along its 6 DOF, which is analysed in order to study the compliance of the linear and angular momenta with the requirements; for this purpose, other important data sets are considered, like the force applied by the plungers to the TM, and the motion of plungers and pins.

The nominal release procedure of section 4.1.2 has been adopted for the releases of February 2016, commented in section 4.2.1. These are the first releases occurred in the LISA Pathfinder satellite, programmed for the injection of the TMs into free fall prior to the science phase.

The releases of February 2016 showed unexpected high release momenta, non-compliant with the requirements. In order to study the problems related to the release procedure and find different release strategies, a *in-flight TM release campaign* was planned (section 4.2.2). The results of this experimental campaign will be deeply discussed in this chapter (sections 4.3, 4.4 and 4.5).

The in-flight TM release campaign has been performed in June 2017, after the end of the science operations and together with other additional end-of-life activities, which included additional mechanical tests that will be described in section 4.2.3. These tests furnished important information regarding the mechanical behaviour of the GPRM, which will be considered in the interpretation of the in-flight releases (sections 4.6, 4.7 and 4.8).

4.2.1 Releseas of February 2016

Prior to the beginning of the science phase, the two TMs have been released in February 2016, according to the nominal strategy described in section 4.1.2. The release for TM2 occurred on February 15, while the release of TM1 on February 16.

Differently than the expectations, both the releases have shown linear and angular momentum out of the requirements, thus suggesting that the release occurred in a non-nominal way.

TM2 release

In figure 4.7 the translation and rotation signals for the TM2 release (February 15th, 2016) are shown. The sampling frequency is 10 Hz. The degrees of freedom are constant until time t_0, when the pins are retracted; the position before the release is close to the zero reference position. At time t_0 the pins are retracted and the mass moves with a residual velocity.

In a nominal case (see the definition of section 1.1.6), we would measure a prevailing (if not unique) linear momentum along z, with a residual velocity lower than 5 μm/s, and negligible velocities for the other DOF. The measured behaviour for TM2 release, summarized in table 4.2, is completely different:

- all the 6 DOF show a relevant velocity, higher than the requirement (5 μm/s for translations, 100 μrad/s for rotations) except for the η angle.

- the higher translational velocity is along y, differently than expected.
- the higher rotational velocity is $\dot{\theta}$; $\dot{\eta}$ is in the requirements, while $\dot{\phi}$ is out of the requirements.
- the quick inversions of the velocities, which occur many times in the signals, reveal impacts with the plungers and the housing: this has been confirmed through a 3D simulation by choosing the measured signal as an input for the position of the bodies.
- the capacitive control was able to move the TM to the zero reference only after many bounces of the TM against plungers and housing.

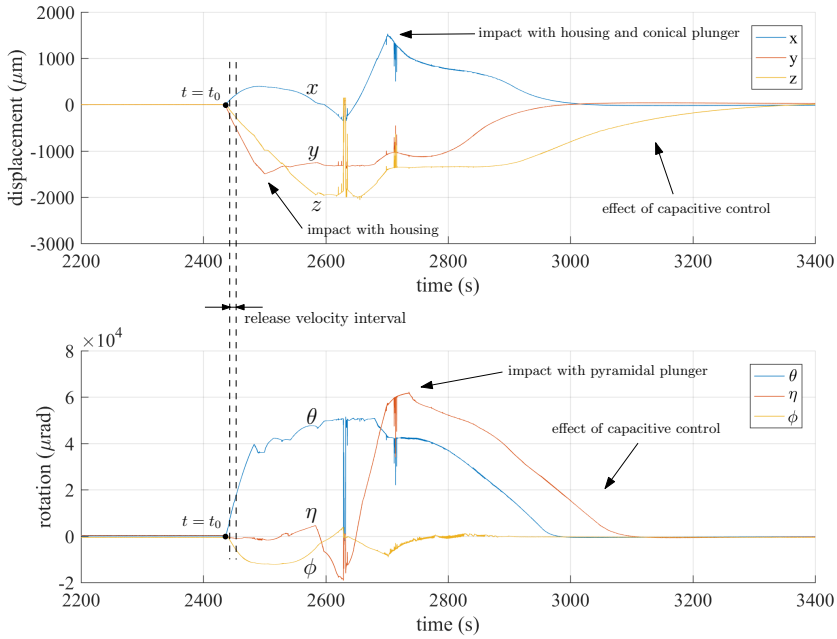

Figure 4.7: capacitive measurement of displacements and rotations of TM2 release (February 15th, 2016). In the picture, we highlight the pin release instant ($t = t_0$), the interval chosen for the computation of the velocities through a linear regression, and some inversion of the velocities due to impacts (visualized through a 3D animation). The artefacts in the telemetry are due to contacts between the TM and the housing or the plungers, which make the capacitive measurement read the reference (zero) position.

As shown in figure 4.7, the TM was finally controlled and captured; however, the TM release was unsuccessful w.r.t. the nominal expectation, i.e. the too high linear and angular momenta at the release did not allow the capacitive control to

	$\dot{x}$	$\dot{y}$	$\dot{z}$	$\dot{\theta}$	$\dot{\eta}$	$\dot{\phi}$
velocities	11.6	-27.2	-16.2	1035.4	-30.0	-429.7

Table 4.2: TM2 release (15.02.2016): velocities after plunger retraction (*plunger release velocities*). Linear velocities are in μm/s, rotational velocities in μrad/s. The velocities are computed through a linear regression of displacement and rotation signals (shown in figure 4.7), with a maximum uncertainty of 3 % (standard deviation of the estimated slope). The artefacts in the telemetry are due to contacts between the TM and the housing or the plungers, which make the capacitive measurement read the reference (zero) position.

avoid bounces between TM and the housing. The high y and θ velocities (which describe the rotation rate of the TM in the yz plane) suggest that a relevant impulse along y direction has been given; moreover, the unexpected ϕ rotation can be hardly explained by a simple nominal release, and a contact with one plunger at the release seems necessary for the explanation of such a rotational impulse (due to its shape, the pyramidal one is more probably involved, as discussed in appendix C.3).

The measured velocities of table 4.2 (whose computation interval is shown in figure 4.7) are the velocities after the retraction of the plungers; by recalling the terms introduced in section 4.1.2, they are *plunger release velocities*. Since in this release the ISFEE bias is switched on after the plungers have retracted, it is not possible to investigate the velocity after the pin release and before the plunger retraction (i.e. we cannot compute the *pin release velocities*), due to the capacitive disturbance of the plungers discussed in section 4.1.3 (an estimation of the capacitive distortion for this release is proposed in [105]). Therefore, we don't know if the measured release momentum is due only to the contact between TM and pin or also due to an impact with the plunger occurred few instants after t_0. However, the measured momenta suggest the higher probability of the second hypothesis, since the release velocity along z would lead to an impact with the retracted pin tenths of seconds after the release (and before the plunger retraction), therefore being not compatible with a "free" motion of the TM along z: according to figure 4.4, the *nominal gap* in z direction between TM and plunger after the pin release is indeed 14 μm, corresponding to the z motion of the TM in one second (according to the measured z release velocity reported in table 4.2).

TM1 release

In figure 4.8 the TM1 release of February 16 is shown. The release has been even worse than the previous one, in terms of deviation from the requirements. As reported in table 4.3, the linear y and z velocities are out of the requirements (with z velocity higher than y velocity), leading to bounces with the Z- (pyramidal) plunger. High rotational velocities (completely out of the requirements) can be seen; the ϕ velocity is especially much higher than the requirements. As shown by a 3D animation and as revealed by the high final value of ϕ in the signal, the high ϕ velocity makes the TM get stuck in the housing; the actuation was not

able to capture the TM, even after many bounces, due mainly to the high angular momentum. An emergency strategy (not shown in figure 4.8) was needed in order to restore the aligned position of the TM, by approaching one of the plunger and push the TM in order to make it move again in the housing; finally, the actuation was commanded and the capture performed.

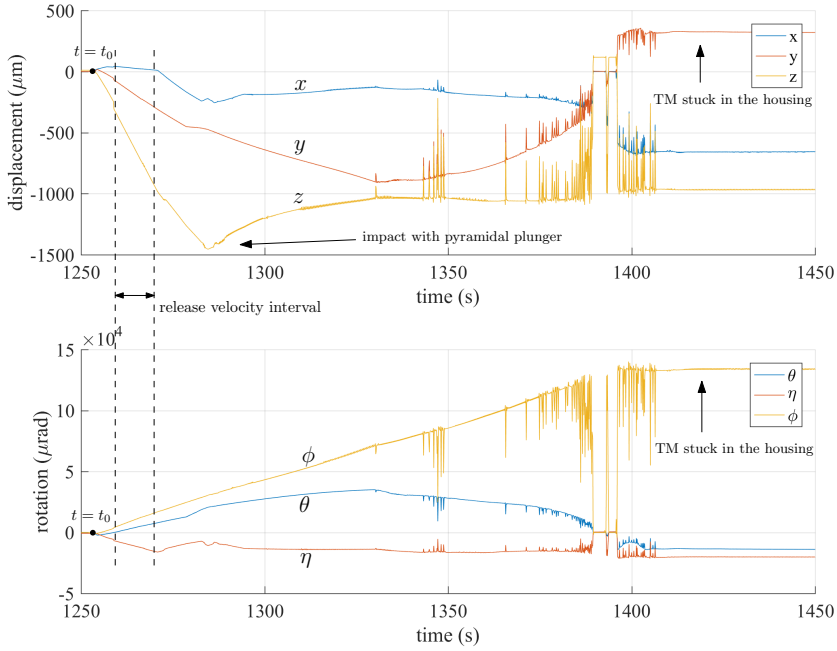

Figure 4.8: capacitive measurement of displacements and rotations of TM1 release (February 16th, 2016). In the picture, we highlight the pin release instant ($t = t_0$), the interval chosen for the computation of the velocities through linear regression, and some inversion of the velocities due to impacts (visualized through a 3D animation). The artefacts in the telemetry are due to contacts between the TM and the housing or the plungers, which make the capacitive measurement read the reference (zero) position.

Other releases and comments

Once both masses were captured and controlled close to the zero position, the two GRS were ready for the science phase, which started on 1st March 2016 and gave the successful results described in section 1.1.2. This means that the non-nominality of the TM releases did not affect the behaviour of the GRS during the science phase.

Further TM releases occurred in May 2016 and October 2016. On the basis of the previous experiences, a different release strategy was planned: starting from the

	$\dot{x}$	$\dot{y}$	$\dot{z}$	$\dot{\theta}$	$\dot{\eta}$	$\dot{\phi}$
velocities	-2.9	-20.3	-56.7	681.3	-797.4	1084.6

Table 4.3: TM1 release (16.02.2016): velocities after plunger retraction (*plunger release velocities*). Linear velocities are in μm/s, rotational velocities in μrad/s. The velocities are computed through a linear regression of displacement and rotation signals (shown in figure 4.8), with a maximum uncertainty of 3 % (standard deviation of computed slope).

nominal blocking condition (extracted pins), the plungers have been retracted with a small commanded displacement, in order to confine the TM motion and reduce its kinetic energy thanks to bounces, prior to the complete plunger retraction and the activation of the capacitive control. The TM motion has shown a non-repeatable behaviour, with low residual momenta for some releases and higher momenta for other releases: in some cases, an emergency strategy similar to the one of TM1 of February 2016 was needed. Moreover, the TM has shown unexpected accelerations, probably related to electrostatic forces due to the ISFEE bias which was not activated.

In conclusion, all the TM releases were quite critical; the nominal release strategy has given unexpected results, and a definitive strategy for a "safe" release was not found. As a consequence, a *TM release campaign* has been planned among the end-of-life activities of 2017; the test campaign has been extremely important for our purposes, since it has given a wide test statistics that can be studied in order to estimate the role of adhesive force in the non-nominality of the release momentum, and investigate the general behaviour of the mechanism.

4.2.2 GPRM identification and release campaign

The failure of the TM releases of February 2016, which were performed according to the nominal strategy described in the previous section, suggested the planning of a dedicated test campaign at the end of the mission.

Several tests with different purposes have been planned in 2017 on June 29 and 30. We can distinguish two groups of tests: *identification tests* and *release tests*.

Identification tests

The identification tests yield important information on the behaviour of the plungers at the release; some of them are further described in section 4.2.3.

The goals of the identification tests performed in June 2017 are the following [112]:

- *characterize the GPRM stiffness vs pin extension.* The GPRM stiffness (and especially the axial stiffness along z axis) is an important parameter which is needed for the tuning of the preload: in a symmetric preload condition, there is a linear relation between the pin extension and the axial preload force depending on the total stiffness of the plungers (given by the series of

the two plungers). Moreover, the stiffness of the plungers can be used for the investigation of the dynamics of the system.

- *detect TM-plunger contact with extended pins.* As explained in the previous section, the high translational and rotational velocities of the TMs at the release suggest that a contact between TM and plunger occurred. In particular, a contact would more likely occur between TM and pyramidal plunger in case of an excessive relative ϕ rotation . In order to detect such a contact, a *hammering* operation is performed. In the hammering operation, the handover to pins (which increases the distance between TM and plunger by extracting the pin and retracting the plunger) is alternated with an opposite procedure, consisting in the retraction of the pin and the extension of the plunger. The multiple repetition of these two alternated steps should contribute to decrease the relative ϕ rotation, by applying impulsive torques on the TM until an alignment is reached.

- *adhesion tests.* Two tests were planned for the investigation of the adhesive force acting between TM and plunger, by measuring the capacitive force needed to detach the TM from a plunger.

- *positioning function investigation.* In one of the planned tests, the TM is grabbed on both sides and moved along the z axis through the synchronous motion of the plungers. Repeatable variations of the TM attitude during the repositioning can yield information about the behaviour of the plungers w.r.t. their extension.

Release tests

The data of the release tests are the main focus of this chapter, and will be analyzed in detail in sections 4.3, 4.4, 4.5.

The release tests of June 2017 can be divided in the following categories [112]:

- *fast pin releases with different conditions.* The releases of February 2016 were performed according to the nominal strategy. As described in section 4.2.1, since the ISFEE plunger bias was not enabled during the release, but was turned on after some seconds, the measurement of the behaviour of the TM immediately after the pin release was not possible. As a consequence, a set of tests has been planned with ISFEE bias enabled during the release, in order to extract information on the TM motion immediately after the pin retraction. Moreover, this family of tests has been divided into specific subsets, in order to test release strategies different than the nominal one:

  - tests with different preloads (0.3 N, 0.2 N, 0.1 N, 0.05 N), in order to investigate the dependency of the release velocity on the preload. The preload can be adjusted by moving the plunger of 1 step ($\approx 1\mu$m); alternatively, a finer preload adjustment can be done by retracting the pin of a smaller displacement ($\approx 0.07\mu$m).
  - tests with nominal preload but lower pin extension. A lower pin extension corresponds to a higher probability of TM-plunger contact.

  - tests with asymmetry of pin extension. The asymmetry between the pin extractions allows to test possible systemic differences of the two plungers.

  Despite the differences w.r.t. the nominal release, all these tests are performed through a quick fall voltage (as in the nominal strategy); from now on, they will be referred to as *fast pin releases*.

- *slow pin releases*. The fast pin releases corresponds to a quick decrement of the preload on the corresponding side of the TM; this can lead to impulsive phenomena like the catapult effect (delay effect described in 1.1.6), or a vibration of the system. On the contrary, a very slow symmetric retraction of the pins corresponds to a slow decrement of the holding force, which minimizes the vibrations of the system and the asymmetry of the pushing forces on the two sides. Moreover, since the velocity of retraction of the pins is lower than 5 μm/s, this dynamics should guarantee a very low release momentum, since during the retraction of the pins the TM is confined between them, thus having no possibility of moving faster than their velocity of retraction.

  In the slow pin releases, when the contact force reaches a null value, only the asymmetry of the adhesive effects should act on the TM. As a consequence, the *slow pin releases* can be analyzed in order to investigate the dependence of the release velocity on the adhesive effect by minimizing the other effects; this analysis must however take into account the very slow velocity of retraction of the pins, which is very different from the nominal release (on which the on-ground predictions of the adhesive effect were based).

- *plunger releases*. In order to investigate the effect of the plungers on the TM release, releases with no pin extension were planned, both symmetrical and unilateral. The results can be compared with the nominal fast pin releases in order to investigate the role of an accidental plunger contact in the nominal release.

A further test strategy, which was originally planned, is the unilateral pin release (nominal situation before the release, but full retraction of one pin only). This procedure, which would have reproduced the unilateral case studied in chapter 2, was unfortunately not possible due to the hardware commanding the pin retractions, which impose a synchronous motion of the two pins with the same velocity.

4.2.3 Identification tests

Here three important identification tests are summarized: GPRM stiffness characterization, positioning function, and adhesive test. These identification tests yield important information for the analysis of the release campaign.

GPRM stiffness characterization

The first operation of the identification campaign is the characterization of the GPRM stiffness. The procedure is sketched in figure 4.9 and consists in the grab-

bing of the TM by the plungers with repeated symmetric extension and retraction of the pins. The extension of the pins increases the holding force depending on the axial stiffness of the plungers, as modeled in the picture.

If the pin is elongated by a quantity Δz, the force is increased from f_0 to $f_0 + \Delta f$. According to the scheme of figure 4.9, the ratio between force and displacement is equal to the equivalent stiffness of the two springs k_1 and k_2 in series:

$$\frac{\Delta f}{\Delta z} = k^{eq} = \frac{k_1 k_2}{k_1 + k_2} \tag{4.1}$$

By following the procedure, only the overall (equivalent) stiffness k_{eq} can be computed, and there is no possibility of distinguishing between the two stiffnesses k_1 and k_2. If we assume the symmetry of the system (due to the fact that Z+ and Z- plungers have the same structure), we get

$$k_1 = k = k_2 \tag{4.2}$$

therefore from equation (4.1) we get for the stiffness of the single plunger:

$$k = 2k^{eq} = 2\frac{\Delta f}{\Delta z} \tag{4.3}$$

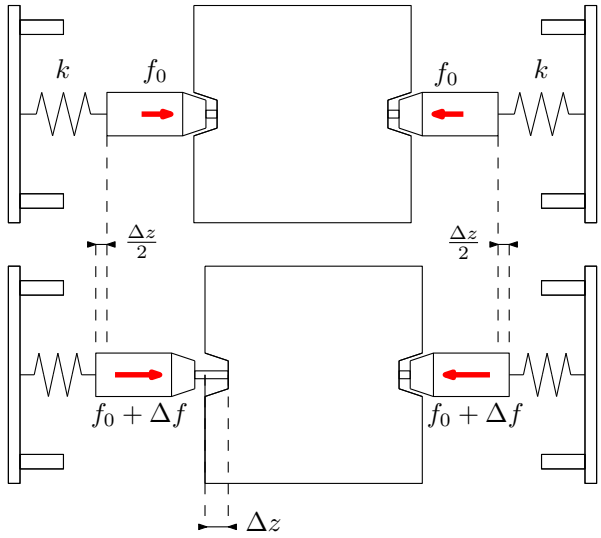

Figure 4.9: model for the estimation of the plunger stiffness (here represented as a spring). The pin of one plunger (left pin in the figure) is extended of a quantity Δ_z; according to the assumption of same stiffness k of the plungers, both the plungers are compressed of a quantity $\Delta z/2$.

In figure 4.10 the output of the GPRM stiffness test for GPRM 1 is shown (the same test is performed for GPRM 2). For each GPRM, the Z- pin is first

slowly retracted, with small displacement steps, then extended; the operation is then repeated for Z+ pin. During each retraction / extension, the ratio between the force slope and the pin displacement slope allows to estimate the equivalent stiffness of the system. The estimated average equivalent stiffness for each GPRM is

$$k^{eq,GPRM_1} \approx 0.19 \frac{\mathrm{N}}{\mu\mathrm{m}} \pm 10\% \tag{4.4}$$

$$k^{eq,GPRM_2} \approx 0.18 \frac{\mathrm{N}}{\mu\mathrm{m}} \pm 10\% \tag{4.5}$$

therefore, according to equation (4.3) we get for a single plunger:

$$k^{GPRM_1} \approx 0.38 \frac{\mathrm{N}}{\mu\mathrm{m}} \pm 10\% \tag{4.6}$$

$$k^{GPRM_2} \approx 0.36 \frac{\mathrm{N}}{\mu\mathrm{m}} \pm 10\% \tag{4.7}$$

It is possible to see in figure 4.10 that a retraction of few micron ($\approx 2\mu$m) makes the preload reach the null value; the further retraction of the pin does not have any effect on the preload, since the pin detaches from the TM.

Positioning function

The positioning test consists in the analysis of the TM attitude when it is grabbed in different positions along the z axis.

The TM is initially grabbed in a position z_1. Then the conical plunger is slowly retracted and the pyramidal one slowly extended, thus moving the TM along the positive direction of z axis, reaching a $z_2 > z_1$ position. The procedure is then repeated, with a finite number of z_i positions. Once a positive z limit is reached, the experiment is repeated in the opposite direction, by retracting the pyramidal plunger and extracting the conical one.

For every z_i position of the TM, the TM is blocked by the plungers, thus showing no motion. As a consequence, its position and orientation can be measured, and a map for every degree of freedom can be drawn as a function of z. Nominally, the functions should be constant for every DOF different than z; if this does not occur, the plungers are giving to the TM a different configuration depending on their extension.

The test shows that many degrees of freedom have a behaviour that differs significantly from the constancy. The more interesting result is shown in figure 4.11, where the positioning function of η angle is shown: a *bistability* of the plungers η orientation can be seen. If we look for instance at the $\eta(z)$ function, we notice that the η distribution for a positive direction of the TM motion is different than the η distribution when the TM moves in the opposite direction.

The results suggest a *hysteresis* of the plunger orientation, as schematized in figure 4.12. This behaviour of the plungers has been detected also for previous copies of the mechanism [53] [54]. An inversion of the motion of the plunger seems

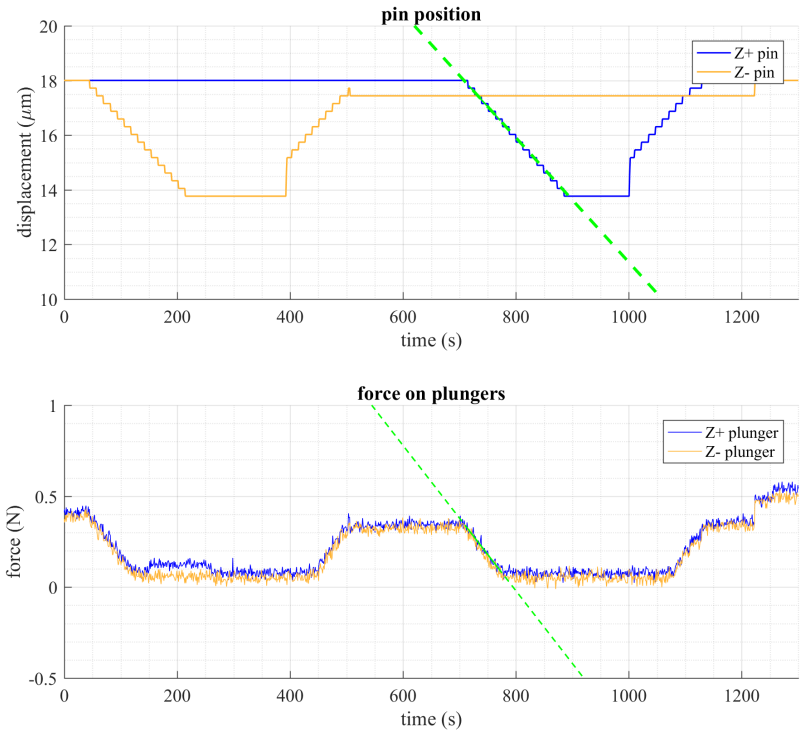

Figure 4.10: GPRM stiffness test for GPRM 1. The green lines correspond to linear interpolations; the ratio of the slopes yields the estimated GPRM stiffness in the interval. It's possible to see that (in the interpolation intervaò) the zero offset of the force is reached before the end of the pin retraction: this means that the pin is detaching from the TM.

to lead to a different orientation; once a plunger has been extended, a commanded retraction could lead to a transversal motion of the plunger ends, with "kicks" (i.e. transversal impulses) that could be in principle given to the TM [44]. For the plungers, this behaviour could be attributed to a mechanical play of the rolling guide of the plunger, which lies in the xz plane (thus affecting the η angle of figure 4.11).

This observation is particularly important for the investigation of the behaviour of the system at the release. In the nominal procedure, the plungers move towards the centre of the housing in order to grab the TM, and then move backwards two times: a small retraction is commanded at the handover to pins, and a quick and wide retraction is commanded after the pin release. As a consequence, we expect that a transversal motion of the plungers can be a motivation of the high transversal velocities and rotation observed in the releases of 2016 (section 4.2.1)

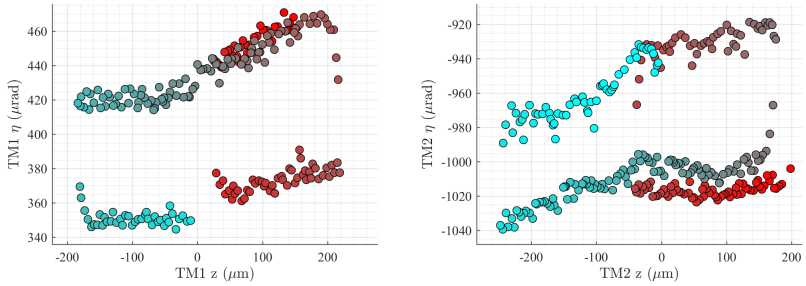

Figure 4.11: plunger bistability: hysteresis for η orientation of the plungers of GPRM1 (left) and GPRM2 (right). For each plot, the variation of the colour of the points (from cyan to red) corresponds to the sequence of the commanded z positions. Courtesy of Davide Vignotto.

as well as in the tests of the release campaign (described in section 4.3).

Adhesive test

As described in section 4.2.2, the adhesive test consists in the estimation of the maximum adhesive force acting between TM and one plunger, by measuring the actuation needed for the rupture of the adhesive bonds.

The test procedure consists of the following steps (represented in figure 4.13), which are applied synchronously to both masses:

1. the TM is grabbed close to the z zero reference.
2. the ISFEE plunger bias is switched on, in order to minimize the electrostatical forces between plunger and TM.
3. the electrostatic actuation is applied in positive z direction.
4. the plungers are retracted. As a consequence, the TM settles on the Z+ plunger as an effect of the electrostatic actuation.
5. the actuation force is decreased with a ramp until it is applied of the same value in the opposite direction, then it is kept constant for 60 seconds.

The test is repeated two times for each TM. According to the ESOC results [112], for both runs, both TMs have detached from the plunger with an actuation force lower than 5.2 μN (f_{lim} in the scheme of figure 4.13), i.e. the maximum detachment force measured in this run of tests was 5.2 μN. Since the pin was not extracted, the TM has been in contact with the coupling surfaces of the plungers. Therefore, the measured force value corresponds to the force required for the rupture of the adhesive bond between TM and plungers.

This test proves that the adhesion between TM and plunger is not critical; however, this is not a measurement of the TM-pin adhesive force. In the adhesive test, the TM rests on the plunger; the preload is not applied through a compression

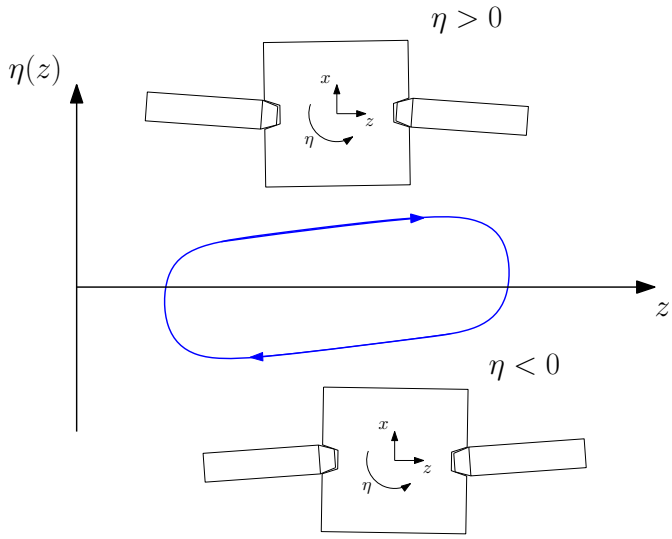

Figure 4.12: hysteresis of the positioning function (scheme related to figure 4.11). Depending on the direction of the motion, the plungers have a different orientation, thus leading to a different orientation of the grabbed TM.

of the plunger like in the nominal case; moreover, there is no possibility of knowing the extension of the adhesive contact surface between TM and plunger (which in principle influences the adhesive contact force). In the following, we will consider the result of this test as a reference for the possible adhesive contact forces between TM and plunger.

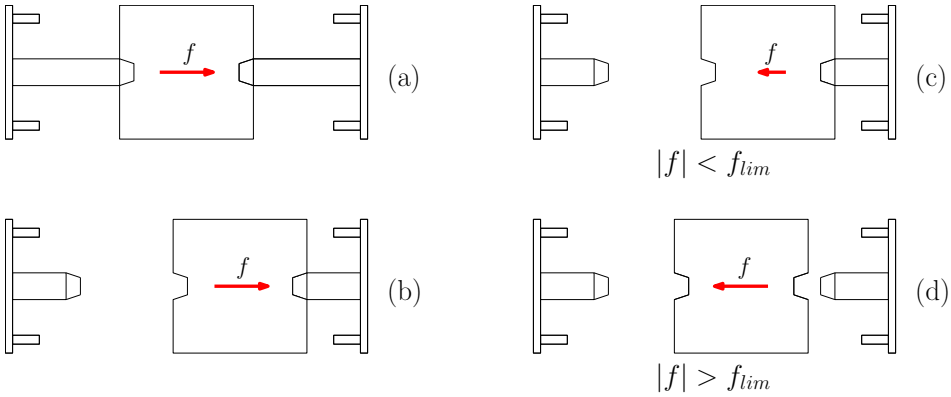

Figure 4.13: principle of the adhesive test procedure. a) TM grabbed and electrostatic force directed rightwards. b) plungers retracted: the TM rests on the right plunger due to the actuation force. c) reversion of the electrostatic force: the TM rests on the plunger until the adhesive force is greater than the actuation force. d) the TM detaches from the plunger when the electrostatic force exceeds a limit.

4.3 Release campaign and plunger release velocities

As described in section 4.2.2, due to the high criticality of the releases of February 2016, a *release test campaign* was planned (together with the identification campaign summarized in section 4.2.3) in order to analyse the behaviour of the GPRM at the release.

The goal of the release test campaign is the investigation of different release strategies, summarized in section 4.3.1. As anticipated, they can be generally classified in *fast pin* releases, *slow pin* releases and *plunger* releases; but each group can be further divided into different sub-groups according to the release parameters.

For each release test, the release velocities (reported in details in appendix C.6) and their compliance with the requirements are commented in section 4.3.2. In this section we summarize the results of the release test campaign of June 2017 and the additional *automatic release* campaign of July 2017.

Notably, all the velocities analyzed in this section are *plunger release velocities*. The plunger release velocity is the most important TM momentum at the release: the capacitive actuation is activated some seconds after the retraction of the plungers, therefore the capacitive actuation must face the plunger release velocity. The criticality of the plunger release momentum w.r.t. the capacitive control authority is indeed briefly discussed in section 4.3.3.

We will see that the (general) non-compliance of the plunger release velocities with the requirements suggests the additional analysis of the pin release velocities (sections 4.4 and 4.5).

4.3.1 Test classifications and release strategies

The list of the releases is reported in appendix C.6 in chronological sequence. The CVM is not involved in the operations. Each test starts with the TM grabbed by the plungers; the TM is then released and its velocity measured; finally, the TM is regrabbed. This allows to complete each test in a maximum time, according to the test schedule. Moreover, each test is done by performing synchronously the same operations on both the TMs: this means that TM release, actuation and TM regrabbing are performed for both the GRS at the same time.

Differently than the cases of February 2016 (section 4.2), the ISFEE bias is activated before the release. This allows to minimize the distortion due to the capacitive effect (section 4.1.3).

Release strategies

The complete description of the release strategy of each test is reported in appendix C.6, by classifying each test according to some release parameters. In the following, we summarize the release strategies by collecting similar strategies in a unique family.

For reasons of clarity, we can divide the tests into the following families (a letter is assigned to each family):

- *fast pin releases*, with a quick retraction of the pins thanks to the inverse-step voltage fall of the pin piezo. They include:
  - *nominal releases* (N). Symmetric pin release with full pin extraction (18 μm nominally) and full pin retraction.
  - *quasi nominal releases*. They differ from the nominal releases because of the not full extraction (a nominal extraction of 17 μm instead of 18 μm).
  - *reduced pin releases* (R). They differ from the nominal releases because of the not full extraction of at least one pin (15 μm or 12 μm). They can be symmetrical (if the extracted length is the same for the two sides) or asymmetrical.
- *slow pin releases* (S). Symmetric releases with slow and partial symmetrical pin retraction (from 18 μm to 15 or 12 μm). The velocity of the pin retraction is ≈ 2.5 μm/s.
- *plunger releases* (P). Releases performed by grabbing the TM with plungers and retracting one plunger or both plungers; the pins are not extracted.

For the tests performed through a pin retraction (N, R, S), the commanded motion of the pin is represented in figure 4.14.

In the following, and especially in sections 4.3.2 and in chapter 4.5, we will comment the tests as part of the macro-groups N, R, S, and P. The quasi-nominal releases will be considered as part of the nominal releases N, for two reasons: because of the very little difference w.r.t. the nominal releases (pin extraction

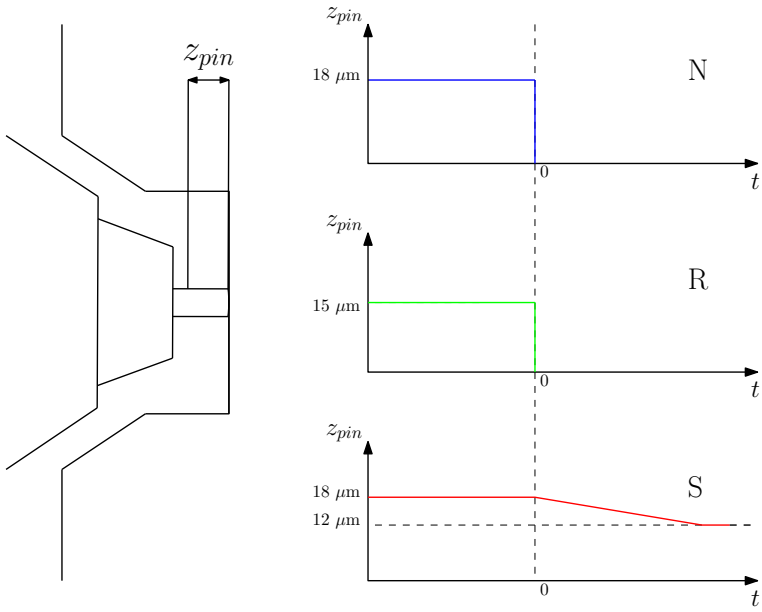

Figure 4.14: commanded extraction z_{pin} of the pin for different release strategies (examples). The pin release occurs at time $t = 0$. N: *nominal pin release*. R: *reduced pin release* (the extracted length is reduced before the release). S: *slow pin release*. Due to the fast pin retraction (inverse step of voltage), N and R compose the group of *fast pin releases*.

reduced of 1 μm) and because of the resulting motion, which can be generally compared to the one obtained with the nominal releases.

We remind that (as described in 4.2.2) a group of fast pin tests has been performed with different preloads (i.e. different holding forces of the plungers on the TM). We report in the table of appendix C.6 the measured preload (which is different from the commanded one, see section 4.4.2). The effect of the preloads on the releases will be further analyzed in section 4.5.2.

4.3.2 Results: plunger release velocities

For each test, the release momentum of each DOF is computed, similarly to the cases of February 2016 (section 4.2): a linear interpolation of the signal after the pin release yields the estimated release velocity (as we will discuss in section 4.4.2).

General results of June 2017

All the different release strategies have been tested at the end of June 2017 (June 29-30). The results are summarized through a histogram in figure 4.15: for each TM and for each macro-group, the distribution of the total linear momentum p at

the release is shown. The total linear momentum p is given by

$$p = |\vec{p}| = M\sqrt{v_x^2 + v_y^2 + v_z^2} \tag{4.8}$$

where v_x, v_y and v_z are the linear release velocities (plunger release velocities) and M is the mass of the TM (≈ 1.93 kg).

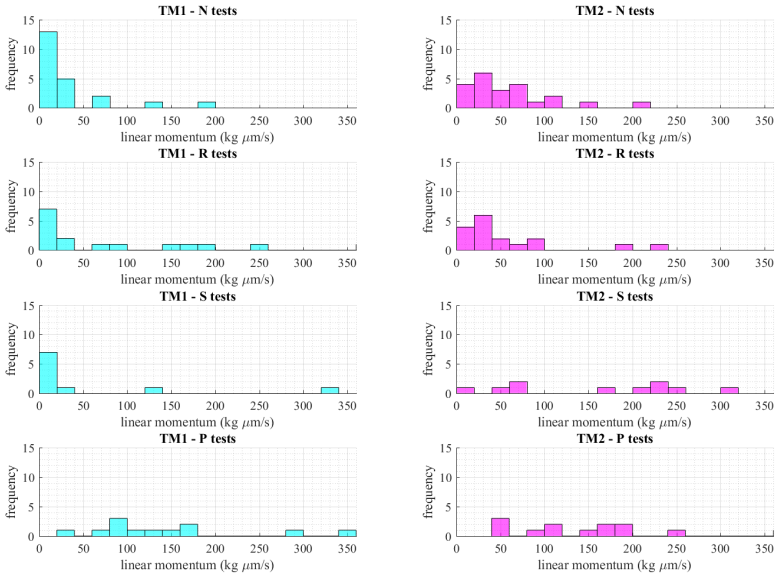

Figure 4.15: tests of June 2017: distribution of the *plunger release momentum* for each family of tests (N = nominal, R = reduced pin, S = slow pin, P = plunger). For each histogram, a test satisfying the requirements for translation belongs to the first bin (but not all the tests in the first bin are compliant).

According to what discussed in sections 1.1.4 and 4.1.3, the requirement for a linear DOF is a velocity lower than 5 μm/s. As a consequence, a test satisfying the requirement for translation has a total linear velocity lower than $\sqrt{3} \cdot 5 \approx 8.7$ μm/s, and therefore a total linear momentum p lower than 15 kg μm/s (thus belonging to the first bin of the histogram of figure 4.15). Notice that the converse does not hold: a test with momentum lower than 15 kg μm/s could be out of the requirement (for example if a momentum equal to 13 kg μm/s is directed along a single direction.)

We remark that the linear release momentum is not exhaustive in describing the behaviour of the TM at the release: theoretically, a test can give linear velocities compliant with the requirements, but angular velocities out of the limits. For this reason, we report for each group of test the percentage of *compliant tests* in table 4.4.

	TM1	TM2
N tests	3/22	1/22
R tests	0/17	0/17
S tests	6/10	0/10
P tests	0/13	0/13

Table 4.4: release tests of June 2017, plunger release velocities. Percentage of compliant releases for each group (N = nominal, R = reduced pin, S = slow pin, P = plunger).

By observing the results reported in figure 4.15 and in table 4.4, the following can be said:

- all the fast pin releases (i.e. N and R groups, see section 4.3.1) have shown a high measured momentum after the plunger retraction. The number of compliant tests is very small for both the TMs, although (as the histograms show) the momentum at the release is significantly lower for TM1, with many tests characterized by $p < 20$ kg μm/s. The distributions show no significant differences between the two strategies N and R: the main difference consists in the absence of compliant tests for R strategy.

- for the fast pin releases N and R, by looking at the complete results reported in appendix C.6 we notice for the non-compliant tests high velocities along x and y directions and high θ and η rotations. A detailed analysis of the signal shows impacts of the TM with the plungers after the release. This behaviour reproduces what occurred in the releases of February 2016 and highlights a completely non-nominal behaviour (the release cannot be described monodimensionally).

- a different situation is observed for the slow pin releases (S). For TM1, the majority of these releases yield velocities in the requirements, with a very low translational momentum. For TM2, an opposite situation is shown: the velocities are out of the requirements, with release momenta even higher than the fast pin case.

- the plunger release is the worst release strategy, with no test satisfying the requirements (for both TMs) and very high momenta. This suggests an important role of the plungers on the final release momentum: we suspect that, also for the tests occurred through a pin release (N, R, S), the commanded motion of the plunger can have a detrimental effect on the final momentum. Moreover, the plunger releases show very high ϕ rotations, thus suggesting an important effect of the pyramidal plunger (see appendix C.3).

Additional test campaign: automatic releases

Based on the results of the first run of tests, an additional test campaign was planned for July 2017. The releases are performed according to two alternated

strategies: nominal fast pin release N (full pin extraction, quick and full retraction), and slow pin releases S (full pin extraction, slow and partial retraction). These two strategies gave indeed the best results in the release campaign of June 2017, as described in the previous paragraph.

Differently than the campaign of June 2017, the tests have been performed through an automatic procedure, with a release commanded every 30 minutes: we will therefore refer to this new set as *automatic releases*. Moreover, for the new run of tests the capacitive control is enabled before the regrab, in order to investigate the performance of the capturing system; the performance of the capacitive control is briefly commented in section 4.3.3.

The results of the automatic tests (shown in figure 4.16) differ significantly among the two GRS.

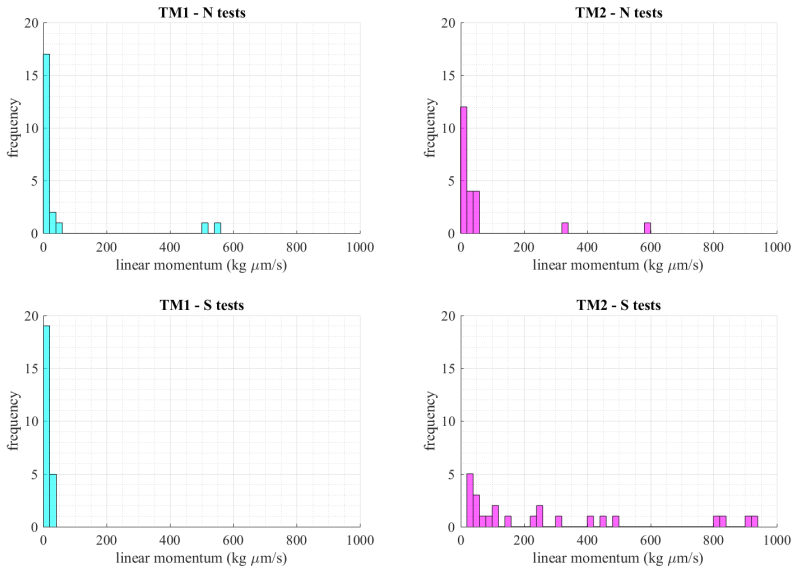

Figure 4.16: automatic tests of July 2017: distribution of the *plunger release momentum* for each family of tests (N = nominal, S = slow pin). For each histogram, a test satisfying the requirements for translation belongs to the first bin (but not all the tests in the first bin are compliant).

For TM1, the percentage of compliant tests has been (as reported in table 4.5) approximately 41% for fast pin releases and 54% for slow pin releases. The slow pin releases have shown in general low release momenta.

For TM2, only few fast pin tests have shown low velocities (although not fully compliant). The more interesting result (which confirms the results of June 2017) is the complete failure of the slow pin releases for TM2, which led to the highest measured momenta.

	TM1	TM2
N tests	9/22	0/22
S tests	13/24	0/24

Table 4.5: automatic tests of July 2017, plunger release velocities. Percentage of compliant releases for each group (N = nominal, S = slow pin).

Overview

The campaigns of June and July 2017 gave important results on the behaviour of the TM at the release. In particular, the plunger release momenta were analyzed. We can summarize the results of the two release campaigns as follows:

- a higher percentage of compliant tests is observed for TM1. This holds in particular for the automatic releases. As a consequence, since for each release the commanded operations were the same for both the TMs, we suspect a *systemic difference* between the two GRS.
- the change of the pin extraction length in the fast pin releases does not affect significantly the results in general (i.e. we do not notice great differences between N and R tests).
- the slow pin releases lead to contradictory results: low velocities for TM1, very high velocities for TM2 (this holds especially for the automatic releases). As observed in section 4.2.2, for this category of tests we expect low *pin release velocities*, due to the low retraction of the pins that should confine the TM motion. If, as we have seen, the *plunger release velocities* of the same tests are completely out of the requirement, we suspect a fundamental role of the plunger retraction in transferring momentum to the mass.
- the effect of the plungers on the final release velocity is also suggested by the very high release velocities of the plunger tests. The transversal motion of the plungers at their retraction (see the comments in section 4.2.3) could be an important motivation for the measured high momenta of the plunger release velocities of the test campaign: if at the release the TM moves towards a plunger and remains close to the plunger when it retracts, high impulses can be given to the TM by the transversal motion of the plunger.

The observations suggest that a more detailed analysis of the release signal is necessary in order to distinguish between residual momentum before and after the plunger retraction; in other words, we want to extract the *pin release velocities* in order to understand if the TM momentum is critical also before the plunger retraction. This is discussed in the next sections.

4.3.3 Capacitive control performance

As described in section 4.3.2, in the automatic tests the capacitive control was enabled in order to recapture the TM and test the performance of the control.

In the following, we discuss briefly the results for the capacitive control in the automatic tests.

It has to be remarked that the performance of the capacitive control, although of high importance for the GRS, is not the object of this work: here we want simply to track the ability of the capacitive control to capture the TM as a function of the TM release momentum, in order to understand the criticality of the high measured momenta of the release campaign. This is done in this section since the capacitive actuation is activated after the retraction of the plunger: as a consequence, the capacitive acutation has to compensate the plunger release momentum, whose distribution has been previously described.

We report here the analyses of ESOC [112].

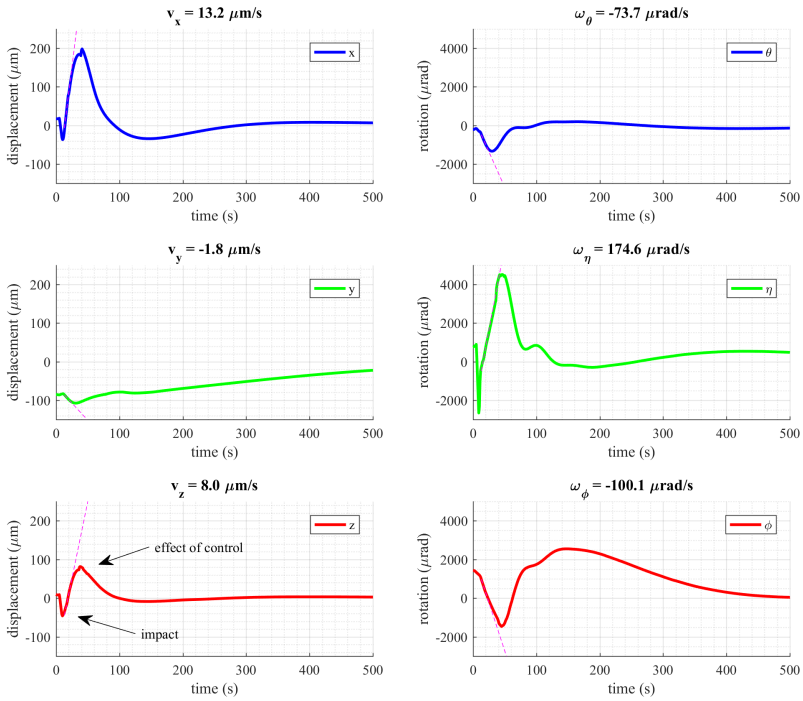

Figure 4.17: test 104, TM1 (slow pin release): effect of capacitive control on the motion of the TM. The capacitive control is able to take back the TM to the 0 position after a first bounce of the TM with the plungers. The origin of time axis correponds to the start of the release; the reported velocities correspond to the slopes of the dashed lines.

When the TM moves with the velocities in the requirements, the control is generally successful; a successful control can occur also with velocities exceeding the requirement of a factor 2. According to [112], the best performance (in terms

	TM1		TM2	
	N	S	N	S
compliancy with requirements	41%	54%	0%	0%
control succesful	91%	100%	78%	43%

Table 4.6: automatic tests: comparison between compliancy of plunger release velocities and success of the control. The control is considered successful if the electrodes are able to centre the TM in the housing, even after some bounces of the TM.

of kinetic energy of the TM at the release) is shown in figure 4.17 (reported in appendix C.6 as test 104, TM1), where the x motion, with a velocity more than two times higher than the requirement, is reversed. However, we see in the figure that the reversion of the velocity due to the capacitive control occurs after an impact of the TM with the pyramidal plunger due to the high momentum at the release.

Higher release velocities lead to a failure in the capture of the TM, not allowing the capacitive control to capture the TM before a bounce (against plungers or the housing) occurs. In this situation, the control has either being successful only after some impacts (which reduce the kinetic energy of the TM), or not able at all to capture the TM, such that the regrabbing was needed to stop the motion of the TM.

In table 4.6 we summarize the ability of the actuation to control the TM attitude after the release: the control is considered successful if the TM is captured independently on the possible impacts occurred between TM and plungers or housing. Since the bounces generally reduce the kinetic energy, the percentage of successful controls is much higher than the percentage of compliant velocities. Despite this, we see for instance for S tests of TM2 that, due to the very high plunger release velocity, the control fails in a half of the cases.

As a consequence, the original requirements are representative of the capacitive control performance: velocities higher than the requirement can difficultly be captured by the control without bounces, and the regrabbing can be required if the velocities are much higher than the requirements. In order to avoid bounces, the release procedure has to be improved or the capacitive control improved (see chapter 5).

The release momentum is therefore a critical quantity for the GRS of LISA Pathfinder; in the following sections, the analysis of the GPRM behaviour will be further analyzed.

4.4 Analysis of the in-flight release data

The plunger release velocities commented in section 4.3 are very important since they describe the TM momentum that the capacitive actuation must compensate. However, they could not correspond to the *pin release velocities*, since (as observed in the previous section) we suspect an important effect of the plungers on the final release velocity.

As explained in the introduction to this chapter, we are interested in studying the motivations of the high release velocities. One of the motivations is the comparison of on-ground predictions (based on a nominal release with unique TM-pin contact) to the completely different in-flight data. For instance, adhesion occurs between TM and pin at the very initial stage of the release, when the pins are retracted and before the plunger retraction, thus affecting the *pin release velocity*. If the effect of the plungers on the final kinetic energy is prevailing, the role of adhesion on the final momentum can be hidden by the plunger effect. On the other hand, if this does not occur a high pin release velocity could be critical for the release.

The plunger release velocity can be easily computed: in general, the retraction of the plungers allows the TM to move linearly for many seconds before eventually impacting with other bodies.

The computation of the pin release velocity is more difficult. Since the plunger retraction occurs approximately 2 seconds after the pin release, 2 seconds are available for the computation of the pin release velocity; being the sampling frequency 10 Hz, this corresponds to approximately 20 samples. Two main problems are related to the analysis of the 10 Hz signal, both due to the low sampling w.r.t. the duration of the observed phenomena:

- the pin retraction occurs in less than 1 ms, therefore much less than the sampling time (0.1 s). As a consequence, the dynamics *during* the pin retraction cannot be captured by the sampling, as well as quick phenomena that can be related with the momentum transferred to the TM (like impacts between TM and plunger due to a reduced gap between them). Only the momentum of the TM *after* the pin retraction can be eventually estimated. This problem is similar to the one of the on-ground testing analysed in chapters 2 and 3, where the information of the adhesive impulse has been extracted from the free flight release velocity.

- if the pin release velocity is very high, since the TM has nominally a maximum displacement in z of 14 μm before impacting with a plunger (nominal gap of section 4.1.2), the number of data samples can be too low for the computation of a slope of the signal in order to detect a velocity.

Information on the pin release momentum can hence be found only through a detailed analysis of the 10 Hz release signal, and the assumptions and the model used for the estimation of the pin release momentum have to be discussed.

We discuss in this section the analysis of the 10 Hz signal. In section 4.4.1 a typical test is described by highlighting in the signals the main instants of the release procedure. In section 4.4.2 the computation of the main quantities related

to each signal is reported. Finally, the detection of the pin release velocity is discussed in section 4.4.3.

4.4.1 Main instants of a single test data set

An example of data set for a single test is shown in figure 4.18. As shown in the figure, each signal is characterized by the following instants:

1. each signal starts with the grab of the TM by the plungers.
2. the TM is repositioned by the plungers.
3. the bias is then switched off in order to perform the handover to pins with a good precision of the applied preload. The pins are extracted and the plunger retracted in order to keep the preload level. In this phase, the position signal is not available.
4. the bias is switched on in order to measure the position of the TM, and the pins are retracted, followed by the plungers.
5. the TM moves due to the momentum transferred by pins or plungers, and it changes its velocity due to impacts or due to the electrostatic actuation. Finally, the plungers regrab the TM.

The regrab, which determines the end of the test, corresponds also to the beginning of the following test.

4.4.2 Detection of the main instants in the data set

In the following, we discuss the detection and the analysis of the main instants and quantities that can be extracted from the signals. The information related to the GPRM (pin and plunger motion, holding force) is extracted from the signals of the Caging Control Unit (CCU), which are sampled at 1 Hz. The information related to the TM motion is extracted from the signals of the Gravitational Reference Sensor (GRS), which allows a 10 Hz sampling of the TM motion.

CCU signals (1 Hz sampling)

For each test, the following instants (which we will refer to in the following) can be recognized in the 1 Hz signal (CCU signal):

- *pin retraction.* The pin extension signal is an indirect measurement: the voltage signal governing the piezo mechanism (see section 1.1.5) is converted into the corresponding pin extension according to the calibration. As a consequence, only the *commanded* pin displacement is available. The pin is generally extracted of 18 μm before the release. We consider the *pin retraction instant* as the last instant before the decrement of the extension (as shown in figure 4.20). As a consequence, since the signal is sampled at 1 Hz, we expect that the real pin retraction has started within one second after the pin retraction instant.

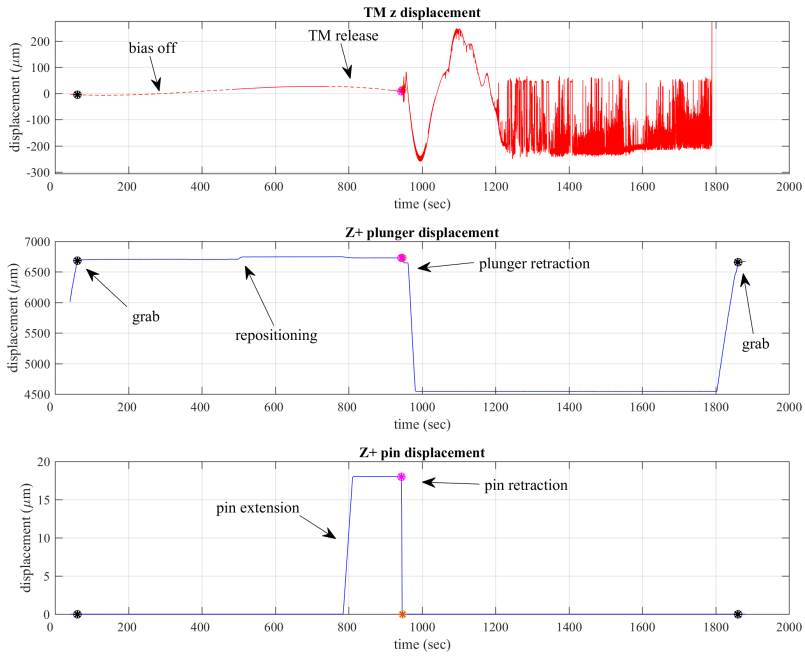

Figure 4.18: main instants of a release (test 89, TM1). In the figure, the 10 Hz z displacement (top), the Z+ plunger extension (centre) and the Z+ pin extension (bottom) are shown. In the example, the bias is switched off two times, for the repositioning of the TM and for the regulation of the holding force at the handover to pins. The z signal is affected by noise from 1200 to 1800 seconds (when the release phenomenon is exhausted).

- *plunger retraction*. A plunger retraction instant is assigned to each plunger (if the retraction occurs). Like for the pin retraction instant, the plunger retraction instant is defined as the last instant of constant value of the plunger displacement signal. Since the plunger signal is a measured signal affected by noise, the detection of the release instant follows an approach similar to the one explained in section 3.1.1 (exit of the signal from a noise band).

- *force intervals*. For each plunger, the measured force is available; once the pin retraction instant is identified, the preload force before the release can be estimated. The force signal is in general affected by a variable offset, therefore the preload at the release can be estimated through the difference of the signal before and after the release. Moreover, due to the high noise of the signal, the preload before the release and after the release have to be computed through the mean of the signal in the chosen interval, as shown in figure 4.19.

As shown in the figure, for each plunger a *mean force before the release* (f_1^P and f_1^M for Z+ and Z- plungers respectively) is estimated with its standard deviation (σ_1^P, σ_1^M). The operation is repeated for the *force after the release*, thus yielding f_2^P, f_2^M and σ_2^P, σ_2^M. The overall force before the preload is given by averaging the corresponding values of the two plungers, thus giving f_1 (with σ_1); the same is repeated for the force after the preload, yielding f_2 and σ_2.

We get the final estimation of the preload by computing the differences (with the associated uncertainty):

$$f^{preload} = f_1 - f_2 \tag{4.9}$$

$$\sigma_f^{preload} = \sqrt{\sigma_1^2 + \sigma_2^2} \tag{4.10}$$

In order to improve the alignment of the TM w.r.t. the plungers, for many test a *hammering* operation (described in section 4.2.2 as an identification test) is performed few seconds before the pin retraction; as a consequence, few instants are available for the estimation of the pre-release force and the estimation is affected by high uncertainty.

Figure 4.19 represents a case with a high preload ($\approx 0.5N$). As reported in the appendix C.6, the estimated preload is quite small for many tests: in this cases, due to the high oscillation of the force signal (≈ 0.1 peak-to-peak), the estimated $f^{preload}$ value can be even lower than its uncertainty $\sigma_f^{preload}$. This means that, in principle, a low estimation of the preload could correspond to a zero preload and therefore to a not-grabbed TM. For some releases, the hypothesis of zero preload is confirmed by a motion in ϕ of the TM before the commanded release. These critical cases (which make the test far different than the nominality) are reported in the appendix.

GRS 10 Hz signal

After the identification of the commanded motion of pin and plunger in the 1 Hz signal, and thanks to the synchronization between CCU and GRS signals, the corresponding samples in the 10 Hz signal (GRS signal) are detected. They allow to identify additional instants and quantities related to the motion of the TM sampled at 10 Hz (as shown in figure 4.20):

- *TM release instant and pin release velocity.* At the pin release instant (detected at 1 Hz), the 10 Hz TM sampling shows in general no motion of the TM. Within 1 second after the pin retraction, we detect a variation in the signal. The TM release instant (shown in figure 4.21) is computed by analysing the z signal (corresponding to the nominal direction of the release phenomenon) and it is considered as the last instant entering the pre-release noise band (following the approach of section 3.1.1; in order to make the release instant detection robust w.r.t. the noise, a 10 σ value for the noise

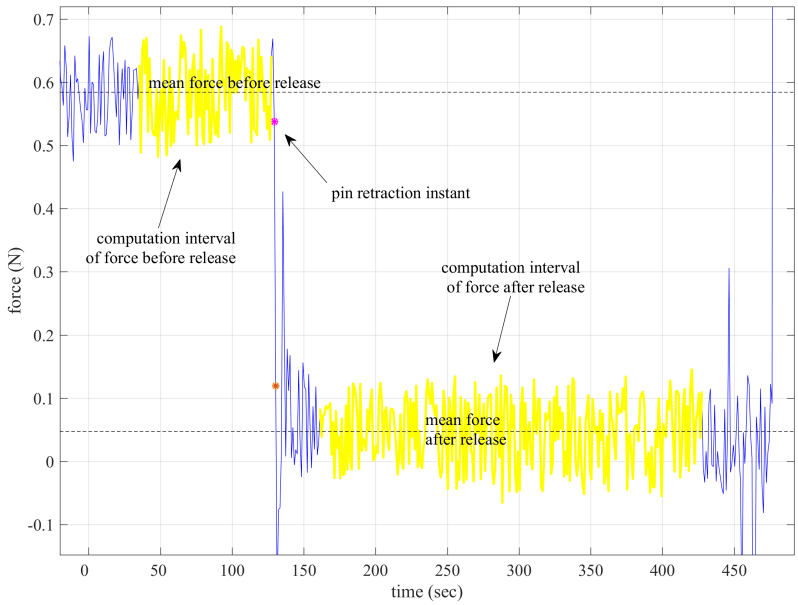

Figure 4.19: Z+ plunger force signal (test 1, TM1). The variation of the force (force drop) estimates the preload force (independently of constant offsets).

band has been chosen). The *pin release velocity* is then computed if the signal after the release can be fitted with a straight line for all the DOF (see the following section 4.4.3).

In few cases (slow pin releases), the algorithm chosen for the detection of the TM release instant detects a variation only after the retraction of the plungers. An analysis of these signals show that the TM motion after the pin release has been too slow in order to detect a significant change in the signal. As a consequence, we impose that the detection of the TM release instant must occur before the plunger retraction; if this does not hold, the pin release momentum is 0 by definition.

- *TM impact.* If the release velocity is detected, when a synchronous and significant change of the velocity is recognized for all the DOF, we recognize an impact of the TM (against the plungers).

- *TM velocity after impact.* If, immediately after the impact, the TM velocity can be again fitted, we compute the velocity after impact. If this is not the case, the velocity after impact is chosen as the first detectable linear behaviour (see section 4.4.3).

- *TM plunger release velocity.* One second after the two plunger retraction instants (detected at 1 Hz), we consider that the plungers are moving. The

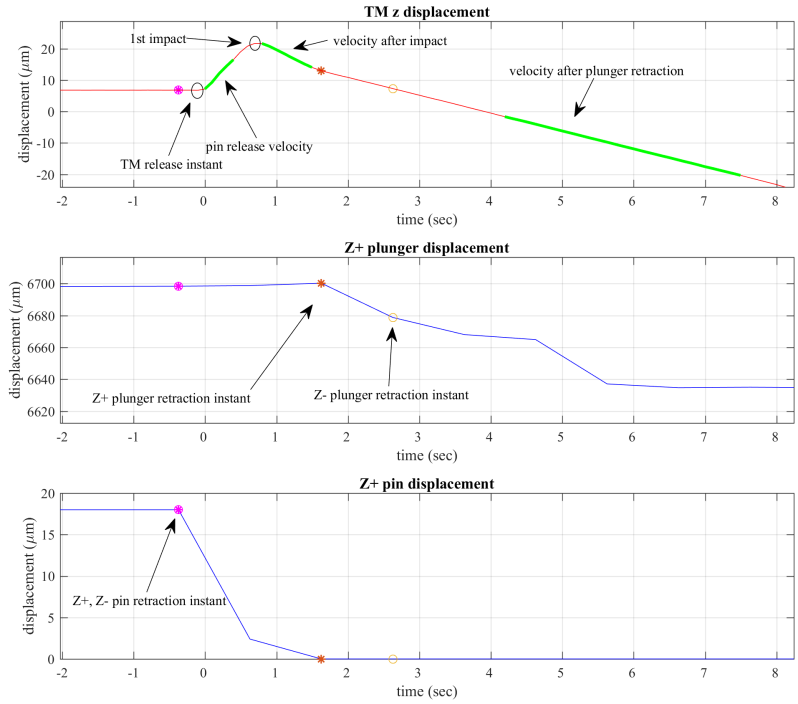

Figure 4.20: main signal instants and intervals (test 97, TM1): 10 Hz z displacement (top), Z- plunger motion at 1 Hz and retraction instant (centre), Z- pin motion at 1 Hz and pin retraction instant (bottom). The time axis is set such that the release occurs at $t = 0$. The variation of the slope of pin retraction is fictitious and due to the low sampling.

first linear behaviour after the plunger retraction has been classified as the *plunger release velocity*. As seen in section 4.3, this velocity is very important for the system since it describes the momentum of the TM when the capacitive control is activated.

4.4.3 Analysis of the pin release velocity

For the computation of the TM velocities, the signal is required to be linear for all the degrees of freedom for a minimum number of points.

If we focus on the pin release velocities, a qualitative estimation reveals that this does not occur in general. For some tests, a linear behaviour can be seen only for some degrees of freedom, while other tests do not show a synchronous linear behaviour for all the DOF. In other cases, a linear synchronous behaviour can be detected, but only for few consecutive points.

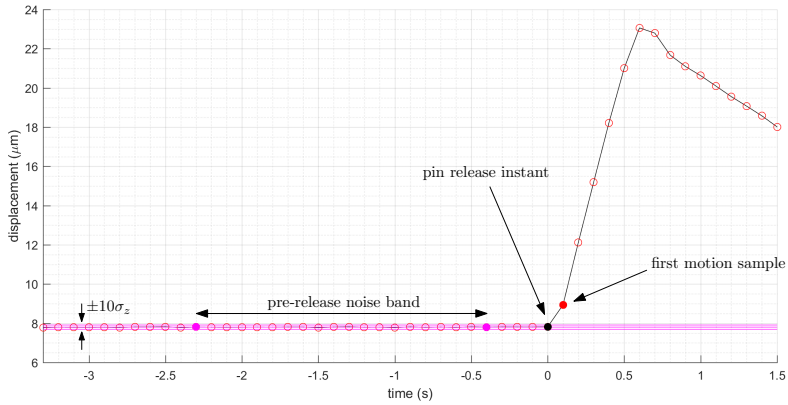

Figure 4.21: detection of the pin release instant, based on the analysis of the z signal. The pin release instant corresponds to the last sample entering the noise band; the first motion sample is the following sample. The real pin release is supposed to occur between the two instants.

Moreover, the possibility of detecting a release velocity is arbitrary, since it depends on the chosen number of samples to be fitted after the pin retraction instant, as well as on the fit conditions.

The method chosen for the analysis of the pin release velocity is based on the linear regression of the first 3 samples after the pin release. We consider these three samples for two purposes: the estimation of the *reliability* of the signal (i.e. the free linear motion of the TM) and the estimation of the *pin release momentum*. For each test, this is done as follows:

- the signals of the 6 DOF are analyzed in order to see if, after the pin retraction instant, each DOF shows (at least) 3 samples on a straight line, based on the expected maximum deviation from the linearity of the third sample w.r.t. the prediction of the first two samples. This is called *reliability test*.

  If the reliability test is satisfied, we can conclude that the 3 samples correspond to the measurement of a *free linear motion* of the TM. As a consequence, a test satisfying the linearity (*reliable test*) is very important for the future considerations of this chapter about the TM dynamics.

- a linear regression is used in order to compute the pin release velocity (with its uncertainty) of each DOF. This is done for all the tests independently on the reliability of the test, in order to have a (eventually rough) estimation of the momentum of every test. However, the estimated velocity of a non-reliable test does not correspond to the linear velocity of a free motion of the TM, therefore dynamical considerations can be difficulty performed in such a case.

Three samples are chosen in order to avoid the trivial situation of two consecutive samples, for which nothing can be said about a possible linear behaviour of

the system between them.

Reliability test

For each test and for each DOF, three consecutive points can be used in order to compute a release velocity through a linear interpolation. However,the computed velocity (the slope of the signal) has a physical sense under the assumption of free motion of the TM in the interval.

Many signals show a significant variation of the slope in the chosen interval of three points: for some DOF (or for all of them), the slope between the first and the second point is significantly different than the slope between the second and the third (see the example of figure 4.24). In this situation, a precise velocity cannot be computed, since we need at least three points on a line to recognize a linear motion.

In general, this is due to impacts between TM and plungers that occur in the first instant after the release (due for instance to the fact that the plungers are very close to the TM, or to high velocity of the TM at the pin release).

In appendix C.1 we report the algorithm that distinguishes the *reliable tests* from the *non-reliable* tests, based on the analysis of the first three samples after the pin release. Figure 4.22 summarizes the principle of the reliability test for a generic signal: the deviation Δ_s between the *measured* third sample $\tilde{s}_3$ and the *predicted* third sample $\hat{s}_3$ is computed, and a kind of hypothesis test is adopted in order to check if the deviation Δ_s can be due to the noise of the signal (null hypothesis) or if alternatively the deviation Δ_s witnesses a real change in the velocity of the signal (such that the tree samples cannot be considered on a straight line). Two different approaches are used:

1. a statistical approach based on the noise of the signal before the pin release. The approach has a rigorous statistical motivation, but leads to the failure of the reliability test for all the tests with high release momentum.

2. in order to avoid the loss of information of the tests with high release momentum, we adopt an empirical method based on the distribution of the deviations Δ_s of some reference tests. Although affected by arbitrariness, this approach allows to consider the reliability of some important tests with high release momentum, which can yield many information on the behaviour of the release mechanism. As discussed in the appendix, this approach is motivated by the presence of additional disturbances that can occur after the pin release.

In appendix C.6, we report for each test the result of the reliability tests. A test is considered *reliable* if it satisfies the reliability test based on the reference distribution (number 2 in the previous list).

Computation of the pin release velocity

For each test, the pin release velocities are computed through a linear regression [92] of the first three points considered in motion. The standard deviation of the

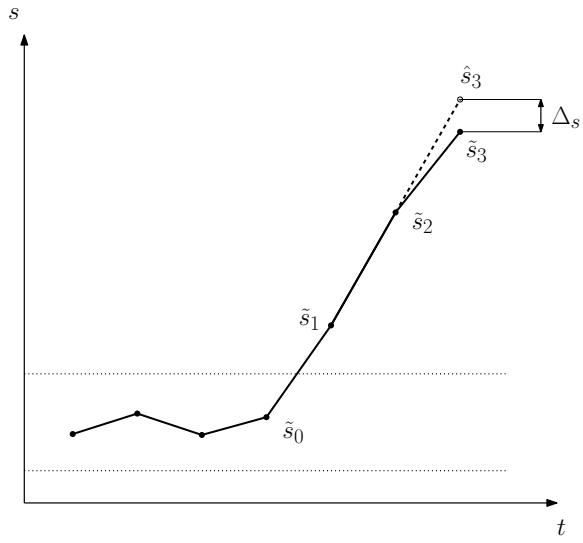

Figure 4.22: reliability test: difference between measured and estimated position of the third sample for a generic signal s. $\tilde{s}_0$ is the TM release instant (last sample considered not in motion) and the three samples considered for the reliability test are $\tilde{s}_1$, $\tilde{s}_2$, $\tilde{s}_3$.

slope is also computed: this allows to consider an uncertainty for all the dynamical quantities (momentum, energy) computed from the velocities.

We remind that in few cases (slow pin releases of TM2) the algorithm does not recognize a TM release instant before the plunger retraction, due to the too slow motion of the TM at the release; in this case the pin release momentum is 0 by definition.

Some reliable tests, for which we assume that the first three samples lie on a straight line, could be further analysed in order to see if also the fourth sample lies on the same straight line, and so on. This would allow to increase the number of samples for the computation of the pin velocity. However, the pin release velocity is computed from the three samples for the sake of uniformity (and for simplicity of the algorithm), since for the majority of the tests the fourth sample would be not considered on the same straight line. We have moreover that the minimum number of points that allows the computation of an uncertainty on the velocity is 3.

For a special set of reliable tests (some fast pin tests), we can extend the number of samples considered for the computation of the velocity, up to 10 points for some release tests; this is done by repeating the algorithm for the detection of the reliability until the detection fails. In general, this would lead to lower uncertainties on the slope of the signal; however, this is not always the case, since the inclusion of samples that barely satisfy the reliability test can lead to a higher uncertainty. When possible, for this set of tests the number of samples has been increased; the difference w.r.t. the 3-points velocity is generally not significant

(as a consequence of the reliability test that guarantees the computation of the velocity in a linear motion). In section 4.7, the main results regarding the non-compliant fast pin test will be considered by computing noth the 3-points velocity and the "extended" one.

In general, the tests that do not satisfy the reliability test are characterized by high velocities. We compute the pin release velocity also for this tests, in order to have an estimation of the release momentum transferred to the TM in these cases (which will be characterized by high uncertainties). Therefore, the computation of the pin release velocity is independent on the result of the reliability test.

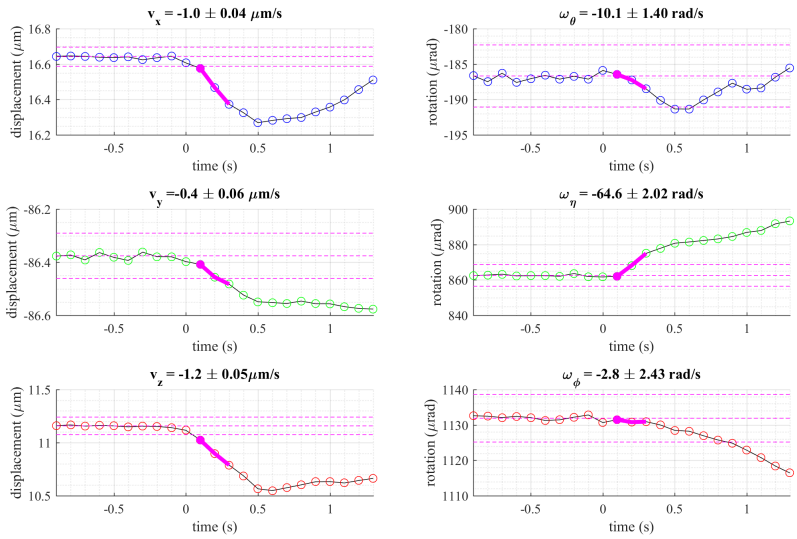

Figure 4.23: example of *reliable test* with low release velocities (test 95, TM 1). The test satisfies both the hypothesis tests discussed in section 4.4.3. All the velocities are inside the requirements (the test is *compliant*). The purple line represents the first sample where the TM is considered in motion along z axis; the purple line represents the three points considered for the computation of the velocity.

Pin release velocities: examples

In figure 4.23, 4.24, 4.25 three examples of test with difference behaviour w.r.t. the hypothesis tests are shown (in each figure, the velocity computed through the fit of the first three samples is reported).

The test of figure 4.23 satisfies the hypothesis test (for every DOF) in both cases (if we consider the pre-release noise distribution or if we consider the distribution based on the reference tests). As a consequence, the first three points can be considered on a straight line and therefore the TM in free flight. This release test is similar to all the ones that satisfy the hypothesis test based on the pre-release

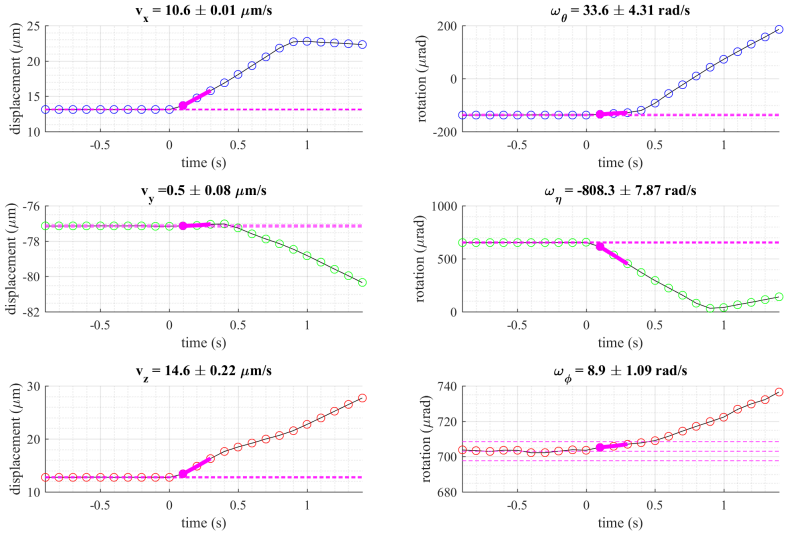

Figure 4.24: example of *reliable test* with high release velocities (tests 14, TM 1). The test satisfies the hypothesis test only if we include the possible distortion due to the capacitance effect. v_x, v_z and ω_η are outside the requirements (the test is *non-compliant*).

noise, with low release velocities (in general inside the requirements).

The test of figure 4.24 satisfies the hypothesis test only if we consider the reference Δ_s distribution (i.e. the reliability test based on the pre-release noise fails). We can see that the velocity is quite high and out of the requirement for many DOF (x, y, η). The reliability test based on the reference distribution allows therefore to consider the reliability for many tests that show high release velocity.

The test of figure 4.25 does not satisfy the hypothesis test (in any case). The release velocity is very high (one order of magnitude more than the requirement for z, η) and the TM shows an impact in z after a displacement of 13 μm (which is close to the nominal gap between TM and plunger after the pin retraction, see section 4.1.2). The first three samples after the TM release sample are not on a straight line mainly due to an important variation of the velocities of x and η DOF (which suggests other impacts between TM and sorroundings).

Velocities after impact

For each test, the computation of the TM velocity after the first impact of the TM with the plungers (figure 4.19) can yield important information about the system behaviour: for instance, we can compute the variation of the kinetic energy after the impact, which should be negative (i.e. energy decrement) in a nominal situation.

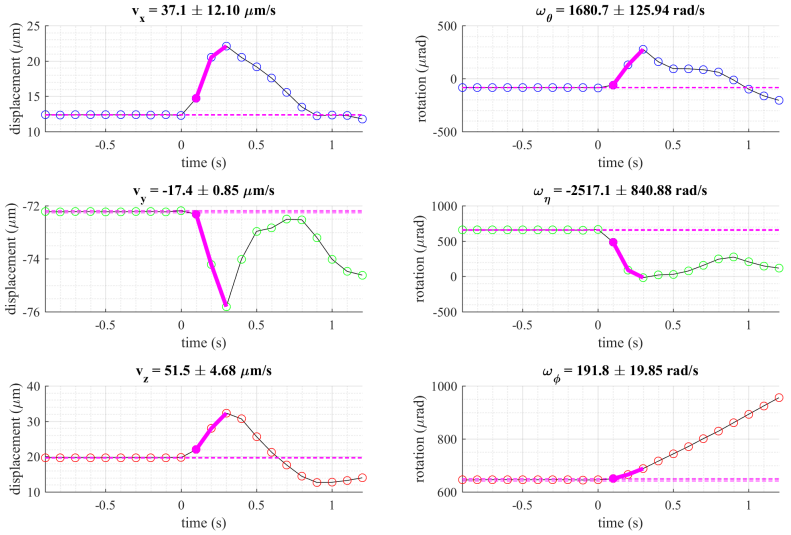

Figure 4.25: example of *non-reliable test* (test 5, TM 1). The test does not satisfy any hypothesis test. The estimated velocities cannot be interpreted as free flight velocities (as one can easily see from x signal).

While the computation of the plunger release velocity is quite easy (after the plunger retraction, we choose a set of samples that lie on the same straight line), the computation of the velocity of the TM *after the first impact* can be very difficult, since the detection of the first impact is often problematic, or it's not easy to find (at least) three points on a straight line also if the first impact is recognized. As a consequence, in the following the momentum after impact is computed through the first set of samples on a line that can be detected in the signals after the first macroscopic variation of the release velocities. This implies that the computed *velocity after impact* could correspond to the velocity of the TM after two or more impacts.

The velocities after impact will be compared to the pin release velocities in section 4.5.4. A more detailed analysis of the bounces between TM and plunger and of the variations of the kinetic energy is planned for the future developments of the work (see chapter 5).

4.5 Pin release velocities in the release campaign

Thanks to the specific data analysis of section 4.4, we are able to describe the momentum of the TM immediately after the pin release (*pin release momentum*). As already discussed in section 4.2 and 4.3, the pin release momentum can yield information on the criticality of the release performed through the pins; moreover, thanks to the comparison with the plunger release momentum (whose estimation is reported in section 4.3.2), it allows to estimate also the criticality of the action of the plungers in the release.

In appendix C.6 the main information of the 10 Hz release signal (figure 4.20) are reported for each test: test parameters, computed preload (with uncertainty), pin release velocities (with uncertainties), TM kinetic energy in the three time intervals (after pin release, after impact, after plunger retraction), reliability properties. The compliance, for each test, of the velocities with the requirements is reported. An additional field corresponds to the maximum z excursion of the mass, i.e. the displacement of the TM along z before an impact (this parameter is computed as the difference between the initial z coordinate and the z coordinate at the inversion of the motion: see for instance figure 4.25 where the impact occurs after a displacement of 13 μm).

In the following, we comment the main results. In section 4.5.1 the pin release momenta are commented based on the total linear momentum (similarly to the case of the plunger release velocities of section 4.3.2); the compliance with the requirements is also commented, by distinguishing the different release strategies. In section 4.5.2 we analyze the relation between the pin release momentum and the measured preload force. All these results are referred to the whole test campaign, independently on the possible reliability (discussed in section 4.4.3).

The specific results and the properties of the reliable tests are summarized in section 4.5.3. In the reliable tests, we can compute the free motion of the TM. As a consequence, the reliable tests will be considered for the dynamical analyses of sections 4.7 and 4.8.

The variation of the pin velocity after impacts and after the retraction of the plungers is discussed in sections 4.5.4 and 4.5.5 respectively. The evolution of the TM velocity in a release test allows to investigate the motivations of the unexpected behaviour of the TM.

Finally, the directions of the release velocities are commented in section 4.5.6; the deviation from the (monodimensional) nominal configuration suggests that a pure pin-TM contact cannot explain the pin release velocities (this hypothesis will be analysed in section 4.6).

4.5.1 Momentum at the release and compliance with the requirements

Here we comment the pin release momentum for all the tests of the release campaign of 2017.

According to the classification of 4.3.1, we consider three main families: N (nominal releases), R (reduced pin releases), S (slow pin releases). We remark that N and R families compose together the group of the *fast pin releases*. In

addition, for each familiy we group together the results of June and July 2017 (which were presented separately in section 4.3.2).

The plunger releases (P) are here not considered since they are performed without the pins (i.e. a pin release velocity does not exist for the plunger releases).

In figure 4.26 and table 4.7 we summarize the pin release linear momentum p and the compliance of the pin release velocity respectively, with the requirements, considering the tests independently on their reliability. We consider indeed that the computed pin release velocity (see section 4.4.3), considered with its uncertainty, is significant also in the case of a non-reliable test. This assumptions is due to the fact that the effect of an impact in a non-reliable test is generally a decrement of the kinetic energy (as we will see in section 4.5.4): as a consequence, the computed momentum for a non-reliable test is generally underestimated. Moreover, we will see in section 4.5.3) that there is a strong correlation between reliability and fulfilment of the requirements, therefore the reliable tests are not representative of the general results of the whole release campaign.

In figure 4.26 a statistics of the overall linear momentum $p = |\vec{p}|$ is shown. The overall linear momentum, defined as in equation (4.8), is an indicator of the criticality of the release w.r.t. the requirements (see the considerations of section 4.3.2). In table 4.7, for each strategy the percentage of tests compliant with the requirement is reported: a test is compliant with the requirements if the linear velocities are lower than 5 μm/s for each DOF (momentum lower than 10 kg μm/s) and the angular velocities are lower than 100 μm/s. The compliance of a DOF is based on the nominal value of the measured velocity. We remark that all the compliant tests belong to the first bin of the histograms of figure 4.26; the first bin of each histogram contains also tests with low release momenta but (nominally) out of the requirements.

	TM1	TM2
N tests	20/44	1/44
R tests	0/17	1/17
S tests	30/34	30/34

Table 4.7: compliance of the pin release velocities: percentage of compliant releases for each group (N = nominal, R = reduced pin, S = slow pin).

Fast pin releases

We can see first of all that, for both TM, the *non-compliant tests* (tests with at least one velocity out of the requirements) are quite uniquely fast pin releases (i.e. they belong to the N or R families). For TM1, the nominal releases (N) satisfy the requirements in many cases, while the reduced pin releases are characterized in general by high velocities; for TM2, the fast pin releases give a high momentum to the mass independently on the N or R strategy.

As can be observed by looking at appendix C.6, for the non-compliant tests, the behaviour is similar to the one of the two examples of figures 4.24 and 4.23:

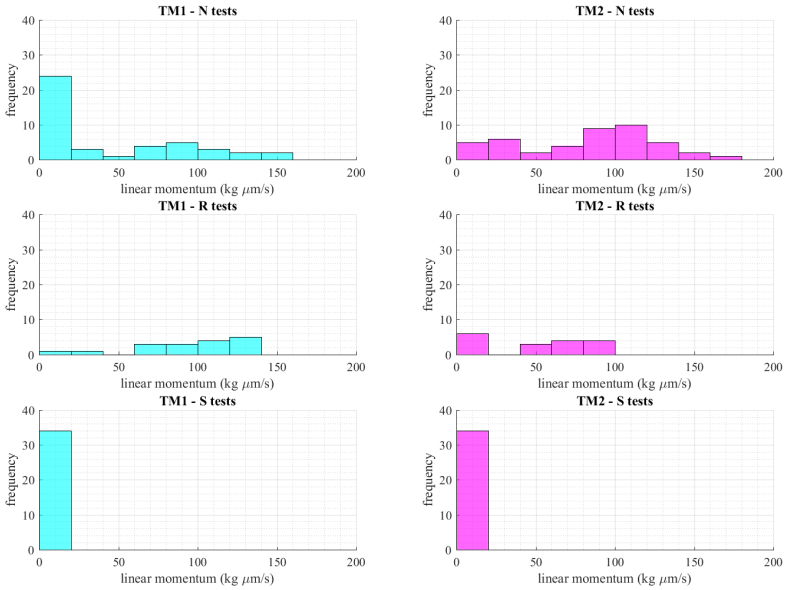

Figure 4.26: distribution of the *pin release linear momentum* in the release campaign of 2017.

high speed for all linear DOF, with higher velocity for z, and high rotations. The velocity for ϕ is generally lower than the other rotational DOF, but sometimes out of the requirements.

This suggests that in the fast pin releases, when the plunger retract, the TM has already a non-compliant momentum, both for translations and rotations. As a consequence, a fast pin release is an extremely critical operation and the motivations of such high velocities at the pin release have to be analyzed (see sections 4.6 and 4.7); the plungers can eventually increase this kinetic energy (see section 4.5.5), but in many cases the non-compliant behaviour of the DOF cannot be attributed exclusively to the plunger behaviour.

Slow pin releases

By looking at figure 4.26 and appendix C.6, we can see that the measured pin release momentum for the slow pin releases is very low for both the TMs. For each TM, 88% of the release tests of S family have pin release velocities compliant with the requirements. For each TM, the 3 non-compliant S tests show only one angular velocities slightly greater than 100 μrad/s (an angular momentum that the capacitive control can compensate, see figure 4.17).

In particular, for all the S tests, all the linear DOF are compliant (and especially z, which is in general the linear DOF with higher velocity). This compliant behaviour is expected, since, as commented in section 4.2.2, the TM is confined

between two pins that retract with a velocity of 2.5 μm/s; as a consequence, we expect for these tests a z linear velocity lower or equal to 2.5 μm/s. This is actually the case, as we will see in detail in section 4.8; in the same section we will also try to extract information on the adhesive pull, based on the observation that the z pin release velocities of the S tests are always lower than the velocity of the pins, thus witnessing a detachment between TM and pins.

The measurement of the pin release velocity is critical since there is uncertainty about the instant of detachment of the pins from the TM; however, in the presence of this kind of uncertainty the velocities reported in the appendix correspond to a worst case estimation (see section 4.8).

For the slow pin releases, the plunger retraction can increase critically the order of magnitude of the kinetic energy of the TM. This is explained by the high plunger release velocities of the S family discussed in section 4.3.2, which are significantly higher that the corresponding pin release velocities. This is particularly critical for TM2. As a consequence, the final velocity with the slow pin release strategy is highly affected by the plunger retraction. This suggests that (as commented in section 4.5.5) the plunger retraction can be a very critical operation of the complete release procedure, since it increases significantly the momentum of the TM also when the pin release (which occurs some seconds before the plunger retraction) is not critical.

4.5.2 Dependence on the preload force

By looking at appendix C.6, we can see that the preload is different from test to test (this is also shown by the dispersion w.r.t. the horizontal axis of figure 4.27, which we comment in the following). For each test a target preload was established, but due to the low reliability of the load cell the actual preload can be quite different from the target one; moreover, for many tests of TM1 the preload is very low (this could be due to the *hammering* procedure performed before the pin release for some tests) and compatible with a null preload according to the uncertainty.

In a nominal release configuration, a high preload can increase the momentum at the release, due mainly to the higher effect of the delay effect (see 1.1.6), to the higher adhesive force in the blocking condition, and to a higher preload of the mechanism that can motivate (for instance) higher vibrations of the plungers.

In figure 4.27 the kinetic energy at the pin release (K_1 in appendix C.6) is plotted versus the preload for the fast pin releases (N and R groups). The kinetic energy is normalized with respect to K_{max}, which is the maximum kinetic energy satisfying the requirements (linear velocities 5 μm/s, angular velocities 100 μrad/s) and is approximately 82 pJ. Due to the high uncertainties of the preload and of the kinetic energy (computed through the error propagation from linear and angular velocities), error bars are shown (corresponding to $\pm 1\sigma$ for each quantity). Each colour corresponds to a specific family of tests.

The preload can be very important for fast pin releases (N and R groups), since the very quick fall of the preload on the pin side can create impulsive forces due to adhesion, delay effect and vibrations of the mechanism. As reported in table C.6 and in figure 4.26, the slow pin releases show a low kinetic energy; however,

the preload for slow pin releases is not significant as for the other groups of tests, since for the S tests the pin release of the TM occurs after the slow decrement of the preload force (see section 4.8). As a consequence, they are not plotted in the figure.

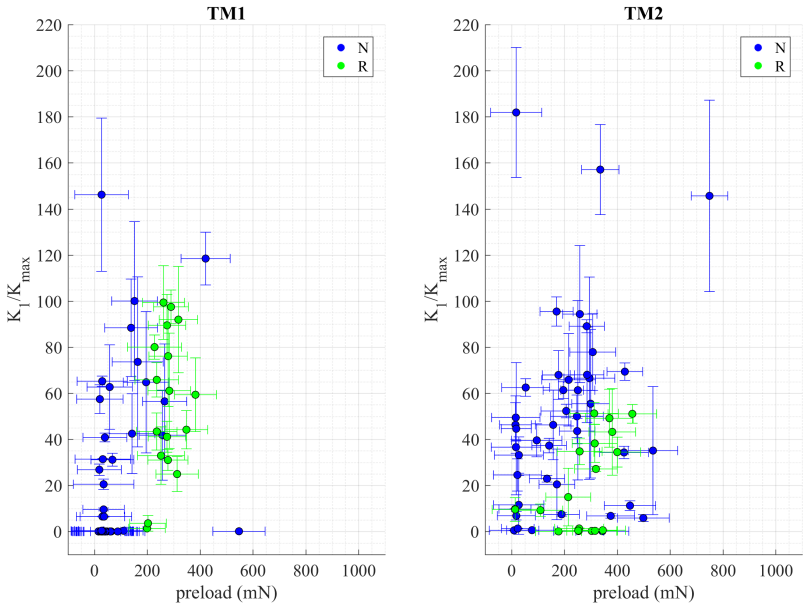

Figure 4.27: relation between measured preload and kinetic energy at the pin release. For each test (point), the $\pm\sigma$ error bars are reported.

If we assume that the kinetic energy at the pin release derives from the elastic energy of the preloaded blocking system, we would expect a dependence of the kinetic energy on the square of the force. No trend of this kind can be seen, and neither a clear linear trend. We see in general that the probability of a higher kinetic energy increases with the preload: this could motivate the higher number of non-compliant tests for TM2, since for TM2 the preload of the automatic tests is generally higher w.r.t. TM1; moreover, the large majority of the R tests could be non-compliant due to the higher preload for this category. However, for both masses many tests show a high kinetic energy also with a low preload (a possible motivation of this fact is given in appendix C.2, on the basis of the model of section 4.7); on the other side, especially for TM2, some R tests have low kinetic energy at the release also with a high preload.

4.5.3 Relation between reliability and momentum

In sections 4.5.1 and 4.5.2 the pin release velocities were commented independently on the reliability, since we assume that the computed velocity can yield information

on the compliance with the requirements also if the test is not reliable.

However, the reliability of a test (section C.1.1) is an important condition if we want to consider the computed velocities of its DOF for dynamical considerations. In order to estimate the impulses applied to the TM, we can write a dynamical model and estimate the inputs (the linear impulse and the torque impulse) from the outputs (the linear and angular momentum); in order to apply this method we require that the velocities are *free flight velocities*, i.e. their estimation is not affected by impacts between TM and plungers. As a consequence, only reliable tests will be considered in the next sections of this chapter (4.6, 4.7, 4.8).

In figure 4.28 we show, for each TM, the release linear momentum of the reliable tests compared to the one of the non-reliable tests (the results of the whole campaign are reported, independently on the release strategy N, R or S).

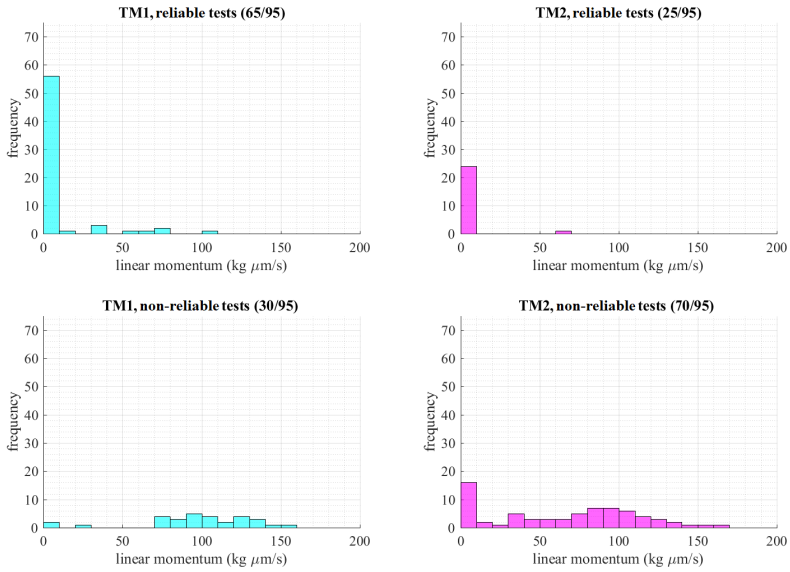

Figure 4.28: pin release linear momentum: classification w.r.t. TM and reliability.

We can see that there is a strong correlation between the linear momentum and the reliability. For TM1, the large majority of the tests in the first bin of the histogram (which contains all the tests satisfying the requirements) are reliable; only a small group of tests with high momentum are reliable. For TM2, the situation is quite different, since we can see that the reliable tests are quite exclusively composed of tests with low velocities; moreover, some tests with low velocities are not reliable.

As expected, the reliability is highly correlated with the transferred momentum at the release. If the release momentum is high, an impact can occur after few samples, thus not allowing a precise estimation of the velocity through a linear fit. If the release momentum is low, the TM moves slowly allowing an easier estimation

of the velocity through a linear fit; this is however not a general rule, as shown by the not reliable tests of TM2.

This kind of dichotomy can be problematic for our purposes. The reliable tests consist mainly in compliant tests; few non-compliant tests are reliable. As observed in appendix C.1.1, the more interesting tests are the non-compliant ones, since they describe the most critical behaviour and constitute therefore a worst case of the release. That's why we included the effect of additional disturbances (as discussed in appendix C.1.2) in the reliability test; if in the reliability test we base only on the statistic of the pre-release noise, we would get that all the non-compliant tests are not reliable (as one can easily see from table C.6), thus losing the most important information for dynamical analyses.

4.5.4 Kinetic energy after impacts

Important information can be extracted from the velocities after impact (see figure 4.20 and section 4.4.3 for its definition).

First, we can have an estimation of the effect of the impact for the TM motion through the *restitution coefficient*, defined as the ratio between kinetic energy after the macroscopic impact (K_2 in appendix C.6) and the pin release kinetic energy (K_1 in appendix C.6). A restitution coefficient lower than 1 suggests that the impacts contribute to the decrement of the release momentum. A restitution coefficient higher than 1 suggests that the plungers are transferring kinetic energy to the TM, through an action of the plungers like a vibration.

In figure 4.29 we plot, for each TM, the dependence of the restitution coefficient K_2/K_1 on K_1. A log-log plot is used since the kinetic energies of the test campaign span of some orders of magnitude. The kinetic energy of the horizontal axis is normalized with respect to K_{max} (maximal kinetic energy compliant with the requirements, see section 4.5.2). Each point of the plot is associated to a test family (N, R, S) according to the colour. We consider here the tests independently on the reliability.

We remind that (similarly to the interpretation of figure 4.26) a test with kinetic energy $K_1 > K_{max}$ is non-compliant, but the converse does not hold.

For TM1 we can see that the restitution coefficient of a test depends on the kinetic energy at the pin release K_1. In particular, if $K_1 > K_{max}$ ($\log > 0$), the effect of the impact is a decrement of the kinetic energy ($\log < 0$). A higher variability occurs for the tests with low velocities: we get the increment of the kinetic energy for some tests (especially for slow pin tests). This increment could be given by a vibration of the plungers after the pin retraction, which confers momentum to the TM at the contact, thus increasing significantly the kinetic energy if its initial value is small. It's important however to remind that, for TM1, a kinetic energy that is lower than K_{max} of one order of magnitude and increases of one order of magnitude remains generally below K_{max}. As a consequence, we can say that for TM1 the impact with the (not yet retracting) plungers does not have a critical effect on the kinetic energy; in addition, the effect is a decrement of the kinetic energy when the kinetic energy at the pin release is out of the requirements.

Again, the situation is different for TM2. We see an increment of the kinetic energy also for high velocities: this would witness the criticality of the impact with

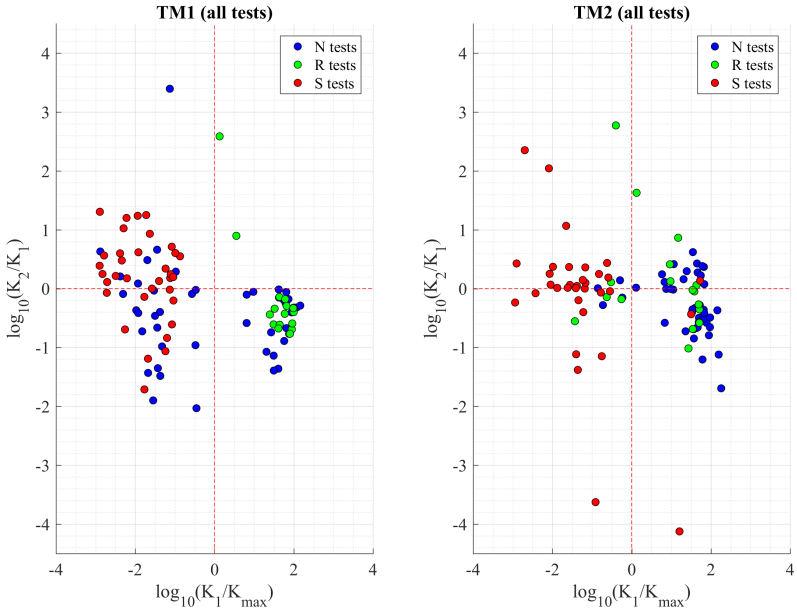

Figure 4.29: log-log plot of the restitution coefficient K_2/K_1 as a function of the normalized kinetic energy at the release K_1/K_{max}. Each point in the plot corresponds to a test. The results of the whole test campaign are shown (independently on the reliability).

the plungers for TM2. However, the high kinetic energies for TM2 are generally based on non-reliable tests with high uncertainties of the pin release velocities (and therefore a high uncertainty of K_1). In figure 4.30 we plot the same result by taking into account only the reliable tests. If we decide to describe the restitution coefficient by trusting only on the reliable test, we see that the consideration made for TM1 are not contradicted by TM2 (simply because all the tests with high velocities disappear for TM2).

The estimation of the restitution coefficient has to be improved due to the low reliability of the velocities of TM2; moreover, we remind that (as described in section 4.4.3) for many tests the velocity after impact could correspond to the velocity after more than one impact, this introducing an irregularity in this computation. The analysis of the energy loss (or increment) after the impact is one issue that will be analysed in the future (see chapter 5).

4.5.5 Kinetic energy variation due to plunger retraction

After the pins are retracted and the TM eventually bounces between the two plungers, the plungers are retracted, and the velocity of the TM after the plunger retraction can be computed (see figure 4.20). The plunger release velocities have

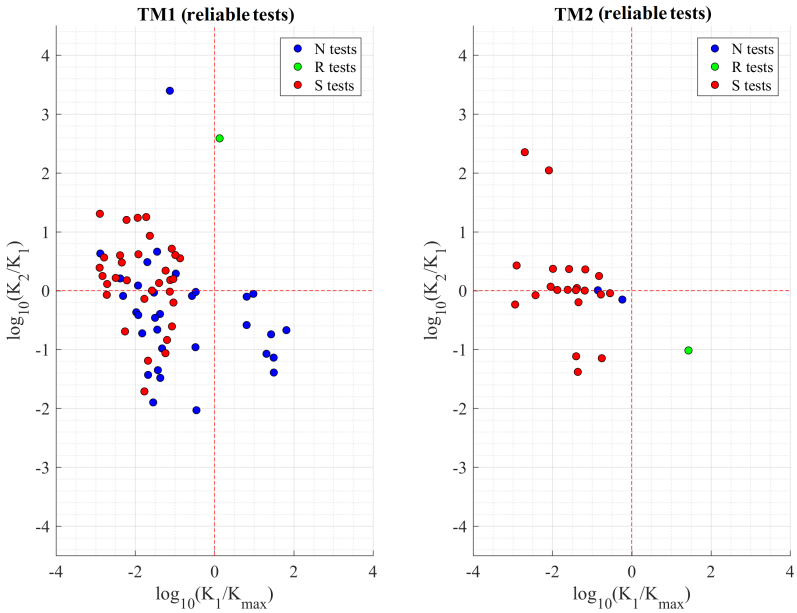

Figure 4.30: restitution coefficient (figure 4.29) of reliable tests only.

already been commented in section 4.3.

In figure 4.31 we show the ratio between kinetic energy after plunger retraction and kinetic energy after pin release (similarly to the plot of figure 4.29). A positive value of $\log_{10}(K_3/K_1)$ implies a growth of the kinetic energy, and a value equal to 2 can be considered equivalent to the increment of the release velocity of one order of magnitude (since the kinetic energy is quadratic w.r.t. velocity).

We can see that the plunger retraction can have a detrimental effect on the final velocity of the TM.

The fast pin tests (N and R) with low values of K_1 (which belong mainly to TM1) can show an increment of the kinetic energy after the plunger retraction; the velocities after the plunger retraction can be higher than the requirements.

The fast pin tests with velocities outside the requirements show generally a decrement of the kinetic energy after the plunger retraction. This means that the kinetic energy at the pin release dominates the additional effect of the plungers.

In figure 4.32 we report the same graph but only for reliable tests. We can see that the previous comments hold also if we restrict to the reliable tests.

As already commented in 4.3.2, the plungers have an important effect for the slow pin releases. This occurs specially for TM2 (as shown in figure 4.33).

The effect of the plunger retraction on the TM kinetic energy seems therefore dependent on the release strategy. A possible explanation is given by the different behaviour of the TM before the plunger retraction. In the fast pin release, the TM bounces between the plungers; in the slow pin releases, the z displacement shows

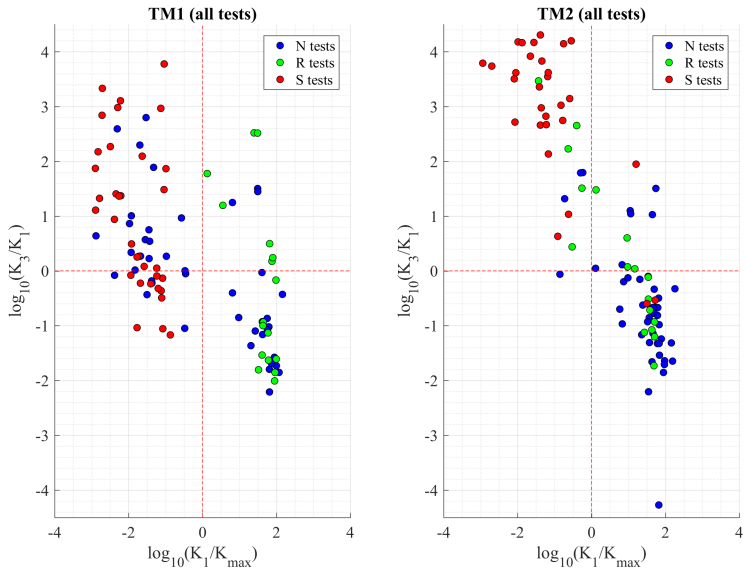

Figure 4.31: log-log plot of the ratio K_3/K_1 as a function of the normalized kinetic energy at the release K_1/K_{max}. Each point in the plot corresponds to a test. The results of the whole test campaign are shown (independently on the reliability).

that the TM rests on one plunger, eventually with rotations (as we will discuss in section 4.8). As a consequence, the probability for the TM to be in contact with the plunger at the plunger retraction highly increases for the slow pin releases; if the commanded plunger retraction produces a transversal motion of the plunger (as commented in section 4.2.3), this leads to an important impulsive effect of the plunger to the TM, thus leading to a behaviour similar to the plunger releases (P tests of section 4.3.2).

4.5.6 Velocity directions and deviation from the nominal pin release

We have seen in section 4.5.1 that the pin release is a critical operation, since many tests show a pin release velocity out of the requirements.

We will focus in the next sections of this chapter on the motivations of this unexpected behaviour of the two GRS. In particular, we want to investigate the role of adhesion in the transferred momentum.

The on-ground tests described in section 1.2 and in chapter 2, as well as the in-flight adhesive test of section 4.2.3, suggested that adhesion should not be critical in a nominal in-flight release. Despite this fact, the high pin release velocities discussed in this section (especially for fast pin tests) suggested a criticality of the pin release operation.

A possible explanation is an underestimation of the adhesive effect in the on-

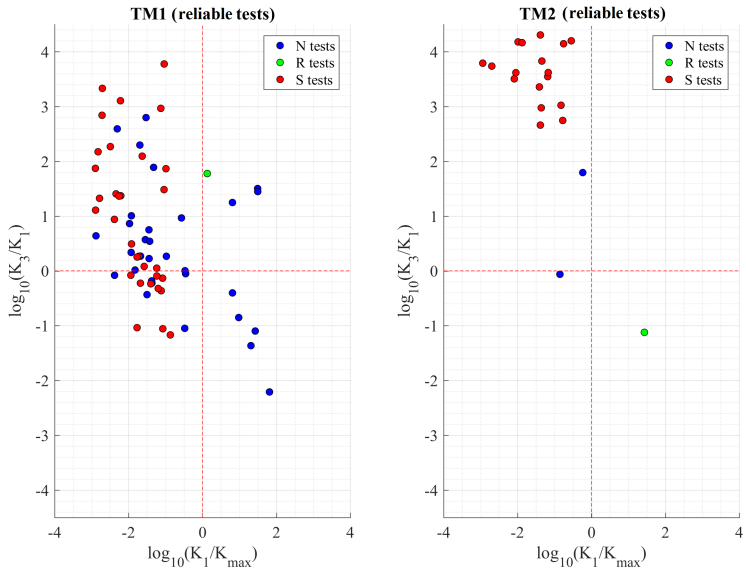

Figure 4.32: K_3/K_1 ratio (figure 4.31) of reliable tests only.

ground tests. Another possible explanation consists in the deviation of the TM release from the nominal release configuration described in section 4.1.2 (which was assumed in the predictions based on the on-ground tests). As described in the following, some evidence suggest the higher probability of the second option.

In a nominal situation, if the test velocity exceeds the requirements, it shows only a high z velocity (or eventually low velocities for the other DOF which can be neglected w.r.t. z). This is not the case for the release test campaign. As observed in section 4.3.2, when a test is out of the requirements, it has not only a high z momentum, but also high x and y translations and important rotations.

In figure 4.34 the release linear velocities for the non-compliant tests of the two TMs are shown, with a vector representing both magnitude and direction of the motion of the TM barycentre. In figure 4.34 left, the tests are considered independently on the reliability (in order to have a visualization for the non-compliant test of TM2, which are generally non-reliable); in figure 4.34 right, only the non-compliant reliable tests are shown.

It can be seen that the group of non-compliant velocities can be divided into two sets, i.e. velocities of TM1 and of TM2, which differ significantly for many aspects. First, the directions are different: TM1 moves in the positive z direction, while TM2 moves generally with negative z velocity. Second, the TM2 velocities show a higher dispersion, in terms of magnitude and direction (this can be due also to the lower reliability of the computation of the high velocities of TM2). As a consequence, we can observe a systemic difference in the two mechanisms; moreover, the releases in TM1 look much more repeatable.

For both the TM, the pin release linear velocities are highly inclined w.r.t. z

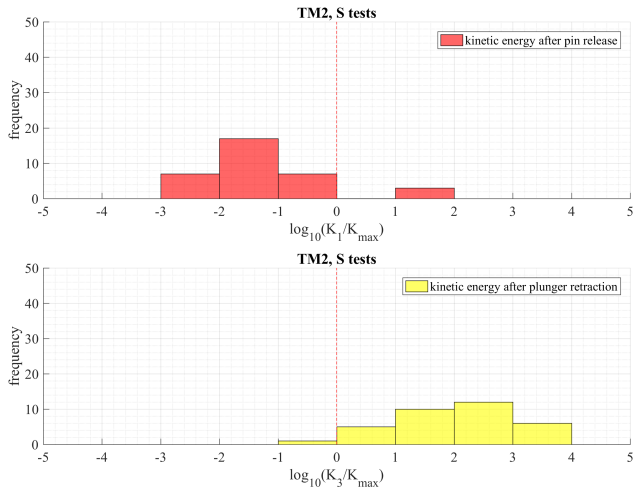

Figure 4.33: slow pin tests of TM2: logarithmic distribution of the normalized kinetic energy K_1/K_{max} at the pin release (top) and logarithmic distribution of the normalized kinetic energy K_3/K_{max} after the plunger retraction (bottom).

axis. For instance, the non-compliant velocities of TM1 have comparable z and x components (i.e. $v_x \approx v_z$), while the y component is lower. This is more evident if we focus only on the reliable tests of TM1. Therefore, some impulses have been given by the plungers to the TM along x and y directions (orthogonally to the plunger axis); this matches also with the high rotations, which can be due only by transversal impulses given to the TM at the pin releases.

This is difficult to explain with a nominal release, where the pins are retracted along z and in contact only with the pins (figure 4.5). In principle, an orthogonal velocity in a pin release with no contacts between TM and plunger can be due to inclinations of the pins, misalignments of the two pin axis, or flexional preloads of the plungers in the blocking configurations. This possibilities will be discussed in section 4.6.

If a nominal pin release (with exclusive contact between TM and pins) cannot explain the measured velocities, the alternative possibility (in absence of electrostatic forces) is a contact between TM and plungers at the release. This can be due to a non-nominal blocking condition with TM and plungers in contact, or to a motion of the plungers after the pin release (due for instance to vibrations or elastical relaxation of the plungers). This possibility will be discussed in section 4.7.

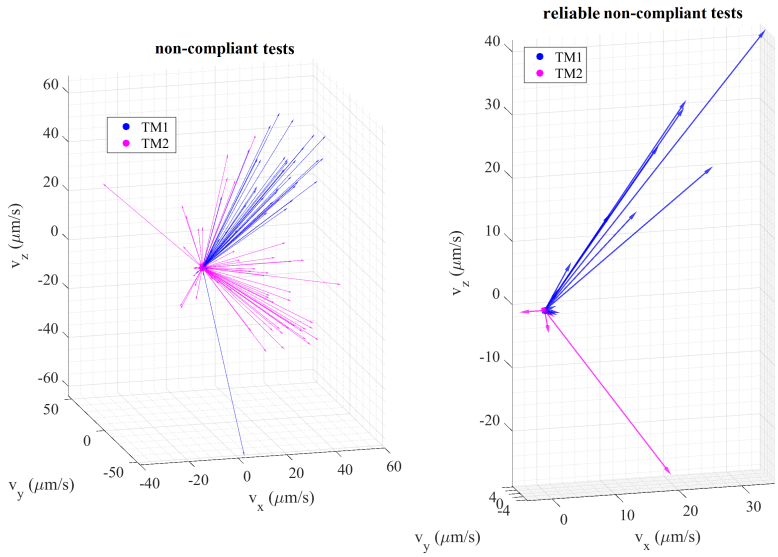

Figure 4.34: direction of pin release linear momenta. Left: non-compliant tests (independently of the reliability). Right: reliable non-compliant tests. In a nominal situation, the pin release velocity vector should be aligned with z axis (vertical axis in the figure).

4.6 Exclusion of the nominal release configuration

In section 4.5, we have seen that some tests show a pin release velocity different than expected, since the momentum at the release is higher than the requirement, high velocities are measured for the degrees of freedom orthogonal to the release axis (x and y), and high rotational velocities are measured. In particular, this holds for the *fast pin releases* (N and R families); the slow pin releases are in general compliant with the requirements and are characterized by very low translational velocities.

If the unexpected behaviour of the fast pin releases is due to the impulsive forces between pins and TM in the nominal condition, which is monodimensional (as reported in the model of 1.1.6), we would get a complete failure of the prediction models discussed in chapters 1 and 2. In this case, we would conclude that the forces acting at the pin release (adhesion and asymmetric motion) were underestimated.

However, due to the unexpected TM motion, which is far from being monodimensional (as shown in figure 4.34), we suspect that unpredicted effects acted on the TM. In particular, we suspect that an exclusive pin-TM contact at the release (as in the nominal case, see figure 1.6) cannot explain the high measured pin release velocities. If this is true, we would conclude that the high momentum at the release is not due to an underestimation of the adhesive forces acting in the model

of section 1.1.6, but rather to a completely different behaviour of the plungers at the pin release; in other words, the assumption of nominal (monodimensional) release was too optimistic.

In this section, we prove that an exclusive pin-TM contact at the pin release cannot explain the pin release velocities of the fast pin release, thus implying an important (not nominal) contact between plungers and TM when the pins are retracted. We consider a reference test (representative of the non-compliant fast pin releases) in section 4.6.1. We try (*per absurdum*) to explain the measured dynamics by taking into account a quasi-nominal configuration at the pin release, i.e. with momenta at the release transferred to the TM uniquely by the pins, but with an inclination of the pins: this is described in section 4.6.2. Under these assumptions, we consider possible explanations of an unexpected behaviour of the pins: an inclined force between pin and plungers (section 4.6.3), a torque produced by a misalignment between the two pins (4.6.4), or a lateral force at the release created by a lateral preload of the plungers (section 4.6.5).

Once this hypothesis will be proved not acceptable (because of not feasible orders of magnitude), a different dynamical model for the fast pin releases (taking into account a non-nominal configuration with the contact between TM and plungers at the release) will be considered in section 4.7.

It has to be remarked that the dynamical analyses of this section and of the following ones (4.7 and 4.8) assume that at the release the TM has no attitude deviations w.r.t. the housing reference frame. This assumption is based on the very low inclinations of the TM measured at the release, in the order of $0.1 \div 1$ mrad.

4.6.1 Reference test

Let's consider the result of test 89, TM 1, shown in figure 4.35, whose release velocities and preload force are reported in table 4.8. The test shows a high velocity along z axis, a similar velocity along x axis, a lower velocity along y. The η rotational velocity is much higher than the requirements, while the other rotations (θ and ϕ) are smaller (ϕ velocity is compliant). A linear behaviour of the 6 DOF after the pin release can be seen, and (as reported in C.6) the uncertainties of the measured velocities are lower than 10%: this is indeed one of the reference tests that contributes to the Δ_s distribution of the reliability test (appendix C.1.2). As a consequence, this test is considered reliable.

The TM impacts against the Z+ plunger after having moved along z of approximately 15 μm (which is approximately the expected gap between TM surface and the conical plunger, see section 4.1.2). The preload is lower than the nominal one, with the preload uncertainty higher than the estimated value.

In figure 4.36 we plot the translational velocity and the rotational velocity; the helicoidal motion axis is also represented, according to the Mozzi-Chasles' theorem [113]. We see that the motion of the TM can be approximated with a two-dimensional motion, since the main velocities are for x, z and η DOF.

We choose here this test as representative of the fast pin releases of TM1 that have a residual momentum higher than the requirement (i.e. non-compliant fast pin releases), since (as observed in section 4.5) these tests have a similar

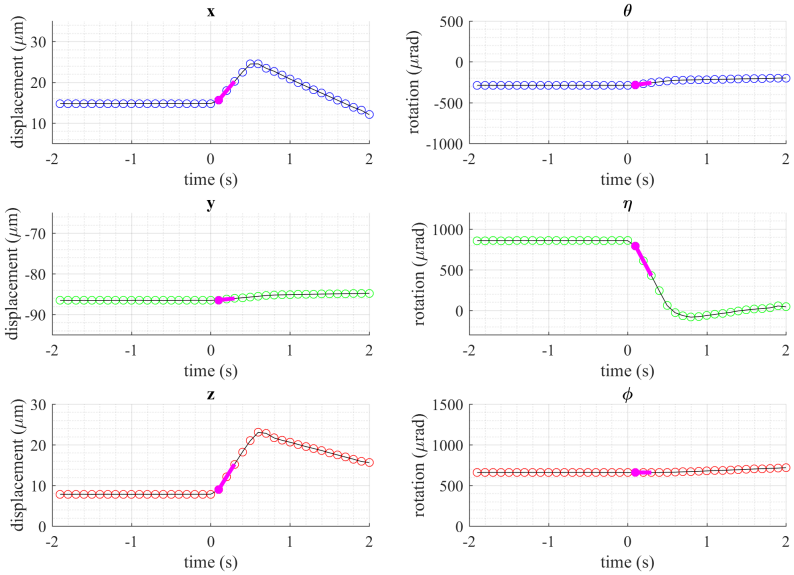

Figure 4.35: pin release of test 89, TM 1. The interval chosen for the computation of the *pin release velocity* is shown. For translations, the scale of the vertical axis is the same in order to highlight the difference between the release velocities (same for rotations).

distribution of the linear and angular momentum (independently on the preload value, which eventually affects the overall kinetic energy but not its distribution along the different DOF). The test is chosen for especially for its clear dynamics. We will therefore refer to this test for the investigation of the causes of the release momentum; at the end of each analysis referred uniquely to the reference test, we will comment the same result for the other non-compliant fast pin tests.

For the fast pin tests, the capacitive control is eventually activated some seconds after the pin release, synchronously w.r.t. the plunger retraction [112]. The timeline is shown in table 4.9.

4.6.2 Assumption: pin impulses on the landing area

In a nominal fast pin release, the kinetic energy should be mainly described by the z component: this is not the case for this test, as it can be seen by comparing x and z velocities reported in table 4.8 and in figure 4.36. Therefore, we can easily exclude a nominal (monodimensional) behaviour for this test, due to the presence of significant motion of x and η velocities.

The release velocities could however be caused only by forces acting on the landing area, like in the nominal configuration (figure 4.5). By looking at the signal of figure 4.35, we see that the transition from an equilibrium configuration

	v_x	v_y	v_z	ω_θ	ω_η	ω_ϕ
estimation	23.0	2.0	31.2	133.3	-1827.4	-2.4
stand. dev.	0.21	0.14	0.34	2.78	2.42	1.63

force drop	0.03 N
standard deviation	0.105 N

Table 4.8: test 89, TM 1: pin release velocities and estimated preload. The units of measurement of the pin release velocities are reported in μm/s for translations and μrad/s for rotations.

time	operation
-1 s	enable DFACS 10 Hz data collection
0 s	TM release (fast retraction of the pins)
4 s	slow plunger retraction for 200 steps
4 s	DFACS Mode Change ACC1
19 s	fast plunger retraction for 1200 steps

Table 4.9: timeline of the fast pin tests when the capacitive control is enabled (this occurs for the *automatic tests* of July 2017) [112]. The commanded release is considered as the zero reference for the timeline.

of the TM to the pin release velocity occurs in 1 or 2 samples. We can reasonably assume that in this sampling interval (0.1-0.2 s) some impulses are applied to the mass at the pin-TM contact, since the TM is nominally blocked by the pins on its two sides.

Through a simple dynamical model with impulses applied on the pin-TM interface (landing area), we can write the equations describing the relations between the impulses acting on the TM and the release velocities (resulting from the integration of the equation of motion). This is shown in figure 4.37 for the xz plane. For each pin, we can consider three impulses (along the three linear DOF) applied on a single point of the TM interface: we are therefore considering the resultant force of the pin-TM contact, and a single point for the contact can be considered thanks to the spherical profile of the pin (see section 1.1.5).

If we write the equations in the plane xz, we get:

$$\iota_1^x + \iota_2^x = M v_x \tag{4.11}$$

$$\iota_1^z - \iota_2^z = M v_z \tag{4.12}$$

$$(\iota_1^x - \iota_2^x)d - \iota_1^z l_1 + \iota_2^z l_2 = I_{yy}\omega_\eta \tag{4.13}$$

where (as shown in figure 4.37) ι_1^x and ι_1^z are the impulses given by the Z+ pin along x and z direction respectively, ι_2^x and ι_2^z are the impulses given by the Z- pin along x and z direction respectively, d is the distance between the TM centre of mass and the landing areas, l_1 and l_2 are the deviations (misalignments) of the force application points w.r.t. z axis, M is the mass of the TM and I_{yy} its inertia

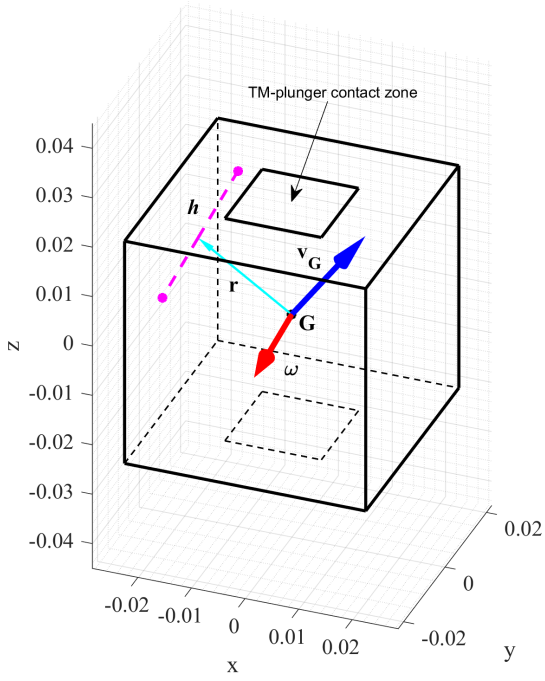

Figure 4.36: test 89, TM1: helicoidal motion of the TM after the pin release, according to Mozzi-Chasles' theorem. The helicoidal motion (dashed coloured line) intersects the two xz faces of the TM (i.e. faces orthogonal to y axis), and shows that the motion of the TM is mainly distributed in the xz plane.

about y axis (which exits the plane w.r.t. figure 4.37). The two impulses along z are defined in opposite directions in order to refer to a symmetrical situation (with this choice $\iota_z > 0$ is an adhesive pulling impulse and $\iota_z < 0$ is a pushing impulse).

Two additional equations (the corresponding ones of equations (4.11) and (4.13) with respect to the impulses along y axis) can be written for the yz plane. They will by now be neglected: they do not affect the resolution of the three equations (4.11) - (4.13), which are representative of the system motion since the majority of the kinetic energy is distributed in the xz plane.

In equations (4.11) - (4.13), the linear and angular momenta are known, but the two misalignments l_1 and l_2 are unknown. As a consequence, we need additional assumptions in order to get a solution (or a range of solutions) for the impulses: this is done in the following.

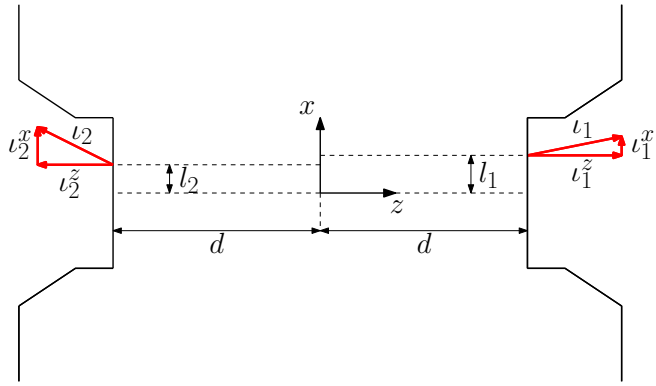

Figure 4.37: exclusive pin-TM contact: impulsive forces on the landing areas. The model takes into account a inclinations of the pins and a variation of the pin-TM contact point.

4.6.3 Centred pin contact

In order to find a solution (or a solution range) for the model described by equations (4.11) - (4.13), we can first of all consider a situation close to the nominal configuration, with no misalignments of the pin-TM contact points: we consider therefore that pin forces are applied at the centre of the landing area. This is an easy specific case of the more general solution that will be discussed in section 4.6.4, but presented separately for reasons of clarity.

In this case, the z components of the impulses give no contribution to the torque, and the two equations (4.11) and (4.13) can be solved independently with the existance of a unique algebraic solution.

$$\begin{aligned} \iota_1^x + \iota_2^x &= Mv_x \\ (\iota_1^x - \iota_2^x)d &= I_{yy}\omega_\eta \end{aligned}$$

The resulting impulses along x direction are the following:

$$\iota_1^x = -12.1 \pm 0.21 \text{ kg } \mu\text{m/s} \quad (4.14)$$
$$\iota_2^x = 56.4 \pm 0.21 \text{ kg } \mu\text{m/s} \quad (4.15)$$

where the uncertainties correspond to the standard deviations of the impulses, computed through the error propagation by considering the uncertainties of v_x and ω_η (reported in table 4.8).

Each impulse along x is associated with a z component: since only the difference of the two z impulses (i.e. Mv_z) is known (from equation (4.12)), the final solution for the impulses applied to the TM depends on a parameter. In figure 4.38 left two examples of possible solutions are shown: two adhesive pulls, with a higher

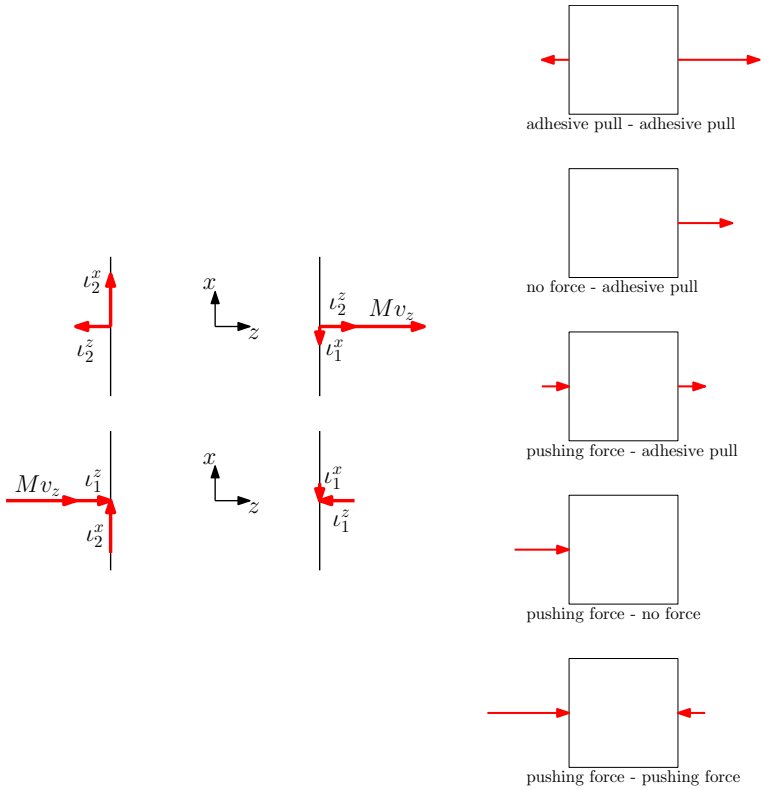

Figure 4.38: possible solutions of equations (4.11) - (4.13), depending to the chosen distribution of the z impulse on the two sides of the TM. Left: impulsive forces on the landing areas in two opposite cases. Right: possible z impulse distributions on the two sides of the TM.

pull applied to the Z+ landing area, or two pushing impulses, with a higher push applied to the Z- landing area.

All the intermediate solutions that preserve the overall z impulse are possible (as shown in figure 4.38 right). In all the situations, the resulting impulsive forces are inclined on the two sides of the TM. By considering the low maximum inclination of the pin with respect to the TM (constrained by the geometry of the blocking and release system), we can consider that the forces (adhesion and push) acting on each side of the TM have the same inclination of the corresponding pin.

As a consequence, the *feasible* solutions are the ones satisfying the geometrical constraints. Since we are assuming x components of the forces, due to the low relative inclinations between pin and TM z axis we are expecting very high forces along z direction.

Thanks to a geometrical simulation, we can find the range of the pin-TM relative inclination in such a case. According to the system geometry, the maximum relative inclination for η angle that allows a unique TM-pin contact is $\eta_{max} = 0.27°$

(figure 4.39). This situation excludes for example the second and fourth case of figure 4.38 right (overall z force acting only on one side), since in those cases the angles associated to the force vector would be much higher than η (in this cases, the z component of an impulse is determined, being equal to Mv_z).

The value $\eta_{max} = 0.27°$ is a very worst case, which is also higher than the sum of the estimated plunger offsets for η angle (≈ 1000 μrad [114]) and the maximum measured η inclination of the TM during the releases (≈ 2000 μrad [114]). Such a worst case value is chosen in order to give a conservative estimation (the higher the inclination, the lower the pin force in order to produce rotations).

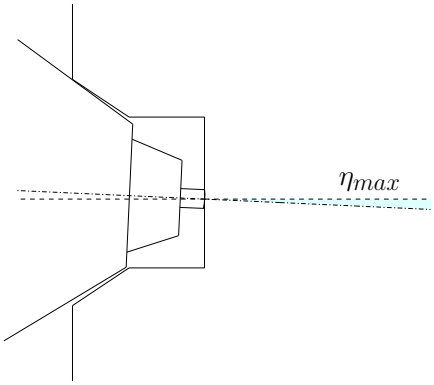

Figure 4.39: representation of the maximum pin-TM relative inclination in the centred case. A higher inclination leads to a contact between the plunger and the TM.

In figure 4.40 the two limit cases are shown. In the first case, the solution has the minimal adhesive (pulling) forces allowed by the geometry; in the second case, the forces are the minimal pushing forces satisfying the geometrical constraints. The two limit cases must satisfy the following system of equations:

$$\iota_1^z - \iota_2^z = Mv_z \tag{4.16}$$

$$\max\left(\left|\frac{\iota_1^x}{\iota_1^z}\right|, \left|\frac{\iota_2^x}{\iota_2^z}\right|\right) = \tan(\eta_{max}) \tag{4.17}$$

The two possible couples of solutions ι_1^z, ι_2^z are reported in equations (4.18) (case with minimal adhesive forces) and (4.19) (case with minimal pushing forces). We remind that the sign of a z impulse is positive if exiting the TM (i.e. adhesive pull).

$$\iota_1^z = 11941 \text{ kg}\frac{\mu\text{m}}{\text{s}}, \quad \iota_2^z = 11883 \text{ kg}\frac{\mu\text{m}}{\text{s}} \tag{4.18}$$

$$\iota_1^z = -11825 \text{ kg}\frac{\mu\text{m}}{\text{s}}, \quad \iota_2^z = -11883 \text{ kg}\frac{\mu\text{m}}{\text{s}} \tag{4.19}$$

In both cases, the minimum impulse is determined by the higher inclination of the Z- pin (due to the higher x impulse).

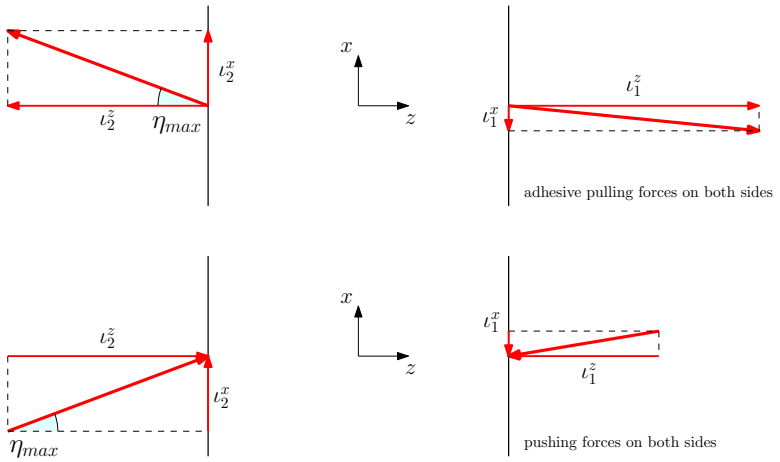

Figure 4.40: minimum z impulses on the landing areas in the case of an exclusive pin-TM contact (test 89, TM1).

Any other feasible solution (with lower inclinations) is necessarily given by forces with modulus higher than the ones computed in equation (4.18) and (4.19). Taking into account the uncertainties of the impulses in the computation (in order to find an uncertainty for the values of equations (4.18) and (4.19)) would not change significantly the result (we are indeed focusing on the order of magnitude of those impulses).

As a consequence, if we prove that the forces of two limit cases of figure 4.40 and equations (4.16) and (4.17) are not realistic, we can exclude that a simple inclination of the pins (in a centred contact case) can motivate the measured release velocities.

It has to be remarked that in the solution of the system of equations (4.16) and (4.17) no constraints on the *relative inclination between the two pins* have been imposed. This is actually not the case for the release mechanism: if we consider that the inclination of each pin corresponds to the inclination of the plunger with respect to the housing, the two inclinations must satisfy the geometrical equations of the blocking system as a mechanical quadrilateral. We are also neglecting the fact that inclined pins could not be able to keep the TM in equilibrium before the release (similar to the case that will be explained in section 4.6.5), since in the nominal case the TM is in equilibrium before the release only if the two pins are aligned (which is not the case in the current hypothesis).

Case 1: adhesive impulses

The solution of equation (4.18) gives the minimal adhesive values for the hypotheses of inclined adhesive pulls: in this case, the impulses applied by the pins to the TM would be exclusively due to the adhesive force profile. It can be easily proved that these solutions are not at all feasible with the maximum momentum transferred by an adhesive contact.

According to the pin motion described in section 1.1.6, the adhesive pull expires in approximately 0.04 ms. In order to minimize the peak of the adhesive force needed for yielding the impulse ι_1^z, we can assume a squared adhesive force profile acting in this interval; moreover, we can consider a higher duration of the adhesive pull τ=0.1 ms as a worst case assumption for the duration of the adhesive pull. We would get that the adhesive force f_{adh} associated to the impulse of equation 4.18 would be:

$$f_{adh}\tau = \iota_1^z \;\Rightarrow\; f_{adh} = \frac{\iota_1^z}{\tau} \approx 100\text{N} \tag{4.20}$$

This peak of adhesive force is higher of approximately 4 orders of magnitude greater w.r.t to the adhesive forces of the on-ground tests (section 3.4 and 1.2.3). Moreover, it is between 2 and 3 orders of magnitude higher than the preload force, while in a worst-case situation the peak of an adhesive force can be at most comparable with the contact force before the adhesive pull (the preload) [85]. In addition, we will see in section 4.8 that the slow pin tests reveal very low adhesive forces.

If we assume in the same computation a more realistic adhesive force profile, we would get an even higher peak of force in order to yield the same impulse. As a consequence, if we rely on the orders of magnitude of the on-ground estimations, we exclude that such a high impulse can be due to adhesive forces.

Case 2: pushing impulses

Let's consider the solution (4.19), which gives the minimal impulses in the case of inclined pushing forces. In the nominal case, pushing forces can be given only by the elastic forces of the plungers that decrease after the retraction of the pin.

In figure 4.41 a simplified diagram of the two pushing forces profiles are shown, according to the model presented in section 1.1.6. At time $t = 0$, the pin Z+ starts its retraction, which ends at time t_1: the loading force applied by the pin, with initial value f_0, decreases to zero. The Z- pin starts its retraction with a delay t_D, and we assume that it retracts with the same velocity of pin Z+, thus completing its retraction at time $t_1 + t_D$. Being the two forces opposite one to each other, the overall linear momentum transferred to the TM between time 0 and the free flight condition is the difference of the two impulses, i.e. the difference between the areas of the two graphs: the final impulse is therefore positive (as in the case of the reference test), due to the delay of the negative pin.

Based on the model of figure 4.41, we can write the following equations:

$$\iota_1^z = \frac{f_0 t_1}{2} \tag{4.21}$$

$$\iota_2^z = f_0\tau + \frac{f_0 t_1}{2} \tag{4.22}$$

For the considered test, the estimated preload is quite low, although affected by a high relative uncertainty (table 4.8). We can consider as a worst case a maximum deviation ($\approx 3\sigma$), corresponding to 300 mN (this is also the measured preload in some tests with similar kinetic energy at the release, see appendix C.6). As a consequence, the minimum t_1 value would be, by solving equation (4.21),

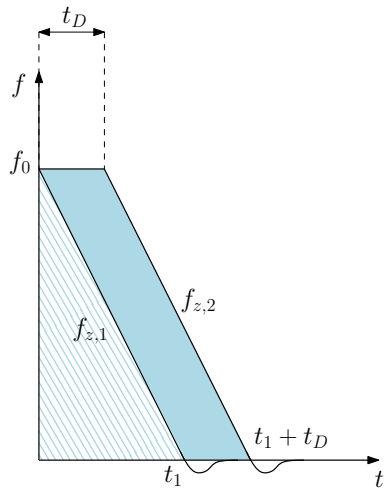

Figure 4.41: pushing forces in the nominal release. The Z- pin force $f_{z,2}$ can be assumed constant for a time interval t_D (for a small value of t_D w.r.t. the period of the plunger elasticity). The blue area represent the total pushing impulse applied to the TM.

$$t_1 = 2\frac{i_1^z}{f_0} = \frac{2 \cdot 11825 \cdot 10^{-6} \text{ kg m/s}}{0.3N} \approx 80\text{ms} \tag{4.23}$$

which is much higher than the time of the pin retraction ($\approx$ 0.1 ms). Alternatively, by imposing a feasible pin retraction time (100 μs approximately) the computation would lead an unrealistic preload ($\approx$ 200 N).

We can therefore say that the minimal impulses compliant with the geometry are completely not compatible with the estimated range for the retraction parameters of the model of figure (4.41). Moreover, the inclination of the pins in the considered hypothesis could lead to an instability of the equilibrium after the handover to pins.

As a consequence, also the case of the two inclined pushing impulses can be excluded for the reference test.

Result for other tests

A similar conclusion holds for the other non-compliant fast pin tests, as reported in table 4.10.

We can see that the tests can be divided into two main groups, with estimated z impulses close to 10^4 kg μm/s (like the reference test) or closer to 10^3 kg μm/s. For the second group, by repeating the same computations of the previous sections we would get the same conclusions, eventually reduced of one order of magnitude (a peak of adhesive force higher of 3 order of magnitudes w.r.t. the on-ground results, and a time of pin retraction $\approx$ 100 times higher than the measured one).

test	z **impulse (kg** μ**m/s), equations** (4.16)**,** (4.17)**)**
1.009	$7 \cdot 10^3$
1.013	$12 \cdot 10^3$
1.014	$5 \cdot 10^3$
1.027	$2 \cdot 10^3$
1.054	$1 \cdot 10^3$
1.055	$5 \cdot 10^3$
1.066	$1 \cdot 10^3$
1.071	$17 \cdot 10^3$
1.085	$12 \cdot 10^3$
1.089	$12 \cdot 10^3$
1.097	$10 \cdot 10^3$
2.006	$2 \cdot 10^3$
2.028	$11 \cdot 10^3$
2.057	$1 \cdot 10^3$

Table 4.10: Solution of equations (4.16) and (4.17) (corresponding of values (4.18) and (4.19) of test 89 TM 1) for the non-compliant fast pin tests. The reported value corresponds to the approximate solution (for each pin and for both adhesive and pushing cases).

Moreover, if we consider the non-reliable non-compliant fast pin tests, which are generally characterized by higher release velocities (see section 4.7.5), the required values of impulses would be even higher than the ones of table 4.10 (which includes only the reliable cases).

As a consequence, we can exclude the case of two inclined pushing impulses for the set of tests.

4.6.4 Decentred pin contact

We have seen that the assumption of centred pin contact leads to unrealistic conditions: as a consequence, we can exclude that the high release velocities and rotations of the reference test were caused exclusively by a pin release with centred contact and inclined pins.

We can consider now the general case of figure 4.37, where the pins are not constrained to touch the TM along the z axis (this is a more general case that includes also the one of section 4.6.3). Since the two parameters l_1 and l_2 are not known a priori, the solution of equations (4.11), (4.12), (4.13) is dependent on the choice for the two parameters. Some maximal values can be chosen. The ground experiments have shown that the pin axis can be slightly decentred w.r.t. the axis of the plunger (see also figure 2.10). By looking at the geometry of the system (see figure 1.10), we can assume a maximum misalignment (which is a very conservative worst case). With reference to the scheme of figure 4.42, by considering the pin diameter and the diameter of its housing in the plunger, we can assume that the maximum misalignment l_i of the i-th plunger is 100 μm, therefore

$$0 \leq l_i \leq 100\ \mu\text{m}, \quad i = 1, 2 \tag{4.24}$$

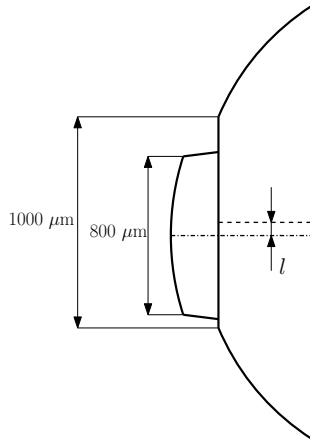

Figure 4.42: pin misalignment.

With a choice of the two misalignments l_1 and l_2 in the limits of equation (4.24), the system composed of equations (4.11), (4.12), (4.13) can be solved as a function of a single parameter (e.g. $\imath_2^z$):

$$\imath_1^x = \frac{Mv_x d + Mv_z l_1 + I_{yy}\omega_\eta + \imath_2^z(l_1 - l_2)}{2d} \tag{4.25}$$

$$\imath_2^x = \frac{Mv_x d - Mv_z l_1 - I_{yy}\omega_\eta - \imath_2^z(l_1 - l_2)}{2d} \tag{4.26}$$

For each choice of l_1 and l_2, the solution for the two equations (4.16) and (4.17) as a function of the unique parameter $\imath_2^z$ be found, thus yielding the minimal value of z impulses. We can consider the same value of η_{max} of figure 4.39 and compute the minimal z impulses values which match with the maximum inclination (like in section 4.6.3).

We can analyse the solutions of a grid of values for l_1 and l_2; it can be proved that, for l_1 and l_2 in the limits of (4.24), the minimum (i.e. most feasible) values for the z components of the impulses are located in correspondence of the limit cases $l_1 = 100\mu$m and $l_1 = -100\mu$m with $l_2 = -l_1$ in both cases. These limit cases correspond to the configurations that maximize the torque given by $\imath_1^z$ and $\imath_2^z$ impulses, thus decreasing the difference between $\imath_1^x$ and $\imath_2^x$ and minimizing their effect (and minimizing therefore the inclination of the pins w.r.t. the TM).

We get that

$$l_1 = 100\mu\text{m},\ l_2 = -100\mu\text{m}: \qquad i_1^z = 5511\text{kg}\frac{\mu\text{m}}{\text{s}}, \qquad i_2^z = 5453\text{kg}\frac{\mu\text{m}}{\text{s}} \quad (4.27)$$

$$l_1 = -100\mu\text{m},\ l_2 = 100\mu\text{m}: \qquad i_1^z = -5426\text{kg}\frac{\mu\text{m}}{\text{s}}, \qquad i_2^z = -5484\text{kg}\frac{\mu\text{m}}{\text{s}} \quad (4.28)$$

We can see that the results of equations (4.27) and (4.28) are similar to the ones of section 4.6.3 (equations (4.18) and (4.19)); they differ only of a factor 2. The same considerations can therefore be repeated for this case.

As a consequence, also the assumption of misaligned pins with decentred pin contact cannot explain the measured velocities at the release for the reference test.

Result for other tests

Similarly to section 4.6.3, we can compute the corresponding of equations 4.27 and 4.28 for the other non-compliant reliable fast pin tests. As for the reference case, the required impulse is reduced of a factor 2 for each test (w.r.t. table 4.10).

Hence, for this test we can exclude the nominal configuration at the pin release, i.e. impulses applied only on the landing area by the pins to the TM. This is mainly due to the low relative inclinations between pin and TM, which cannot explain the high pin release velocities in x and the rotation in η.

4.6.5 Buckling instability of the plungers

A third possibility that could explain the high lateral impulses with no contact between TM and plunger at the release is shown in figures 4.43 and 4.44. After the handover to pins, we assume that the plungers are holding the TM at the preload force, which, acting on the plungers, leads to a *buckling instability* and to an inclined equilibrium configuration of the plungers (thanks to the elastical force of the guiding system of the plungers, considered as a flexional spring). In this condition, the TM is in equilibrium also with high preloads, since the holding forces are in opposite directions. A retraction of one pin would lead to the exclusive action of the opposite one, which, through the lateral oscillation of the plunger due to its lateral preload, could give a lateral impulse to the TM (thanks for instance to the friction between pin and TM). In this situation, the impulse in z direction could be given by one of the two effects of the nominal model of section 1.1.6 (i.e. adhesion or push due to the delay effect).

Again, in the following we prove *per absurdum* that this hypothesis can be discharged.

It has to be remarked that refusing the buckling hypothesis does not mean that the plunger is perfectly aligned w.r.t. the mass: a misalignment of the two bodies can be due to a mechanical offset of the plunger (the analysis of these effects is part of the future developments, see 5).

Symmetric configuration

In figure 4.43 a simple model considering a symmetric situation is considered. In the model, we report the equivalent angular stiffness k_ϵ of the plunger (the axial

stiffness of the plunger is neglected since it would lead simply to a small variation of the length); the plungers are both inclined of a quantity ϵ w.r.t. their equilibrium configuration.

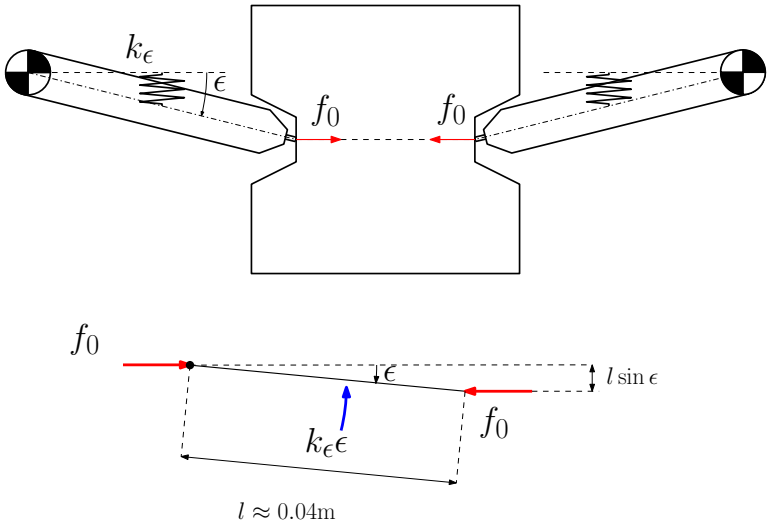

Figure 4.43: buckling hypothesis (symmetric configuration). Top: the two plungers, inclined of a small angle ϵ and preloaded in lateral direction, block the TM symmetrically. The two springs represent the equivalent angular stiffness due the guiding system of the plungers. Bottom: scheme of the forces acting on the plungers.

This case can be rejected *a priori* since the structural parameters of the system do not allow this configuration. Thanks to the symmetry, we can compute the equilibrium of one plunger. In this condition the preload force along z axis would be in equilibrium with the elastic torque according to the equation:

$$f_0 \cdot l \sin \epsilon = k_\epsilon \epsilon \tag{4.29}$$

where f_0 is the preload, l is the distance between the pin and the centre of rotation of the plunger, ϵ the equilibrium angle and k_ϵ the equivalent angular stiffness of the plunger. A non-trivial solution (i.e. different than 0) for ϵ in equation (4.29) can be found only if

$$f_0 l > k_\epsilon \tag{4.30}$$

If we consider a nominal preload force of 0.3 N (which is higher than the measured force of many tests, like the reference test of table 4.8), and according to an estimation of k_ϵ through to the lateral stiffness of the plunger (reported in [44]), we get

$$f_0 l \approx 0.3\text{N} \cdot 0.04\text{m} = 0.012\text{Nm} << 100\text{Nm} \approx k_\epsilon \tag{4.31}$$

thus contradicting the condition of equation (4.30).

As a consequence, this hypothetical configuration has to be discharged since the preload applied to the tip is too low to cause the laterally preloaded plunger configuration of figure 4.43.

Antisymmetric configuration

A different configuration is shown in figure 4.44, with the plungers both inclined of an angle ϵ w.r.t. their equilibrium, but with an antisymmetric configuration. In this case, the TM is inclined of an angle η. Based on the analysis of the TM rotation before the release, we can assume $\eta \approx 1000$ μrad (see for instance figure 4.35).

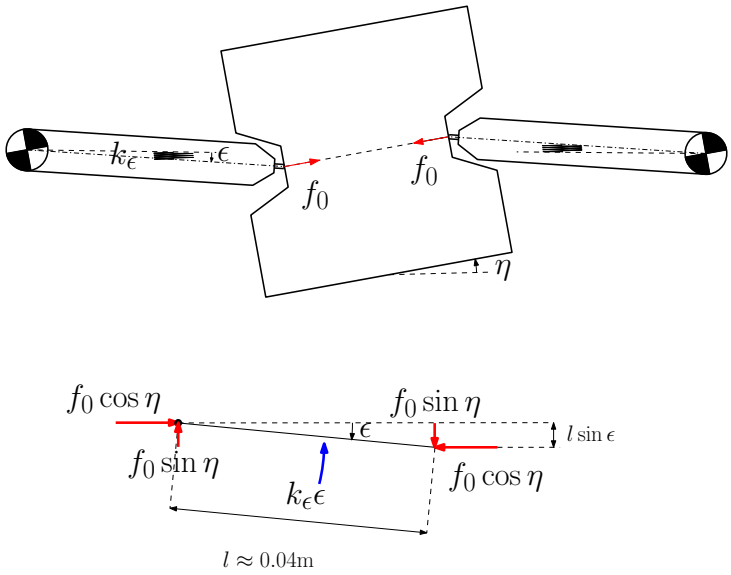

Figure 4.44: buckling hypothesis (antisymmetric configuration). Top: the two plungers, inclined of a small angle ϵ and preloaded in lateral direction, block the TM anti-symmetrically; the TM has an inclination η. The two springs represent the equivalent angular stiffness due the guiding system of the plungers. Bottom: scheme of the forces acting on the plungers.

Like for the previous case, we can analyse the equilibrium of one plunger. Based on the scheme of figure 4.44, we find:

$$f_0 l \sin(\epsilon + \eta) = k_\epsilon \epsilon \tag{4.32}$$

and by assuming small rotations:

$$f_0 l(\epsilon + \eta) = k_\epsilon \epsilon \tag{4.33}$$

therefore, solving for ϵ

$$\epsilon = \frac{f_0 l}{k_\epsilon - f_0 l}\eta \tag{4.34}$$

According to the quantities reported in (4.31), and by assuming $\eta = 1000$ μrad, we get

$$\epsilon \approx 0.1 \ \mu\text{rad} \tag{4.35}$$

This value of ϵ would be associated to a elastic potential energy of the plunger before the pin release. We compare now this potential energy to the kinetic energy of the TM according to the scheme of figure 4.45. If one pin retracts, the TM is free on one side (right side in the figure) and the elastic energy of the plunger can be converted into kinetic energy of the TM. In the figure, we are referring to a worst case configuration where the pin of the left plunger remains extracted during the rotation of the system (hence with a very high delay w.r.t. the other pin) and the TM-pin contact behaves like a rotational joint.

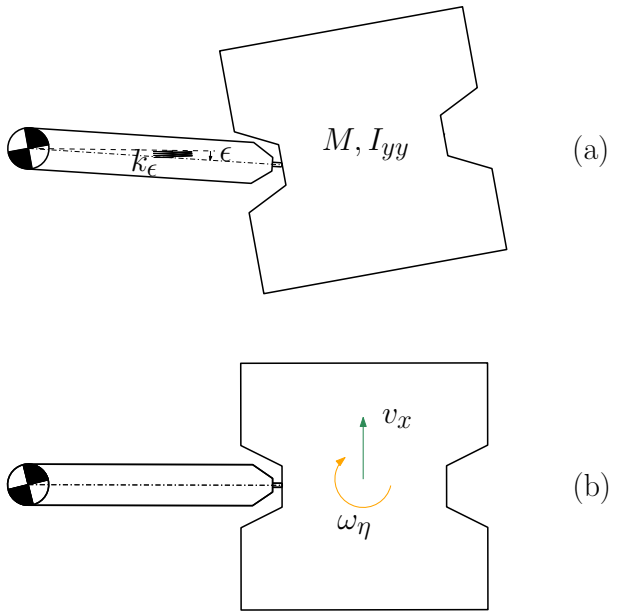

Figure 4.45: conversion of the elastic energy of one plunger into kinetic energy of the TM (for the DOF x and η). (a) plunger with stiffness k_ϵ rotated of an angle ϵ w.r.t. the equilibrium. (b) elastic energy of the plunger converted into velocities v_x and ω_η after the rotation of the plunger. The joint between pin and TM is here considered as a rotational joint.

With reference to the picture, the potential energy in (a) is

test	x-η **kinetic energy (J), eq.** (4.37)
1.009	$5 \cdot 10^{-10}$
1.013	$2 \cdot 10^{-9}$
1.014	$3 \cdot 10^{-10}$
1.027	$5 \cdot 10^{-11}$
1.054	$1 \cdot 10^{-11}$
1.055	$3 \cdot 10^{-10}$
1.066	$1 \cdot 10^{-11}$
1.071	$3 \cdot 10^{-9}$
1.085	$2 \cdot 10^{-9}$
1.089	$2 \cdot 10^{-9}$
1.097	$1 \cdot 10^{-9}$
2.006	$2 \cdot 10^{-11}$
2.028	$1 \cdot 10^{-9}$
2.057	$1 \cdot 10^{-11}$

Table 4.11: Buckling hypothesis: energy produced by the system of figure 4.45 (according to equation (4.37)) for each test.

$$U = \frac{1}{2} k_\epsilon \epsilon^2 \approx 5 \cdot 10^{-13} J \tag{4.36}$$

while the kinetic energy created by the plunger rotation in (b), according to the TM parameters ($M \approx 2$ kg, $I_{yy} \approx 7 \cdot 10^{-4}$ kg·m^2) and the velocities of table 4.8 ($v_x \approx 23$ μm/s, $\omega_\eta \approx -1800$ μrad/s), is

$$K = \frac{1}{2} M v_x^2 + \frac{1}{2} I_{yy} \omega_\eta^2 \approx 1.7 \cdot 10^{-9} \tag{4.37}$$

where we have neglected the mass of the plunger.

We have therefore that, due to the difference of more than 3 orders of magnitude (in a worst case assumption with one pin not retracted), the potential energy of the plunger cannot explain the kinetic energy associated to the DOF x and η. We can hence discharge also this second hypothesis for the reference test.

Result for other tests

The result of equation (4.37) for each test is reported in table 4.11. We see that in the cases with smallest kinetic energy (tests 54, TM 1 and test 57, TM 2) the kinetic energy is higher than the one of equation (4.36) of more than one order of magnitude. Moreover, as commented in section 4.7.5 the kinetic energies of the non-reliable tests are even higher than the gretest ones of table 4.11.

4.7 TM-plunger contact in the fast pin releases

The considerations of section 4.6 suggest that for a reference test of the fast pin releases (test 89, TM1) an exclusive contact of the pin with the TM at the pin release does not motivate the high impulses along directions different than z; this holds for many non-compliant tests, since test 89 is high representative of the typical behaviour for the fast pin releases of TM1. For TM2, the pin release velocities of the fast pin releases are characterized by a very high inclination w.r.t. z axis (see figure 4.34), thus leading to similar conclusions if we repeat the approach of the previous section.

As a consequence, we can assume that, when a fast pin release shows velocities out of the requirement, at the pin release some unexpected contact between plungers and TM has occurred; in other words, some impacts between TM and plungers occur *immediately* as the pin retraction is commanded. We remark that this assumption is not the same of the impacts between plunger and TM that change the pin release velocity creating the *velocities after impact* or the *plunger release velocities*. With reference to figure 4.3 of section 4.1.2, we are assuming the following situation:

- as the pins retract, in addition to the impulse given by the pins to the TM, an impulse is given by the plungers to the TM; the resulting velocity of the TM is the pin release velocity (figure 4.3 b).
- the TM can then have additional impacts with the plungers (figure 4.3 c), which modify the TM momentum until the plunger release velocity can be measured (figure 4.3 d).

Therefore, we are still distinguishing pin release velocity and plunger release velocity, but we are now considering that the pin release momentum is affected by an additional contact between TM and plungers when the pins retract.

In this section, similarly to the approach of section 4.6, we investigate the consequences of this assumptions for the fast pin releases. In section 4.7.1 we consider the possible motivations of such a contact between TM and plungers at the pin release. In section 4.7.2, we describe a model that allows to estimate the impulses exchanged by TM and plungers at the pin release under our assumption; we will see that, according to this model, for the non-compliant fast pin tests the large majority of the TM momentum at the release can be explained (with further considerations discussed in appendices C.2 and C.3).

The possible influence of the electrostatic attraction for the dynamical model is commented in section 4.7.3.

The information of the orthogonal impulse model is discussed in section 4.7.4; the representativeness of the compliant tests for the analysis is discussed in section 4.7.5, where the model is applied to many categories of test.

4.7.1 Possible motivations of TM-plunger contact at the pin release

A push at the pin release between TM and plungers could be motivated by the following mechanical behaviours of the release mechanism:

- a horizontal motion of a plunger at the release, with an axial push of the plunger in the z direction. Let's consider the axial stiffness of the plungers (like in figure 4.9). Before the pin release, the plungers are compressed. At the pin release, the quick fall of the preload force can cause the relaxation of the plunger elastical energy and therefore make the plunger move towards the mass, creating an impact between TM and plungers on the coupling surface. Due to the estimated stiffness of the plungers (section 4.2.3), the transformation of the elastical energy of the plunger into kinetic energy of the plunger would occurd in less than 0.1 s (sampling time), thus matching with a quick change of the TM velocity from the equilibrium condition to the pin release velocity.

  In appendix C.2 we discuss a possible model for the axial push of the plungers, applied to some of the non-compliant tests.

- a lateral motion of a plunger at the release, that makes the plunger rotate until it touches the TM at the coupling surface. It has been shown (section 4.2.3) that the plungers of both the GRS are characterized by a bi-stable behaviour on a plane: this means that the plunger has an equilibrium inclination depending on the direction of its last motion. This shows an instability of the alignment of the plungers w.r.t. z axis.

  A possible influence of the plunger bi-stability at the release is supported by the fact that (as we will se at the end of section 4.7.2) the main impulses given by the plunger to the TM belong to the xz plane, which is the same plane of the bi-stable behaviour of figure 4.11. The lateral motion of the plunger at the pin release is being currently measured in the new ground test campaign (see chapter 5).

The probability of a TM-plunger contact at the pin release is higher if the configuration of the system at the pin release is not nominal, i.e. the plungers are closer to the TM w.r.t. the nominal configuration of figure 4.4. The probability of a lower gap between TM and plunger before the release is supported by the fact that, for many test, the inversion of the z velocity after the pin release (see figure 4.20) occurs after less than the expected 14 μm, as reported also in appendix C.6.

Moreover, if we assume a misalignment between TM and plungers, that nominal clearance can be reduced. In [44] some worst cases are described: the clearance can be reduced up to 5 μm as an effect of relative rotations between TM and plunger before the release. In such a condition, a smaller translation/rotation of the plunger is needed in order to touch the TM.

4.7.2 Orthogonal impulse model

As shown in figure 4.34, for the non-compliant tests of TM1 we notice a high inclination of the pin release velocity w.r.t. the expected direction z (the direction of the nominal mono-dimensional case). In particular, we notice that x and z components of the pin release velocities are comparable. This occurs especially for the reliable not-compliant tests like the reference test of the previous section (see figure 4.36). We notice therefore that the relative inclination between x and z

components is close to 45°: as a consequence, the linear momentum is close to be orthogonal to the coupling surfaces of the TM indentation, which are inclined of 41.5° w.r.t. z axis. This consideration leads us to assume the following hypothesis: the impulses applied from the plungers to the TM have been orthogonal to the coupling surface. This is a reasonable assumption since (if the pin is retracted) a contact between TM and plunger occurs on the coupling surfaces with a higher probability.

In figure 4.46 the projection on a single plane (xz) of the impulses assumed on a side of the TM are shown (a similar situation occurs in the yz plane). The impulses applied by the plungers are orthogonal to the coupling surfaces. We remark that this hypothesis does not take into account a possible friction between plunger and TM, which would allow different inclinations of the contact forces.

In general, an orthogonal impulse is applied on each of the two coupling surfaces: the impulse is the resultant of a distributed impulse on the surface. As shown in the figure, we can split the total impulse applied to the TM as the sum of a contribution with exclusive effect along z direction (vectors $\vec{u}$ and $\vec{w}$), and a remaining impulse ($\vec{t}$) applied only on one of the two surfaces, which gives a contribution also along x and (due to the distance between the coupling surface and the center of the TM) affects the rotation η.

For each vector, the x and z components are related as follows, according to the inclination of the coupling surface shown in the figure:

$$\frac{\iota^z}{\iota^x} = \tan 41.5^\circ \tag{4.38}$$

Notice that only the *unbalanced* component (t in figure 4.46) affects the translation x and the rotation η of the TM. The two *balanced* components (u and w in figure 4.46) yield only a total impulse in z, and do not affect x and η DOF. As a consequence, for the xz plane a system of equations (similar to the ones of section 4.6) that takes into account translation x and rotation η will give information only on the unbalanced components of the two sides.

In figure 4.47 the complete model (in the planes xz and yz) is shown. For each side of the TM and each plane, an impulse (the unbalanced component with effects for rotation) is assigned to a single side of the coupling surface (the one with positive x or y coordinate). If the impulse turns to be negative, it is assigned to the opposite face of the indentation.

The equivalence between impulses and measured momenta is given by the following equations:

$$\begin{aligned}
Mv_x &= \iota_1^x + \iota_2^x && (4.39)\\
Mv_y &= \iota_1^y + \iota_2^y && (4.40)\\
Mv_z &= -\left(|\iota_1^x| + |\iota_1^y|\right)\tan\alpha + \left(|\iota_2^x| + |\iota_2^y|\right)\tan\alpha + \iota_{res}^z && (4.41)\\
I_{xx}\omega_\theta &= \left(\iota_2^y - \iota_1^y\right)a + \left(\iota_2^y - \iota_1^y\right)\tan\alpha \cdot b && (4.42)\\
I_{yy}\omega_\eta &= \left(\iota_1^x - \iota_2^x\right)a + \left(\iota_1^x - \iota_2^x\right)\tan\alpha \cdot b && (4.43)
\end{aligned}$$

where ι_{res}^z is the *residual* impulse along z that has no effect on the rotations θ and η: for instance, the sum of vectors $\vec{u}$ and $\vec{w}$ in the scheme of figure 4.46

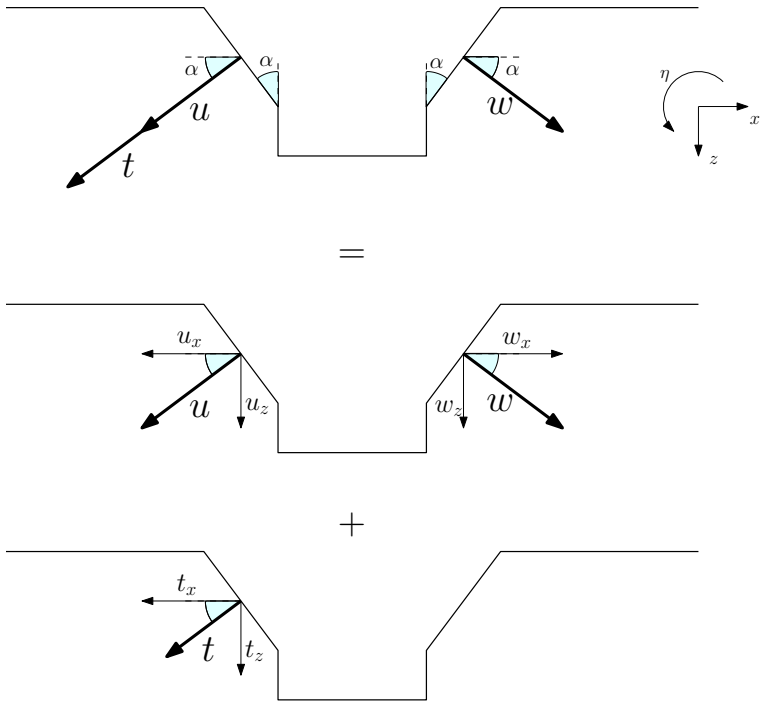

Figure 4.46: impulses between TM and plungers for one side of the TM (in xz plane). The angle α is 41.5°. u and w are balanced components that give no contribution to translation x and rotation η; t is the unbalanced contribution that affects both translation and rotation.

contributes to the total residual ι^z_{res}. a is the arm of the the rotation for the x and y components of the impulses, corresponding to the distance between the TM centre and the point of application of the impusles, while b is the arm of the rotation for the z component of the impulses, corresponding to the half distance between the application points of the same side of the TM. The analysis of the TM geometry yields:

$$a = 21.726 \text{ mm}$$
$$b = 3.872 \text{ mm}$$

The geometrical parameters a and b are nominal quantities (corresponding to the mean coordinates of the coupling surface) and can have a variation if the relative inclination between plunger and TM is not negligible. However, by assuming small inclinations between TM and plunger we consider that the variation of the coordinates of the contact points is negligible w.r.t. a and b.

Equations (4.42) and (4.43) are written such that the sign of the impulses matches with the effect of their torque: if for example i^x_1 turns out to be negative in equation (4.43), it means that the impulse is applied on the opposite face w.r.t. figure (4.47), thus leading to a negative torque about y axis.

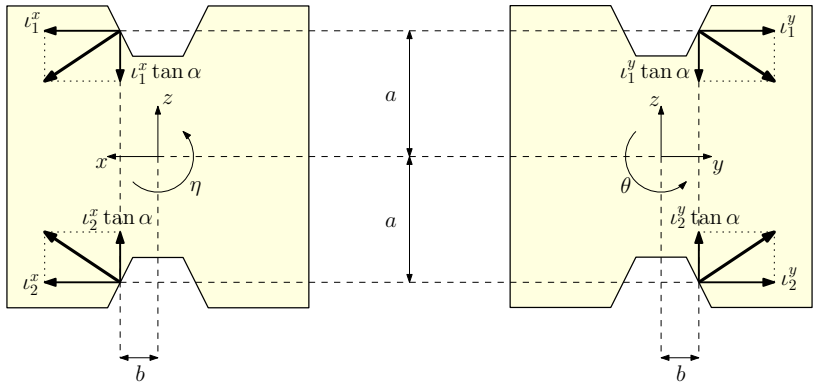

Figure 4.47: impulses between TM and plungers orthogonal to the coupling surface.

The algebraic system has 5 equations and 5 unknowns, and can be easily solved linearly (the solution of equation (4.41) follows immediately after solving equations (4.39), (4.40), (4.42), (4.43)).

Similarly to the dynamical models of section 4.6, an indetermination for z components of the impulses occurs. As shown by equation 4.41, the solution for ι_1^x, ι_1^y, ι_2^x, ι_2^y impulses implies a corresponding value of impulse along z according to equation 4.38; by subtracting it from the total momentum Mv_z, only the residual ι_{res}^z can be estimated.

The residual z impulse ι_{res}^z cannot be attributed *a priori* to any of the two sides of the TM: in principle, it is the sum of two unknown impulses along z, with infinite solutions (similarly to the case of figure 4.38 right). The residual z impulse ι_{res}^z could be due to any effect that gives no rotation about x and y axis, like balanced impulses acting on both sides of the TM (u and w in figure 4.46), or forces given by the pin to the TM (like adhesive impulses between pin and TM at the release).

Result for a single test

We can for example apply the model to the test 89 of TM1 (the reference test of section 4.6, represented in figure 4.35 and with velocities reported in table 4.8).

The result is reported in table 4.12 and in figure 4.48, with the uncertainties related to the uncertainties of the measured linear and angular velocities. It can be seen that, according to the model equations, the larger impulse is given to the mass by the pyramidal plunger (Z-) in positive x direction, while much smaller impulses are given in the other directions. The linear momentum along x and the angular η momentum, which are outside of the requirements, can be described as caused by the pyramidal impulse ι_2^x alone. The momentum along z direction is mainly due to the z component associated to ι_2^x, which is given by

$$\iota_2^{x,z} = \iota_2^x \cdot \tan 41.5^\circ = 41.4 \text{ kg}\frac{\mu\text{m}}{s}$$

and to the impulse ι^z_{res}, which (in this case) is lower than $\iota_2^{x,z}$. As a consequence, the high velocities of test 89 are mainly due to the high pyramidal impulsive force.

According to the model of section 1.1.6 and the analysis of section 4.6, the effect of forces applied by the pin to the mass are aligned with the z axis, and can therefore be included in the residual. Since ι^z_{res} is out of the requirement for translations, we cannot say for test 89 that the impulses given by the pin to the TM are compliant with the limits (although we know that the forces of the pin are not due only to adhesion, since a delay effect is possible, see equation (1.7)). On the other hand, we remind that the ι^z_{res} can also contain a "hidden" plunger impulse (the vectorial sum of $\vec{u}$ and $\vec{w}$ in figure 4.46): we cannot say that ι^z_{res} is due only to forces exchanged by pin and TM.

	Mv_x	Mv_x	Mv_x	$I_{xx}\omega_\theta$	$I_{yy}\omega_\eta$	ι_1^x	ι_1^y	ι_2^x	ι_2^y	ι^z_{res}
value	44.3	3.8	60.2	0.09	-1.24	-2.5	0.1	46.8	-2.5	17.85
st.dev.	0.41	0.27	0.67	0.002	0.002	0.21	0.14	0.21	0.14	0.73

Table 4.12: test 89, TM1: linear and angular pin release momenta and impulses resulting from the model (with their uncertainties). Impulses and linear momenta in kg·μm/s = μNs, angular momenta in μNms.

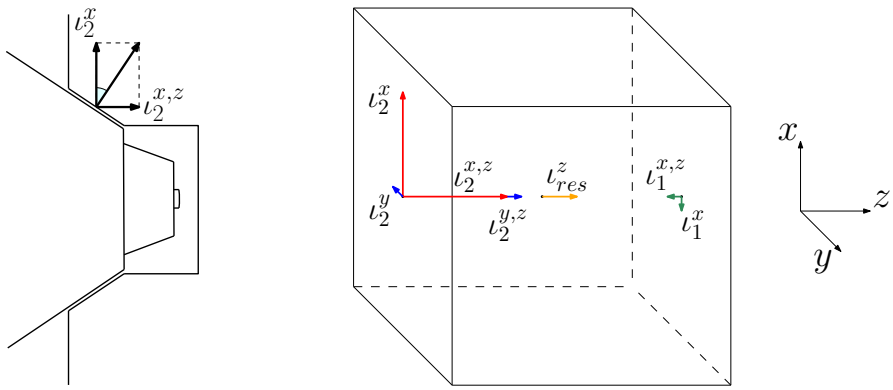

Figure 4.48: TM-plunger contact after the pin release (left) and results of the impulse model applied to test 89, TM1 (right, values in table 4.12).

Results for non-compliant fast pin tests

The computations can be repeated for other non-compliant fast pin tests of the release campaign: in figure 4.49 and 4.50 we plot the impulses ι_1 and ι_2 and the residuals ι^z_{res} (compared to the z momentum) for the non-compliant fast pin tests with reliable velocities (reliable tests), by taking into account also the uncertainty related to the computations of the momenta. We consider only the reliable tests since the computations of equations (4.39) $\div$ (4.43) require all the velocities to be free flight velocities. This choice allows to consider only 13 TM1 fast pin tests and

3 TM2 fast pin tests (the non-compliant tests of TM2 are generally not reliable, see section 4.5.3).

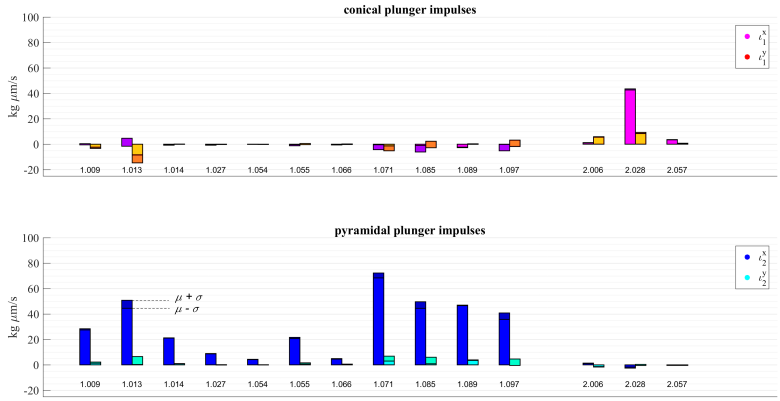

Figure 4.49: orthogonal impulse model: x and y impulses of the two plungers for non-compliant fast pin tests. Only reliable tests have been considered in the computation. The captions under each group of columns report the test number (e.g. 1.089 is TM1, test 89). The end of each column (of a darker colour) indicates the range of the uncertainty, as shown in the figure (μ is the estimated value and σ its standard deviation).

We can see in figure 4.49 that all the shown tests of TM1 are characterized by high pyramidal x impulse, similarly to test 89 of TM1; on the contrary, for TM2 we get that the higher impulses are given by the conical plunger. This difference matches with the difference in the signs of v_z for TM1 and TM2: as shown in figure 4.34, if the test is non-compliant TM1 moves generally with positive z velocity (thanks to the prevailing push of the pyramidal plunger), while TM2 moves generally with negative z velocity (prevailing push of the conical plunger).

In figure 4.50 an interesting result is shown: for the considered subset of tests, the residuals are always significantly lower than the overall z momentum, and with the same sign. This means that the orthogonal impulse model can justify a high percentage of the overall z momentum, which is therefore related to the lateral impulses between plungers and TM.

Moreover, the residuals are generally lower than 20 kg μm/s and in some cases lower than the requirement for z momentum (10 kg μm/s), especially if we consider also the uncertainty on ι^z_{res}.

In figure 4.51 the same result is computed by considering (when possible) additional samples in the computation of the velocity (as described in section 4.4.3). The result is very similar and the same conclusions hold; the main difference is a general decrement of the momenta (for TM1 tests) and a lower uncertainty of the residuals.

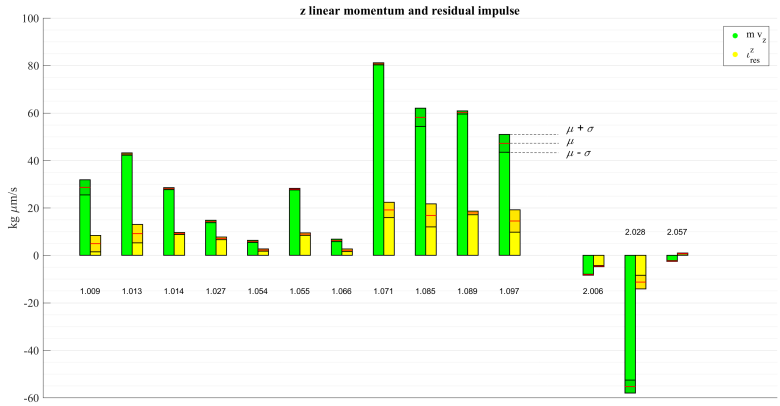

Figure 4.50: orthogonal impulse model: comparison between total z momentum and residual impulse ι^z_{res} for non-compliant fast pin tests. Only reliable tests have been considered in the computation. The captions under each group of columns report the test number (e.g. 1.089 is TM1, test 89). The end of each column (of a darker colour) indicates the range of the uncertainty, as shown in the figure (μ is the estimated value and σ its standard deviation).

4.7.3 Electrostatic effect

As commented in section 4.1.2, in a nominal release procedure (with velocities in the requirements) the electrostatic attraction between TM and plungers can be neglected, since it gives a negligible contribution to the final TM velocity. If we assume instead that a contact between TM and plunger occurs, the capacitive forces could affect the dynamics due to the low distance between the bodies (which increases the relative capacitance).

If the difference of voltage is due to a charge of the TM produced at the detachment between TM and plunger, and by assuming the same charge estimated in the TM charge tests performed before the release campaign (see appendix C.5), we get that the attraction between TM and plunger is negligible for the test with non-compliant velocity analysed in this section. If TM is increasing its distance from a plunger due to a contact between them, the electrostatic effect would indeed decelerate the TM of a quantity that can be neglected if compared with the high measured velocities.

Also if we consider a capacitive effect due to a constant voltage of the TM, the TM dynamics of the tests analysed in this section (and in the previous one) could not be due to an electrostatic effect: the TM is moving of several micrometers with a constant velocity, and according to [104] the electrostatic effect is not significant when the distance between TM and plunger is higher than 1-2 μm (i.e. the free flight velocity cannot be due to the attraction of one plunger).

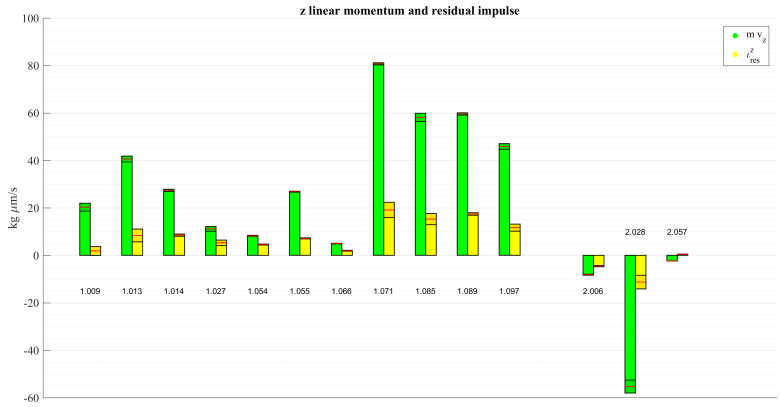

Figure 4.51: orthogonal impulse model: comparison between total z momentum and residual impulse ι^z_{res} for non-compliant fast pin tests. Same result of figure 4.50, but considering (when possible for a test) a larger number of samples in the computation of the velocities.

4.7.4 Information of the orthogonal impulse model

As seen in section 4.6, a nominal pin release configuration cannot explain the TM dynamics of the non-compliant fast pin releases. On the contrary, impulses applied by the plungers to the coupling surfaces of the TM can explain x and y pin release momenta, as well as θ and η angular momenta. In particular, they justify a high percentage of the z momentum, as summarized by figure 4.50. In other words, if we assume the existence of lateral impulses between TM and plungers in order to explain the high lateral and rotational velocities, these impulses must be necessarily associated to a impulse along z axis that constitutes the majority of the z momentum.

The dynamical problem cannot be completely solved for z momentum, since the composition of the residual impulse ι^z_{res} is unknown. The residual impulse can be attributed not only to a balanced impulse between plungers and TM, but also to the pulling impulse (adhesion) or pushing impulse (delay effect) of the pins, both described in equation (1.7).

As shown in figure 4.50, if we attribute the residual impulse to the adhesive pull, in some cases we would get a total z adhesive impulse higher than the limit of 10 kg μm/s (corresponding to the requirement of 5 μm/s); however, these values of impulse would correspond to a momentum of the TM that could be controlled by the capacitive actuation (see section 4.3.3), thus meaning that the adhesive contribution wouldn't be so problematic as the effect of the plunger.

However, we have no elements to state that the residual ι^z_{res} is due to adhesion: this is just one of the (theoretically infinite) possible solutions. The residual ι^z_{res} could be due to the combined effect of balanced plunger push (on both sides),

adhesive pulls (on both side) and delay effect (on one of the two sides). These effects could be additive or subtractive. In particular, since for the analysed test the prevailing effect of one plunger is shown for the lateral impulses (figure 4.49), an associated axial push of this plunger is suspected.

Being the problem of ι^z_{res} not solvable without further assumptions, we focus on the main result given by the orthogonal impulse model: it can explain the unexpected behaviour of 4 DOF (x, y, θ, η), and tells that the high momenta of these DOF are necessarily associated to a very high z momentum due to the push of the plunger, which transfers to the TM a momentum higher than the requirement and comparable with the overall z momentum measured for the test. In other words, independently of the composition of the residual ι^z_{res}, the orthogonal impulses at the coupling surfaces transfer a critical momentum to the TM, for 5 of the 6 DOF.

A possible compliance of the model with the measured behaviour of the remaining DOF (ϕ) is discussed in appendix C.3, where a model that relates the impulses between plunger and TM with the ϕ rotation is discussed. The compliance of the ϕ rotation with the model can be proved only with some assumptions on the composition of the residual impulse ι^z_{res}. Future analyses or dynamical simulations of the release mechanism could lead to additional information in order to solve the complete TM dynamics (see chapter 5).

It has to be remarked that the results of this section cannot explain completely the dynamics of the fast pin release since they are based on a very small set of reliable tests (see section 4.7.5). However, the model explained in this section can justify (in some distinct cases) the high momentum at the release, and can be therefore the basis of future analyses based on the dynamics of the plungers. Notably, we notice from figures 4.49 and 4.50 that the main impulses are in the xz plane, which is the plane of the plunger bi-stability of section 4.2.3. The analysis of the mechanical behaviour of the plungers at the pin release is being currently analyzed by the Trento University (also through a new experimental campaign, see chapter 5).

4.7.5 Representativeness of the reliable tests

In this section, the orthogonal impulse model has been applied to the non-compliant reliable tests. In section 4.5.3 we have seen that, when the tests are not compliant, the reliable tests constitute a small subset (this holds for TM2 in particular). As a consequence, we ask ourselves if the conclusions of section 4.7.4 can be extended also to the non-reliable tests that show velocities higher than the requirement.

The analysis of this chapter cannot be repeated in the same way for the non-reliable tests, since by definition a non-compliant test does not show a free flight velocity. The release velocity of the non-reliable tests is computed from the first three samples and is used only to consider a order of magnitude for the momentum (see section 4.4.3).

However, the analysis of the relation between reliability and momentum (figure 4.28) shows that the non-reliable tests have in general a higher momentum when compared to the reliable ones. Reliability is highly dependent on the release momentum: a very high release momentum leads to impulses after few samples, thus not allowing the detection of three (or more) consecutive points on a straight

line (an example is shown in figure 4.25).

This difference (in terms of momentum) between reliable and non-reliable tests suggests therefore an analysis of the non-reliable tests, which are mostly non-compliant.

A typical non-reliable test has been already shown in figure 4.25; in figure 4.52 left we sketch a typical behaviour of the measured z DOF for a non-reliable test, with the absence of three consecutive points on a line due to the high momentum (the red line just connects the measured points and does not have a physical meaning). Point a is the last sample with no motion of the TM (zero reference for time axis), point b is the first sample with the TM in motion.

The absence of three consecutive points on a line is due to impacts of the TM with the plungers; however, impacts do not necessary occur in correspondence of the observation. As a consequence, the signal can be interpreted in different ways.

For instance (*interpretation A*), we could have an initial velocity in a, an impact in b with a change of slope, another impact in c, and so on. In this case, the red line would correspond to the TM motion, and the z pin release velocity would be the slope between a and b.

Another possible interpretation (*interpretation B*) is shown in figure 4.52 right: the TM starts its motion between the samples a and b, and the impact occurs between c and d; in this case, the z pin release velocity would be represented by the slope between b and c.

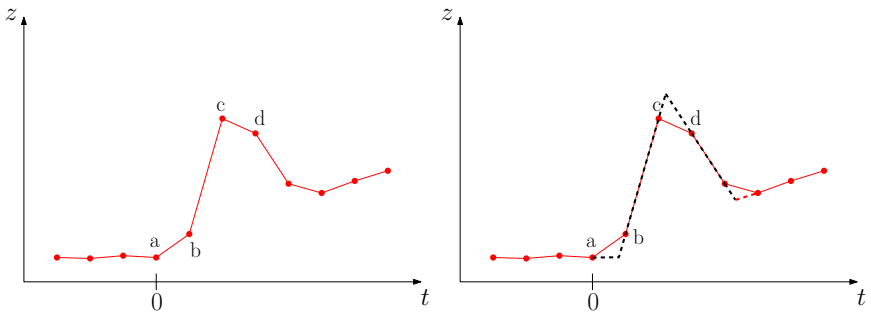

Figure 4.52: typical behaviour of a non-compliant and non-reliable fast pin test. Left: sketch of the z measured motion at the release; yhe red dots correspond to the sampled motion, while the red segments connect the dots (without physical meaning). Right: possible physical interpretation of the signal.

In principle, many interpretations of the signal (which should take into account the behaviour of all the 6 DOF) are possible, and a computation of the pin release velocities (and therefore of the impulses) depends on the interpretation of the signal.

In the following, we apply the impulse model to the non-reliable non-compliant tests; the comparison of momentum and residual impulse is shown for TM1 (figure 4.53) and for TM2 (figure 4.54). For each TM1, we consider the two described interpretations (A and B).

We remark that the first motion interpretation (A) yields in principle a *rescaled*

mean velocity, since the start of the TM motion could occur in any instant between samples a and b of figure 4.52.

Moreover, momentum and residual impulse are reported with no uncertainty, since they are computed from the variation of two consecutive samples.

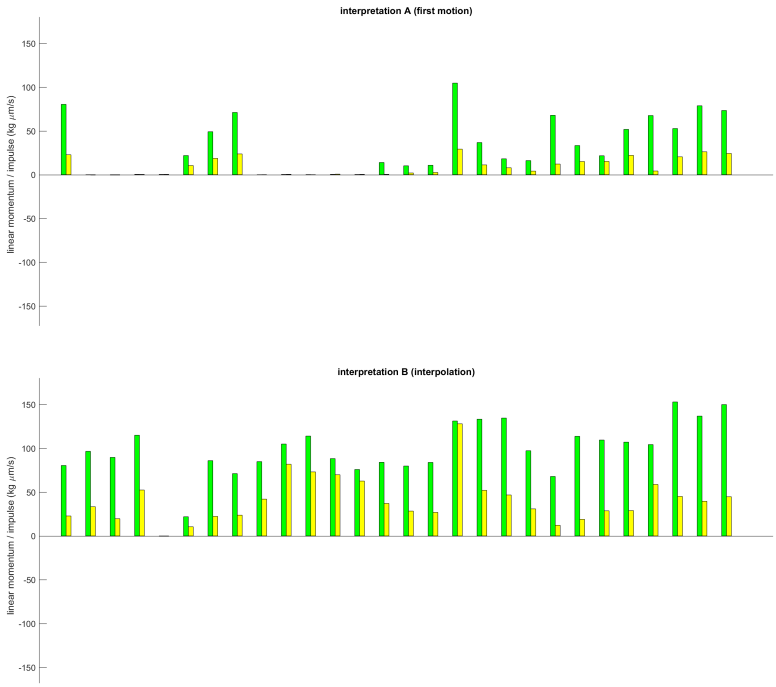

Figure 4.53: TM1: application of the orthogonal impulse model to the non-compliant non-reliable fast pin tests. Comparison between total z momentum and residual impulse ι^z_{res}, according to the interpretation of the signal. Each couple composed of a green and a yellow bar represents a test. No uncertainty band is computed, since the estimation of the velocity is based on two consecutive samples.

In figure 4.53 the results for TM1 are represented. We can see that, independently of the interpretation, the general behaviour is very similar to the one of TM1 in figure 4.50: the TM has a positive momentum (green bar), and the residual (yellow bar) is positive and always lower than the momentum. In many cases, the momentum is significantly higher than the residual, thus suggesting that the momentum is mainly due to the z impulse related to the plunger lateral impulses. For some tests, the residual has a high value (sometimes greater than 50 kg μm/s), but this could be due to an important axial effect of the pyramidal plunger, correlated with the lateral push of the plunger. In some cases impulse and residual are comparable: this would correspond to a prevailing axial effect (combination of balanced $Z+$ plunger impulse, vibration of the plunger with impact on the opposite surfaces, delay effect of the pin, adhesion).

However, due to the lack of the uncertainty of the estimation and to the dependence on the interpretation (which could significantly scale the velocities), no detailed conclusions are possible. We can just observe (qualitatively) that the "general behaviour" of TM1 is well represented by figure 4.50.

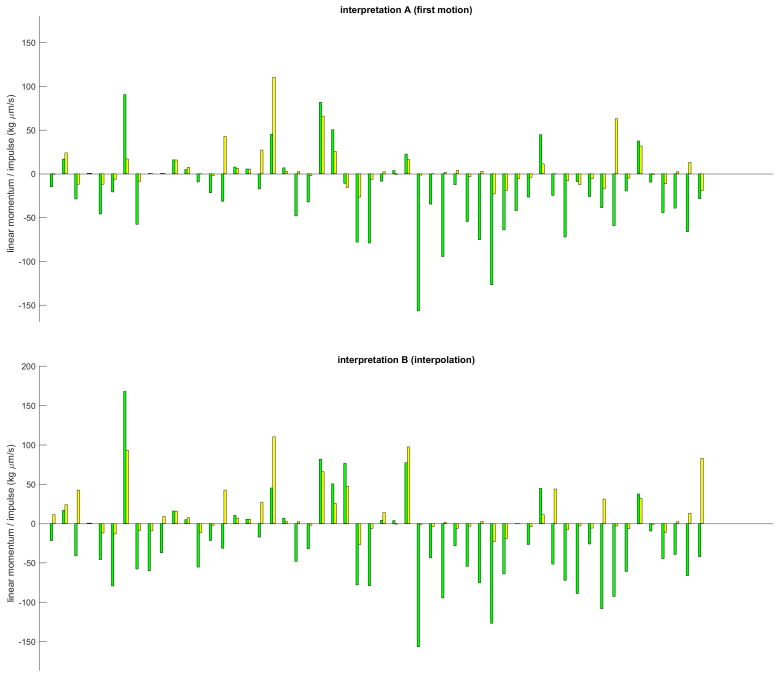

Figure 4.54: TM2: application of the orthogonal impulse model to the non-compliant non-reliable fast pin tests. Comparison between total z momentum and residual impulse ι^z_{res}, according to the interpretation of the signal. Each couple composed of a green and a yellow bar represents a test. No uncertainty band is computed, since the estimation of the velocity is based on two consecutive samples.

The case for TM2 (figure 4.53) is different. In the majority of the cases, when the z momentum is negative, the residual is very small (at least according to one of the two interpretations). This confirms the behaviour of the few TM2 tests of figure 4.50, thus suggesting a very important role of the conical plunger. In other cases, momentum and residual are comparable, with the same sign (i.e. prevailing axial effect) or opposite sign (i.e. sum of axial effect and high effect of lateral impulses). Only in one case we have a residual significantly higher than the momentum, thus suggesting that the lateral push of the (conical) plunger "mitigated" a very high axial effect.

Again, no strong conclusions can be drawn from the graph, due to the lack of the uncertainty bands and to the dependence on the interpretation (with possible scaling and distortion effects). We can however deduce that for TM2 the impulses of the conical plunger have a very important effect (leading to negative

z momentum in the majority of the cases), but with a high positive axial effect (probably due to the pyramidal plunger) in some cases. The behaviour for TM2 seems less repeatable if compared to TM1, and the results for TM2 of figure 4.50 seem therefore not fully representative, although they reflect the behaviour of the majority of TM2 tests.

Application of the model to the compliant fast pin tests

The orthogonal impulse model can be also applied to the compliant reliable tests. The set of fast pin compliant tests is composed of few tests, all belonging to TM1 (we remind that the majority of the compliant tests is composed of the slow pin tests).

The result is shown in figure 4.55. We can see that the residual impulses are generally comparable w.r.t. the z momentum; this would correspond to a negligible effect of the lateral impulses for the z momentum. In few cases, the residuals are statistically higher than the momentum: this shows a role of the lateral impulses of the plunger.

We can conclude that for the compliant reliable fast pin tests the z momentum is mainly due to an axial effect; independently on its motivation (plunger push or force due to the pin), the axial effect corresponds however to small impulses (TM velocities lower than 2.5 μm/s). Moreover, the significant difference between z momentum and residual for some tests suggests that the TM-plunger contact occurred also for compliant tests.

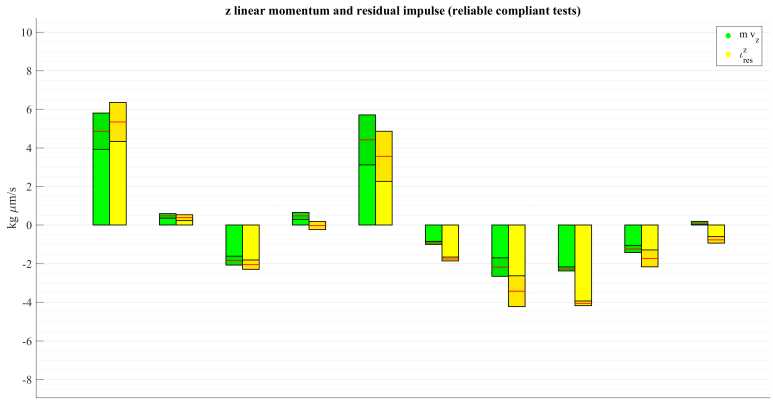

Figure 4.55: orthogonal impulse model: comparison between total z momentum and residual impulse ι^z_{res} for the compliant reliable fast pin tests. All the tests belong to TM1.

Application of the model to the slow pin tests

The result for all the S tests is shown in figure 4.56. We see that for the majority of the tests the z momentum and the residual ι^z_{res} are comparable, but in other cases the residual is different (sometimes higher) than the momentum, thus highlighting a contribution in z direction of a plunger contact. The residuals are however (except for one case) always lower than 5 kg μm/s, which is the momentum corresponding to a velocity of 2.5 μm/s.

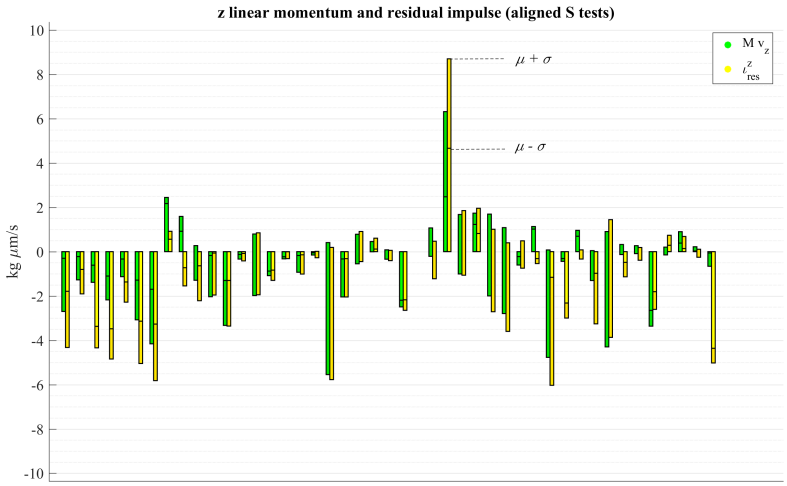

Figure 4.56: orthogonal impulse model: comparison between total z momentum and residual impulse ι^z_{res} for slow pin tests. Only reliable tests have been considered in the computation. Each pair of columns corresponds to a single release test. The end of each column (of a darker colour) indicates the range of the uncertainty, as shown in the figure (μ is the estimated value and σ its standard deviation).

4.8 Slow pin releases

The release momentum for the slow pin releases (S tests) has been commented in section 4.3 (plunger release velocities) and in section 4.5 (pin release velocities).

The large majority of the measured pin release momenta of the S tests have been inside the requirements; in particular, for all the tests the translational DOF have been compliant. This was expected due to the slow dynamics of the pin releases, which (in a nominal situation) confines the TM between two pins moving with opposite velocities of 2.5 μm/s (a velocity lower than the requirement of 5 μm/s).

The slow pin tests could be interesting for our purposes since, in their nominal dynamics, their final velocity along z should be mainly affected by the difference of the two adhesive pulls, thanks to the minimization of other effects that could occur (for instance) in the fast pin releases. However, as commented in section 4.5.4, the slow pin releases (like the fast pin releases) are affected by variations in the momentum due to impacts, which can slightly increase the TM momentum (although not critically in general).

In section 4.8.1 we describe the behaviour of the release mechanism in a slow pin release according to the nominal configuration (i.e. contact occurring uniquely between TM and pins, and mono-dimensional dynamics along z axis): we prove that in this case the final momentum of the TM should be uniquely due to the difference of the adhesive pulls on the two sides of the TM.

In section 4.8.2 we discuss a typical slow pin test, commenting the criticalities in the interpretation of the signal. In section 4.8.3 we discuss the main information obtained from the slow pin releases, by taking into account the differences between the slow pin release dynamics and the nominal fast pin case (which was the reference case of the on-ground testing).

Finally, we recall briefly in section 4.8.4 the comparison between the pin release velocities and the plunger release velocities of the S tests, which (especially for TM2) shows an important effect of the plungers on the final momentum of the TM.

Notice that all the considerations of this section are based on the analysis of the reliable slow pin tests (which constitute the majority of them). For the non-reliable slow pin tests, the computed velocities (reported in appendix C.6) are always in the requirements (except for one case); although we cannot rely completely on these quantities, they show that the TM pin release momentum is always small also for the non-reliable tests. Since no significant difference occurs between the reliable and non-reliable tests (based on the release velocities), we can consider the subset of the reliable tests representative of the whole set of S tests.

4.8.1 Slow pin release: nominal case

In figure 4.57 the steps of a slow pin release test are shown, according to the nominal configuration. As described in section 4.2.1, the pin retraction occurs symmetrically on both sides. After the handover to pins, the TM is in contact with the pins (figure 4.57 a), which are extracted of 18 μm, with a preload f_0. The pins start their motion, with a commanded velocity of 2.5 μm/s (thanks to a slow

voltage fall of the piezo).

Similarly to what discussed in section 4.2.3, the contact force between TM and pin is 0 (figure 4.57 b) when each pin is retracted of the quantity

$$\Delta z = \frac{f_0}{k}$$

since (as shown in the picture) Δz is the compression of a single plunger (stiffness k) at the preload f_0. If the system is perfectly symmetric (i.e. equal stiffnesses of the two plungers), the two opposite pin retractions guarantee that the TM does not move during the preload decrement.

The further retraction of the pin (figure 4.57 c) gives an adhesive pull to the TM due to the elongation of the adhesive bonds; after the rupture of the adhesive bonds, the TM moves in z direction with a residual momentum, given by:

$$Mv_z = \iota_{adh,1} - \iota_{adh,2} \tag{4.44}$$

where $\iota_{adh,1}$ and $\iota_{adh,2}$ are the opposite adhesive pulls of Z+ pin and Z- pin respectively.

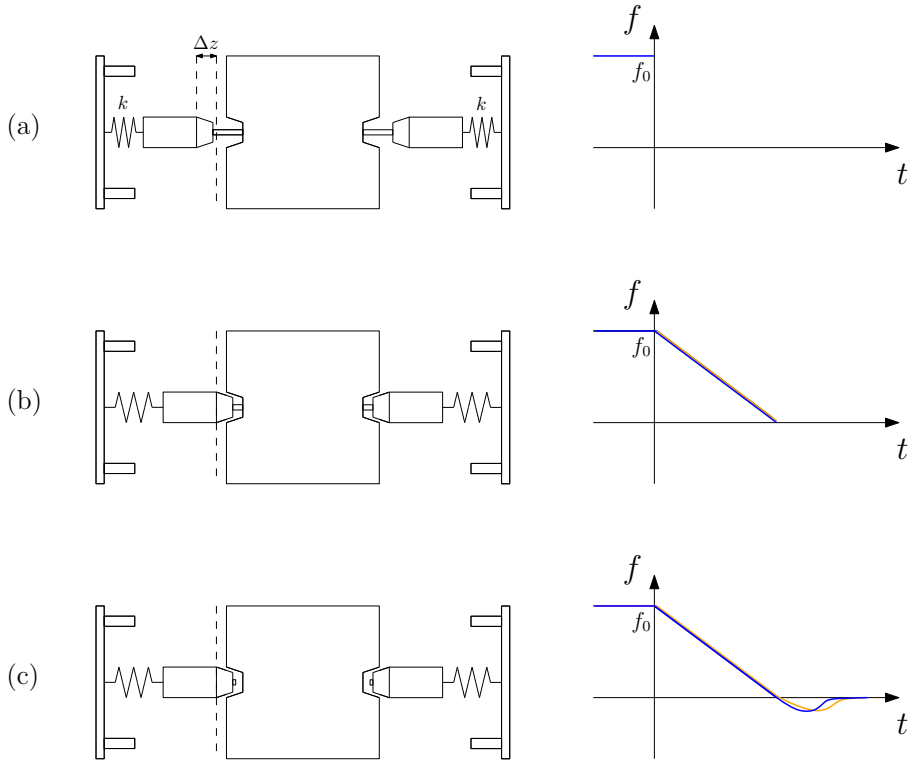

Figure 4.57: slow pin release (nominal situation). TM blocked by the pins (a); fall of the preload until a zero contact force between TM and pins (b); adhesive pulls and detachment between TM and pins (c).

time	operation
-1 s	enable DFACS 10 Hz data collection
0 s	TM release (slow retraction of the pins)
4 s	slow plunger retraction for 200 steps
4 s	DFACS Mode Change ACC1
19 s	fast plunger retraction for 1200 steps

Table 4.13: timeline of the slow pin tests when the capacitive control is enabled (this occurs for the *automatic tests* of July 2017) [112]. The commanded release is considered as the zero reference for the timeline.

This release model is similar to the nominal model for a fast pin release (section 1.1.6), but in this case no pushing effect is given by the delay among pin retractions or by the different velocities of the pins (for this reason, the two decreasing forces are overlapped in figure 4.57). The duration of the fall of the preload force has indeed a duration of tenth of ms, which is higher than the quarter of period of the TM-plunger oscillator. If we consider for instance a very small preload of 20 mN (worst case), the unloading duration would be (according to the estimation of k of section 4.2.3)

$$\Delta t = \frac{\Delta z}{v_{pin}} \approx \frac{f_0/k}{v_{pin}} = \frac{0.02\text{N}/(0.38\text{N}/\mu\text{m})}{2.5\ \mu\text{m/s}} \approx 20ms$$

while the quarter of period of the TM-plunger system is

$$\frac{T}{4} = \frac{1}{4}\frac{2\pi}{\omega} = \frac{\pi}{2}\sqrt{\frac{m}{k}} \approx \frac{\pi}{2}\sqrt{\frac{2\text{ kg}}{380000\text{ N/kg}}} = 3.6\text{ ms}$$

As a consequence, as shown in figure 4.58, if we consider that only one pin starts the motion and the other does not move (worst case for delay effect), the effect of the delay is exhausted when the TM is still in contact with both the pins; therefore, the delay effect cannot give momentum to the TM (the resulting force on each side is similar to the response to a slow ramp, simplified in the figure). As a consequence, we can consider the unload procedure as a quasi-static release w.r.t. the stiffness of the system: when the preload is 0 on one pin, is 0 also for the other one, therefore no pushing effect exists.

In a nominal situation, the slow release procedure allows therefore to make the release velocity depend uniquely on the opposite adhesive pulls, eliminating the effect of the preload; moreover, due to the controlled decrease of the preload, also the vibrations of the release mechanism are minimized.

For the slow pin tests, the capacitive control is eventually activated some seconds after the pin release, synchronously w.r.t. the plunger retraction [112]. The timeline is shown in table 4.13.

4.8.2 Pin release velocity in the slow pin releases

In figure 4.59 an example of slow pin test is chosen (test 74, TM1). In figure 4.60 the comparison between z motion (measurement) and Z+ pin (commanded

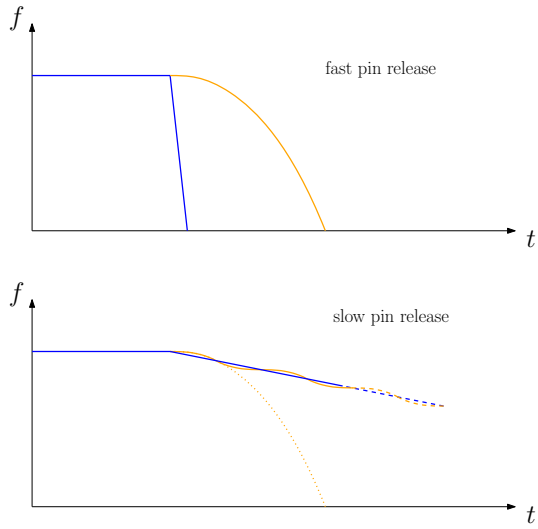

Figure 4.58: delay effect in the fast pin releases (top) and in the slow pin releases (bottom). In a fast pin release, if a delay between the two pins exists we obtain a continuous push of one pin as a cosine. In a slow pin releases, if only one pin starts its motion, its slow retraction allows to eliminate the push due to the delay effect (the represented behaviour of the two pins during the decrease is a simplification of a similar but more complicated 2 DOF oscillation).

displacement) is shown for the same test (there is no difference between Z+ pin signal and Z- pin signal since the commanded motion is the same). The two time axes are aligned, but the pin release signal has a lower sampling w.r.t. z signal (in the figure, the pin start occurs therefore between points A and B).

In figure 4.60, two velocities for the signals are computed: a first slope $v_{z,1}$, and a second slope $v_{z,2}$. According to the classification procedure described in 4.4.1, $v_{z,1}$ has been classified as the pin release velocity, and $v_{z,2}$ as a velocity after impact. As a consequence, we assume that the detachment has occurred before the interval associated to $v_{z,1}$. The samples of the measured velocity $v_{z,1}$ satisfy indeed the reliability tests, therefore we consider that the TM is moving freely in that interval.

The majority of the S tests (in particolar the automatic tests of July 2017) show a behaviour similar to the test of figure 4.59, with the TM moving mainly along z (z is the unique DOF that exits its $\pm 10\sigma$ noise band), therefore with a behaviour close to the nominality. However, another group of S test (especially the ones of June 2017, TM1) is characterized by a x velocity higher than the z one, thus suggesting a behaviour different than the nominal and a possible effect of plunger contacts also for the slow pin releases.

In the following, we analyze the reference test of figure 4.59. We prove that the z velocity can be due to the two opposite adhesive pulls described in section 4.8.1; as an alternative motivation for the momentum at the release, we investigate the

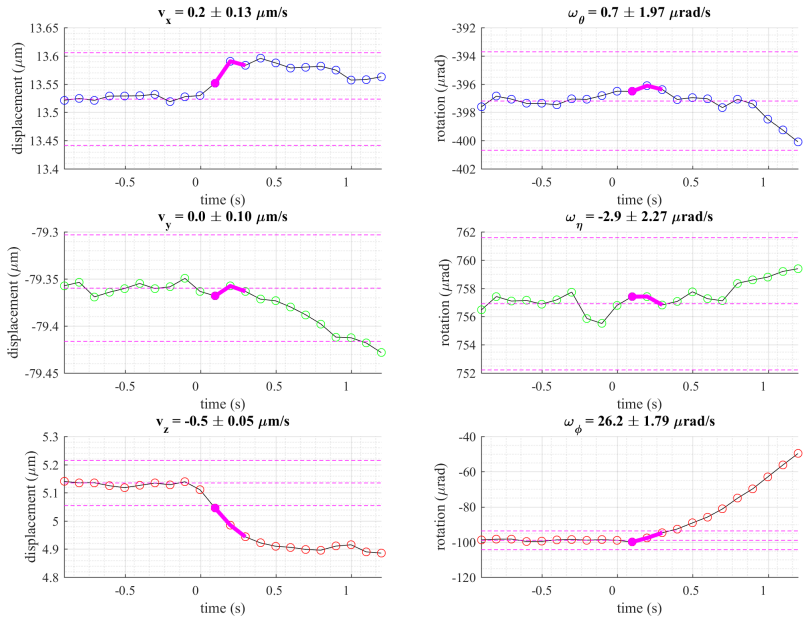

Figure 4.59: slow pin release: example (test 74, TM1). For each DOF, the interval chosen for the computation of the pin release velocity is shown. For each DOF, the dashed lines correspond to the $\pm 10\sigma$ interval, with σ standard deviation of the pre-release noise.

possibility of the TM-plunger impulses applied in the slow pin tests.

Preliminary consideration: exclusion of stiffness asymmetry

If the TM is moving freely in the interval of velocity $v_{z,1}$, the detachment between TM and pins must have occurred before that interval. However, by looking at figure 4.60, we see that the pin is still retracting when the velocity $v_{z,1}$. Therefore, the velocity $v_{z,1}$ could be actually not a free flight velocity, but it could be produced by an asymmetry of the two plunger stiffnesses, which relax with a different elongation rate (thus contradicting the hypothesis of equal stiffnesses). Under this alternative hypothesis, $v_{z,1}$ would correspond to the TM moved by the two pins retracting at different velocities; the real release velocity after the detachment of the TM could be in this case $v_{z,2}$.

In appendix C.4, we refuse this alternative hypothesis, by means of the model of figure 4.57, thus confirming that $v_{z,1}$ is a free flight velocity of the TM.

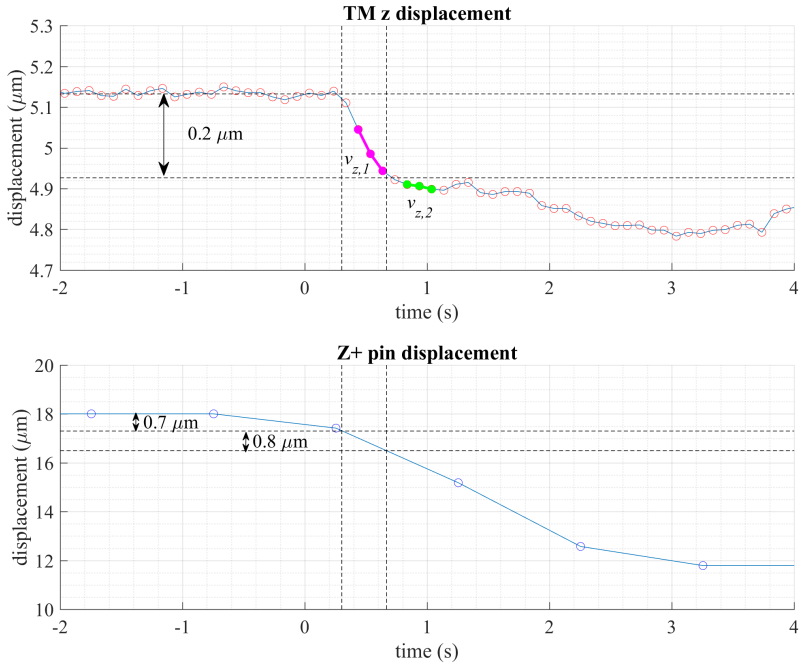

Figure 4.60: slow pin release (test 74, TM1): comparison between z signal (10 Hz) and pin Z+ signal (1 Hz).

Uncertainties in the TM dynamics: elongation of the adhesive bonds

For the previous test, we can consider that $v_{z,1}$ corresponds to the free velocity of the TM: $v_z = v_{z,1}$.

We have moreover that the velocity v_z is lower than the velocity of the pin retraction (which is 2.5 μm/s). We would therefore conclude that the TM has detached from both the pins, thus applying equation (4.44) in order to state that the elimination of the two opposite adhesive pulls transferred a low residual momentum to the TM.

However, we can see that, before the change in the velocity (discussed in the following), the TM has moved of a total displacement of ≈ 0.2 μm; in the same interval, the Z- pin has moved of ≈ 1.5 μm; therefore, assuming a nominal situation, the distance between TM and Z- pin is ≈ 1.3 μm when the velocity changes (instant B in figure 4.60). With a similar computation, we get that the distance between TM and Z+ pin should be ≈ 1.7 μm.

We can see therefore that the velocity v_z is computed in a range where the adhesive bonds could still not be broken (as explained in 1.1.6, we expect a maximum elongation of 2 μm in the in-flight case). Although we are here considering a case far different than the nominal fast pin case assumed in the on-ground testing (the pin velocity for the S tests is lower of many orders of magnitude), we cannot

exclude that an elongation of the adhesive bonds still arises before the TM changes its velocity.

Despite this uncertainty, we can say that a cancelation of the two adhesive effects is occurring in this case, since the distance between the TM and the pins is increasing. In particular, we have that the two adhesive pulls are equilibrated (i.e. with a low net pulling impulse), thus allowing the detachment of the TM from the pins. If an adhesive pull is much higher than the opposite one, the TM could indeed remain rigidly attached to one pin, following its motion with the same velocity (we remind that the very quick retraction of the pins in the nominal release was chosen to avoid this situation, see section 1.1.4).

Uncertainties in the TM dynamics: change in the TM velocity and contact with the plungers

A further uncertainty of the TM dynamics arises if we focus on the change of the TM z velocity (from $v_{z,1}$ to $v_{z,2}$). This change, which has been classified as an "impact", is quite repeatable for the S tests of the release campaign, and it occurs after a very little displacement of the TM.

According to the previous observations, the change in the z velocity could correspond to the complete rupture of the adhesive bonds between the TM and the pins (which were elongating in the interval of $v_{z,1}$ computation). In the case of figure 4.60, this would witness a perfect cancelation of the opposite adhesive impulses.

A different explanation is the existence of an impact between TM and the plungers, that stops the motion of the TM (maybe contributing to the complete rupture of the adhesive bonds, if we assume they were still elongating). This hypothesis seems supported by the observations of the previous section 4.7, where we have proved that impulses between the TM and the plungers on the coupling surfaces can explain the momentum at the release; since these impulses occurred immediately after the pin release, we suspected that the TM is very close to the plungers (or already in contact with them) before the pin release. Moreover, for the slow pin test of figure 4.60, the translational velocity reduces significantly after the impact, and the main behaviour is a rotation of the TM (especially about z axis). If the impact has occurred against the pyramidal plunger (as we can deduce from the behaviour of the z degree of freedom), the pyramidal shape can create a momentum in ϕ (according to the dynamics presented in appendix C.3); we see indeed from figure 4.59 that the slope of the ϕ DOF increases after the impact.

This would witness a non-nominality of the pin releases. This hypothesis is supported by the analysis of another group of tests (slow pin tests of June 2017), where, compared to the reference case of this section, we see that:

1. after the impact, the velocities of x and η increase (in some cases, exceeding the requirements), and the velocity in z can change sign.

2. the x pin release velocity can be higher than the z pin release velocity, thus suggesting a deviation from the nominal release.

Point 1 highlights the impulse between TM and plunger *after* the release; while point 2 suggests a contact between TM and plunger *at* the pin release (exactly like

in section 4.7).

We could therefore ask ourselves if the orthogonal impulse model of section 4.7.2 can explain the z momentum of the reference test better than the nominal model of equation (4.44).

The result for the reference test is shown in figure 4.61. Although we know that ι^z_{res} could be the sum of many effects (additive or subtractive), we can see that the residual ι^z_{res} (i.e. the part of the z momentum that cannot be explained by orthogonal impulses between TM and plunger) does not differ significantly from the z momentum. This suggests that the momentum z of the test can be effectively due to the opposite adhesive impulses between TM and pin, which are not considered in the orthogonal impulse model.

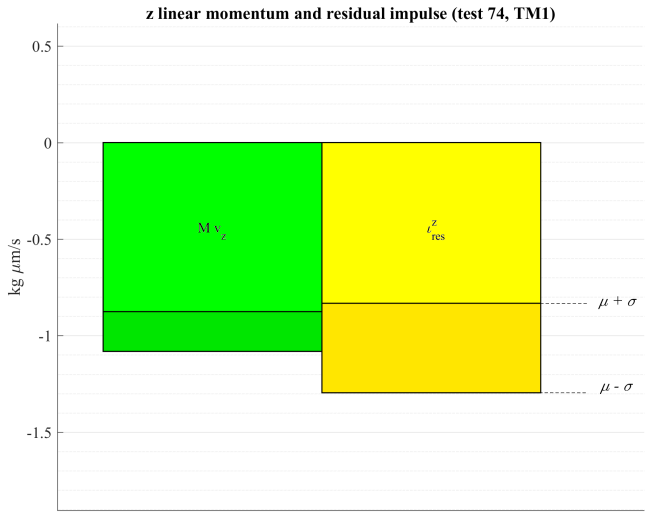

Figure 4.61: slow pin release (test 74, TM1): comparison between z momentum Mv_z and the residual impulse ι^z_{res} according to the model of section 4.7.2.

We have seen in figure 4.56 that this condition (momentum similar to the residual) holds for the majority of the tests, but for some tests the TM-plunger contact at the release cannot be excluded.

Uncertainties in the TM dynamics: electrostatic attraction between TM and plunger

The previous observations suggest that the slow pin releases do not occur nominally: a contact with the plunger at the release is suspected (due for instance to high translational velocity), and the TM stops its motion after a small displacement (also lower than 1 μm).

The proximity between TM and plunger suggests that the electrostatic attraction between the two bodies (due to the difference of voltage) can have an important effect.

If we consider a constant different of voltage between TM and plunger, the TM motion of the reference test of figure 4.60 is compatible with the TM-plunger attraction. According to the electrostatic models of [104] and [105], if we simulate an initial distance between TM and Z- plunger of 0.2 μm, a constant difference of voltage of 0.1 V could create a motion of the TM towards the plunger similar to the measured one.

If we consider instead a constant TM charge, according to the model of appendix C.5 the TM motion could be explained by an electrostatic effect only in a worst case.

In conclusion, the electrostatic effect for the slow pin releases cannot be excluded, due to the low pin release velocities whose order of magnitude is not significantly different than a velocity due to capacitive forces. A more accurate FEM analysis (which would be an improvement of [104]) should take into account both the capacitive forces, the TM dynamics and the TM-plunger contact.

If the plungers are very close to the TM, the important effect of the difference of voltage was observed also in previous simulations of the release [104].

As a consequence, we cannot exclude that the pin release velocity of the slow pin releases is affected by an electrostatic attraction between TM and plunger, due to the slow dynamics of the TM and the proximity of the bodies.

4.8.3 Information in the slow pin releases

As for the example of figure 4.59, in the slow pin tests the TM moves with a very low velocity when the pins start their retraction; the TM changes its velocity after a small displacement (less than 1 μm), as a consequence of an impact with the plunger. These behaviours are independent on the initial preload force before the retraction of the pins.

In the following, we discuss the main information that can be extracted from the pin release velocities of the S tests. The information is unfortunately highly affected by the uncertainty of the dynamics described in section 4.8.2.

Hypothesis: momentum transferred by adhesive pulls

If we look at the in-flight results (table C.6), we see that the reliable S tests have generally a z velocity inside the range -2.5÷2.5 μm/s, as expected. Few of tests show a higher z velocity (e.g 4 μm/s), which contradicts the dynamics since the TM would move faster than the pin retraction; however, these tests can be neglected since they show anomalies in the ϕ rotation before the release (as reported in appendix C.6), thus revealing that the TM was in motion before the release. It has been indeed proved that all the tests with significant ϕ rotation before the release are characterized by a level of preload (force drop of figure 4.19) that is statistically compatible with a null force [114]. Moreover, a missing contact between TM and one plunger allow a higher motion in z of the TM (thus making possible a velocity higher than 2.5 μm/s).

In figure 4.62 we plot the distribution of the z pin release velocity of all the reliable S tests of TM1 and TM2 (we have neglected the tests with ϕ anomalies before the release).

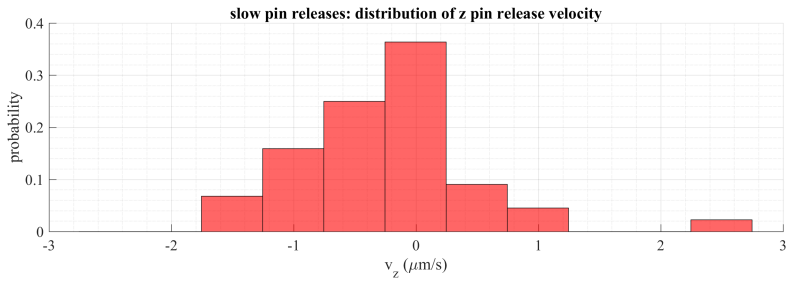

Figure 4.62: probability distribution of the pin release velocity v_z for the S tests of the release campaign (44 tests). We have considered here only tests with reliable measurement of the velocity, i.e. reliable tests without ϕ rotation before the pin release (which generally witnesses a TM not held firmly by the pins).

For all the slow pin release tests (except for one case) the velocity is lower than the pin release velocity. This means that, if these velocities are produced only by contacts with the pins, in the large majority of the cases a detachment of the TM from the pins has occurred (or is occurring) as a consequence of the cancelation of the opposite adhesive pulls. This would make us conclude that the cancelation of the opposite adhesive pulls in the slow pin releases makes the TM move with a very small velocity after the release. Moreover, it has to be remarked that in the slow pin tests the velocity of the pin at the retraction is very low: as discussed in section 1.1.6, a higher velocity of retraction would further decrease the impulse due to adhesion (if we assume the same value of binding energy).

However, the very low velocity of retraction of the pin in the S tests w.r.t. the fast pin releases (2.5 μm/s versus $\approx 10^5$ μm/s) does not allow to state that this situation can be transferred to the fast pin case through a model that scales the velocity of the pin retraction (for instance by considering equation (1.8)). The scale factor is too high, and the dynamics time scale too different, in order to consider the slow pin a worst case with low velocity and the same value of binding energy.

Therefore, the main conclusion we can draw (if we interpret the pin release momentum through the nominal model of section 4.8.1) is related to the equilibrium of the adhesive forces in the slow pin release, that creates the detachment of the TM: this suggests that the probability distribution of the opposite impulses has a reduced dispersion, thus yielding to low values of their differences. This conclusion is supported in particular by the fact that only in 1 of the considered 44 tests of figure 4.62 the TM remains attached to one of the two pins.

Contacts with the plungers and electrostatic effect

In section 4.8.2 we have seen that, for some tests, the pin release velocities show x components higher than the z one, thus suggesting the application of the orthogonal impulse model (figure 4.47) which yielded the result of figure 4.56. For each test, the residual impulse is not so different from the measured z momentum. As a consequence, if we assume that the residual (which is the part of linear momentum not explained by the impulse model) is due to the adhesive pulls, the previous considerations still hold: the action of the adhesive pulls produce a cancelation and a velocity of the TM lower than the velocity of the pins (and, as a consequence, the detachment from the pins).

However, as discussed in section 4.7.4, once we assume a contact with the plunger, we cannot exclude that the residual impulse ι^z_{res} is also due to the plunger effect.

Moreover, the proximity of the plunger w.r.t. the TM could produce a non-negligible electrostatic attraction.

Based on these observations, the only conclusion that we can draw is the following. The slow pin release momenta can be affected by opposite adhesive pulls, by contacts with the plungers, by electrostatic attraction, or by a combination of all these factors. For each test, if we assume that the z velocity is produced by the opposite adhesive pulls, this suggests a cancelation of the opposite pulls (notably, only one of 44 has the same velocity of a pin). If we consider instead that a contact with a plunger has occurred, no significant conclusion can be drawn due to the uncertainty of the dynamics (since we cannot identify a priori the residual with the adhesive impulse). In this case, we can only observe that in the large majority of the cases a detachment between TM and pin can be considered, due to the z velocity of the TM lower than the pin velocity.

Deviation from the nominal release: first impact

In the slow pin releases, the change in the TM z motion after a very small displacement reveals that the system configuration at the detachment is not nominal, since the nominal gap would be higher than 1 μm. This fact suggests that the plungers are very close to the TM when the pins start their retraction.

4.8.4 Effect of plunger retraction

As already observed in 4.5.5, the kinetic energy at the pin release for the S tests is completely different than the one after plunger retraction (i.e., for the S tests the *plunger release velocities* are much more critical than the *pin release velocities*). This occurs especially for TM2. When the plungers are retracted, high impulses are given to the TM, transferring a momentum which is comparable to the one observed for the plunger releases (section 4.3.2). Again, the behaviour for TM2 has a low repeatability w.r.t. the more regular behaviour of TM1. The high impulses given by the plunger in this situation can be due to the kick effect (plunger bistability discussed in section 4.2.3).

For tests like the one of figure 4.60, the important effect of the plunger retraction on the slow pin tests can be explained with the fact that the TM rests on one

plunger after the first impact (as we can suppose from figure 4.60), thus increasing the effect of the irregular motion of the plunger on the TM when the plunger is retracted.

As a consequence, the slow pin strategy could not work if the plungers show an irregular behaviour. For TM2, the fast pin releases give a better result in terms of plunger release velocity (as shown in figure 4.16): this could be due to the high kinetic energy of the TM at the fast pin release, which can be gradually reduced by bounces and which makes the motion of the TM between the plungers reduce the probability for the TM to rest on one plunger.

4.9 Future development of the GPRM

In this section we collect some hints for the future development of the GPRM, based on the preliminary analyses described in this chapter.

Since the scientific task of the LISA Pathfinder mission was fulfilled, all the components of the GRS involved in the science phase have to be maintained. As a consequence, the housing (with the electrodes) and the TM cannot be modified. In particular, the TM material and geometry have to be maintained. Slight modifications are allowed only for the GPRM.

We discuss first the possible motivations of the non-nominal behaviour of the GPRM, based on the analyses reported in this thesis and on a more detailed geometrical analysis which was performed in 2019.

In section 4.9.2 we discuss the best release strategies if no modifications of the GPRM are possible. In section 4.9.3, we propose possible changes to the GPRM design. Finally, in section 4.9.4 we propose experimental strategies for the testing of the GPRM in view of LISA mission.

We remind that these hints are based on a preliminary analysis of the in-flight data, and their feasibility (in terms of construction of compliance with the tasks of the GRS) should be further discussed. Moreover, due to these limitations we propose here qualitative solutions (i.e. no detailed quantities are reported).

4.9.1 Possible motivations of the non-nominal behaviour of the GPRM

In this chapter we have discussed some possible motivations of the non-nominal behaviour of the GPRM at the release, which are due (with a high probability) to the undesired contact between TM and plungers.

- bistability of the plungers (section 4.2.3). The bistability of the plunger (i.e. change of the orientation when the motion is reversed) can have two effects. It can lead to a rotation of the plungers at the handover to pins, which reduces the clearance between TM and plungers when the TM is held by the pins. Its main effect can be a lateral motion of the plungers when the plungers are retracted, which can explain the high plunger release velocities of the release campaign.

- plunger oscillation at the release. Due to the axial preload applied on each plungersbefore the release, the quick fall of the preload force at the release can make the plunger oscillate axially. This can create a push of the plunger to the TM (if the plunger is already in contact with the TM before the release) or an axial oscillation of the plunger, which can create an impact if the clearance is reduced. These hypothesis have been explored through simple linear models in the preliminary analysis of the appendix C.2.

- the high oscillation of the load cell signal did not allow the application of a precise preload before the release. Moreover, the load cell seems affected by a constant offset (a positive value can be read when the effective force is zero). These problems led to the strategy described in section 4.4.2, where

the a force drop between two averages was considered (see figure 4.19). As a consequence of the low preload, some tests showed a ϕ rotation before the release.

In 2019 a detailed analysis of the relative position between TM and plungers at the release has been performed [114]; the analysis took into account previous documents (regarding tolerances and on-ground tests) and the analysis of the position of the mechanism in the release campaign. The results are the following:

- the analysis of the relative position and attitude of TM and plunger is affected by high uncertainty w.r.t. the estimated offsets; a precise estimation of the gaps between TM and plungers is not possible.
- additional TMMF tests have shown that the effective stroke of the pin is approximately 15-16 μm (instead of 18 μm). This contributes to the reduction of the nominal clearance between TM and plungers of $\approx$ 2-3 μm.
- additional TMMF tests have shown that after the release the plunger can have an axial oscillation with 2 μm amplitude, and a lateral oscillation of 0.5 μm; the oscillations can contribute to the reduction of the gap after the pin release.
- the uncertainties on the rotations of the plungers are compatible with the rotational gap in the case of a reduced clearance; this means that the sum of reduced gap and plunger rotation can lead to a contact before the release. A possible contact is suggested by very high ϕ rotations (especially for TM2).

4.9.2 Release strategies without modifications of the GPRM

In the in-flight release campaign of 2017 many release strategies have been tested. Notably, a "safe" strategy was not found, since each one led to critical velocities of the TM for a subset of the release tests.

In particular, the following observations have been made:

- the plunger relase strategy (P tests, i.e. release performed with no retraction of the pins) always leads to very high linear and angular momenta of the TM. This is probably due to the "kicks" of the plungers at their retraction (see sections 1.1.5 and 4.2.3).
- the fast pin strategy (N, R tests) can lead to high momenta of the TM at the pin release, exceeding the requirement (also of 1 order of magnitude). As discussed in section 4.7, contacts with the plunger at the pin release are highly suspected to be responsible for this behaviour. However, it was observed that in these cases the kinetic energy of the TM decreases after the impacts and it decreases generally also after the plunger retraction is commanded (sections 4.5.4 and 4.5.5). Therefore, for this strategy the final momentum is dominated by the pin release momentum.

  Regarding the fast pin tests, no systematic difference was observed between a nominal release with full pin extraction (N tests) and a release with reduced pin extraction (R tests).

As commented in section 4.5.2, for this category of tests a poor correlation between the preload and the final momentum was observed.

- the slow pin releases (S tests) gave contradictory results: the final momentum was quite low for TM1, but for TM2 was often uncontrollable by the capacitive system. In general, all the slow pin releases have shown a very low pin release momentum, but the plunger retraction was critical in many cases, probably due to the lateral motion of the plunger at the retraction: the TM rests close to one plunger after the retraction, thus increasing the effect of the plunger motion. Moreover, a contact with the plunger at the pin release is suspected.

All the observations highlight the detrimental effect of the plungers.

In general, at the pin release a contact with the plunger cannot be excluded for any category of test; the contact could occur due to the elastical relaxation of the plunger (see appendix C.2), or due to a pre-existing contact after the handover to pins.

As a consequence, the effect of the lateral motion at the plunger retraction must be minimized and the TM-plunger clearance increased.

We propose in the following an alternative strategy, which is an improvement of the fast pin release. This strategy necessarily relies on bounces between the TM and the plungers, and should be performed manually or thanks to a control loop (automatic procedure that takes into account the feedback of the signals).

1. before the grabbing, the oscillation of the force read by the load cell is analyzed in order to define a zero level of the force (as discussed in section 4.4.2, the preload corresponds to the *force drop*, due to the constant offest of the load cell).

2. the TM is grabbed. In principle, repeating many times the handover to pins (*hammering* procedure) can improve the alignment of the TM.

3. the handover to pins is performed, with full pin extension, and the preload is kept at a level o 0.2 N. This allows to apply a low force on the plungers, but at a level that can be considered significantly higher than the noise of the load cell (i.e. statistically greater than 0). A necessary condition for a successful handover to pins is the observation of a constant value for all the DOFs; for instance, no drift of the ϕ signal must be seen.

4. the pins are quickly retracted (nominal release). This could confer a high momentum to the TM.

5. the capacitive control is enabled and the plungers are retracted, but immediately stopped after a displacement of few microns. This allows to reverse the motion of the plungers, thus inducing their lateral motion. According to [55], a retraction of ≈ 50 μm should exhaust the lateral motion due to the bistability (as shown in figure 4.64). The TM will eventually acquire further kinetic energy, but (since the plungers are stopped and kept close to the TM) repeated bounces between TM and plunger will decrease the kinetic energy of the TM, maintaining it in a limited displacement range.

6. when the kinetic energy of the TM is close to the requirement, and if the ϕ rotation is controllable, the plungers are retracted immediately after a bounce with the TM. This allows the plungers to retract without unexpected lateral motion (the reversion of their motion was already performed at point 5) with a TM kept close to the zero reference and with a limited momentum.

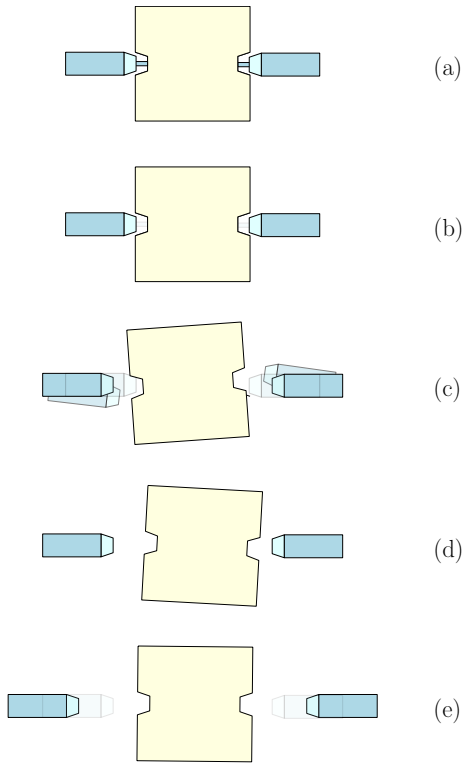

Figure 4.63: possible release strategy in absence of changes to the GPRM. (a) TM held by the pins (completely extended), low preload. (b) quick pin retraction. (c) short and slow retraction of the plungers, in order to revert their motion and exhaust the lateral motion due to bistability. (d) reduction of TM kinetic energy due to bounces. (e) quick retraction of the plungers.

4.9.3 Modifications of the GPRM

Based on the considerations of section 4.9.1, we propose here possible modifications of the GPRM.

A possible re-design of the GPRM should focus on avoiding contacts between plunger and TM. In particular, a modification of the mechanism should:

- avoid contacts between plunger and TM after the passover and before the release.

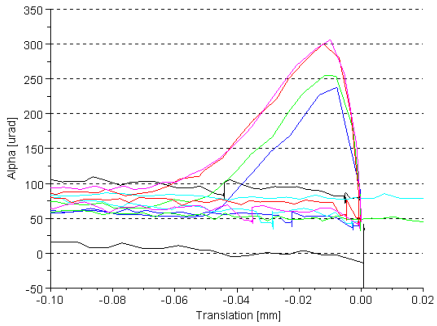

Figure 4.64: rotation of a plunger at the inversion of the motion: measurement performed by RUAG (from [55]). Each coloured line corresponds to a test. The plunger is first extracted and then retracted; at the retraction, the inclination has a significant oscillation (w.r.t. the initial value) for approximately 50 μm.

- avoid contacts between plunger and TM when the pins are retracted and when the plungers are retracted.

We propose here some possible modifications (discussed also in [114]).

Improvement of the load cell reliability

The load cell should be modified in order to avoid constant offsets and high noise. Such an improvement would allow to have a reliable feedback on the effective grab of the TM (avoiding unexpected ϕ rotations before the pin release) and to apply low preloads with a high precision (thus minimizing the elastical relaxation of the plungers).

Improvement of the GPRM guiding system

The GPRM mechanism should be re-designed first (or at least analysed and tested more in detail). According to previous on-ground tests of the GPRM (see section 1.1.5), the slider-roller guiding mechanism was considered as a possible motivation of the lateral motion of the GPRM, leading to a "moderate" risk of contact after the handover to pins and a "high" risk of contact after the release. This is described in [55], where the performance of alternative guiding systems is commented. For instance, the ceramic ball bearings should lead to a more precise in-flight performance, although they are affected by a high risk of change of alignment during launch.

Increment of the TM-plunger distance through a longer pin

In order to avoid the contact between TM and plunger at the handover to pins, the pin length could be increased. A longer pin extraction was attempted in the release campaign of 2017, but the simultaneous activation of the nominal and redundant

piezo mechanism was not possible due to constraints of the mechanism and of the circuit.

A higher pin length should increase the distance between TM and plunger after the handover to pins, thus reducing the probability of a contact.

However, this could create (in principle) a higher rotational instability of the system, since a higher length of the pin allows a higher relative rotation of each plunger w.r.t. the TM (for instance, the increment of the clearance could allow a higher ϕ rotation). As a consequence, this change should take into account also a modification of the plunger end shape.

4.9.4 Experimental testing of the GPRM

In the following some strategies for the testing of the adhesive effect and of the GPRM performance are proposed.

Test of adhesion between pin and TM

The modal approach presented in chapter 3 is a valuable strategy for the estimation of small adhesive effects, since it allows an estimation of amplitude and duration of the impulse. However, the test mass of the TMMF was not designed specifically for the modal-based experimental method.

By maintaining the same setup of the TMMF, a thinner TM would allow to increase the sensitivity of the mode shapes w.r.t. the force, and of the measurement w.r.t. to the modes; this is due to the fact that a thinner plate leads to higher amplitudes of vibrations (due to the lower bending stiffness).

The reduction of the plate thickness should result from a trade-off by taking into account possible disadvantages. A too high amplitude of vibration could lead to a nonlinear vibration of the plate; moreover, the reduction of the thickness would lead to lower frequencies, which are more affected by the needles push.

In order to increase the accuracy of the estimation, the sampling frequency can be increased. This would also allow the measurement of further modes, leading to a least square solutions of the equations that compare measured amplitude with predicted amplitude.

Another possibility is the construction of a completely different setup. A thin rectangular plate clamped on each side could be excited by the pin force at its center. This would avoid the presence of needles push in the dynamics.

Test of the delay between the pins

The effective delay between the retraction of the two pins should be estimated in representative experimental conditions (only rough estimations based on the electrical circuit were available, see section 1.1.6).

According to the analyses of chapter 4, an effect of the delay was not detectable from the in-flight data, the TM-plunger contact can (in principle) explain the dynamics at the release. However, it cannot be excluded that a percentage of the TM momentum along z was due to this phenomenon. Moreover, if the goal is the elimination of the TM-plunger contact risk (leading therefore to a nominal release condition), the delay could be much more critical than adhesion. We remind that,

with a preload of 0.3 N, a delay of approximately 40 μs could make the TM z velocity exceed the requirement.

The two pins can be extracted in order to grab at the target preload a small body (a plate or a cylinder), which can be also fixed but must reproduce the surface properties of the TM landing area (like the insert of the TMMF, see section 2.2.3). The dynamics of the pins can be captured by a high-speed camera, with a minimum sampling frequency in the order of $10^5 \div 10^6$ fps (one order of magnitude higher than the sampling frequency of the TMMF camera).

Test of the GPRM grabbing and release

The lateral motion (rotation) of the plunger should be tested, and the mechanism eventually improved in order to avoid this unexpected motion.

On-ground campaign and in-flight analyses have proved that the plunger bistability affects mainly one of the plane (xz). This is confirmed also by the plunger impulses of section 4.7, which are mainly directed along x axis.

As a consequence, the analysis of the grabbing of the TM could focus mainly on the behaviour of the mechanism in the xz plane. This allows the suspension of the TM in order to compensate gravity (similarly to the TMMF). The grabbing and the handover to the pins could be tested; thanks to the slow dynamics of these operation, a control loop applied to the hanging point of the TM could compensate the TM motion along the axis (and the torsion of the wire), in order to simulate a free fall of the TM. This operation would allow to test the effect of the plunger bistability with representative dynamical conditions. The geometry of the TM could be modified and eventually reduced, by maintaining mass and inertia w.r.t. the rotation in the plane, in order to reduce the inertia w.r.t. other rotations; modifications of the TM indentation would allow to avoid impacts along the vertical direction.

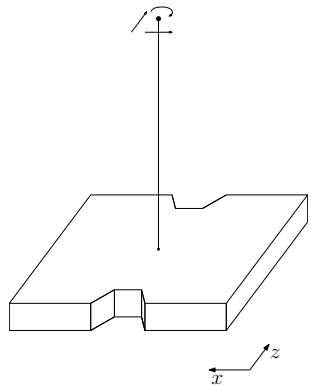

Figure 4.65: sketch of the TM mock-up for the investigation of the plunger dynamics in the xz plane. The suspension point can be controlled by a feedback control loop in order to avoid lateral or torsional loads of the wire during the grabbing and the handover. A system of interferometers and optical levers can be installed in order to measure x, z and η.

4.10 Summary of the in-flight release tests

In this chapter the most important results of the in-flight releases of LISA Pathfinder have been discussed. The focus was the analysis of the behaviour of the Grabbing and Positioning Release Mechanism (GPRM), to be compared with the on-ground predictions discussed in the previous chapters.

The releases of February 2016 (section 4.2), scheduled before the scientific phase of the mission, were characterized by unexpected momenta of the two test masses (TMs), with translational and rotational velocities out of the requirements.

As a consequence, at the end of the mission (June 2017) some identification tests for the analysis of the GPRM mechanical behaviour were planned, together with a *release test campaign* in which different release strategies have been experimented.

Each release test has been analysed by focusing on two main quantities: the initial momentum measured after the pin release (*pin release momentum*, section 4.5) and the momentum that is measured after the plunger retraction (*plunger release momentum*, section 4.3). The separated analyses of the two quantities and their comparison can indeed determine the most critical phase of a release strategy. Due to the low sampling w.r.t. the quickness of the release phenomenon, and in order to reduce the arbitrariness in the recognition of the free fall velocity of the TM in a test, a specific strategy for the analysis of the release signal was required (section 4.4).

The results of the release test campaign, which confirmed the criticality of the operation due to the high measured momentum of the TMs (difficultly controlled by the capacitive actuation), allowed to determine the detrimental *effect of plungers* on the final TM velocity. The unexpected effect of the plungers (which, in a nominal configuration, should not touch the TM at the release) is explained by the following facts:

- the worst release strategy (in terms of comparison of the TM momentum with the requirements) was the *plunger release*, i.e. the release performed through the retraction of the plungers (with no extension of the pins).

- many *fast pin releases* were charaterized by high pin release momentum. It has been proved that for these non-compliant tests the momentum cannot be created by a nominal TM-pin contact (section 4.6); therefore, a TM-plunger contact was required for a feasible explanation of the results. The TM-plunger contact model (section 4.7) can justify a high percentage of the TM momentum for the tests with non-compliant velocities.

- every *slow pin release* (section 4.8) was generally characterized by a very low pin release momentum and a very high plunger release momentum: therefore, for these tests the release becomes critical only when the plungers are retracted.

- for some slow pin releases, the non-nominal (monodimensional) behaviour at the pin release and at the first impact suggests a contact between TM and plunger before the plunger retraction.

On the contrary, we have no evidences of a possible criticality of adhesion in the release, thus not contradicting the on-ground predictions:

- a dedicated in-flight test proved that a very low capacitive force is required in order to overcome an adhesive pull between the TM and one plunger.
- the number of tests whose linear momentum can be considered closer to the nominality (i.e. prevailing z velocity) is very limited; these tests are mainly slow pin releases and the measured z velocity is significantly lower than the requirement of 5 μm/s.
- in general, when the effect of the TM-pin adhesion cannot be determined in a test, if the test is non-compliant this is mainly due to the TM-plunger contact (prevailing effect that can hide any contribution of adhesion).
- in the large majority of the slow pin releases, the TM has a z velocity lower than the velocity of retraction of the pins, thus suggesting a detachment between TM and the pins due to a cancelation of the opposite adhesive pulls (strong conclusions are however not possible due to the uncertainty of the slow pin release dynamics, which can be affected by a contact with the plungers and by an electrostatic effect).

We have also seen that, in the case of a high pin release momentum and before the plungers are retracted, the bounces of the TM with the plungers can have a positive effect by decreasing the kinetic energy of the TM.

In general, the analysis of the releases revealed that the *nominal release configuration* (section 4.1), which was assumed as a fundamental hypothesis in the on-ground predictions, does not occur in the reality. This conclusion is supported by the unexpected effect of the plungers at the pin release, the misalignment of the TM motion w.r.t. the nominal z axis, the low gaps between TM and plungers deduced from the analysis of the first impact in the slow pin releases, and recent analyses of the relative positions of the devices (performed in 2019, see section 4.9).

Chapter 5

Conclusions and future perspectives

The on-ground testing of the GPRM, whose goal was the estimation of the effect of adhesion on the residual momentum of the TM in LISA Pathfinder, confirmed the results obtained with previous experimental setups.

Thanks to a conservative estimation based on the free flight velocities of the test mass in the on-ground setup (chapter 2), we found that, in absence of other important mechanical effects, the contribution of adhesion to the residual momentum of the TM in LISA Pathfinder is not critical, being 96 % of the predicted probability distribution inside the requirement (with more than 50 % of the distribution lower than 1/2 of the requirement).

The prediction has been then further improved by considering a more accurate estimation of the momentum transferred by the GPRM through the adhesive pull (chapter 3). The vibration mode-based estimation of the adhesive impulse, based on the correspondence between the measured amplitudes of the TM mode oscillations and the dynamical model, allowed to predict a lower residual momentum for the in-flight release, with a maximum equal to 1/10 of the requirement.

Compared to previous experimental campaigns of the TMMF, the high velocity of retraction of the release tip of the GPRM (the pin) did not allow to study the dynamics *during* the application of the adhesive pull (e.g. by applying a double differentiation of the signal in order to estimate the acceleration and thus the force). This fact was due to the uncertainty of the structural parameters of the blocking system (the needles), which did not allow a easy "subtraction" of their effect, and especially the low sampling ratio w.r.t. the duration of the phenomenon. As a consequence, the prediction of the adhesive effect has been based on the steady state dynamics of the system (free flight) *after* the exhaustion of the adhesive pull, through the measurement of oscillations with higher period w.r.t. the sampling time and through methods that are independent on the effect of the needles (the difference distribution in chapter 2, and the oscillation of modes not affected by the needles push in chapter 3).

Due to the lack of knowledge about the behaviour of the system during the pin release, for the on-ground estimation of the adhesive impulse a model of the

TMMF dynamics has been assumed. The dynamical model has been chosen on the basis of previous observations and by considering a nominal dynamics of the system, assured by the alignment of the devices and by the architecture of the experimental setup. In order to reduce the uncertainty of the estimation, the sensitivity of the model predictions to the model parameters has been investigated, as well as the dependence of the results on the uncertainties of the measurement.

Summarizing, we can say that, for each stage of the TMMF development, the effect of adhesion on the residual velocity of the TM in LISA Pathfinder was estimated not critical. We have however to remark that all the predictions of the in-flight behaviour assumed a *nominal in-flight release*, i.e. a monodimensional release along one axis (z) with exclusive contacts between TM and pins at the landing areas, and no additional contacts with the plungers. In other words: if in LISA Pathfinder the release occurs according to a nominal configuration, and if no other asymmetry effects occur (like a relative delay of the two pins), the residual velocity due to the cancelation of the two opposite adhesive pulls should be (much) lower than the maximum limit (the requirement).

The LISA Pathfinder mission was finally launched on December 3, 2015. Due to the unexpected behaviour of the TM releases of February 2016 (with a momentum of the TM completely out of the requirements), a in-flight release test campaign was planned in 2017, in order to investigate the GPRM behaviour and additional release strategies. A "safe" strategy allowing the TM to be recaptured without bounces with the sorroundings was not found; the tests performed on the capacitive control actuation have proved indeed the criticality of high release momenta, i.e. the nominal requirements are generally representative of the maximum control authority. In general, in order to recapture the TM, bounces between the TM and the plungers (not considered in a nominal situation) were necessary in order to reduce the kinetic energy of the TM.

The detailed analysis of the in-flight data (chapter 4), based on the computation of the momentum of the TM at the release, has proved a non-nominal behaviour of the mechanism.

This is demonstrated by the following observations. First, the *pin release momentum* of the TM, i.e. the momentum acquired by the TM at the retraction of the pins, is far from being mono-dimensional, i.e. directed along the nominal axis z. This fact cannot be explained simply through an inclination of the pins w.r.t. the TM; therefore, we must consider that an unexpected contact between TM and plungers occurred when the pins retract. A model for this non-nominal dynamics has been developed, and it shows the following: when the pin release momentum of the TM is non-compliant, impulses are applied by the plungers to the TM at the coupling surfaces, transferring an important momentum to the TM, higher than the requirement.

Another evidence is given by the difference between the momentum measured immediately after the pin release (pin release momentum) and the momentum measured after the retraction of the plungers (*plunger release momentum*). Many tests that show a low pin release momentum can have a very high plunger release momentum, thus proving that the retraction of the plunger has a detrimental effect

on the final momentum of the TM (this occurs especially for the slow pin tests of TM2).

These effects allowed to state that the non-compliance with the requirements was due to a non-nominal dynamics where the plungers had a fundamental role. The unexpected behaviour of the plunger seems due to the instability of its lateral motion (measured by on-ground tests and by a specific in-flight investigation), and by a low gap between TM and plungers at the release (as shown by the analyses of the slow pin releases), with the possibility of a contact existing before the retraction of the pins.

The unexpected behaviour of the plungers transfers therefore a non-compliant momentum to the TM; this means that, independently of the adhesive pulls between pins and TM at the release, the plungers have a detrimental effect on the final release velocity, and an improvement of the GPRM must face this problem first. Nevertheless, we asked ourselves if it was possible to investigate the effect of adhesion in the in-flight releases.

We started analysing the in-flight data with the following purpose: proving the non-criticality of adhesion for the residual momentum of the TM (thus *confirming* the on-ground predictions). At the end of the analysis, due to the non-nominal behaviour of the mechanism in the nominal release strategy (which does not allow to state that the final release momentum is the difference of the two opposite adhesive impulses), all we can say is that there are no evidences of the criticality of adhesion for the residual momentum (thus *not contradicting* the on-ground predictions). This can be concluded after the following three observations. First, the adhesive test has proved that the adhesion bonds produced between plunger and TM can be ruptured by a low actuation force. Second, in the slow pin releases (whose dynamics is affected by uncertainties and which are also far different than the nominal strategy) the z velocity of the TM is lower than the velocity of retraction of the pins (if the TM remains rigidly attached to one of the two pins, this would mean an imbalance of the two adhesive forces). Third, when the effect of adhesion cannot be determined and a release test performed with the nominal strategy has a momentum outside the requirement, the non-compliant behaviour is mainly affected by the TM-plunger contact (i.e. we don't need to assume an unexpected effect of adhesion).

The analysis of the in-flight releases is not trivial due to the large number of tests. The release tests, which have been initially studied one-by-one, have been analysed by an algorithm in order to reduce the arbitrariness in their interpretation. The choice of an automatic and objective algorithm is difficult due to the presence of many different release strategies and to the high variability of the TM behaviour: this observation holds for the detection of the reliable tests (i.e. tests with reliable pin release velocity determination) as well as for the computation of the velocities, or the detection of the impacts. Moreover, these investigations have been complicated by the low sampling w.r.t. the fast dynamics of the system at the release; the sampling frequency of the measurement system is indeed thought for the science phase, where the dynamics of the TM are quasi-static if compared with those at release. Further, we have based our consideration only on the varia-

tions of the TM velocities, thus not taking into account the complete information of the configuration of the system at the release: so far, we have considered that the small rotations of the TM w.r.t. to the high inclination of its velocities allow to neglect the measured position and attitude, but a more accurate analysis of the measured position of TM and plungers can yield more information (for instance about the possibility of a contact between the two bodies before the release).

The approach here presented for the analysis of the in-flight data can therefore be considered only as a preliminary approach, based on comparisons of orders of magnitude and simple dynamical models, in order to determine the best future direction of research.

In conclusion, the non-criticality of adhesion was confirmed by further on-ground predictions and was not contradicted by the analyses of the in-flight data; moreover, it was proved that the high momentum at the release is due to unexpected impacts between TM and plungers. As a consequence, the focus of future researches should move on the dynamics of the plungers at the release.

This is currently being done by the Department of Industrial Engineering through an additional TMMF campaign, that, based on the same on-ground experimental setup of chapter 2, measures the lateral motion of the plunger at the release (instead of the z displacement of the test mass). This experiment can yield information on the behaviour of the plungers at the retraction of the pin and at the retraction of the plungers.

The analyses that we presented in chapter 4 are being followed by analysing the configuration of the mechanism (i.e. the relative position between TM, plungers and housing) and through dynamical simulations in order to reconstruct the behaviour of the system at the release, for instance by looking for an initial condition that explains a motion compatible with the measurements; some highlights (which confirm that the nominal gap between the TM and the plungers can be reduced) are reported at the end of chapter 4.

Another issue is a more detailed analysis of the variation of the kinetic energy of the TM when it bounces against the plunger, through a better identification of the impacts and a more precise computation of the velocity after the impacts.

The unexpected behaviour of the GPRM was not critical for the scientific operations of LISA Pathfinder, since in the releases the TM has been always recaptured, although through a non-nominal strategy (relying on bounces in order to reduce the kinetic energy or by re-grabbing the TM). Moreover, the success of the scientific measurements (reported at the beginning of chapter 1) does not allow any change of the devices involved in the experiment, i.e. electrode housing and TM.

As a consequence, in view of the future LISA mission the modifications of the GPRM must be limited. Modifications of the GPRM are however recommended in order to improve the release dynamics and avoid collisions between the TM and the electrodes of the housing (which occurred in the releases of February 2016).

The two main issues are an improvement of the capacitive control (in order to increase the requirements for the momentum of the TM at the release), and an investigation of the structural dynamics of the plungers, by considering little im-

provements that could lead to a more regular (nominal) behaviour of the plungers at the release. Some hints are reported at the end of chapter 4: in particular, the lateral motion of the plunger should be reduced and the gap between TM and plungers should be increased.

Appendix A

On-ground GPRM testing

A.1 Alignment procedure

The alignment procedure allows to regulate the position of the devices involved in the experiment, i.e. interferometer and optical lever, needles, TM and GPRM. The operation is performed through the positioners of the devices (section 2.2.5) and the measurement system (section 2.2.6). The goal is the alignment of all devices w.r.t. the z axis, such that the release event in the experiment occurs along a unique dimension and a monodimensional simplification can be considered in the analysis.

We report here the main steps of the alignment procedure, by referring to figure A.1:

- the TM is placed in front on the needles and the interferometer pointed at the TM: the interferometer pitch is regulated until the signal is maximized when the laser beam is orthogonal to the TM surface (a). In this condition the laser beam is orthogonal to the y axis: the TM pitch (depending on gravity) is indeed the reference for the vertical direction.

- the TM is lifted up and the plunger moved in x and y directions until the interferometer points at the plunger. The round shape of the pin allows the reflection of the laser beam. The interferometer yaw is regulated (b) until the signal power remains constant when the plunger support is repeatedly moved back and forward. In this condition, the laser beam is aligned w.r.t. z axis (which corresponds to the axis of the linear runner supporting the GPRM).

- the laser beam is now the reference for the alignment. The plunger pitch and yaw are regulated (c) until the signal power remains constant when the plunger is repeatedly extracted and retracted. In this condition, the plunger is aligned w.r.t. z axis.

- the TM is finally lowered and its yaw regulated until the signal power is maximized (d). In this condition, the TM surface is orthogonal to z axis.

The TM x and y position is finally regulated through the camera feedback in order to centre the insert (contact zone of the release) with z axis. Once the TM is at its final configuration, it serves as a reference for the calibration of the optical lever.

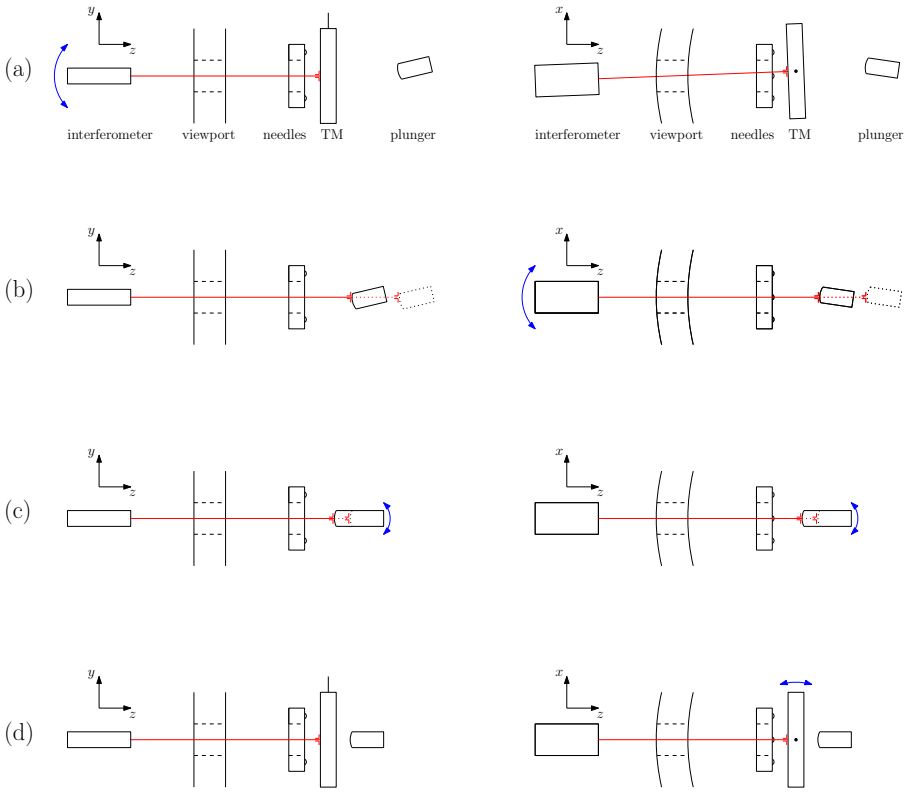

Figure A.1: steps of the alignment procedure; representation in the yz vertical plane (left) and xz horizontal plane (right). a) regulation of the pitch of the interferometer. b) regulation of the yaw of the interferometer. c) regulation of pitch and yaw of the plunger. d) regulation of the yaw of the TM.

Once the alignment of the devices is reached, the position of the TM insert is improved in order to make the TM point at the centre of the insert on one side, and the plunger touch the centre of the insert on the other side. This is done by moving the TM along a direction in order to study the insert dimension; the centre is considered as the mean of the explored range. The uncertainty of the operation, based on the dimension of the laser spot, allows to consider that the laser points in a circle of radius 100 μm centred in the insert centre.

Appendix B

Vibration mode-based impulse estimation

B.1 Identification of the peaks

We summarize here the algorithm (presented in [93]) that allows to define the oscillations appearing in the signal.

For each test, we focus on a frequency ω_0 under the Nyquist frequency (100 kHz), and in particular we consider only its associated vibration $h(t)$, defined as

$$h_{\omega_0}(t) = a \sin \omega_0 t + b \cos \omega_0 t \tag{B.1}$$

with an amplitude defined as:

$$c^2 = a^2 + b^2 \tag{B.2}$$

We want to establish a hypothesis test in order to evaluate if a real oscillation at frequency ω_0 is present in the signal $z(t)$; this will be done by comparing an appropriate estimator for c^2 ($\widehat{c^2}$) with a threshold $\widehat{c^2}_\alpha$. The two hypotheses are:

$$H_0 : c = 0 \Leftrightarrow \widehat{c^2} < \widehat{c^2}_\alpha \qquad \text{null hypothesis (no oscillation)} \tag{B.3}$$

$$H_1 : c \neq 0 \Leftrightarrow \widehat{c^2} \geq \widehat{c^2}_\alpha \quad \text{alternative hypothesis (oscillation)} \tag{B.4}$$

We set a 0.5% probability for the type I error in order to provide high significance: this means that, if a oscillation is recognized (i.e. H_0 rejected), the risk of rejecting H_0 when it is true is 0.5%.

The problem reduces hence to the computation of estimator and threshold. We summarize here the main steps of the computation.

B.1.1 Estimation of the amplitude of oscillation

The estimation of the parameters of harmonic oscillation in a measurement affected by noise is a common problem [115] [116] [117]. The problem consists usually in

finding the sine and cosine amplitudes of a harmonic oscillation of known frequency in a noisy signal $z(t)$ with an observation window $[0, T_w]$:

$$z(t) = a \sin \omega_0 t + b \cos \omega_0 t + n(t) = h_{\omega_0}(t) + n(t) \tag{B.5}$$

with a, b amplitudes, ω_0 angular frequency of the signal and $n(t)$ noise.

The estimation can be performed by means of two filter functions h_a and h_b:

$$\hat{a} = \int_0^{T_w} h_a(t) z(t) dt \tag{B.6}$$

$$\hat{b} = \int_0^{T_w} h_a(t) z(t) dt \tag{B.7}$$

$$\tag{B.8}$$

The estimators are determined such that a and b are unbiased and with minimum variance:

$$E(\hat{a}) = a \tag{B.9}$$

$$E(\hat{b}) = b \tag{B.10}$$

$$\sigma^2_{\hat{a},\hat{a}} = \min \tag{B.11}$$

$$\sigma^2_{\hat{b},\hat{b}} = \min \tag{B.12}$$

where E is the expected value of the variable. In the case of white noise, an analytical solution (dependent on ω_0 and T_w) for the functions $h_a(t)$ and $h_b(t)$ can be found in [116], together with analytical solutions for the variances $\sigma^2_{\hat{a},\hat{a}}$ and $\sigma^2_{\hat{b},\hat{b}}$ and the covariance $\sigma^2_{\hat{a},\hat{b}}$.

If we assume that the joint probability distribution of the estimators is Gaussian, an unbiased estimator of the squared amplitude c^2 is given by:

$$\widehat{c^2} = \hat{a}^2 + \hat{b}^2 - \sigma^2_{\hat{a},\hat{a}} - \sigma^2_{\hat{b},\hat{b}} \tag{B.13}$$

such that:

$$E(\widehat{c^2}) = a^2 + b^2 = c^2 \tag{B.14}$$

$$\sigma^2_{\widehat{c^2}} = 2\sigma^2_{\hat{a},\hat{a}}(\sigma^2_{\hat{a},\hat{a}} + 2a^2) + 2\sigma^2_{\hat{b},\hat{b}}(\sigma^2_{\hat{b},\hat{b}} + 2b^2) + 4\sigma^2_{\hat{a},\hat{b}}(\sigma^2_{\hat{a},\hat{b}} + 2ab) \tag{B.15}$$

A solution minimizing $\sigma^2_{\widehat{c^2}}$ is not available in closed form, but when the covariance $\sigma^2_{\hat{a},\hat{b}}$ is negligible, $\sigma^2_{\hat{a},\hat{a}}$ and $\sigma^2_{\hat{b},\hat{b}}$ are minimum. The resulting solution, yielding the estimated amplitude as a function of the frequency, is in this case

$$\widehat{c^2}(\kappa) = \left(\int_0^{T_w} h_a(t) s(t) dt \right)^2 + \left(\int_0^{T_w} h_b(t) s(t) dt \right)^2 - \frac{2S_0}{T_w} \frac{4\kappa^2}{2\kappa^2 + \cos(2\kappa) - 1} \tag{B.16}$$

where S_0 is the noise power spectral density and κ is defined as follows:

$$\kappa = \omega \; T_w \tag{B.17}$$

An example is shown in figure B.1, where the solution (B.16) is applied for a case with a known oscillation of frequency ω_0 and amplitude c. We see that the filter of equation (B.16) applied to the signal yields exactly the expected amplitude and frequency. As expected, the identification of the oscillation is more accurate if $\kappa_0 = \omega_0 \; T_w$ is greater, i.e. if the observation window is wider. It is possible to see that some secondary peaks are present; a signal with many harmonics produces a $\widehat{c^2}(\kappa)$ function with many main peaks (one for each oscillation), each one associated with its secondary peaks. In principle, the secondary peaks associated to a main peak could exceed the threshold, thus leading to the detection of fictitious oscillation. This problem is solved through an algorithm that detects only the main peaks discarding the secondary ones [93].

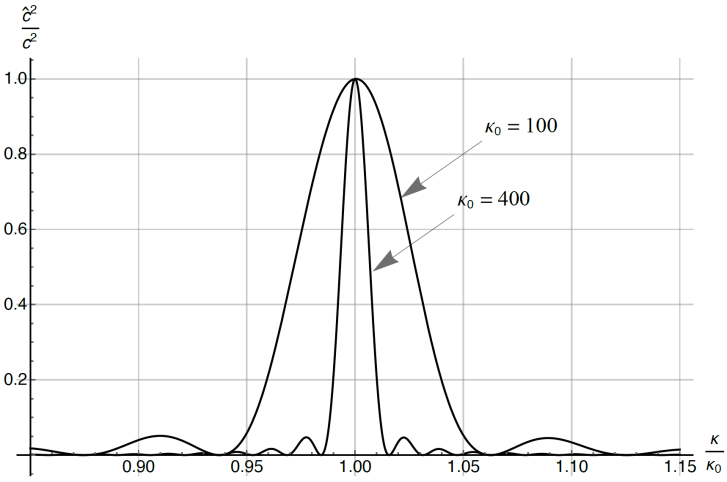

Figure B.1: normalized response of the optimal filter to a harmonic oscillation for two values of $\kappa_0 = \omega_0 T_w$.

B.1.2 Probability density function and threshold

The distribution of the biased estimator (B.2) is a quadratic form qf in two random variables ($\hat{a}$, $\hat{b}$) which belong to a multivariate normal distribution:

$$qf = \hat{a}^2 + \hat{b}^2 = \widehat{c^2} + \sigma^2_{\hat{a},\hat{a}} + \sigma^2_{\hat{b},\hat{b}} \tag{B.18}$$

The probability density function $p(y)$ related to q_f can be found if the quadratic form is reformulated as a function qf_n of uncorrelated standard normal variables

x_1 and x_2 [118]; according to equation (B.13), the probability density function of the estimator $\widehat{c^2}$ needs to be unbiased:

$$p_{\widehat{c^2}} = p(y + \sigma^2_{\hat{a},\hat{a}} + \sigma^2_{\hat{b},\hat{b}}) \tag{B.19}$$

If H_0 is true, qf_n becomes:

$$qf_{n,0} = d_1 x_1^2 + d_2 x_2^2 \tag{B.20}$$

where d_1 and d_2 are appropriate numerical coefficients. Through a linear combination of two independent chi squared distributions (each with 1 degree of freedom), the related probability density function can be computed [119]:

$$p_0(y) = \frac{1}{4d_1 d_2} e^{-\frac{d_1+d_2}{4d_1 d_2} y} I_0 \left(\frac{d_2 - d_1}{4d_1 d_2} y \right) H(y) \tag{B.21}$$

where y is a variable for the amplitude of oscillation, I_0 is the Bessel function of the first kind and H is the Heavyside function.

In order to compute the critical value associated to the chosen probability α (significance level), the cumulative distribution at the frequency of interest ω_0 has to be computed and inverted. This operation must be performed numerically; however, it can be proved that if $\omega_0\, T_w > 10$, p_0 becomes:

$$p_0(y) \approx \frac{T}{4S_0} e^{-\frac{T}{4S_0} y} H(y) \tag{B.22}$$

and unbiasing according to (B.19):

$$p_{\widehat{c^2}} = p_0 \left(y + \frac{4S_0}{T} \right) \tag{B.23}$$

We can therefore compute the cumulative density function:

$$P_{\widehat{c^2}} = \int_{-\frac{4S_0}{t}}^{Y} p_{\widehat{c^2}}(y) dy = 1 - e^{-(1+\frac{T}{4S_0} Y)} \tag{B.24}$$

The threshold for Y variable is found by imposing:

$$1 - P_{\widehat{c^2}}(Y_\alpha) = \alpha \tag{B.25}$$

Since $Y_\alpha = c^2_\alpha$, we find the critical value for the amplitude of oscillation from (B.25):

$$\widehat{c^2}_\alpha = -\frac{4S_0}{T}(1 + \log \alpha) \tag{B.26}$$

For the signal $z(t)$, the estimation of the peak amplitude (B.16) is therefore compared with the threshold of equation (B.26), according to the hypothesis test of equations (B.3) and (B.4).

Thanks to the low noise level of the laser interferometer that can be estimated in the pre-release interval (S_0 about $10^{-12}\text{um}^2/\text{Hz}$, with T_w about 1.5 ms), oscillations of the order of 0.1 nm can be detected with high significance.

B.2 Pattern recognition

We summarize here a result of [93].

The behaviour described in section 3.2.2 (time and space harmonics), shown in figure 3.9 through interpolating lines, can be identified through a *pattern recognition algorithm*.

First of all, a *cluster recognition algorithm* is applied to the peaks that exceed the threshold. In this case, a cluster corresponds to a set of points with similar behaviour w.r.t. the frequency as a function of the velocity. The numerical procedure considers a single point of the diagram of 3.9 and eventually associates the point to a specific cluster. The procedure works iteratively as follows:

- step 0.

  The test with lower free flight velocity (i.e. horizontal coordinate on the diagram) is considered first: let the test be referred to as t_0. A cluster index is associated to each of its m_0 peaks: $c_1 = \{p_1\}, ..., c_{m_0} = \{p_{m_0}\}$, where c_i is the i-th cluster and p_i the i-th peak frequency.

- from step n to step $n+1$.

  Let's consider that n tests have been analyzed and their peaks grouped in l clusters: $c_1, ..., c_l$. Define the test $n+1$ as the remaining test with lowest free flight velocity. Take the peaks of the $n+1$ test: $p_1, ..., p_{m_{n+1}}$. For each peak (say p_i, with $1 \leq i \leq m_{n+1}$), assign p_i to the cluster that contains the peak closer to p_i (in terms of frequency of the peak) and whose difference w.r.t. p_i is lower than a threshold (chosen by taking into account equation (3.5)). In the case this peak does not exist, create a new cluster $c^i = \{p_i\}$, which will be added to the set of clusters once all the peaks of the $n+1$-th test are analyzed.

The cluster recognition algorithm yields therefore a set of clusters.

Each cluster can be then be associated to a specific *pattern* (corresponding to a space harmonics or a time harmonics) or is discarded. For a single cluster, the procedure is made by interpolating linearly the cluster with a simple linear regression [92], thus yielding a slope a and an intercept b, with their uncertainties. The parameters of the interpolation are then considered: a time harmonics is recognized if the slope of the linear fit is statistically compatible with a constant frequency (i.e. $a \approx 0$) while a space harmonics is recognized if the parameters are statistically compatible with the behaviour of equation (3.5) (i.e. $a \approx \frac{n}{\lambda}$ and $b \approx 0$ for some $n \in \mathbb{N}$ and nominal λ).

The results of the pattern recognition are reported in table 3.1.

The pattern recognition is performed through a linear fit of the clusters. For each pattern, the residuals of the linear fit have been analyzed through a Shapiro test and their compatibility with a Gaussian distribution has been confirmed.

The linear fit of the space harmonics (i.e. pattern with linearly increasing frequency) has been further checked by comparing the computed slope with the relation of equation 3.5: for each test, the corresponding number λ (by fixing slope and n) has been computed, with the result reported in table B.1. In particular, it

pattern	$n \in \mathbb{N}$	$\lambda(nm)$
1	2	627
2	4	629
3	8	630

Table B.1: estimation of λ parameter associated to the interpolation of each space harmonics.

is possible to see that for each pattern, by fixing a proper value of n the resulting λ is close to the nominal value.

B.3 Fit of the free flight interval

B.3.1 Fit model

For the fitting model of the measured signal $z(t)$, two contributions are considered:

- $z_t(t)$, *true displacement*, dependent on time (μm)
- $z_s(z_t)$, *spatial noise*, dependent on true displacement (μm)

The fitting model corresponds to the *measured displacement*, defined as follws:

$$z_m(t) = z_t(t) + z_s(z_t(t)) \tag{B.27}$$

The true displacement is given by the linear motion of the mass in the free flight, to which the time harmonics are added. This implies that we consider the time harmonics as mechanical displacements of the insert of the TM. We will see in section 3.3.2 that this is true for harmonics 4 and 5, which correspond to vibrations of the TM as a thin plate. We don't have any information on the nature of harmonics 6 and 7. However, if we assume that they are related to a mechanical relative displacement of the TM w.r.t. the interferometer, we can consider them in the term x_t (it has been proved that this assumption does not significantly change the final result, since the estimation of the space harmonics depends mainly on the linear velocity of the TM barycentre in the free flight).

The true displacement is therefore defined as follows:

$$z_t(t) = vt + b + \sum_{j=1}^{M} A_i \cos(\omega_i t + \phi_i) \tag{B.28}$$

where v is the straight line slope (free flight velocity, μm/s), b a bias (μm), A_i the amplitude of the i-th time harmonics (μm), ω_i its natural angular frequency (rad/s) and ϕ_i its phase shift (rad).

The spatial noise is related to the cyclic effect of the interferometer, and it is defined as

$$z_s(z_t) = \sum_{j=1}^{N} B_k \cos(2\pi \frac{n_j}{\lambda} z_t + \psi_j) \tag{B.29}$$

where B_j is the amplitude of the j-th time harmonics (μm), $\frac{\lambda}{n_j}$ its associated submultiple of the wavelength λ (μm), ψ_j its phase shift (rad).

The fit is nonlinear, since a subset of the fit functions (space dependent) depends on another subset of fit functions (time dependent). An iterative fit procedure is therefore chosen, with the increment of the model complexity by adding a new harmonics to the fit for any iterative step. This allows also to find a good first guess for any iteration step, based on the result of the previous iteration step.

B.3.2 Steps of the iterative fit

The three steps of the fitting algorithm are described as follows. For each step of the estimation, the optimal parameters of the model are found through a Levenberg-Marquardt algorithm. The fitting algorithm is applied to a single test.

1. all the harmonics of the test appearing in the chart of figure 3.9 are ordered based on the amplitude measured through the FFT of the detrended signal (figure 3.5). The (time or space) harmonics with the higher amplitude will be fitted first. For the fit of each harmonics, the amplitude and (for time harmonics) the frequency estimated by the spectrum of the free flight are used as first guess.

2. step 0. The signal z is fitted with a simple straight line (i.e. is detrended) in order to have

$$z_t^0(t) = vt + b \tag{B.30}$$
$$z_s^0(t) = 0 \tag{B.31}$$
$$z_m^0(t) = z_t^0(t) + z_s^0(z_t^0(t)) \tag{B.32}$$

   and the number of fitting parameters is $p_0 = 2$ (i.e. v and b).

3. step k. The k-th harmonics is added to the model (by following the previously described order of amplitude).

   - if the k-th harmonics is a time harmonic, the initial guess for the phase of the harmonics is given by the fit of the residuals of the previous step: therefore the fitted signal is $z - z_m^{k-1}(t)$ and the fitting model is simply $\tilde{A}_k \cos(\tilde{\omega}t + \phi_k)$, with ϕ_k fitting parameter and $\tilde{A}_k$ and $\tilde{\omega}_k$ initial guesses given by the FFT.

     The optimal phase shift ϕ_k is taken then as initial guess ($\tilde{\phi}_k$) for the complete estimation of the harmonics, while $\tilde{A}_k$ and $\tilde{\omega}_k$ remain the initial guesses for amplitude and frequency. The initial guesses for the other parameters appearing in the model at this step correspond to their estimation in the previous step $k-1$.

     The new model for the fitting of the complete data set z is therefore

$$z_t^k(t) = z_t^{k-1}(t) + A_k \cos(\omega_k t + \phi_k) \tag{B.33}$$
$$z_s^k(z_t) = z_s^{k-1}(z_t) \tag{B.34}$$
$$z_m^k(t) = z_t^k(t) + z_s^k(z_t^k(t)) \tag{B.35}$$

     and the number of parameters is $p_k = p_{k-1} + 3$ (the additional parameters are A_k, ω_k and ϕ_k).

   - if the k-th harmonics is a space harmonic, the initial guess for the phase shift of the harmonics is given by the fit of the residuals of the previous step: therefore the fitted signal is $z(t) - z_m^{k-1}(t)$ and the fitting model is simply $\tilde{B}_k \cos(2\pi \frac{n_k}{\lambda} z_t + \psi_k)$, with ψ_k fitting parameter and $\tilde{B}_k$ initial guess for the amplitude given by the FFT.

The optimal phase shift ψ_k is taken as initial guess ($\tilde{\psi}_k$) for the complete estimation of the harmonics, while $\tilde{B}_k$ remains the initial guess for the amplitude. The initial guesses for the other parameters appearing in the model at this step correspond to their estimation in the previous step $k-1$.

The new model for the fitting of the complete data set z is therefore

$$z_t^k(t) = z_t^{k-1}(t) \tag{B.36}$$

$$z_s^k(z_t) = z_s^{k-1}(z_t) + B_k \cos(2\pi \frac{n_k}{\lambda} z_t + \psi_k) \tag{B.37}$$

$$z_m^k(t) = z_t^k(t) + z_s^k(z_t^k(t)) \tag{B.38}$$

and the number of parameters is $p_k = p_{k-1} + 2$ (the additional parameters are B_k, ψ_k).

B.4 Analytical response of TM continuous model

B.4.1 Modal projection of concentrated forces

When a force acting on the body is a (spatially) concentrated force, its modal projection (i.e. the modal force) can be easily computed. This is useful for our case, since the forces acting on the TM (needles and pin) can be considered as concentrated forces. The result of this paragraph will be frequently used in the following.

A concentrated force $f(t)$ acting on a point of coordinates x', y' can be written as

$$f(x, y, t) = f(t)\ \delta_D(x - x', y - y') \tag{B.39}$$

where δ_D is the Dirac delta (which is zero everywhere except in x' and y' and whose double integral in the integration variables x and y is 1).

By applying equation (3.11), the corresponding modal force of the generic j-th modal coordinate is therefore:

$$\begin{aligned}
Q_j &= \int_A f(x, y, t)\ W_j(x, y)\ dx\ dy && \text{(B.40)}\\
&= \int_A f(t)\ \delta_D(x - x', y - y')\ W_j(x, y)\ dx\ dy && \text{(B.41)}\\
&= f(t) \int_A \delta_D(x - x', y - y')\ W_j(x, y)\ dx\ dy && \text{(B.42)}\\
&= f(t) \int_A \delta_D(x - x', y - y')\ W_j(x', y')\ dx\ dy && \text{(B.43)}\\
&= f(t)\ W_j(x', y') \int_A \delta_D(x - x', y - y')\ dx\ dy && \text{(B.44)}\\
&= f(t)\ W_j(x', y') && \text{(B.45)}
\end{aligned}$$

Hence, the modal projection of a concentrated force on the j-th modal coordinate is simply obtained by multiplying the force ($f(t)$) by the evaluation of the corresponding mode shape at the coordinate of the force application ($W_j(x', y')$).

B.4.2 Modal projection of forces acting on the TM

During the release procedure, the forces acting on the TM and causing its initial deformation can be considered as concentrated forces, acting on a single coordinate of the xy reference frame of the TM. This assumption follows directly from the rounded shape of the needles and of the pin (see section 2.2.4), which can therefore be considered in contact with the TM through a single point.

In figure B.2 a scheme of the forces applied on the TM is shown. The three needles forces are acting in three points A, B, and C, according to the needles geometry (we consider here a nominal situation where the TM is aligned with the

needles). We define the three corresponding forces as p_A, p_B, p_C. On the opposite side, the force of the pin f is acting at the origin O of the reference frame. The forces are here considered positive if acting in the positive direction of z axis (an adhesive pull applied by the pin is therefore positive).

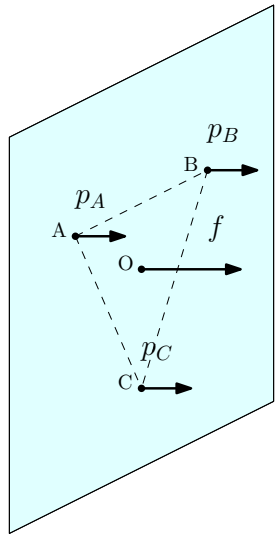

Figure B.2: forces acting on the centre plane of the TM. p_A, p_B, p_C correspond to the needles push while f is the force applied by the pin.

We can therefore write the concentrated forces as

$$f(x,y,t) = f(t)\cdot\delta_D(x,y) \quad \text{(B.46)}$$
$$p_A(x,y,t) = p_A(t)\cdot\delta_D(x-x_A,y-y_A) \quad \text{(B.47)}$$
$$p_B(x,y,t) = p_B(t)\cdot\delta_D(x-x_B,y-y_B) \quad \text{(B.48)}$$
$$p_C(x,y,t) = p_C(t)\cdot\delta_D(x-x_C,y-y_C) \quad \text{(B.49)}$$

As anticipated in section B.4.1 and according to equation (B.45), we get the following corresponding modal forces for the j-th mode:

$$Q_j^f(t) = f(t)\cdot W_j(0,0) \quad \text{(B.50)}$$
$$Q_j^A(t) = p_A(t)\cdot W_j(x_A,y_A) \quad \text{(B.51)}$$
$$Q_j^B(t) = p_B(t)\cdot W_j(x_B,y_B) \quad \text{(B.52)}$$
$$Q_j^C(t) = p_C(t)\cdot W_j(x_C,y_C) \quad \text{(B.53)}$$

In figure B.3 the evaluation of the mode shapes of the considered modes at the application points of the forces is shown, and the values of the mode shapes at the points A, B, C, O is reported in table B.2. Both mode shapes have a local maximum at the (0,0) coordinate (point O), thus suggesting a high sensitivity of the modes w.r.t. forces applied at the centre. The evaluation is lower at points A, B, C, since they are close to the node lines of the modes.

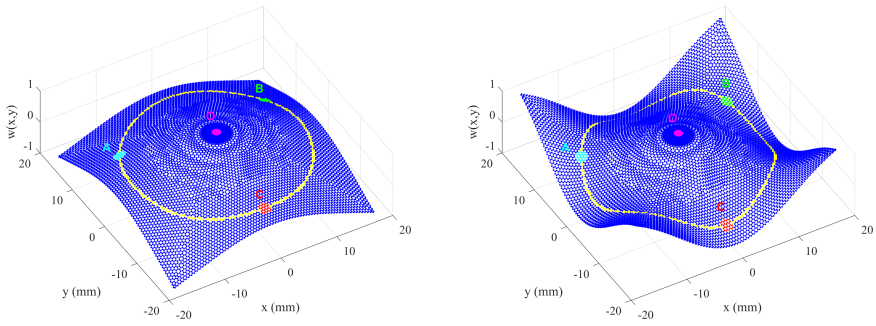

Figure B.3: evaluation of mode shapes for the application points of the external forces. The yellow circle circuscribes the needles' equilateral triangle.

	$W(x_A, y_A)$	$W(x_B, y_B)$	$W(x_C, y_C)$	$W(x_O, y_O)$
mode 1	-0.0687	-0.0687	0.0105	0.6813
mode 2	-0.1107	-0.1107	-0.5349	0.6496

Table B.2: evaluation of the displacement of the points A, B, C, O for the two mode shapes.

We can in general consider the needles modal forces in a unique term:

$$Q_j^p(t) = Q_j^A(t) + Q_j^B(t) + Q_j^C(t) \tag{B.54}$$
$$= p_A(t) \cdot W_j(x_A, y_A) + p_B(t) \cdot W_j(x_B, y_B) + p_C(t) \cdot W_j(x_C, y_C) \tag{B.55}$$

The total force given by the needles on the TM is $p(t)$:

$$p(t) = p_A(t) + p_B(t) + p_C(t) \tag{B.56}$$

The alignment procedure (appendix A.1) guarantees a uniform push of the needles on the TM; as a consequence, we can write

$$p_A(t) = p_B(t) = p_C(t) = \frac{p(t)}{3} \tag{B.57}$$

Therefore, equation (B.55) can be rewritten as follows:

$$Q_j^p(t) = p(t)\frac{W_j(x_A, y_A) + W_j(x_B, y_B) + W_j(x_C, y_C)}{3} \tag{B.58}$$

If we define with η_j the average value of the mode shape at the needles position:

$$\eta_j = \frac{W_j(x_A, y_A) + W_j(x_B, y_B) + W_j(x_C, y_C)}{3} \tag{B.59}$$

we can write finally

$$Q_j^p(t) = \eta_j \cdot p(t) \tag{B.60}$$

Similarly we define

$$\alpha_j = W_j(0,0) \tag{B.61}$$

such that the modal projection of the pin force is

$$Q_j^f(t) = \alpha_j \cdot f(t) \tag{B.62}$$

The coefficients η and α are reported in table 3.5.

For the j-th mode, according to equation (3.9) the complete differential equation is therefore given by

$$\begin{cases} \ddot{q}_j(t) + \omega_j^2 q_j(t) &= \frac{\alpha_j f(t) + \eta_j p(t)}{b_j} \\ q_j(0) &= q_{j0} \\ \dot{q}_j(0) &= 0 \end{cases}$$

B.4.3 Initial mode deformation

Let's consider the system in equilibrium under the actions of constant forces $f(t) = f$ and $p(t) = p$:

$$f + p = 0 \tag{B.63}$$

For each mode, the corresponding of the modal differential equation (3.9) can be written; by imposing $\ddot{q} = 0$ because of the equilibrium condition, we have

$$\omega_j^2 q_j(t) = \frac{1}{b_j}(Q_j^f + Q_j^p) \tag{B.64}$$

and therefore

$$q_j = \frac{1}{\omega_j^2 b_j}(Q_j^f + Q_j^p) \tag{B.65}$$

where the dependence on time has be discarded and Q_j^f and Q_j^p are the constant modal force resulting from the modal projection of the forces f and p. Being the deformation created the blocking forces (needles and pin) an initial displacement for the modal coordinates, and according to equations (B.60) and (B.62), we can write

$$q_{j0} = \frac{Q_j^f + Q_j^p}{\omega_j^2 b_j} = \frac{\alpha_j \cdot (-f_0) + \eta_j \cdot f_0}{\omega_j^2 b_j} \tag{B.66}$$

since, according to the representation of figure 3.20, in the blocking condition we have that the forces of pin and needles are opposite and equal to f_0 in modulus. Therefore:

$$q_{j0} = (-\alpha_j + \eta_j)\frac{f_0}{b_j \omega_j^2} \tag{B.67}$$

B.4.4 Pin force

According to equation (3.9) and equation (B.62), we can find the oscillation of the j-th mode resulting from the application of the pin force:

$$\begin{cases} \ddot{q}_j(t) + \omega_j^2 q_j(t) &= \frac{\alpha_j f(t)}{b_j} \\ q_j(0) &= 0 \\ \dot{q}_j(0) &= 0 \end{cases} \tag{B.68}$$

The solution can be found through the convolution integral:

$$q_j^f(t) = \frac{\alpha_j}{b_j \omega_j} \int_0^t f(u) \sin \omega_j (t-u) du \tag{B.69}$$

where u is the integration variable and $q_j^f(t)$ is the response of the j-th modal coordinate to the force $f(t)$, which (according to the definition of $f(t)$ of equation (3.22)) allows to split the integral into three contributions (one of which is null):

$$q_j^f(t) = \frac{\alpha_j}{b_j \omega_j} \int_0^{t_1} f_r(u) \cdot \sin \omega_j (t-u) du + \tag{B.70}$$

$$+ \frac{\alpha_j}{b_j \omega_j} \int_{t_1}^{t_1+\tau} f_{adh}(u-t_1) \cdot \sin \omega_j (t-u) du + \tag{B.71}$$

$$+ \frac{\alpha_j}{b_j \omega_j} \int_{\tau}^{t} 0 \cdot \sin \omega_j (t-u) du \tag{B.72}$$

As a consequence we have

$$q_j^f(t) = q_j^r(t) + q_j^{adh}(t-t_1) \tag{B.73}$$

where $q_j^r(t)$ is the response to the decreasing preload force and $q_j^{adh}(t)$ is the response to the adhesive force:

$$q_j^r(t) = \frac{\alpha_j}{b_j \omega_j} \int_0^{t_1} f_r(u) \sin \omega_j (t-u) du \tag{B.74}$$

$$q_j^{adh}(t) = \frac{\alpha_j}{b_j \omega_j} \int_0^{\tau} f_{adh}(u) \sin \omega_j (t-u) du \tag{B.75}$$

The solutions, i.e. the responses to the decreasing preload and the response to the three adhesive forces, are the following (according to the definitions of the forces given in equations (3.23), (3.24), (3.25), (3.26)):

$$q_j^r(t) = \alpha_j \frac{f_0}{b_j \omega_j^2} \left(\cos \omega_j t - \frac{\sin \omega_j t}{\omega_j t_1} + \frac{\sin \omega_j (t-t_1)}{\omega_j t_1} \right) \tag{B.76}$$

$$q_j^{adh,1}(t) = \alpha_j \frac{\iota}{b_j \omega_j^2 \tau} \frac{4\pi^2}{4\pi^2 - \omega_j^2 \tau^2} \left(\cos \omega_j (t-\tau) - \cos \omega_j t \right) \tag{B.77}$$

$$q_j^{adh,2}(t) = \frac{\alpha_j}{2} \frac{\iota}{b_j \omega_j} \frac{\pi^2}{\pi^2 - \omega_j^2 \tau^2} \left(\sin \omega_j (t-\tau) + \sin \omega_j t \right) \tag{B.78}$$

$$q_j^{adh,3}(t) = \alpha_j \frac{\iota}{b_j \omega_j^2 \tau} \left(\cos \omega_j (t-\tau) - \cos \omega_j t \right) \tag{B.79}$$

B.4.5 Needles force

According to equation (3.9) and equation (B.60), we can find the mode oscillation deriving from the needles push:

$$\begin{cases} \ddot{q}_j(t) + \omega_j^2 q_j(t) &= \frac{\eta_j p(t)}{b_j} \\ q_j(0) &= 0 \\ \dot{q}_j(0) &= 0 \end{cases} \tag{B.80}$$

The solution can be again given by the convolution integral, where for $p(t)$ we consider equation (3.31):

$$q_j^p(t) = \frac{\eta_j}{b_j \omega_j} \int_0^t p(u) \sin \omega_j (t-u) du \tag{B.81}$$

$$= \frac{\eta_j}{b_j \omega_j} \int_0^T f_0 \cos \frac{\pi u}{2T} \sin \omega_j (t-\tau) d\tau \tag{B.82}$$

where $q_j^p(t)$ is the response of the j-th modal coordinate to the force $p(t)$. By solving the integral, we get:

$$q_j^p(t) = 2\eta_j \frac{f_0 T}{b_j \omega_j} \frac{1}{\pi^2 - 4\omega_j^2 T^2} \left(2\omega_j T \cos \omega_j t + \pi \sin \omega_j (t-T)\right) \tag{B.83}$$

B.5 Monte Carlo simulation in a case with no adhesion

We can prove that the existence of solutions with negative impulse is related to the fact that the measured amplitudes are mainly due to the effect of the preload (phasor $\alpha_j \widetilde{M}_{j0}$). Let's consider indeed a fictitious case where the amplitudes are uniquely due to the effect of the preload $f_0 = 300$mN (as observed in section 3.4.3, we can neglect the needles effect):

$$A_1 = |\alpha_1 \widetilde{M}_{10} + \alpha_1 M_1^r| = \alpha_1^2 \frac{f_0}{b_1 \omega_1^2} \sqrt{\left(1 + \frac{\omega_1 t_1 - \sin \omega_1 t_1}{\omega_1 t_1}\right)^2 + \left(\frac{\cos \omega_1 t_1 - 1}{\omega_1 t_1}\right)^2} \quad \text{(B.84)}$$

$$A_2 = |\alpha_2 \widetilde{M}_{20} + \alpha_2 M_2^r| = \alpha_2^2 \frac{f_0}{b_2 \omega_2^2} \sqrt{\left(1 + \frac{\omega_2 t_1 - \sin \omega_2 t_1}{\omega_2 t_1}\right)^2 + \left(\frac{\cos \omega_2 t_1 - 1}{\omega_2 t_1}\right)^2} \quad \text{(B.85)}$$

In these conditions, the adhesive impulse is 0.

We consider now that the measurements of fit (A_1 and A_2) and load cell (f_0) correspond to the real value, but are affected by the same uncertainties of the case described by table 3.10. We repeat then the Monte Carlo simulation for this case, by considering the same distributions of the parameters of figure 3.28 (which are translated in order to make the mean value of each distribution equal to the corresponding amplitude predicted by equation (B.84) or (B.85)). The result, shown in figure B.4, corresponds to the output of the Monte Carlo simulation in a case corresponding to zero adhesive force.

As shown in figure B.4, if we consider the feasible results (positive τ) with exact solution of the equation (3.4.4), we get 52388 results with negative ι (41.9% of the whole set of simulations) and 60476 (48.4%) with positive ι. We can see that in this case the two percentages are much closer than the reference case of figure 3.29.

The fictitious case with the hypothesis of zero adhesive impulse has been considered for the following reasons:

- it shows that the solutions with negative impulses of the simulation of figure 3.29 are due to the fact that the amplitudes of the modes are very close to the ones due only to the preload. The same consideration holds for the existence of non-exact solution (10% in this case).
- we cannot consider only the distribution with $\iota > 0$, but we must include also the part of the distribution having negative impulses. For the fictitious distribution of this paragraph (figure B.4), if we consider the mean value of the complete distribution, we would get a mean impulse of 0.024 kg μm/s (with a standard deviation of 0.311 kg μm/s), very close to the effective null impulse. Considering only the positive impulses as a general rule would lead to a positive mean value for figure B.4, which is actually not the case.
- the distribution of figure B.4 can be considered as a theoretic distribution for the null adhesive impulse, if (for instance) we want to use a test hypothesis to prove the existence of a positive impulse in the case of figure 3.29 (by rejecting the null hypothesis of a null adhesive impulse).

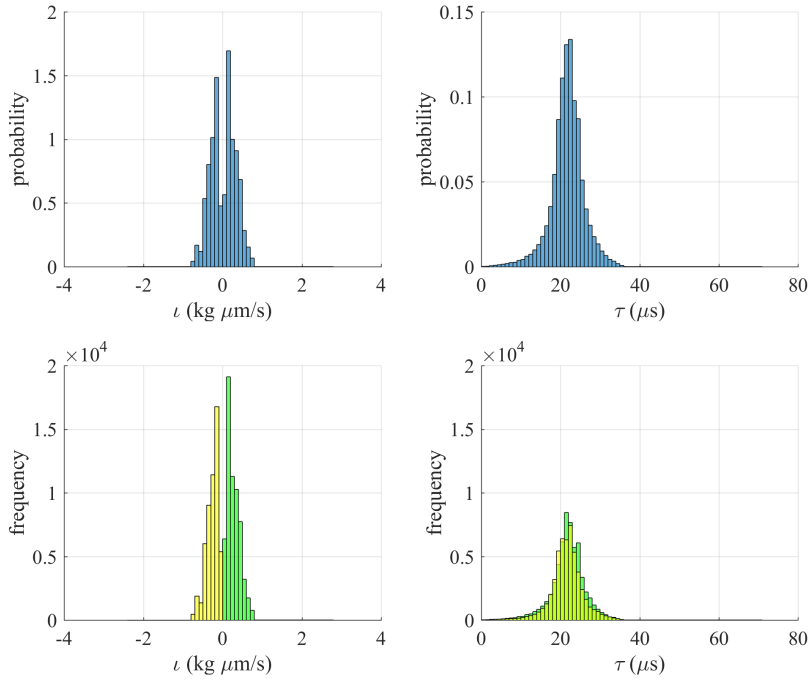

Figure B.4: Monte Carlo simulation for the case with no adhesion: feasible solutions (i.e. $\tau > 0$). Complete probability distributions of ι and τ (blue histograms) and distributions for each sign of the estimated impulse (green histograms for $\iota > 0$, yellow histograms for $\iota < 0$).

.

B.6 Compliance with the measured phases

B.6.1 Result for 1 test

In figure B.5 we report in the complex plane, for the two modes of the reference test, the nominal result of the model (figure 3.26) compared with the measurements.

We can see that the model phasors $\alpha_1 M_1$ and $\alpha_2 M_2$, which were computed through the equality of the amplitudes, are characterized by a specific value of phase (i.e. the inclination of the phasor w.r.t. positive real axis). In the same graphs, the $\pm 2\sigma_\phi$ uncertainty bands for the measured phases ϕ_1 of ϕ_2 (estimated by the fit of the free flight signal) are reported. We can see that there is no correspondence, i.e. the two phasors of the model do not touch the circles in the expected phase interval.

However, we have to remark that the phases of the model (inclinations of the phasor) refer to the *zero time of the event*, i.e. when the pin starts its retraction. In the model definition, the origin of time t is indeed referred to the release

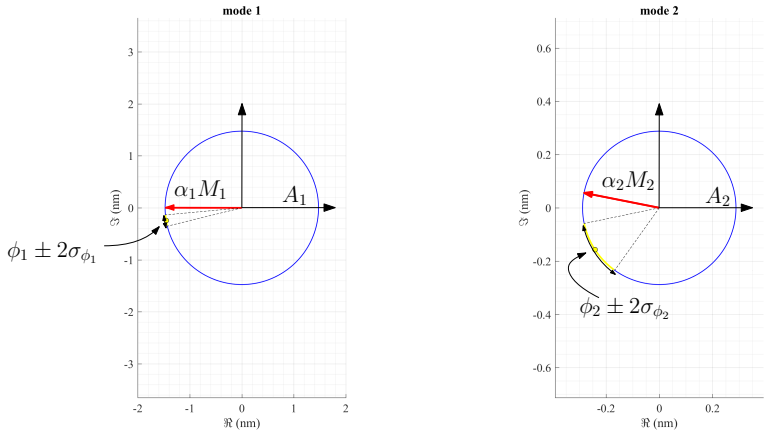

Figure B.5: Comparison between phase of the modes estimated by the model (red phasor) and $\pm 2\sigma_\phi$ uncertainty intervals of the measurement, without the correction due to the different time reference frames (see figure B.7).

phenomenon, as shown in figure 3.21.

The reference *zero time for the measured oscillations* has been defined based on the variation of the release signal w.r.t. the pre-release interval (figure 3.2). The zero time for the measured oscillation has been so far only a useful choice in order to approximate the time of the release event; however, as commented in section 3.1.1 and as shown in figure 3.3, we know that the release event should probably occur within one sample ($\pm$ 5 μs) from the 0 reference time of the signal.

As a consequence, if we want to refer to the zero time of the event (and not of the signal), we have to shift the measured phases accordingly. The principle is shown in figure B.6. If the release event has occured at a time t_0 in the signal reference frame, the measured phases must be shifted proportionally to the angular velocities, according to the following equations:

$$\phi_1^{event} = \phi_1 + \omega_1 t_0 \tag{B.86}$$
$$\phi_2^{event} = \phi_2 + \omega_2 t_0 \tag{B.87}$$

where for mode 1 ϕ_1^{event} is the phase of the measured oscillation w.r.t. the release event, ϕ_1 is the phase estimated by the fit of the signal (measured phase), ω_1 is the angular frequency of the mode and t_0 is the *time shift*, which defines when the event starts w.r.t. the time axis of the signal.

We expect therefore that a feasible choice of t_0, i.e. in the range

$$t_0 = -5 \div 5 \ \mu\text{s} \tag{B.88}$$

can improve the correspondence between measurement and model.

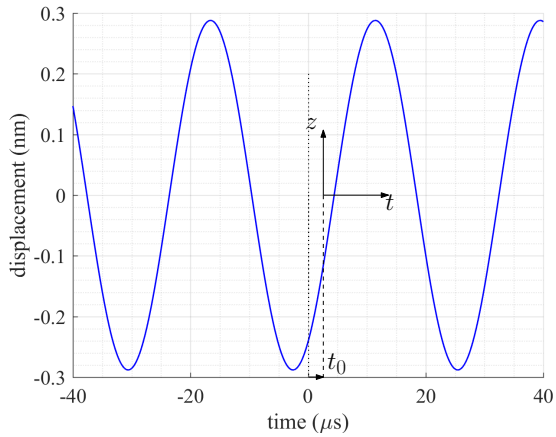

Figure B.6: evaluation of the oscillation of mode 2 at the origin of the measured signal, and new time reference frame referred to the start of the release event. The event starts at time t_0 w.r.t. the time axis of the measured signal.

In figure B.6 we have an example for a time shift t_0 = -2.2 μs. We see that the shift of the measured phases (clockwise due to the negative t_0) makes the model phasors touch the circle in the expected range. Being t_0 in the expected range, we say that it's possible to find a feasible value of time shift that (for each mode) match the phases in the $2\sigma_\phi$ interval.

The value of t_0 of figure B.7 is not the unique solution that allows a $2\sigma_\phi$ compliance: for the test, such a compliance can be given by all the values t_0 in the interval

$$t0 = -2.6 \div -1.8 \ \mu\text{s} \tag{B.89}$$

B.6.2 Results for 10 tests

The same approach can be adopted for the whole group of 10 release tests, according to the nominal solutions of table 3.9. In table B.3 we report the mean t_0 value that (for each test) allows the $2\sigma_\phi$ compliance of the two modes, or (if this is not possible) the $3\sigma_\phi$ compliance.

We see that the majority of the values t_0 are negative, thus meaning that (according to our model) the zero reference time of the signal has been taken $\approx$ 1-2 μs *after* the start of the release event.

We can see also that the matching of the phases fails for one test (test 10 in the table). For this test, we can have a value of t_0 that has a $3\sigma_\phi$ compliance for each mode; if the $2\sigma_\phi$ compliance is obtained for one mode is not obtained for the other mode, and viceversa.

This missing $2\sigma_\phi$ compliance for this test has been investigated, leading to the following observations:

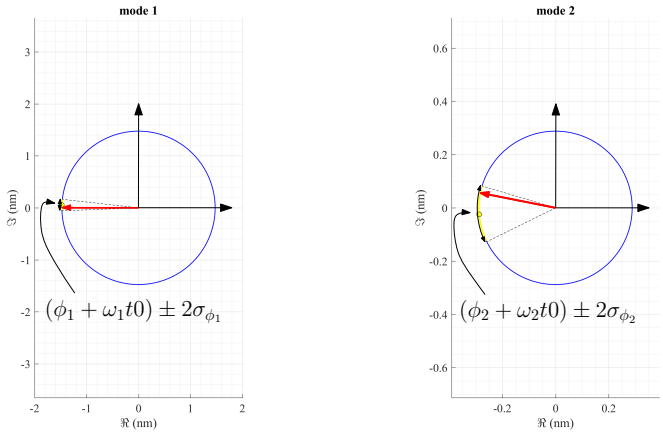

Figure B.7: comparison between phase of the modes estimated by the model (red phasor) and $\pm 2\sigma_\phi$ uncertainty intervals of the measurement, with the correction due to the different time reference frames; compared to figure B.5, the two uncertainty intervals of the measured phase have been shifted of a quantity proportional to t_0.

test	1	2	3	4	5	6	7	8	9	10
t_0 (μs)	-2.2	-1.6	-0.3	-0.6	-2.6	-0.2	-1.3	-1.0	-2.0	*-0.65*

Table B.3: estimation of the start of the event t_0 for each test, in order to yield compliance between measured phases and phases of the model. The reported t_0 values are the mean values that allow a $2\sigma_\phi$ compliance for each mode, except for test 10 for which the reported value is the mean value of the $3\sigma_\phi$ compliance.

- we can consider that, for each mode j, the real phase w.r.t. the event ϕ_j^{event} is normally distributed with the standard deviation σ_{ϕ_j} of the fit; moreover, let's consider as a null hypothesis the correspondence (for each mode) between phase of the model (inclination of the phasor) and measured phase. In this case, we have that for each mode the phasor of the model has a probability of $\approx 95\%$ of entering the $\pm 2\sigma_{\phi_j}$ uncertainty interval. This means that, for each test, in the null hypothesis the $2\sigma_\phi$ compliance is satisfied at the same time for both modes in $\approx 95\% \cdot 95\% \approx 90\%$ of the cases. As a consequence, the probability of $2\sigma_\phi$ compliances for 10 tests is defined by a binomial distribution with parameters n=10 and p=0.9; the mean value for this distribution is $n \cdot p$=9, which is exactly the number of matches in our case. As a consequence, the success of 9/10 tests in matching the phases with a $2\sigma_\phi$ compliance for both modes is statistically compatible with the null hypothesis; i.e., we can accept that for one test the compliance is rejected.

- the estimation of table B.3 is based on nominal solutions (section 3.4.3), but

we have seen that each solution is affected by a high uncertainty. If for a single test we consider the set of the Monte Carlo solutions (section 3.4.4), for each test is possible to find a subset of solutions for which the $2\sigma_\phi$ compliance of the phases can be obtained. For some tests, all the Monte Carlo solutions have a value t_0 that matches the phases with a $2\sigma_\phi$ compliance; for other tests (like test 10 of table B.3) the percentage of Monte Carlo solutions with a feasible value of t_0 is smaller, but always greater than 30%.

In other words, for the test 10 of table B.3 the nominal solution does not admit a feasible t_0, but a subset of the Monte Carlo solution does.

It has been proved that the choice of a different force profile (among the ones described in figure 3.22) or a different parameter t_1 does not change this result. In conclusion, we get that the solutions of the impulse estimations, based on the matching of the amplitudes, is $2\sigma_\phi$ compliant with the measured phase (for both modes).

Appendix C

In-flight TM release

C.1 Reliability tests

C.1.1 Reliability test based on pre-release noise

For each test and for all the DOF, the linearity of the first three points (i.e. the fact that the points lie on a straight line) is checked through a statistical test.

We refer for the statistical test to the example of a generic DOF s, whose hypothetical signal is shown in figure 4.22. In the figure, the *measured displacement* at the TM release instant is $\tilde{s}_0$ and the measured displacements of the first three samples considered in motion are $\tilde{s}_1$, $\tilde{s}_2$, $\tilde{s}_3$; for the same instants, the tree true displacement are s_1, s_2 and s_3. We want to check if these three samples lie on a line: this is done through a hypothesis test based on the difference Δ_s between $\tilde{s}_3$ (measured value of the third sample) and $\hat{s}_3$ (predicted value of the third sample based on the two previous samples).

In the null hypothesis, the *true displacements* s_1, s_2, s_3 are on the same line according to a linear displacement with velocity v_s; the discretized equation is

$$s_k = s_1 + v_s \cdot (k-1)T \tag{C.1}$$

where $s_k = s(t_k)$, T is the sampling time and $k = 1, 2, ...$

For each sampling time (k index), the measured displacement is the sum of the real displacement plus the signal noise n:

$$\tilde{s}_k = s_k + n_k \tag{C.2}$$

where $\tilde{s}_k = \tilde{s}(t_k)$ and $n_k = n(t_k)$.

The signal noise is estimated by analyzing the pre-release noise band (figure 4.21). Through the autocorrelation analysis it is possible to see that the noise in the pre-release noise band is uncorrelated and with null average; moreover, we assume (as a first approximation) that the pre-release noise is representative of the noise after the release (when the TM is in motion).

As a consequence, for every analyzed sample, the random component $n(t)$ can be characterized by the (discrete) noise probability distribution computed in the pre-release noise band.

From the measurements $\tilde{s}_1$ and $\tilde{s}_2$, we can estimate the velocity of the degree of freedom:

$$\hat{v}_s = \frac{\tilde{s}_2 - \tilde{s}_1}{T} \tag{C.3}$$

and we can therefore predict the position of the next sample, i.e. $\hat{s}_3$:

$$\hat{s}_3 = \tilde{s}_2 + \hat{v}_s T \tag{C.4}$$

In the null hypothesis, we can estimate the probability distribution of the difference $\Delta_s = \hat{s}_3 - \tilde{s}_3$.

$$\begin{aligned}
\Delta_s = \hat{s}_3 - \tilde{s}_3 &= \left[(s_2 + n_2) + \left(\frac{\tilde{s}_2 - \tilde{s}_1}{T}\right) T\right] - (s_3 + n_3) && \text{(C.5)}\\
&= s_2 + n_2 + \tilde{s}_2 - \tilde{s}_1 - s_3 - n_3 && \text{(C.6)}\\
&= s_2 + n_2 + s_2 + n_2 - s_1 - n_1 - s_3 - n_3 && \text{(C.7)}\\
&= 2s_2 - s_1 - s_3 + 2n_2 - n_1 - n_3 && \text{(C.8)}
\end{aligned}$$

From the linearity of the null hypothesis represented by equation (C.1), we derive

$$s_3 = 2s_2 - s_1 \tag{C.9}$$

therefore equation (C.8) becomes

$$\Delta_s = \hat{s}_3 - \tilde{s}_3 = 2n_2 - n_1 - n_3 \tag{C.10}$$

Equation (C.10) tells that, in the null hypothesis, the difference Δ_s has a probability density function (pdf) given by

$$\text{pdf}(\Delta_s) = 2\ \text{pdf}(n) * \text{pdf}(n) * \text{pdf}(n) \tag{C.11}$$

where the symbol $*$ corresponds to the convolution operation. Equation (C.11) comes from the assumption of uncorrelation of the noise $n(t)$ and has been tested experimentally in a case with normal distribution of the noise (for which $\text{pdf}(\Delta_s) = \sqrt{6}\ \text{pdf}(n)$).

As a consequence, we can reject the null hypothesis at the 5% significance level if Δ_s is outside the 95% range of the estimated distribution of equation (C.11) (this means that 5% of the tests recognized as non-reliable are reliable in the reality).

In figure C.1 an example for the y signal of one test (TM1, test 89) is shown; for the same test and the same DOF, the pre-release noise and the probability distribution of equation (C.11) are reported in figure C.2. We can see that the computed Δ_y (blue line in figure C.2 b)) is inside the 95% range, therefore the null hypothesis cannot be rejected and we consider that the 3 measured points $\tilde{y}_1$, $\tilde{y}_2$, $\tilde{y}_3$ lie on a straight line. This means that a linear motion can be considered for the y signal (i.e. without velocity variations due to impacts) and a free flight velocity v_y can be computed for the signal by interpolating the three points.

C.1.2 Reliability test based on reference signals

Unfortunately, few tests satisfy the reliability test based on the pre-release noise. Many tests satisfy the reliability test (i.e. do not reject the null hypothesis) for

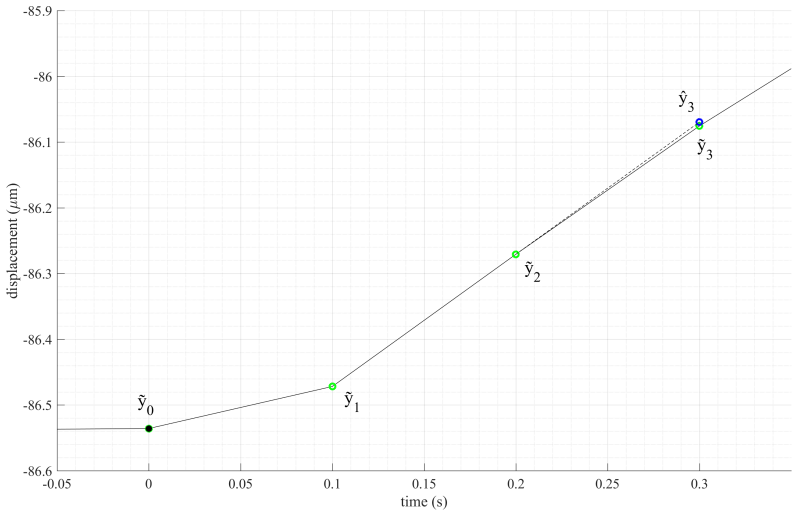

Figure C.1: measured ($\tilde{y}$) and estimated ($\hat{y}$) position of the third sample for the y signal (test 89, TM1).

some DOF, but fail the test (i.e. reject the null hypothesis) for other DOF. Notably, all the tests satisfying the described reliability procedure are characterized by low release velocities. This can be problematic for our purposes, since the tests with high release velocities can yield important information on the non-nominal behaviour of the release mechanism: we would like therefore to identify a free flight velocity of the TM for a minimum subset of these tests.

The higher the velocity of a DOF, the more common is the rejection of the null hypothesis for that DOF (this is for instance the case of the test 89: the y signal, shown in figure C.1, satisfies the test, but this does not occur for the z signal, which is characterized by a much higher velocity).

The failure of the reliability test for these cases can be explained by considering additional disturbances that could introduce a curvature in the signal:

- tribological electrification: at the release, despite the effect of the ISFEE bias, the detachment between pin and TM produces charge patches on the two opposite surface, thus leading to an electrostatic force between them. This effect could affect in particular the tests with high release momentum, since a high release momentum corresponds to higher forces exchanged by TM and plunger or pin.

- effect of the acceleration of the satellite. The TM moves freely, but forces acting on the satellite (which are not compensated since we are not in the science phase) could create a fictitious acceleration of the TM w.r.t. the housing and the electrodes.

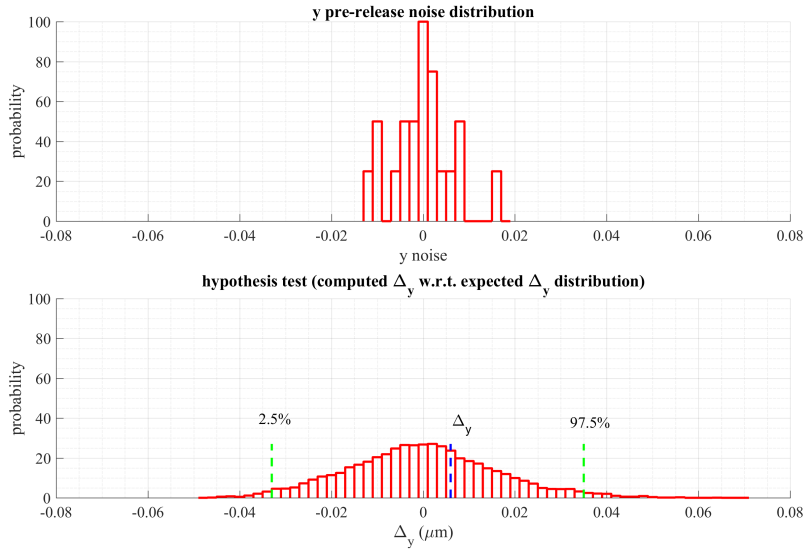

Figure C.2: reliability test for the y signal of figure C.1 based on the pre-release noise. Top: discrete probability density function of the pre-release noise. Bottom: corresponding pdf of equation C.11, with the computed Δ_y value (blue dashed line) and the limits for the satisfaction of the hypothesis test (green dashed lines).

- residual distortion due to the capacitive effect of the plunger (see section 4.1.3), not completely compensated by the bias. This effect could affect in particular the tests with high release momentum, since a high velocity corresponds to a higher variation rate of the capacities between TM and plunger.

Therefore, in order to consider the additional disturbances in the reliability test, we extend the probability distribution of Δ_s (of equation C.11, shown in figure C.2). This is done by computing a statistical distribution of the Δ_s of each DOF (as shown in figure C.3) for a chosen set of tests: the variations Δ_s are due to the additional disturbances but also to the signal noise. The chosen set of test here considered is composed of signals with a good qualitative reliability of the degrees of freedom and high displacements and rotation: this choice allows to consider some cases where the TM is supposed to move linearly (i.e. with no impacts) with a distortion of the signal mainly due to the additional disturbances.

This allows to get for each degree of freedom a new distribution of the deviations, i.e. pdf(Δ_s), which takes into account additional disturbances and the signal noise in a unique distribution. We can apply then the hypothesis test for each DOF of a single test: again, a test is reliable if the null hypothesis is not rejected for all the DOF. Notice that, compared to the previous hypothesis test, which was a theoretical approach based on equation C.11, we are here considering an experimental estimation of the probability density function of Δ_s.

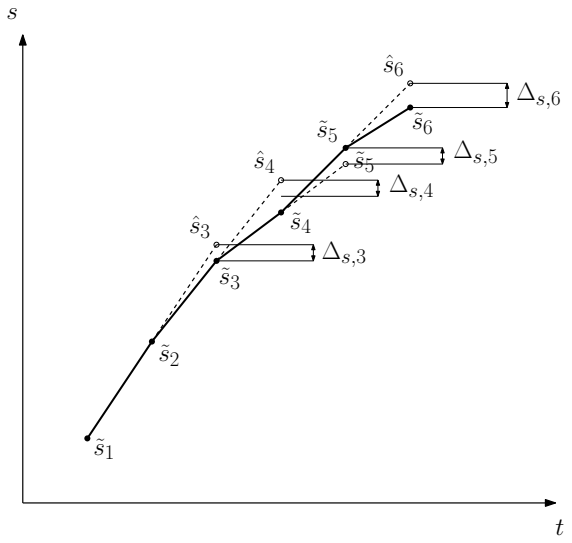

Figure C.3: experimental estimation of the Δ_s distribution from a reference signal (the deviations from the linearity are here exaggerated for sake of clarity.)

This approach is affected by arbitrariness in the choice of the reference tests for the computation of the Δ_s distribution of each DOF. However, this solution is necessary if we want to avoid the loss of the important information associated to the tests with high release velocity, which witness a fundamental deviation from the nominal expected behaviour (and which would not satisfy the statistical test based on the noise, equation (C.11)).

In order to establish a quantitative criterion for the choice of the set of reference test considered in the computation of the distributions Δ_s, we consider release tests having at least 3 consecutive points that, fitted through a straight line, yield a ratio between the uncertainty on the slope σ_{v_s} and the slope v_s lower than 10 % for all the DOF different than ϕ (whose slope is generally affected by a higher uncertainty, since the low variation of the ϕ coordinate after the release leads to a small signal-to-noise ratio). An example is shown in figure C.4.

7 tests have been selected for the estimation of the Δ_s distribution. The number of chosen reference tests is small due to the difficulty of finding release tests with all the DOF moving linearly in the same interval. A reduced number of selected tests is also required since each of these tests will satisfy the hypothesis test trivially (since the test contributes to the Δ_s distribution). As a consequence, the Δ_s distribution of each DOF is composed of few samples (15): in this case, the null hypothesis is not rejected if the estimator $\hat{s}_3 - \tilde{s}_3$ is inside the range described by the Δ_s distribution.

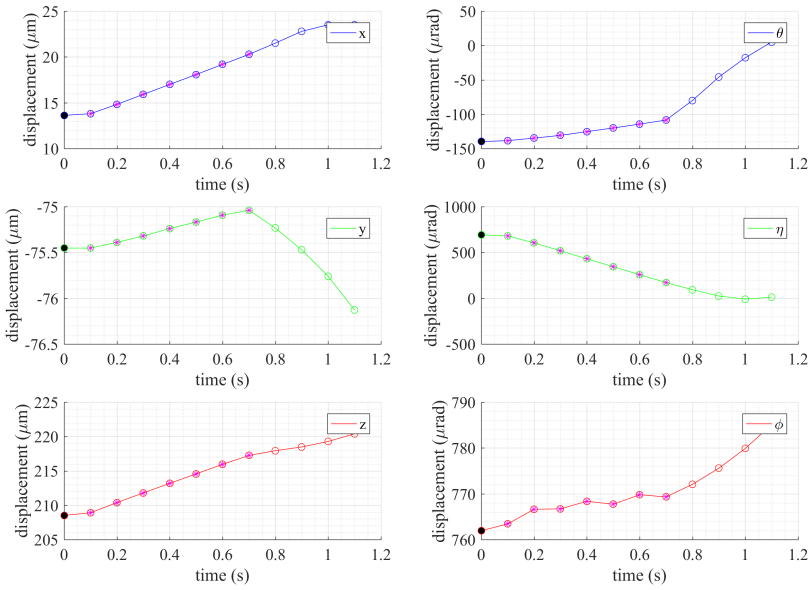

Figure C.4: example of reference test for the reliability (test 55, TM1). The black sample is the pin release instant while the purple samples are the samples that we consider on a line. According to the scheme of figure C.3, this test contributes with 5 values to the Δ_s distribution of each DOF. The maximum σ_s/v_s ratio is 4 % for the DOF different than ϕ.

C.2 Motivations of the TM-plunger impulses

As explained in section 4.5.2, the fast pin release velocity can be affected by the preload: in the nominal condition, the combined effect of preload and delay of a pin can give a push to the TM (equation 1.7).

According to the considerations of section 4.6 and section 4.7.2, a contact between plunger and TM occurs. As explained in section 4.7.1, a possibility for such a contact is an axial motion of the plunger due to its elasticity. An axial motion can be given by the elastic relaxation of the plunger stiffness after the fall of the contact force, which could give an impulse in two different ways: an impact between plunger and TM (in a case where the TM is not in contact with the plunger before the release) or a continuous push of the plunger to the TM (if the plunger is already in contact before the release).

In the following, we consider simple models depending on the preload: an order of magnitude of the transferred impulse can be computed and compared with the observed velocities. Due to their simplicity, these models can be considered only as a starting point for further analyses (see chapter 5).

C.2.1 Impact between plunger and TM

In figure C.5 a simple model for the impact of the plunger against the TM is shown. The plunger is initially preloaded due to the holding force; at the pin release, the elastic force of the spring moves the plunger towards the TM; finally, the plunger impacts against the TM. The impulse given by the plunger to the TM is maximum if the velocity of the plunger at the contact is maximized. The energy conservation for the plunger system yields

$$\frac{1}{2}k(\Delta z)^2 = \frac{1}{2}m_p v_{p,1}^2 \tag{C.12}$$

where k is the plunger stiffness, Δ_z is the plunger compression, m_p is the plunger mass and $v_{p,1}$ the plunger velocity before the impact. As a consequence, the *maximum* plunger momentum before the impulse is

$$\max(m_p v_{p,1}) = \sqrt{k m_p}\Delta z = \sqrt{\frac{m_p}{k}} f_0 \tag{C.13}$$

since the compression Δ_z is linear w.r.t. the preload f_0 (see also section 4.2.3).

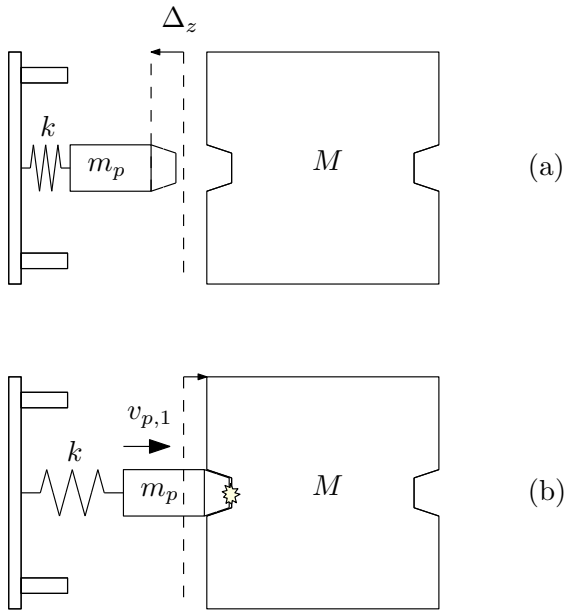

Figure C.5: dynamical model of the impact between plunger and TM due to a preload of the plunger: initial condition (a) and impact between plunger and TM (b).

A percentage of the momentum before the impact is converted into the momentum for mass M (mass of the TM), if we assume the conservation of the linear momentum:

$$mv_{p,1} = mv_{p,2} + Mv_{TM} \tag{C.14}$$

where $v_{p,2}$ is the velocity of the plunger after the release, M the mass of the TM and v_{TM} is the velocity of the TM after the impact. According to the percentage of kinetic energy lost in the impact, we can consider two limit cases: the completely elastic impact (conservation of the kinetic energy) and the anelastic impact ($v_2 = v_{TM}$). In the two cases, the final momentum of the TM due to the impact can be proved to be

$$(Mv_{TM})_{anelastic} = \frac{M}{M+m_p} m_p v_{p,1} \tag{C.15}$$

$$(Mv_{TM})_{elastic} = \frac{2M}{M+m_p} m_p v_{p,1} \tag{C.16}$$

If we consider for $v_{p,1}$ the maximum velocity of equation (C.13), then the two equations (C.15) and (C.16) describe the following range:

$$Mv_{TM} = \lambda \frac{M}{M+m_p} \sqrt{\frac{m_p}{k}} f_0, \quad 1 \leq \lambda \leq 2 \tag{C.17}$$

where λ is a parameter depending on the loss of kinetic energy at the impact. As a consequence, thanks to the range predicted by equation (C.17), we can compute an order of magnitude for the linear momentum due to the impact (in the hypothesis of maximum kinetic energy of the plunger before the impact, see equation (C.13)).

C.2.2 Continuous push of the plunger

A different case occurs if the TM is already in contact with the plungers before the release. In figure C.6 the contact configuration between TM and plunger is shown for the xz plane (since the contact can occur only on the coupling surfaces, the problem can be analyzed in two dimensions). If a contact force occurs on one coupling surface, a similar force must be applied on the opposite one, in order to avoid a net push in the vertical direction, which would be not compatible with the equilibrium of the TM in the blocked configuration. As a consequence, three forces are applied to the TM.

Let's consider the situation of figure C.6 for the pyramidal plunger. In principle, a similar situation can occur on the opposite plunger. We can assume that on the opposite side the TM is in contact only with the pin; this situation could occur especially if the z velocity is positive, since (as one can see from appendix C.6) when the z velocity is positive and out of the requirement the displacement of the TM before the impact with the conical plunger is generally close to the nominal gap (14 μm).

In this configuration, a push to the TM can be given also if no delay occurs between the pin retractions. Let's consider the two pins retract synchronously. Then the only contact remaining between TM and plunger is the one on the Z-coupling surfaces.

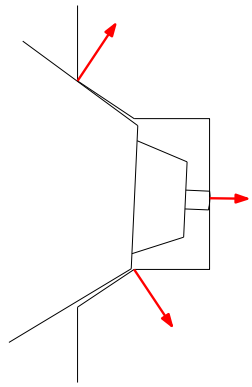

Figure C.6: TM-plunger contact and push of the plunger on the TM (condition before the pin release).

We can therefore consider the relaxation of the plunger stiffness, preloaded with 0.3 N, applied to the plunger-TM system, whose mass can be approximated with the TM one, since the mass of the plunger is much smaller than the one of the TM [47]. The total impulse given to the TM is given by the integral of a quarter of period of the plunger-TM system modeled as a mass-spring system:

$$\iota = \int_0^{\frac{\pi}{2\omega}} f_0 \cos\omega t \; dt = \frac{f_0}{\omega} \tag{C.18}$$

where ω is given by the ratio between the stiffness of the plunger k (see section 4.2.3) and the total mass involved ($m + M \approx M$). Therefore, by equating impulse and linear momentum, we get

$$M v_{TM} = \frac{f_0}{\omega} \tag{C.19}$$

Equations (C.17) and (C.19) describe therefore two different dependences of the linear momentum of the TM on the preload force f_0, each one related to a model that can explain an impulse applied by the plunger to the TM.

In figure C.7 we plot the z momenta (absolute value) of the reliable non-compliant fast pin tests (see figure 4.50) versus the preload force.

Approximately half of these tests are located between the two models of equations C.16 and C.19, which correspond to two cases conserving the total energy between pin release and TM motion (although the high preload uncertainty must be considered). In particular, all these tests belong to TM1 and have a positive z momentum, mainly due to the effect of the pyramidal plunger; as previously commented, a momentum due to the continuous push of the plunger is possible due to the nominal gap on the opposite side (which allows to consider the detachment between TM and conical plunger). Moreover, a contact between TM and pyramidal plunger is easier due to the pyramidal shape.

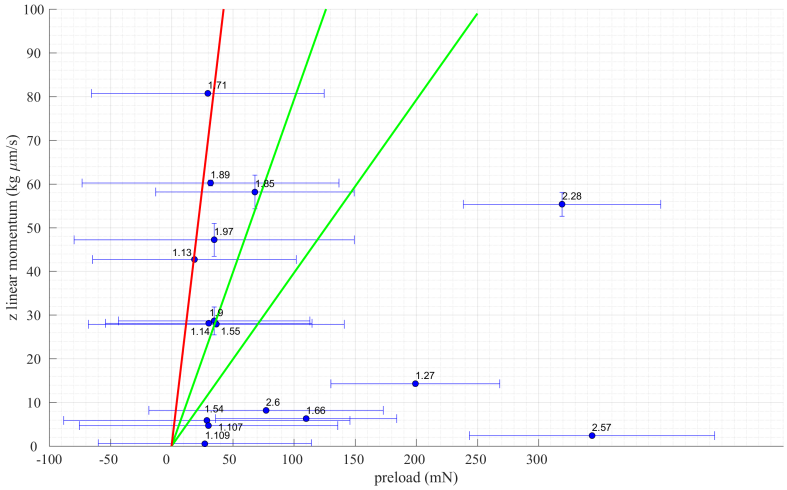

Figure C.7: reliable non-compliant fast pin tests: measured z momentum (absolute value) versus preload and comparison with the models of equations (C.17) (green lines) and (C.19) (red line). For each test, the uncertainties ($\pm\sigma$) of the coordinates f_0 and Mv_{TM} are reported. For each point, the caption corresponds to the test number (for insance, 2.57 is test 57 of TM2).

Many tests do not show such a behaviour: they are characterized by a lower momentum/preload ratio. But if we assume that the kinetic energy of the plungers not maximum at the impact (i.e. lower than the maximum one of equation (C.13)), we have that the momenta of these tests can be explained with the same principle (we would have in this case different straight lines in figure C.7, with lower slopes).

The uncertainty of the preload force and the approximation of the model do not allow strong conclusions. However, the plunger push due to the axial stiffness is a possible motivation of the plunger push at the pin release that can explain the high z momentum obtained with low preloads; the problem can be further investigated through dynamical simulations.

C.3 Effect of pyramidal plunger on ϕ rotation

The model of section 4.7.2 considers as an assumption a pyramidal plunger not rotated w.r.t. the TM. If there is a relative ϕ inclination between TM and the pyramidal plunger, a contact like the one of figure 4.46 can give a rotational impulse for ϕ angle. Analysing the possible relation between the TM-plunger contact and the ϕ rotation is important in order to give a model that explains the behaviour of all the DOF.

The situation is described in figure C.8. For Z+ plunger, the conical shape of the edge makes it possible to assume that the impulses are always applied with no arm for ϕ rotation. The situation for the Z- plunger is different: through a simplified model, we can assume that a relative ϕ inclination makes the pyramidal plunger touch each coupling surfaces at a distance c from the mean xz and yz planes of the TM. In the following, we consider c positive if it corresponds to a rotation of the plunger that makes the orthogonal impulses give a positive torque about z axis (i.e. positive ω_ϕ variation).

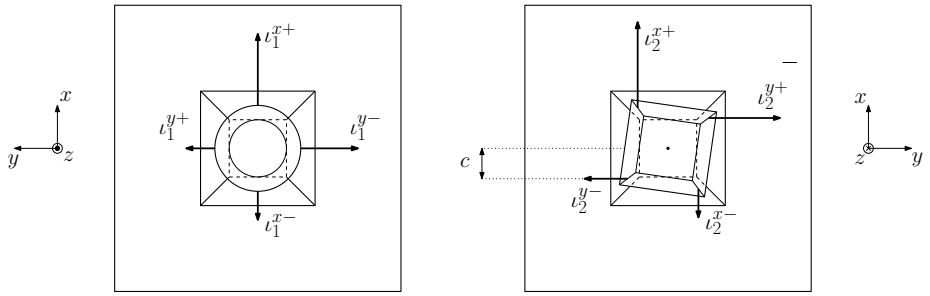

Figure C.8: plunger impulses and ϕ torque. Due to the different shapes of the plungers, no torque about z axis is given by the conical Z+ plunger (left), while the pyramidal Z- plunger can give a torque to the TM if it is misaligned w.r.t. the TM (right; the arm w.r.t. ϕ rotation is c for each impulse).

By means of a geometrical analysis, an estimation for the range of c parameter can be found:

$$c = -3.7\text{mm} \div 3.7\text{mm} \tag{C.20}$$

The c range is estimated from the TM geometry as half of the mean length of the TM-plunger coupling surface (mean of the two quotes of figure C.9).

Similarly to the case of section 4.7.2, we can split the impulses given by the pyramidal plunger into a "hidden" contribution (i.e. balanced pushing impulses with no resultant in the xy plane) and the two total impulses in x and y directions, as shown in figure C.10.

The hidden contribution gives only a total impulse in z, i.e. $\iota^z_{h,2}$ (which contributes to the residual impulse ι^z_{res}), according to the following equation:

$$(2|\iota^x_{h,2}| + 2|\iota^y_{h,2}|)\tan\alpha = |\iota^z_{h,2}| \tag{C.21}$$

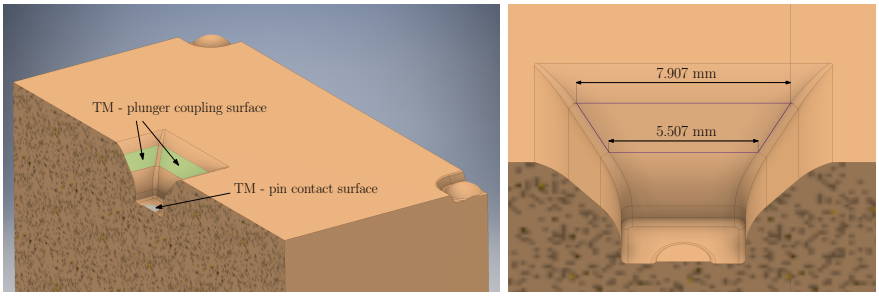

Figure C.9: section of the TM w.r.t. mean xz plane (equivalent to the section w.r.t. mean yz plane). The contact surfaces between TM and pin and plunger are shown. The reported quotes are considered for an estimation of the range of c (equation C.20)

.

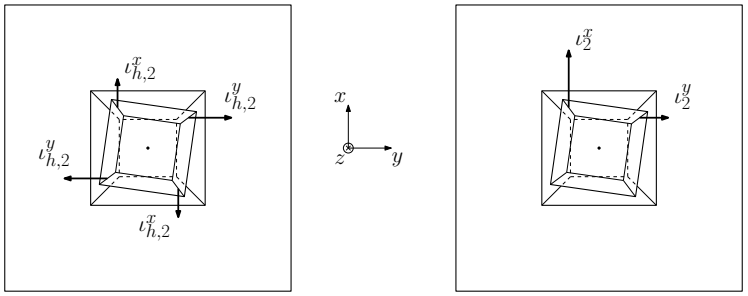

Figure C.10: the impulses of the pyramidal plunger of figure C.8 are split into two components. Left: hidden contribution, i.e. impulses which contribute to the ι^z_{res} impulse and to the ϕ rotation (with no effects on θ and η rotations). Right: impulses which affect θ and η rotations (as well as ϕ rotation).

The equilibrated impulses give also an impulsive torque $\tau^{\phi}_{h,2}$:

$$(2|\iota^x_{h,2}| + 2|\iota^y_{h,2}|)c = \tau^{\phi}_{h,2} \tag{C.22}$$

hence, by combining equations (C.21) and (C.22) we get that the hidden contribution in z of the pyramidal plunger can be related to a impulsive torque according to the following equation:

$$\frac{|\iota^z_{h,2}|}{\tan\alpha}c = \tau^{\phi}_{h,2} \tag{C.23}$$

According to this model, the ϕ impulse given by the pyramidal plunger is the sum of the torque $\tau^{\phi}_{h,2}$ (associated to $\iota^z_{h,2}$ through equation (C.23)) and the torque given by the two net impulses along x and y direction ι^x_2 and ι^y_2:

$$I_{zz}\omega_\phi = |\iota_2^x|c + |\iota_2^y|c + \tau_{h,2}^\phi = \left(|\iota_2^x| + |\iota_2^y| + \frac{|\iota_{h,2}^z|}{\tan\alpha}\right)c \tag{C.24}$$

Through the impulsive model of section 4.7.2, impulses ι_2^x and ι_2^y can be computed for each test, while the angular momentum $I_{zz}\omega_\phi$ derives from the measurements of ϕ rotation. If $\iota_{h,2}^z$ is known, equation (C.24) can be reversed in order to estimate c:

$$c = \frac{I_{zz}\omega_\phi}{|\iota_2^x| + |\iota_2^y| + \frac{|\iota_{h,2}^z|}{\tan\alpha}} \tag{C.25}$$

If the estimation enters the range (C.20), we consider that the ϕ rotation is compliant with the orthogonal impulse model (as a first approximation, i.e. in terms of order of magnitude).

Unfortunately, $\iota_{h,2}^z$ cannot be estimated: only the residual impulse ι_{res}^z can be computed (equation (4.41)). Theoretically, the residual impulse is the sum of many components:

$$\iota_{res}^z = \iota_{res,1}^z + \iota_{res,2}^z = -(|\iota_{h,1}^z| + \iota_{pin,1}^z) + |\iota_{h,2}^z| + \iota_{pin,2}^z \tag{C.26}$$

where $\iota_{res,1}^z$ and $\iota_{res,2}^z$ are the contributions of the two plungers to the residual impulse, each composed of the uniform push of the plunger ι_h^z (as in figure C.10 left) and the push of the pin ι_{pin}^z along z axis. According to (C.26), infinite solutions are possible for $\iota_{h,2}^z$.

As a consequence, we can solve equation (C.24) only under some assumptions.

In figure C.11 we estimate the value of c according to equation (C.25), for the same test set of test considered in section 4.7.2: some tests which showed a significant ϕ rotation before the release have been excluded, since they revealed a missing blocked condition of the TM before the release. The results of figure C.11 are computed under some assumptions. For the tests with positive ι_{res}^z (see figure 4.50), we suspect an important action of the pyramidal plunger and we assume therefore the uniform (hidden) push of the Z- plunger equal to the measured residual, i.e. $\iota_{h,2}^z = \iota_{res}^z$; for the tests with negative ι_{res}^z, we suspect an important action of the conical plunger and we assume therefore $\iota_{h,2}^z = 0$ (the pyramidal plunger is not contributing to the ϕ rotation).

We can see that the estimated values for TM1 match with the range of equation (C.20).

This is not the case for test 28 of TM2: under our assumption, the required arm for the rotation (1 cm approximately) is out of the geometrical limit. This is a consequence of the assumption. For this test, we are indeed assuming $\iota_{h,2}^z = 0$ due to the main action of the conical plunger; since the pyramidal impulse of test 28 is very low (figure 4.49), we get that the denominator of equation (C.25) goes to zero and the estimated value of c exceeds therefore the limit. However, due to the indetermination in z it is possible to assume that:

$$\iota_{res}^z = |\iota_{h,2}^z| - |\iota_{h,1}^z| \tag{C.27}$$

i.e. the residual impulse is the difference between two balanced impulses, such that a proper choice of $\iota_{h,2}^z$ can lead to a feasible value of c. For instance, if for test

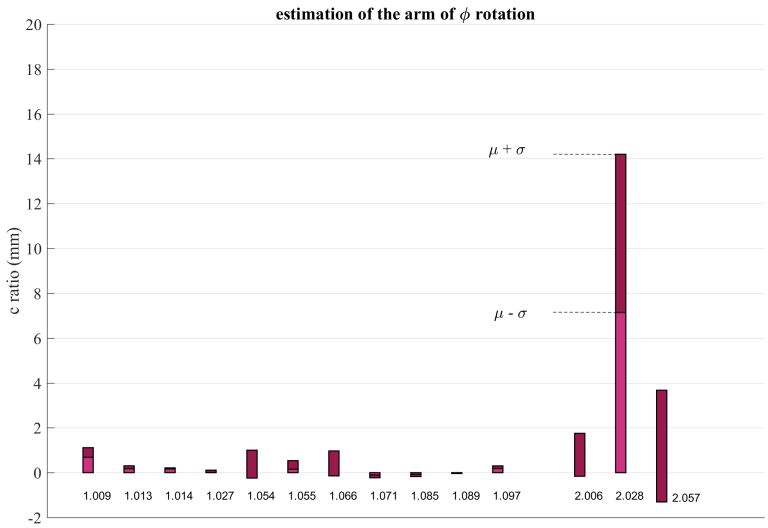

Figure C.11: estimation of c according to equation (C.25). The captions under each group of columns report the test number (e.g. 1.089 is TM1, test 89). The end of each column (of a darker colour) indicates the range of the uncertainty, as shown in the figure (μ is the estimated value and σ its standard deviation).

28 of TM2 we choose $\iota^z_{h,2} = 10$ kg μm/s, we would get an estimation of c in the limit; this would imply that, according to the new assumption of equation (C.27) and the value of ι^z_{res} of figure 4.50:

$$|\iota^z_{h,1}| = |\iota^z_{h,2}| - \iota^z_{res} \approx 10 \text{ kg } \mu\text{m/s} - (-10 \text{ kg } \mu\text{m/s}) = 20 \text{ kg } \mu\text{m/s}$$

which would be a balanced impulse of the conical plunger similar to the balanced impulses of the pyramidal plunger for the TM1 tests of the previous hypothesis (which were equal to the values ι^z_{res}). We remark that, giving the conical plunger no contribution for ϕ rotation, $\iota^z_{h,1}$ could be due to a uniform push of the conical plunger or to the push of the Z+ pin.

We get therefore that, if we assume that $\iota^z_{res} = \iota^z_{h,2}$, the ϕ rotation associated to the orthogonal impulse model is compliant with the system geometry for TM1; for test 28 of TM2, we must assume that the residual impulse ι^z_{res} is the difference of two opposite balanced impulses of the plungers.

C.4 Exclusion of stiffness asymmetry in the slow pin tests

For the reference test represented in figures 4.59 and 4.60, the measured preload is very small (approximately 2 mN), with an estimated uncertainty (standard deviation) of 0.1 N. According to the nominal preload, by applying equation (4.8.1), we would get a null time of detachment (i.e. the detachment occurs immediately as the pins start their retraction). Due to the low reliability of the load cell and by considering a worst case, we can assume a preload of the test of 0.2 N (two times the standard deviations). In this condition, the Δz displacement is reached after a time

$$\Delta t = \frac{\Delta z}{v_{pin}} = \frac{f_0/k}{v_{pin}} = \frac{(0.2\text{ N})/(0.38\text{ N}/\mu\text{m})}{2.5\ \mu\text{m/s}} \approx \frac{0.53\mu\text{m}}{2.5\ \mu\text{m/s}} \approx 0.2\text{ s}$$

In this case, the required retraction for the pins in order to reach a null preload is 0.5 μm (since the pins retract with a velocity of 2.5 μm/s).

We can see from figure 4.60 that the pin effectively retracts of a similar quantity (0.7 μm) before we can detect a change in the TM position. As a consequence, we would conclude that the pin retracts in the time between A and B, in B the null preload is reached and the adhesive forces applied, and the TM moves then freely with velocity $v_{z,1}$.

Alternatively (if, for instance, we do not rely on the fair synchronization of the two signals of figure 4.60) we can assume (*per adsurdum*) that velocity $v_{z,1}$ is not a free flight velocity, but is produced by the stiffness asymmetry of the two plungers, and we can compute the stiffness asymmetry that is needed in order to create this situation.

In this hypothesis, we consider that the stiffness of Z+ plunger can be different than the stiffness of Z- plunger ($k_1 \neq k_2$). The TM moves of approximately $\Delta z = 0.2\mu$m (in negative direction) during the preload force decrement, up to the (supposed) detachment. If this displacement of the TM is due to an asymmetry of the stiffnesses, the following relation holds:

$$\Delta z = \Delta_1 z - \Delta_2 z \tag{C.28}$$

where $\Delta_i z$ is the relaxation of the i-th spring:

$$\Delta_i z = \frac{f_0}{k_i} \tag{C.29}$$

where k_i is the stiffness of the i-th plunger.

Therefore, expanding (C.28) according to the definition of (C.29),

$$\frac{\Delta z}{f_0} = \frac{k_2 - k_1}{k_1 k_2} \tag{C.30}$$

The two stiffnesses k_1 and k_2 must satisfy equation (C.30) and also the measured total stiffness (section 4.2.3), which is given by the series of the two springs. The following relations must be simultaneously satisfied:

$$\begin{aligned} \frac{k_2 - k_1}{k_1 k_2} f_0 &= -0.2\mu\text{m} = \Delta z \\ \frac{k_1 k_2}{k_1 + k_2} &= 0.19 \frac{\text{N}}{\mu\text{m}} = k_{eq} \end{aligned}$$

In the worst-case for preload ($f_0 = 0.2$N), we get

$$\begin{aligned} k_1 &\approx 0.47 \frac{\text{N}}{\mu\text{m}} \\ k_2 &\approx 0.32 \frac{\text{N}}{\mu\text{m}} \end{aligned}$$

which would mean a difference of stiffness of more 50% of the Z+ plunger w.r.t. the negative one. A even higher asymmetry would come from the computation if we assume a lower preload, closer to the measured one. Moreover, some tests with similar preload show a higher displacement Δ_z of the TM, or negative displacement Δ_z, which would yield completely different values of k_1 and k_2.

As a consequence, the hypothesis of displacement due to stiffness asymmetry can be discharged.

C.5 Capacitive forces between plunger and TM

Let's consider the situation sketched in figure C.12. z is the displacement of the TM w.r.t. the zero reference. In the nominal situation, the TM is at a distance d from the plunger. As z increases, the distance decreases according to the function $d - z$.

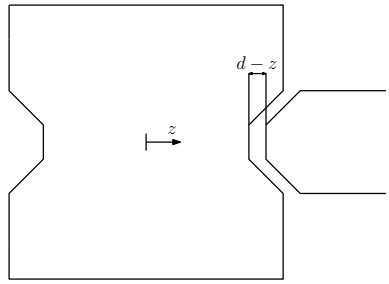

Figure C.12: TM-plunger distance as a function of the z displacement of the TM.

In [104] and [105], the relative capacitance between TM and plunger $C_{PL}(z)$ has been computed (through e FEM model) as a function of z: the function is plotted in figure C.13. The capacitance for $z = 0$ is approximately 40 pF. The relative capacitance is a function of the form:

$$C_{PL}(z) = \frac{A}{B - z}$$

where A and B are constants:

$$\begin{aligned} A &= 0.575 \cdot 10^{-15} \text{ F} \cdot \text{m} \\ B &= 14 \cdot 10^{-6} \text{ m} \end{aligned}$$

The capacitance is inversely proportional to the distance; the case is similar to the one with infinite parallel capacitors.

Figure C.14 shows a circuit representing the capacitive interaction between TM and its sorroundings: plunger (PL) and electrode housing (EH). We are considering here a case with a single (Z+) plunger close to the TM, and the other plunger completely retracted. This is a worst case if our goal is the estimation of a possible capacitive force between TM and the plunger: with two plungers close to the TM, we would have indeed a cancellation between the opposite electrostatic forces.

EH and PL have the same voltage, and $\Delta V(z)$ is their voltage difference w.r.t. the TM. C_{EH} is the capacitance between the TM and the electrode housing, which can be considered as constant if the TM is positioned in the centre of the housing and its motion is negligible w.r.t. the housing dimension:

$$C_{EH} \approx 35pF \tag{C.31}$$

The total capacitance $C(z)$ between TM and the sorroundings is given by the sum of the two capacitances (parallel capacitors):

$$C(z) = C_{EH} + C_{PL}(z)$$

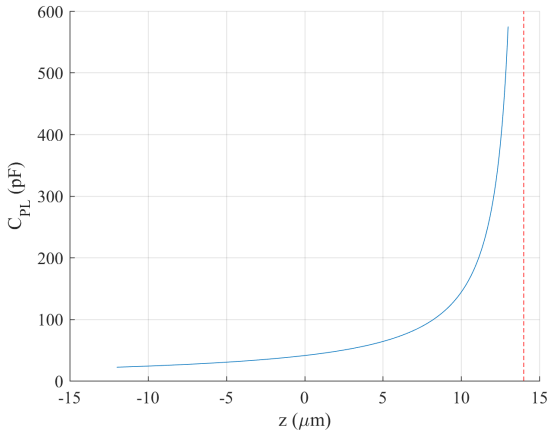

Figure C.13: graph of the function $C_{PL}(z)$. The asymptote corresponds to the contact between TM and plunger.

$Q_{EH}(z)$ is the charge distributed on the TM surfaces, while $Q_{PL}(z)$ is the charge distributed on the indentation. If we are considering a free motion of the TM, the TM is not in contact with its sorroundings, and maintains a constant charge Q. Therefore, for a free motion of the TM we can consider:

$$Q_{EH}(z) + Q_{PL}(z) = Q \tag{C.32}$$

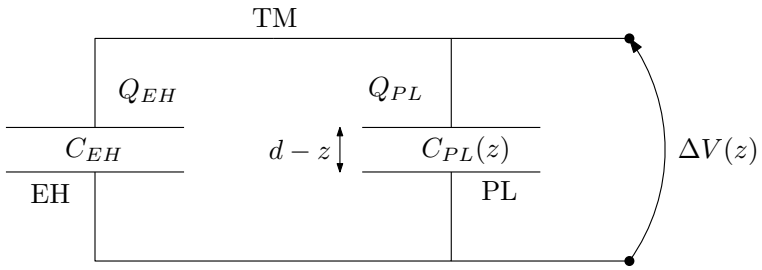

Figure C.14: circuit representing the interaction between TM and its sorroundings (plunger PL and electrode housing EH) when the TM is moving freely with a constant total charge $Q = Q_{EH} + Q_{PL}$.

In a capacitor, the electrostatic force of attraction between the plates is given by the following relation:

$$f(z) = \frac{1}{2}\frac{\partial C(z)}{\partial z}(\Delta V(z))^2$$

The derivative of the total capacitance can be computed according to (C.5) and

(C.31):

$$\frac{\partial C(z)}{\partial z} = \frac{\partial}{\partial z}(C_{EH} + C_{PL}(z)) = \frac{\partial C_{PL}(z)}{\partial z} = \frac{A}{(B-z)^2} \tag{C.33}$$

$\Delta V(z)$ can be written as a function of Q and the capacitances:

$$\Delta V(z) = \frac{Q}{C(z)} = \frac{Q}{C_{EH} + C_{PL}(z)}$$

As a consequence, equation (C.5) becomes

$$\begin{aligned} f(z) &= -\frac{1}{2}\frac{A}{(B-z)^2}\frac{Q^2}{(C_{EH}+C_{PL}(z))^2} \\ &= -\frac{1}{2}\frac{A}{(B-z)^2}\frac{Q^2(B-z)^2}{(C_{EH}(B-z)+A)^2} \\ &= -\frac{1}{2}\frac{A\cdot Q^2}{(C_{EH}(B-z)+A)^2} \end{aligned}$$

where the "minus" sign appears since the force is attractive. We get therefore that (as expected) the attractive force increases as the relative distance between plunger and TM decreases, reaching a maximum as $z = B$ (asymptote of the capacitance):

$$\max|f(z)| = \frac{1}{2}\frac{Q^2}{A}$$

If the total charge Q is determined, the maximum force can be computed.

Based on the TM charge analyses performed in LISA Pathfinder, the relative voltage ΔV has been estimated in the order of tenth of Volt with the plungers completely retracted. No charge measurements were possible in the release test campaign of 2017; we can therefore consider the same order of magnitude for the voltage with the TM completely retracted. If we consider that in this condition $z \to -\infty$, we assume:

$$\Delta V(z = -\infty) = 0.5\text{V}$$

If we assume that the difference of voltage is due to the charge patches created at the separation between TM and plunger (due for instance to a triboelettrification at the detachment), we get from equation (C.5):

$$\begin{aligned} Q &= \Delta V(z=-\infty)\cdot C(z=-\infty) && \text{(C.34)} \\ &= \Delta V(-\infty)\cdot C_{EH} \approx 0.5\text{ V }\cdot 35\text{ pF} && \text{(C.35)} \\ &= 17.5\text{ pC} && \text{(C.36)} \end{aligned}$$

We get therefore that:

$$\max|f(z)| = \frac{1}{2}\frac{Q^2}{A} \approx 0.27\ \mu\text{N}$$

This corresponds to the following acceleration (with $m = 1.928$ kg mass of the TM):

$$\max|\ddot{z}| = \frac{\max f(z)}{m} \approx 0.14\ \mu\text{m/s}^2$$

We get therefore that the maximum acceleration produced by the TM charge is 0.14 μm/s^2. In a worst case where we consider the maximum acceleration acting constantly for one second, we would get an (additional) velocity along z of approximately 0.14 μm/s; if we consider that all the release velocities are computed after a maximum time of 0.2 seconds after the retraction of the pin, we would get that the additional velocity due to the TM charge effect is 0.03 μm/s.

As a consequence, the velocity due to the TM charge is negligible if we assume that the TM charge is of the same order of magnitude of the observations.

Similarly to [104], we can consider a worst case with $\Delta V = 2$V. In this situation, we would get a maximum additional velocity of 2.2 μm/s, which is not negligible if compared to the release velocities of some tests (e.g. slow pin tests).

C.6 Results of the in-flight release campaign

We report here a table with the results of the in-flight campaign.

In the following, we explain the meaning of each field of the table.

code	parameters		quality	preload	release velocities						kinetic	gap
1	0	0	0	32	23,0	2,0	31,2	133,3	-1827,4	-2,4	3,4	
89	0	0	1	*105*	*0,2*	*0,1*	*0,3*	*2,8*	*2,4*	*1,6*	2,0	15,1
NH	0	1	0-10%	0	129,2	9,5	-226,8	255,0	632,1	-4384,8	4,9	

Code

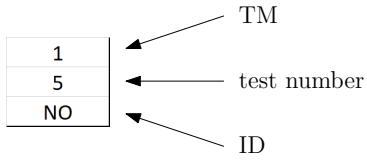

The meaning of the test ID is explained in the following table:

NO	nominal release
NQ	quasi-nominal release (pin extraction: 17 μm)
NH	nominal release with hammering before the release
RS	reduced symmetric pin release
RA	reduced asymmetric pin release
SO	slow pin release
SH	slow pin release with hammering before the release
PS	symmetric plunger release
PP	asymmetric plunger release (Z+ retracted)
PM	asymmetric plunger release (Z- retracted)

Parameters

The tests have been classified based on six binary indeces. Index 0 refers to the *nominal* situation (see section 4.1.2).

- **p: pin / plunger release**

  0: release performed through a pin retraction.

  1: release performed through a plunger retraction, with no pin extraction (i.e. the handover to pins is not performed).

- **s: symmetric / asymmetric release**

  0: symmetric release (i.e. pin or plungers move synchronously and symmetrically on both sides of the TM).

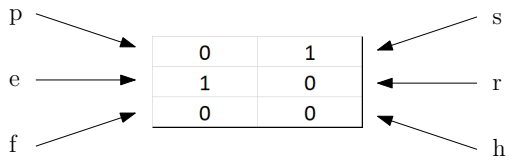

1: asymmetric release (asynchronous motion and/or different pin extractions).

- **e: full / partial pin extraction**

  0: both pins are extracted of 18 μm (commanded extraction), thus maximizing the distance between plunger and mass indentation.

  1: at least one of the two pins is extracted of less than 18 μm.

- **r: full / partial pin retraction**

  0: the pins are completely retracted.

  1: the pins are not completely retracted.

- **f: fast / slow pin release**

  0: the pin is retracted with the maximum velocity, corresponding to the response of the piezo to the inverse step of voltage.

  1: the pin is retracted with a low velocity ($\approx$ 2.5 μm/s).

- **h: no hammering / hammering**

  0: no hammering is performed before the release (i.e. repeated pin extraction and retraction prior to the release in order to adjust the TM attitude, see section 4.2.2).

  1: hammering is performed before the release.

We define the *nominal release* as the release with pin symmetric release, full pin extension, full pin retraction, fast retraction, and no hammering. As a consequence, the nominal release code is 000000. For each parameter, index 1 refers therefore to a variation of the corresponding parameter with respect to the nominal situation.

Quality

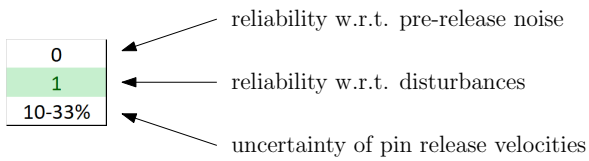

For each of the two reliability tests (see appendix C.1), the index is 1 if the test is considered reliable.

A test is consider reliable if it satisfies the reliability test w.r.t. disturbances (second index). The second index is red-coloured if equal to 0, green-coloured if equal to 1.

The third field (uncertainty of the pin release velocity) is equal to the range of the maximum uncertainty of the pin release velocities (except ϕ rotation). In the example, the higher relative uncertainty of the pin release velocities different than ω_ϕ is in the range 10-33%.

The fields are not defined for the plunger releases (PS, PP, PM).

Preload

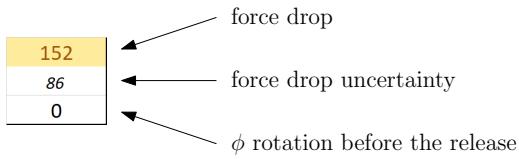

The first index (force drop) is yellow-coloured if it is higher than its uncertainty (standard deviation of the force drop). The third index (ϕ rotation before the release) is 1 if we notice a ϕ rotation of the TM before the pin release; in general, this occurs for test with very low preload before the release.

Release velocities

v_x	v_y	v_z	ω_θ	ω_η	ω_ϕ	
0,1	0,1	-1,3	9,4	-14,5	-17,9	pin release velocities
0,0	*0,1*	*1,5*	*6,5*	*4,0*	*2,6*	uncertainty of pin release velocities
-8,0	0,3	-8,8	-18,9	-546,1	-46,0	plunger release velocities

The second row corresponds to the uncertainty of the pin release velocities (standard deviation of the linear interpolation).

For the pin release velocities and the plunger release velocities, each velocity is green-coloured if its modulus is lower than the requirements (5 μm/s for translations, 100 μrad/s for rotations).

The first two rows are not defined for the plunger releases (PS, PP, PM).

Kinetic energies

K_1 is the kinetic energy at the pin release (i.e. computed from pin release velocities), K_2 the kinetic energy after impact, K_3 the kinetic energy after the plunger retraction (i.e. computed from plunger release velocities); see figure 4.20 for the distinction between the three velocities. All the kinetic energies are in pJ.

The logarithm is chosen in order to deal with the variation of the kinetic energy, which can span of several orders of magnitude. If K_{pJ} is the kinetic energy in pJ,

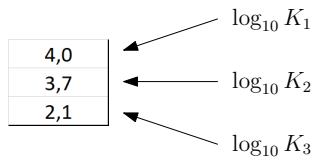

the logarithm of the corresponding energy in J (K_J) can be found through the following relation:

$$\log_{10} K_J = \log_{10} K_{pJ} - 12 \tag{C.37}$$

The first two cells ($\log_{10} K_1$, $\log_{10} K_2$) are not defined for the plunger releases (PS, PP, PM).

z gap before impact

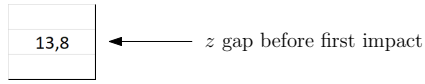

The gap before impact is defined as the z displacement of the TM before a significant variation of z velocity can be seen (see for instance figure 4.25, where the impact occurs after a z displacement of approximately 13-14 μm).

If the impact has not been identified, it is not reported (in this case, the TM generally moves without bounces after the pin release).

The quantity is not defined for the plunger releases (PS, PP, PM).

1	0	0	0	547	0,4	-0,9	2,5	49,9	-42,8	18,6	0,9	
1	0	0	1	*99*	*0,0*	*0,1*	*0,5*	*15,3*	*18,3*	*6,6*	1,2	
NO	0	0	33-100%	0	0,8	-0,7	3,2	28,2	-116,5	2,4	1,2	
1	0	0	0	421	45,5	-18,5	55,7	1709,8	-3196,9	111,0	4,0	
2	0	0	0	*93*	*1,7*	*2,5*	*8,1*	*159,8*	*132,6*	*28,5*	3,7	13,0
NO	0	0	10-33%	0	0,1	4,6	8,3	-232,3	88,4	295,1	2,1	
1	0	0	0	257	29,0	-6,4	31,1	727,0	-2094,4	36,8	3,5	
3	0	0	0	*88*	*12,6*	*4,3*	*11,0*	*437,9*	*897,2*	*15,5*	3,5	13,8
NO	0	0	33-100%	0	-5,1	-10,9	14,7	403,2	-104,5	69,9	2,6	
1	0	0	0	143	30,2	-3,9	31,5	549,2	-2138,6	56,3	3,5	
4	0	0	0	*87*	*11,4*	*2,4*	*8,6*	*295,7*	*788,5*	*21,5*	3,4	14,3
NO	0	0	33-100%	0	-5,8	-0,3	13,7	72,8	-158,1	223,9	2,4	
1	0	0	0	139	37,1	-17,4	51,5	1680,7	-2517,1	191,8	3,9	
5	0	0	0	*100*	*12,1*	*0,9*	*4,7*	*125,9*	*840,9*	*19,9*	3,5	12,9
NO	0	0	33-100%	0	-5,2	-0,8	8,3	-378,4	-254,6	295,7	2,3	
1	0	0	1	16	0,1	0,0	0,2	-5,5	-8,5	3,6	-1,0	
6	0	0	1	*84*	*0,0*	*0,0*	*0,1*	*3,0*	*1,8*	*1,5*	-0,3	
NO	0	0	10-33%	0	0,2	0,0	0,6	1,9	-10,4	-6,7	-0,3	
1	0	0	1	28	0,1	0,0	-1,0	0,0	-14,5	1,2	0,0	
7	0	0	1	*87*	*0,0*	*0,1*	*0,1*	*1,0*	*1,7*	*3,3*	0,1	
NO	0	0	33-100%	0	0,6	0,1	-1,3	8,1	-25,4	0,3	0,3	
1	0	0	0	27	3,4	-51,4	-63,8	4050,7	170,4	49,0	4,1	
8	0	0	0	*101*	*0,7*	*9,6*	*12,1*	*763,0*	*30,8*	*5,8*	3,8	-28,3
NO	0	0	10-33%	0	29,7	-8,4	17,4	-1682,7	-2575,8	-462,9	3,7	
1	0	0	0	35	14,5	-0,6	14,9	170,6	-1037,5	46,4	2,9	
9	1	0	1	*78*	*0,4*	*0,7*	*1,7*	*71,9*	*20,3*	*9,7*	2,8	4,5
NQ	0	0	33-100%	0	-8,6	0,1	0,5	-24,2	-338,7	-3,4	2,0	
1	0	0	0	40	32,7	-7,9	24,2	824,2	-2088,3	79,2	3,5	
10	1	0	0	*83*	*1,3*	*1,5*	*2,2*	*132,3*	*18,9*	*3,5*	2,2	13,8
NQ	0	0	10-33%	0	-7,9	25,5	-20,0	1533,6	1937,6	47,3	3,5	
1	0	0	0	58	36,9	-8,9	35,0	873,5	-2628,3	44,9	3,7	
11	1	0	0	*86*	*10,2*	*4,4*	*5,5*	*376,9*	*700,7*	*11,1*	3,5	13,0
NQ	0	0	33-100%	0	-10,0	-1,6	-1,0	1040,6	-189,8	199,0	2,7	
1	0	0	0	21	36,8	-6,1	32,8	652,2	-2556,6	47,0	3,7	
12	1	0	0	*88*	*4,5*	*2,8*	*2,3*	*264,1*	*206,1*	*11,8*	2,8	14,7
NQ	0	0	33-100%	0	0,6	-8,9	-14,8	-445,2	327,2	84,2	2,6	
1	0	0	0	19	25,5	-4,2	22,1	553,8	-1709,9	21,6	3,3	
13	1	0	1	*83*	*2,8*	*1,6*	*0,2*	*152,4*	*115,3*	*5,1*	2,6	8,3
NQ	0	0	33-100%	0	2,0	-5,7	-4,5	-511,7	250,9	184,4	2,2	
1	0	0	0	30	10,6	0,5	14,6	33,6	-808,3	8,9	2,7	
14	1	0	1	*84*	*0,0*	*0,1*	*0,2*	*4,3*	*7,9*	*1,1*	2,6	5,6
NQ	0	0	10-33%	0	-1,1	-3,8	12,5	283,5	237,6	32,6	2,3	
1	1	0	0	230	-1,0	-19,7	6,1	1548,2	-1682,0	-49,9	3,3	
15	0	1	0	*92*	*0,9*	*17,1*	*17,5*	*1198,9*	*960,7*	*27,3*	4,0	2,4
PT	1	0	33-100%	0	-29,0	-27,8	-34,8	1300,6	386,6	-64,5	3,5	
1	0	0	0	252	27,2	-6,6	27,0	758,7	-1771,5	61,2	3,4	
16	1	0	0	*89*	*10,2*	*4,0*	*9,8*	*386,3*	*572,0*	*24,7*	3,1	11,6
RS	0	0	33-100%	0	-1,0	0,2	-2,0	-95,4	-312,2	68,8	1,6	
1	0	0	0	236	32,1	-10,7	44,1	1407,6	-2284,7	157,1	3,7	
17	1	0	0	*82*	*2,2*	*2,4*	*5,9*	*290,6*	*101,4*	*67,7*	3,4	10,4
RS	0	0	33-100%	0	-35,1	-9,1	-125,3	268,4	-1216,0	609,5	4,2	
1	0	0	0	383	33,5	-11,3	38,1	1144,5	-2336,1	70,8	3,7	
18	1	0	0	*79*	*5,9*	*4,8*	*12,2*	*427,0*	*522,7*	*19,5*	3,3	11,3
RS	0	0	33-100%	0	-7,2	1,1	-0,4	32,6	-956,3	3,2	2,6	

1	0	0	0	313	3,8	-15,2	32,8	1042,8	-1101,0	82,0	3,3	
19	1	0	0	*80*	*13,5*	*0,7*	*7,5*	*184,2*	*498,9*	*13,9*	2,9	9,2
RS	0	0	33-100%	0	766,1	2,2	24,5	1293,5	18117,9	257,6	5,8	

1	0	0	0	278	22,5	-10,3	30,1	928,0	-1537,8	50,6	3,4	
20	1	0	0	*76*	*0,9*	*3,5*	*5,3*	*252,1*	*104,4*	*0,4*	2,8	8,9
RS	0	0	33-100%	0	404,8	-8,1	-828,9	-2703,5	-6020,5	1219,6	5,9	

1	0	1	0	348	16,7	-9,6	49,9	981,1	-1270,2	174,7	3,6	
21	1	0	0	*81*	*8,6*	*3,2*	*3,7*	*227,4*	*568,1*	*50,2*	2,9	14,3
RA	0	0	33-100%	0	-4,4	-15,2	-5,4	-549,5	-292,8	269,6	2,6	

1	0	1	0	275	22,3	-6,2	44,4	928,4	-1414,6	60,8	3,5	
22	1	0	0	*71*	*4,7*	*3,4*	*1,7*	*303,3*	*472,6*	*19,5*	2,9	15,1
RA	0	0	33-100%	0	-9,2	-1,9	2,4	-8,2	-122,7	-74,3	2,0	

1	0	1	0	236	21,2	-5,0	44,6	913,2	-1645,0	148,5	3,6	
23	1	0	0	*77*	*6,4*	*3,5*	*0,6*	*393,1*	*497,4*	*68,5*	3,4	6,9
RA	0	0	33-100%	0	-1,1	-11,9	-9,2	-527,7	207,0	295,8	2,6	

1	0	1	0	275	34,6	-10,3	61,2	1198,7	-2444,8	129,8	3,9	
24	1	0	0	*71*	*6,0*	*5,6*	*4,0*	*414,1*	*510,9*	*47,3*	3,2	14,6
RA	0	0	33-100%	0	0,2	-1,7	7,0	198,3	-94,9	138,2	1,9	

1	0	0	0	279	23,9	-15,1	60,6	1370,3	-1975,5	98,2	3,8	
25	1	0	0	*73*	*17,6*	*4,7*	*4,9*	*219,8*	*1107,3*	*14,1*	3,0	14,5
RA	0	0	33-100%	0	0,9	10,3	-97,6	-22,0	486,0	-69,4	4,0	

1	0	1	0	318	27,6	-14,9	65,4	1403,9	-2330,0	88,1	3,9	
26	1	0	0	*73*	*17,0*	*5,4*	*2,5*	*277,1*	*1023,3*	*10,4*	3,3	15,4
RA	0	0	33-100%	0	-1,9	-0,3	7,3	356,5	-84,3	127,8	2,0	

1	0	1	0	199	4,2	0,0	7,4	4,5	-349,0	1,5	2,0	
27	1	0	1	*69*	*0,1*	*0,1*	*0,3*	*9,3*	*6,7*	*1,3*	4,6	4,3
RA	0	0	0-10%	0	19,3	9,1	-75,8	1370,4	202,6	67,5	3,8	

1	0	1	0	284	35,6	-6,0	27,0	1298,4	-2719,8	96,5	3,7	
28	1	0	0	*81*	*17,1*	*7,2*	*13,5*	*516,6*	*800,8*	*11,4*	3,5	7,5
RA	0	0	33-100%	0	2,3	-4,2	3,5	282,0	405,9	67,3	2,1	

1	0	1	0	228	44,4	-10,4	35,2	1244,1	-2913,5	86,6	3,8	
29	1	0	0	*102*	*2,6*	*1,2*	*0,0*	*123,9*	*180,9*	*13,3*	3,1	8,5
RA	0	0	10-33%	0	1,2	57,6	-63,8	-3578,1	-115,6	334,1	4,1	

1	0	0	0	266	33,6	-0,1	38,1	370,4	-2501,3	33,4	3,7	
30	0	0	0	*83*	*13,3*	*0,6*	*12,0*	*204,4*	*967,6*	*5,0*	3,5	13,4
NO	0	0	33-100%	0	6,4	-6,1	-6,1	1058,0	-551,8	337,8	2,8	

1	0	1	0	261	45,4	-9,2	43,6	1443,0	-3252,9	105,6	3,9	
31	1	0	0	*79*	*7,6*	*0,4*	*7,6*	*51,7*	*428,2*	*24,2*	3,5	10,0
RA	0	0	10-33%	0	-6,2	0,9	-5,2	-140,9	-463,9	414,5	2,3	

1	0	1	0	203	7,4	1,0	11,3	16,3	-587,9	7,3	2,5	
32	1	0	0	*69*	*5,6*	*0,9*	*9,0*	*0,7*	*464,8*	*2,5*	3,4	10,8
RA	0	0	33-100%	0	7,8	28,0	-40,8	-2403,4	794,7	-207,8	3,7	

1	0	1	0	290	46,6	-11,0	44,6	1449,4	-3071,5	112,5	3,9	
33	1	0	0	*66*	*1,4*	*3,9*	*5,5*	*324,6*	*63,4*	*29,5*	3,6	10,2
RA	0	0	33-100%	0	11,9	-18,0	31,2	-3455,9	-97,1	253,4	3,7	

1	0	0	0	374	1,2	0,0	-0,8	-2,8	-62,5	103,3	0,8	
34	0	1	1	*94*	*0,2*	*0,1*	*0,6*	*4,1*	*15,7*	*3,5*	1,5	-0,5
SO	1	0	33-100%	0	0,2	-0,4	-0,8	-14,6	-12,9	110,5	0,7	

1	0	0	1	222	0,6	0,0	-0,4	-6,8	-25,0	27,3	0,0	
35	0	1	1	*94*	*0,0*	*0,1*	*0,3*	*2,6*	*0,5*	*8,8*	1,2	-0,3
SO	1	0	33-100%	0	0,3	0,1	-0,8	-3,4	8,6	12,2	-0,1	

1	0	0	0	70	2,4	-0,2	-0,5	4,5	-124,3	-12,0	1,0	
36	0	1	1	*86*	*0,1*	*0,1*	*0,2*	*2,5*	*14,1*	*4,1*	1,6	-0,4
SO	1	0	33-100%	0	0,3	0,0	-0,4	-15,7	32,3	-17,3	-0,1	

1	0	0	0	196	2,0	0,0	-0,8	0,5	-106,3	4,3	0,9	
37	0	1	1	*91*	*0,3*	*0,1*	*0,3*	*0,6*	*12,0*	*1,3*	1,5	-0,5
SO	1	0	10-33%	0	-13,8	-0,6	-11,0	-68,2	-967,7	-16,2	2,8	

1	0	0	1	224	0,9	0,1	-0,4	0,6	-45,2	7,4	0,2	
38	0	1	1	*94*	*0,1*	*0,1*	*0,2*	*0,5*	*8,4*	*1,3*	1,4	-0,3
SO	1	0	33-100%	0	1,2	-0,1	-0,8	-17,0	49,6	5,3	0,5	

1	0	0	0	276	1,7	0,1	-1,1	-2,6	-82,7	9,3	0,8	
39	0	1	1	*79*	*0,3*	*0,1*	*0,5*	*0,4*	*4,0*	*2,4*	1,0	-0,4
SO	1	0	33-100%	0	1,3	-0,1	-0,6	2,2	47,2	-5,7	0,4	

1	0	0	0	59	1,1	0,0	-1,5	-1,0	-66,7	-3,1	0,7	
40	0	1	1	*81*	*0,2*	*0,1*	*0,6*	*0,4*	*9,3*	*1,8*	1,0	-0,4
SO	1	0	33-100%	0	-1,3	-1,1	-0,5	-32,8	41,7	-6,5	0,6	

1	1	0										
41	1	0										
PS	1	0		0	-44,1	31,5	-65,8	-1992,4	-1388,3	-1363,3	4,0	

1	1	0										
42	1	0										
PS	1	0		0	-18,5	-23,4	71,4	148,2	807,3	1539,7	3,8	

1	1	0										
43	1	0										
PS	1	0		0	-19,5	-45,7	-141,2	11607,6	-155,6	-728,7	4,8	

1	1	0										
44	1	0										
PS	1	0		0	536,3	-36,7	-370,9	-309,0	-5497,9	6350,2	5,6	

1	1	1										
45	1	0										
PP	1	0		0	20,8	3,8	40,5	128,9	1072,6	256,4	3,4	

1	1	1										
46	1	0										
PP	1	0		0	27,8	-11,5	81,0	868,8	559,8	-1487,3	3,9	

1	1	1										
47	1	0										
PP	1	0		0	-22,6	-5,8	59,2	1477,2	-917,5	-1475,4	3,8	

1	1	1										
48	1	0										
PP	1	0		0	0,5	-30,3	182,4	2962,0	359,1	-5138,7	4,7	

1	1	-1										
49	1	0										
PM	1	0		0	-35,2	-4,3	-27,1	-213,7	732,0	-76,7	3,3	

1	1	-1										
50	1	0										
PM	1	0		0	-35,2	1,1	-36,3	-121,6	996,7	-430,8	3,5	

1	1	-1										
51	1	0										
PM	1	0		0	-13,9	0,5	-5,7	-33,6	591,5	7,0	2,5	

1	1	-1										
52	1	0										
PM	1	0		0	-20,5	0,7	-25,2	-6,5	837,4	-3,0	3,1	

1	0	0	1	31	0,3	0,0	0,2	-9,8	-19,8	10,6	-0,5	
53	0	0	1	*98*	*0,1*	*0,0*	*0,1*	*2,7*	*3,9*	*2,7*	-0,3	0,4
NH	0	1	33-100%	0	0,2	0,0	0,5	-3,1	-9,3	2,2	-0,5	

1	0	0	0	29	2,2	0,0	3,0	4,1	-160,4	3,8	1,3	
54	0	0	1	*117*	*0,0*	*0,1*	*0,2*	*8,6*	*6,7*	*6,2*	1,3	7,7
NH	0	1	0-10%	0	-7,7	0,6	-5,9	-35,6	-580,9	-10,8	2,3	

1	0	0	0	37	10,6	0,7	14,5	38,3	-813,5	16,4	2,7	
55	0	0	1	*105*	*0,2*	*0,0*	*0,2*	*1,1*	*29,5*	*9,0*	2,1	9,7
NH	0	1	0-10%	0	25,9	-18,1	-89,9	-1038,4	974,0	187,4	4,0	

1	0	0	0	16	0,6	0,1	2,3	-10,9	-45,5	2,3	0,8	
56	0	0	1	*101*	*0,0*	*0,0*	*0,7*	*2,0*	*12,6*	*0,9*	4,2	4,9
NH	0	1	10-33%	0	6,2	-11,1	-69,2	1633,3	173,3	-110,8	3,8	

1	0	0	0	152	43,9	-7,3	53,5	1241,1	-3002,7	90,6	3,9	
57	0	0	0	*86*	*11,6*	*3,7*	*14,9*	*182,0*	*1067,0*	*20,6*	3,6	14,5
NO	0	0	33-100%	0	-7,0	1,7	1,9	-0,1	-364,9	400,9	2,2	

1	0	0	0	196	32,0	-7,7	45,4	1275,4	-2279,5	105,6	3,7	
58	0	0	0	*86*	*16,2*	*2,7*	*14,8*	*85,5*	*1248,7*	*23,2*	3,7	13,9
NO	0	0	33-100%	0	-0,9	-2,7	1,0	124,9	-156,2	429,9	1,9	

1	0	0	0	164	36,3	-7,6	43,6	1346,1	-2600,6	128,6	3,8	
59	0	0	0	*97*	*17,2*	*1,8*	*19,7*	*10,1*	*1275,9*	*35,3*	3,6	14,0
NO	0	0	33-100%	0	-1,3	-6,9	-1,3	238,7	-82,2	395,6	2,1	

1	0	0	1	190	1,5	-0,2	1,2	19,9	-82,2	15,3	0,8	
60	0	1	1	*97*	*0,0*	*0,0*	*0,1*	*3,5*	*3,3*	*8,2*	0,8	3,2
SO	1	0	10-33%	0	34,0	5,2	-61,3	-1497,0	675,3	49,8	3,8	

1	0	0	0	79	1,8	-0,2	0,7	7,2	-107,4	0,5	0,9	
61	0	1	1	*90*	*0,0*	*0,0*	*0,2*	*3,2*	*13,2*	*4,4*	0,7	3,5
SO	1	0	10-33%	0	93,2	51,8	-127,8	-36,4	7403,2	10,5	4,7	

1	0	0	0	339	0,9	0,0	-0,3	-4,7	-41,2	-6,2	0,1	
62	0	1	1	*101*	*0,1*	*0,1*	*0,4*	*2,1*	*0,8*	*2,3*	0,0	-0,4
SO	1	0	33-100%	0	0,1	0,0	0,1	3,0	8,9	-15,6	-0,9	

1	0	0	0	275	-0,2	0,2	-2,6	11,2	6,1	17,0	0,8	
65	0	1	0	*70*	*0,1*	*0,1*	*2,3*	*8,0*	*10,6*	*13,0*	1,1	-0,1
SH	1	1	33-100%	0	-0,3	0,0	-0,6	-16,2	63,9	19,1	0,3	

1	0	0	0	110	2,3	0,2	3,3	14,1	-188,5	4,5	1,4	
66	0	0	1	*74*	*0,1*	*0,1*	*0,3*	*0,5*	*14,8*	*6,1*	0,5	2,9
NH	0	1	0-10%	0	0,6	0,1	1,4	8,6	-29,2	1,8	0,4	

1	0	0	0	47	0,1	0,0	-0,6	-1,6	2,3	2,8	-0,5	
67	0	1	1	*72*	*0,0*	*0,1*	*0,5*	*3,9*	*7,1*	*2,1*	0,1	-0,2
SH	1	1	33-100%	0	-0,7	-0,1	-0,8	3,9	73,3	-16,2	0,5	

1	0	0	0	30	0,1	0,0	-1,2	1,8	-1,4	4,3	0,1	
68	0	1	1	*94*	*0,1*	*0,1*	*0,5*	*0,9*	*6,2*	*0,2*	-1,6	-0,6
SH	1	1	33-100%	0	-0,8	0,0	-0,8	-1,6	61,5	-7,0	0,4	

1	0	0	1	88	-0,5	0,0	-0,5	-1,5	60,8	-12,1	0,2	
69	0	0	1	*103*	*0,0*	*0,0*	*0,0*	*1,8*	*4,6*	*0,8*	-1,2	0,1
NH	0	1	0-10%	0	-0,7	0,0	-0,8	0,8	77,8	-12,5	0,5	

1	0	0	1	53	0,0	0,0	-0,1	0,5	0,3	-17,8	-0,9	
70	0	1	1	*85*	*0,0*	*0,1*	*0,1*	*0,4*	*6,5*	*4,1*	-0,7	-0,3
SH	1	1	33-100%	0	-2,7	0,0	-2,2	-14,3	134,9	33,4	1,3	

1	0	0	0	30	35,2	0,9	41,9	303,3	-2694,9	-23,4	3,7	
71	0	0	1	*95*	*1,7*	*0,8*	*0,2*	*87,2*	*77,3*	*8,9*	3,1	15,6
NH	0	1	33-100%	0	-1,6	-3,4	-0,9	69,6	37,6	221,2	1,5	

1	0	0	0	12	0,1	0,0	-0,3	-4,1	2,1	2,3	-1,0	
72	0	1	1	*114*	*0,0*	*0,1*	*0,7*	*5,6*	*1,3*	*3,8*	-0,6	-0,3
SH	1	1	33-100%	0	-1,1	-0,5	-1,3	18,7	115,0	-13,3	0,9	

1	0	0	0	39	-0,4	-0,4	-1,1	-20,5	41,2	-3,5	0,4	
73	0	0	1	*110*	*0,4*	*0,1*	*0,2*	*2,6*	*24,0*	*1,2*	-1,5	-0,5
NH	0	1	33-100%	0	-1,5	-0,2	-1,4	9,0	112,7	-16,7	0,9	

1	0	0	0	2	0,2	0,0	-0,5	0,7	-2,9	26,2	-0,3	
74	0	1	1	*115*	*0,1*	*0,1*	*0,1*	*2,0*	*2,3*	*1,8*	-0,1	-0,2
SH	1	1	10-33%	0	-2,0	-0,1	-1,7	8,1	125,4	-24,7	1,1	

1	0	0	0	60	-0,9	0,1	-0,6	6,4	75,2	8,1	0,5	
75	0	0	1	*99*	*0,1*	*0,0*	*0,1*	*2,1*	*3,6*	*4,4*	-0,9	0,2
NH	0	1	10-33%	1	-1,3	-0,2	-1,5	7,0	137,2	-26,0	1,0	

1	0	0	0	13	0,1	-0,1	-0,1	6,3	-1,5	24,5	-0,6	
76	0	1	1	*106*	*0,0*	*0,1*	*0,0*	*1,7*	*2,7*	*5,4*	-0,4	-0,2
SH	1	1	10-33%	0	-3,6	-0,2	-3,5	-10,7	270,0	14,0	1,7	

1	0	0	0	64	-0,8	-0,1	-0,9	-0,1	65,9	-15,7	0,5	
77	0	0	1	*106*	*0,1*	*0,1*	*0,1*	*0,7*	*4,1*	*4,5*	-0,2	-1,1
NH	0	1	33-100%	1	-0,7	-0,1	-1,0	7,6	91,7	-43,8	0,7	

1	0	0	0	6	0,2	0,0	-0,3	4,3	-2,4	-26,3	-0,4	
78	0	1	1	*99*	*0,1*	*0,1*	*0,2*	*6,1*	*3,9*	*1,3*	0,1	-0,2
SH	1	1	33-100%	0	-1,4	0,0	-1,4	1,9	117,5	-52,8	1,0	

1	0	0	1	41	-0,1	-0,3	-0,4	-11,2	20,7	-6,6	-0,4	
79	0	0	1	*99*	*0,1*	*0,2*	*0,1*	*3,1*	*4,4*	*6,6*	-0,5	-0,3
NH	0	1	33-100%	1	-7,1	0,1	-6,9	-45,8	-434,0	6,6	2,2	

1	0	0	0	10	0,5	-0,1	-2,2	6,5	-25,0	-13,5	0,7	
80	0	1	1	*99*	*0,1*	*0,1*	*0,1*	*2,6*	*1,5*	*3,3*	-0,1	-0,8
SH	1	1	10-33%	1	-0,7	-0,6	-0,8	18,2	54,7	6,0	0,4	

1	0	0	1	29	0,0	-0,1	-0,4	-0,2	81,3	-15,5	0,4	
81	0	0	1	*95*	*0,1*	*0,2*	*0,0*	*2,2*	*3,5*	*3,8*	0,4	
NH	0	1	33-100%	1	-21,0	0,8	-19,5	36,1	-1481,3	-2,8	3,2	

1	0	0	1	9	0,0	0,0	-0,1	4,7	-1,6	-20,9	-0,8	
82	0	1	1	*87*	*0,1*	*0,1*	*0,0*	*0,9*	*2,2*	*7,6*	-0,7	-0,1
SH	1	1	33-100%	0	-11,0	0,5	-12,2	-67,3	-489,5	31,6	2,5	

1	0	0	1	47	-0,4	-0,2	-1,8	-9,6	26,4	-5,8	0,5	
83	0	0	1	*97*	*0,0*	*0,3*	*0,0*	*4,9*	*5,7*	*3,0*	-0,9	-1,3
NH	0	1	10-33%	1	-0,5	-0,5	-0,9	-7,7	53,0	-9,0	0,3	

1	0	0	0	7	-0,4	-0,2	-0,4	12,2	5,2	-0,9	-0,4	
84	0	1	0	*110*	*0,1*	*0,1*	*0,0*	*5,5*	*0,7*	*10,2*	0,6	-0,8
SH	1	1	33-100%	0	-10,3	0,1	-11,1	-42,5	-726,9	7,0	2,6	

1	0	0	0	68	22,6	1,7	30,2	136,0	-1876,3	-12,6	3,4	
85	0	0	1	*81*	*1,7*	*0,2*	*2,0*	*13,3*	*145,4*	*5,0*	2,3	15,9
NH	0	1	10-33%	0	18,1	-12,4	-284,1	1183,7	2227,0	2001,6	4,9	

1	0	0	0	59	0,1	0,1	-1,3	9,4	-14,5	-17,9	0,3	
86	0	1	1	*112*	*0,0*	*0,1*	*1,5*	*6,5*	*4,0*	*2,6*	1,2	-0,3
SH	1	1	33-100%	0	-8,0	0,3	-8,8	-18,9	-546,1	-46,0	2,4	

1	0	0	0	32	-0,7	0,4	-0,8	35,6	59,4	38,5	0,5	
87	0	0	1	*100*	*0,0*	*0,1*	*0,1*	*2,9*	*5,3*	*4,0*	0,1	-0,6
NH	0	1	33-100%	1	-0,5	-0,3	-0,6	2,9	54,0	41,7	0,4	

1	0	0	0	19	0,0	0,0	-0,6	15,8	-2,2	-3,8	-0,3	
88	0	1	1	*104*	*0,1*	*0,0*	*0,4*	*2,8*	*2,0*	*8,2*	-1,0	-0,1
SH	1	1	33-100%	0	0,0	0,6	-3,0	32,3	55,1	-28,9	1,0	

1	0	0	0	32	23,0	2,0	31,2	133,3	-1827,4	-2,4	3,4	
89	0	0	1	*105*	*0,2*	*0,1*	*0,3*	*2,8*	*2,4*	*1,6*	2,0	15,1
NH	0	1	0-10%	0	129,2	9,5	-226,8	255,0	632,1	-4384,8	4,9	

1	0	0	0	-8	-0,2	-0,3	-2,1	6,5	29,0	-2,9	0,7	
90	0	1	1	*128*	*0,1*	*0,3*	*0,4*	*10,9*	*2,0*	*5,7*	-0,4	-0,6
SH	1	1	33-100%	1	-0,7	0,0	-0,8	6,5	74,5	-81,3	0,7	

1	0	0	1	23	-0,3	-0,1	-0,7	-3,8	7,9	82,7	0,5	
91	0	0	1	*101*	*0,0*	*0,2*	*0,1*	*3,8*	*6,5*	*2,2*	1,1	
NH	0	1	10-33%	1	-1,5	-0,1	-2,6	-7,9	124,9	87,5	1,2	

1	0	0	0	16	0,1	-0,2	1,0	7,3	-6,8	4,2	0,0	
92	0	1	1	*122*	*0,1*	*0,1*	*0,8*	*2,7*	*6,6*	*1,3*	0,6	-0,1
SH	1	1	33-100%	1	-0,1	-0,8	-0,6	35,0	66,8	-20,6	0,5	

1	0	0	0	61	0,0	-0,1	-0,8	12,9	15,8	-15,1	-0,1	
93	0	0	1	*103*	*0,1*	*0,2*	*0,3*	*3,3*	*12,5*	*4,4*	-0,4	-0,4
NH	0	1	33-100%	1	-1,5	-0,2	-1,1	21,5	89,6	-25,1	0,8	
1	0	0	1	9	-0,4	0,0	-2,5	28,3	35,5	29,6	0,8	
94	0	1	1	*122*	*0,0*	*0,1*	*0,2*	*2,8*	*5,1*	*3,7*	0,2	-0,7
SH	1	1	33-100%	1	0,1	-0,2	-0,2	19,4	34,4	-3,3	-0,2	
1	0	0	1	36	-1,0	-0,4	-1,2	-10,1	64,6	-2,8	0,6	
95	0	0	1	*112*	*0,0*	*0,1*	*0,1*	*1,4*	*2,0*	*2,4*	-0,4	-0,6
NH	0	1	10-33%	0	-11,7	-7,7	-6,3	46,3	-438,5	-168,1	2,5	
1	0	0	0	19	0,0	-0,1	0,1	13,5	9,9	-3,6	-1,0	
96	0	1	1	*98*	*0,1*	*0,1*	*0,3*	*3,5*	*1,7*	*0,4*	0,3	-0,2
SH	1	1	33-100%	0	-0,3	-0,4	-0,5	15,8	45,5	-8,3	0,1	
1	0	0	0	35	18,5	1,4	24,5	50,9	-1519,1	20,3	3,2	
97	0	0	1	*115*	*1,7*	*0,2*	*1,9*	*1,8*	*144,2*	*4,3*	2,2	15,5
NH	0	1	10-33%	0	-5,8	0,0	-5,7	41,4	146,4	57,4	1,9	
1	0	0	0	2	-0,1	-0,1	0,1	12,3	5,0	-13,4	-0,8	
98	0	1	1	*116*	*0,0*	*0,0*	*0,1*	*0,1*	*3,6*	*5,0*	-0,9	-0,1
SH	1	1	33-100%	0	0,6	5,0	-7,0	318,9	44,1	63,6	2,0	
1	0	0	0	27	-0,6	-0,1	-0,6	6,2	25,3	-12,9	0,0	
99	0	0	1	*110*	*0,1*	*0,0*	*0,1*	*1,1*	*16,6*	*0,7*	-0,4	-0,4
NH	0	1	10-33%	0	-2,4	0,0	-1,8	0,9	-58,8	-32,7	1,0	
1	0	0	1	0	-0,1	-0,1	1,3	3,0	-0,1	38,5	0,3	
100	0	1	1	*97*	*0,0*	*0,0*	*0,1*	*3,3*	*6,3*	*3,1*	0,3	-0,2
SH	1	1	0-10%	1	0,7	-0,2	-1,1	15,9	-33,4	39,1	0,4	
1	0	0	1	43	-0,2	0,1	-0,6	14,1	44,8	13,6	0,1	
101	0	0	1	*101*	*0,1*	*0,0*	*0,2*	*1,5*	*7,1*	*0,3*	-0,6	-1,1
NH	0	1	10-33%	1	-0,7	-0,3	-0,6	13,8	26,8	-7,3	0,1	
1	0	0	1	18	0,2	-0,1	-0,1	14,6	-8,0	-0,9	-0,9	
102	0	1	1	*100*	*0,0*	*0,0*	*0,1*	*1,2*	*5,3*	*2,7*	-0,3	-0,2
SH	1	1	33-100%	0	-0,7	0,5	-0,5	38,2	63,6	14,1	0,5	
1	0	0	0	40	-0,2	-0,1	-1,6	0,3	18,7	-1,0	0,4	
103	0	0	1	*103*	*0,0*	*0,0*	*0,2*	*1,2*	*3,6*	*0,1*	0,0	-3,1
NH	0	1	10-33%	1	-0,7	-0,1	-0,4	22,0	18,8	-14,9	0,0	
1	0	0	0	12	0,0	0,0	0,6	9,5	-14,4	-0,8	-0,3	
104	0	1	1	*111*	*0,0*	*0,0*	*0,5*	*2,4*	*7,2*	*3,3*	0,9	-0,2
SH	1	1	0-10%	1	-12,4	0,6	-13,8	-38,0	-939,1	-32,6	2,8	
1	0	0	1	33	-0,3	0,5	0,1	18,0	59,5	-6,3	0,2	
105	0	0	1	*87*	*0,1*	*0,0*	*0,0*	*3,3*	*0,1*	*1,3*	0,7	0,1
NH	0	1	33-100%	0	-1,4	-1,3	-17,1	173,5	-269,3	167,2	2,5	
1	0	0	1	21	0,4	-0,3	-1,2	5,5	-8,3	-9,2	0,2	
106	0	1	1	*105*	*0,1*	*0,1*	*0,1*	*3,3*	*0,9*	*4,1*	-1,0	-0,9
SH	1	1	0-10%	0	-0,4	0,0	-0,4	2,8	37,5	-26,6	0,0	
1	0	0	1	30	-3,0	0,2	-2,4	-13,3	-205,4	-31,6	1,5	
107	0	0	1	*106*	*0,1*	*0,0*	*0,1*	*1,9*	*0,7*	*4,7*	-0,6	-0,1
NH	0	1	10-33%	1	-3,2	0,2	-2,6	-16,1	-165,4	-23,4	1,4	
1	0	0	0	16	-0,1	-0,2	1,7	2,7	-17,2	39,5	0,5	
108	0	1	1	*92*	*0,1*	*0,0*	*0,2*	*0,8*	*3,0*	*0,3*	0,6	-0,3
SH	1	1	0-10%	1	-0,6	-0,4	-0,7	7,2	15,8	49,4	0,3	
1	0	0	1	27	0,2	0,1	-0,3	3,5	18,7	-284,2	1,4	
109	0	0	1	*87*	*0,0*	*0,1*	*0,0*	*0,3*	*1,9*	*1,2*	1,4	-0,1
NH	0	1	10-33%	1	0,3	0,0	-0,8	6,5	62,2	-275,7	1,4	
1	0	0	0	3	0,8	1,1	-1,8	77,1	-40,0	-33,4	0,9	
110	0	1	1	*114*	*0,2*	*0,1*	*0,2*	*12,4*	*11,7*	*1,5*	1,1	-0,2
SH	1	1	10-33%	1	-1,7	0,2	14,8	53,8	137,1	-156,4	2,4	

2	0	0	0	499	9,2	9,4	-9,5	-424,1	701,7	28,9	2,7	
1	0	0	0	*98*	*2,1*	*3,4*	*1,0*	*24,1*	*203,5*	*1,4*	2,9	-2,2
NO	0	0	33-100%	0	-6,4	1,8	2,8	-297,6	-212,4	38,1	2,0	
2	0	0	0	448	-4,6	12,8	5,9	-707,8	1266,5	0,5	3,0	
2	0	0	0	*97*	*0,7*	*2,2*	*1,6*	*94,9*	*181,2*	*18,6*	2,9	2,2
NO	0	0	10-33%	0	-34,4	4,3	-98,8	-543,3	-1643,6	-235,8	4,1	
2	0	0	0	216	38,0	47,4	-18,1	-383,4	2106,8	-131,3	3,7	
3	0	0	0	*102*	*15,7*	*11,9*	*1,8*	*256,7*	*324,6*	*100,2*	3,4	-3,1
NO	0	0	33-100%	0	-23,4	-3,3	-28,3	144,0	-1075,3	-251,8	3,2	
2	0	0	0	207	12,8	54,1	1,1	-1721,0	956,7	-233,8	3,6	
4	0	0	0	*95*	*0,5*	*1,9*	*9,1*	*120,7*	*4,5*	*57,0*	3,4	-3,1
NO	0	0	33-100%	0	-0,3	22,9	9,0	-716,1	-88,0	-713,4	3,0	
2	0	0	0	247	34,8	-3,0	-26,7	-971,6	2392,0	61,4	3,6	
5	0	0	0	*100*	*7,3*	*0,4*	*1,7*	*224,2*	*344,5*	*10,9*	3,1	-6,0
NO	0	0	10-33%	0	8,0	-1,8	-40,4	564,9	-116,1	672,4	3,3	
2	0	0	0	77	1,2	2,2	-4,2	-269,9	-3,7	3,2	1,7	
6	0	0	1	*96*	*0,2*	*0,1*	*0,1*	*37,2*	*7,7*	*3,8*	1,5	0,1
NO	0	0	33-100%	0	14,4	6,3	-50,2	646,3	-703,3	166,9	3,5	
2	0	0	0	16	46,4	3,5	-26,8	-210,8	1945,5	-10,9	3,6	
7	0	0	0	*92*	*5,4*	*0,1*	*8,3*	*29,1*	*328,6*	*28,8*	3,0	-6,4
NO	0	0	10-33%	0	14,1	-0,2	-14,6	-23,7	926,6	11,5	2,8	
2	0	0	0	18	8,0	-51,4	67,0	-4305,5	2273,3	307,2	4,2	
8	0	0	0	*97*	*3,7*	*3,9*	*11,6*	*523,9*	*536,1*	*27,8*	2,5	20,4
NO	0	0	33-100%	0	38,8	8,9	-42,3	736,0	3247,9	397,5	3,8	
2	0	0	0	54	44,6	-2,4	-27,5	-1138,5	2463,6	136,4	3,7	
9	1	0	0	*91*	*3,2*	*2,8*	*1,4*	*96,0*	*65,9*	*16,8*	3,2	-7,4
NQ	0	0	33-100%	0	2,8	-2,8	-31,1	90,2	267,8	611,7	3,0	
2	0	0	0	95	39,6	20,8	2,2	-1113,8	1625,9	-164,7	3,5	
10	1	0	0	*95*	*2,6*	*3,0*	*8,8*	*56,6*	*488,4*	*29,4*	3,2	-4,6
NQ	0	0	33-100%	0	22,6	3,9	-10,0	346,3	83,9	196,3	2,8	
2	0	0	0	27	22,1	7,0	-4,8	-317,5	1044,1	-173,1	3,0	
11	1	0	0	*95*	*14,6*	*3,6*	*4,5*	*145,7*	*1198,9*	*3,6*	3,4	-3,6
NQ	0	0	33-100%	0	-58,4	1,4	-56,6	473,3	-3456,1	-115,6	4,0	
2	0	0	0	9	2,4	0,2	3,8	-62,1	238,2	73,9	1,6	
12	1	0	0	*94*	*0,8*	*0,7*	*1,1*	*39,6*	*36,2*	*6,9*	1,8	1,2
NQ	0	0	33-100%	0	-12,0	7,3	-38,8	934,5	1376,2	-38,8	3,4	
2	0	0	0	22	-2,8	23,7	-21,7	-1724,0	188,6	35,1	3,3	
13	1	0	0	*90*	*2,2*	*6,9*	*2,7*	*400,2*	*168,1*	*1,9*	3,6	0,4
NQ	0	0	33-100%	0	11,8	-9,6	-7,4	681,1	68,7	369,0	2,7	
2	0	0	0	17	29,4	1,6	-28,4	-432,9	1992,8	57,9	3,5	
14	1	0	0	*93*	*2,9*	*0,2*	*0,2*	*54,2*	*105,5*	*17,3*	2,8	-8,0
NQ	0	0	10-33%	0	-11,7	7,7	9,7	93,0	-640,5	74,6	2,6	
2	1	0	0	295	2,2	10,4	27,8	980,5	3429,5	-1312,6	3,8	
15	0	1	0	*92*	*1,3*	*21,8*	*25,9*	*1137,5*	*1403,6*	*563,7*	4,8	20,2
PT	1	0	33-100%	0	-33,0	-9,3	-74,4	-644,6	1605,5	-4647,8	4,2	
2	0	0	0	178	0,0	0,9	1,0	-41,6	-45,5	19,0	0,5	
16	1	0	0	*87*	*0,1*	*0,3*	*0,7*	*16,7*	*5,2*	*8,5*	-0,1	0,7
RS	0	0	33-100%	0	-2,2	-9,4	-94,7	550,0	538,3	-51,6	4,0	
2	0	0	0	381	23,6	39,1	-4,9	-1631,0	1253,7	-522,7	3,6	
17	1	0	0	*88*	*3,7*	*20,1*	*0,6*	*177,4*	*196,8*	*87,2*	3,6	-1,4
RS	0	0	33-100%	0	-7,6	8,4	-2,6	-440,9	-314,0	-456,6	2,5	
2	0	0	0	313	30,9	34,3	-11,5	-1603,8	1854,2	-155,6	3,6	
18	1	0	0	*92*	*2,2*	*4,4*	*2,8*	*194,3*	*9,5*	*62,5*	3,3	-2,9
RS	0	0	33-100%	0	-14,3	-0,6	-7,7	-38,0	180,5	-2,6	2,4	

2	0	0	0	304	-1,7	-1,5	2,7	-98,2	105,8	-6,1	1,3	
19	1	0	0	*95*	*0,6*	*0,4*	*1,5*	*19,6*	*51,8*	*18,9*	1,1	1,0
RS	0	0	33-100%	0	-15,4	5,7	-0,2	420,2	2945,7	-5,8	3,5	
2	0	0	0	316	-0,2	2,3	0,4	-239,0	-16,8	7,4	1,4	
20	1	0	0	*85*	*0,2*	*0,7*	*1,5*	*1,6*	*21,5*	*19,2*	1,5	0,6
RS	0	0	33-100%	0	-1,7	1,4	-3,0	128,0	346,4	-155,3	1,8	
2	0	1	0	315	37,4	2,2	-0,5	-556,3	2229,4	-162,8	3,5	
21	1	0	0	*85*	*7,5*	*0,3*	*4,9*	*100,8*	*269,6*	*79,0*	3,5	-1,2
RA	0	0	33-100%	0	-11,3	6,3	-16,5	543,8	-463,2	189,1	2,8	
2	0	1	0	400	38,8	27,1	18,5	-573,6	816,9	-199,0	3,5	
22	1	0	0	*88*	*5,7*	*1,4*	*2,8*	*270,8*	*502,9*	*8,2*	3,4	4,6
RA	0	0	33-100%	0	-5,4	-2,0	-45,1	329,3	612,0	242,3	3,3	
2	0	1	0	345	-3,9	-1,3	0,7	-72,6	278,8	38,2	1,7	
23	1	0	0	*86*	*0,4*	*1,1*	*1,7*	*80,4*	*34,7*	*4,2*	1,5	0,7
RA	0	0	33-100%	0	-2,9	0,8	-37,3	523,2	295,0	56,7	3,2	
2	0	1	0	457	30,4	11,3	-17,5	-1543,8	2483,5	137,0	3,6	
24	1	0	0	*92*	*4,9*	*2,0*	*4,3*	*76,7*	*18,1*	*20,2*	3,0	-4,1
RA	0	0	10-33%	0	-6,9	1,0	-15,2	-278,8	225,1	724,5	2,7	
2	0	1	0	258	31,3	15,1	-8,2	-1314,4	1752,6	168,1	3,5	
25	1	0	0	*85*	*3,9*	*2,8*	*5,7*	*150,5*	*311,4*	*29,8*	2,8	-3,7
RA	0	0	33-100%	0	-22,4	3,7	-15,8	-93,7	178,0	600,7	2,9	
2	0	1	0	370	9,9	-1,8	46,3	-1603,7	1727,0	104,5	3,6	
26	1	0	0	*90*	*3,0*	*13,0*	*2,3*	*832,8*	*389,0*	*118,8*	3,3	10,4
RA	0	0	33-100%	0	-2,6	6,7	0,2	-187,5	91,9	-177,2	1,9	
2	0	1	0	109	-8,0	-4,5	23,3	-402,3	122,6	-530,4	2,9	
27	1	0	0	*84*	*3,8*	*7,6*	*1,6*	*428,6*	*147,5*	*409,5*	3,3	4,3
RA	0	0	33-100%	0	10,8	0,0	-4,3	-565,6	-144,4	-2866,3	3,5	
2	0	1	0	319	21,2	4,6	-28,7	-330,9	1676,7	34,1	3,4	
28	1	0	1	*81*	*0,4*	*0,3*	*1,4*	*11,3*	*37,4*	*0,3*	2,3	-8,5
RA	0	0	0-10%	0	-7,1	0,4	7,0	108,5	-442,3	90,8	2,2	
2	0	1	0	14	-7,9	2,4	25,7	86,5	0,3	-498,6	2,9	
29	1	0	0	*87*	*7,7*	*0,2*	*8,1*	*36,5*	*690,1*	*236,1*	3,0	4,9
RA	0	0	33-100%	0	2,2	-0,1	5,9	413,0	-946,4	-1252,3	3,0	
2	0	0	0	307	48,8	23,8	-34,9	-384,3	2637,1	-80,8	3,8	
30	0	0	0	*87*	*13,6*	*4,5*	*3,2*	*19,8*	*225,2*	*97,9*	3,2	-7,0
NO	0	0	33-100%	0	-11,8	-4,5	-12,8	-71,3	-248,1	-317,4	2,6	
2	0	1	0	215	1,9	16,9	-17,5	-1245,3	627,1	6,4	3,1	
31	1	0	0	*85*	*1,0*	*12,7*	*13,6*	*944,8*	*499,7*	*6,9*	4,0	-6,5
RA	0	0	33-100%	0	9,7	-15,6	-7,9	83,5	-223,6	-1661,0	3,1	
2	0	1	0	256	-0,4	5,6	-1,8	-473,8	-7,2	21,3	2,0	
32	1	0	0	*93*	*0,4*	*1,4*	*1,5*	*3,4*	*15,7*	*15,9*	3,7	-0,6
RA	0	0	33-100%	0	37,2	10,7	24,3	192,8	-1939,4	78,4	3,5	
2	0	1	0	253	2,8	1,0	1,0	-41,0	-258,4	39,3	1,5	
33	1	0	0	*89*	*0,1*	*0,7*	*0,1*	*33,8*	*6,0*	*22,6*	4,3	
RA	0	0	33-100%	0	36,2	-11,2	-112,7	512,6	1763,1	47,3	4,2	
2	0	0	0	19	0,6	-0,4	-2,6	-1,3	19,0	93,1	1,0	
34	0	1	0	*89*	*0,3*	*0,4*	*1,9*	*5,4*	*11,4*	*68,1*	-2,6	-1,0
SO	1	0	33-100%	0	0,4	2,6	-5,3	-169,6	-8,8	-4,1	1,6	
2	0	0	0	413	0,2	-0,3	0,2	-28,9	-24,0	-90,3	0,5	
35	0	1	1	*90*	*0,1*	*0,2*	*0,3*	*20,5*	*18,0*	*1,7*	0,6	
SO	1	0	33-100%	0	3,8	0,7	-37,3	348,6	698,2	-80,3	3,2	
2	0	0	0	285	1,9	0,8	2,3	-10,3	85,5	-81,2	1,1	
36	0	1	1	*93*	*0,5*	*0,0*	*1,0*	*2,2*	*2,8*	*6,2*	1,1	-0,5
SO	1	0	10-33%	0	-2,7	17,5	-85,8	-349,6	821,3	-87,1	3,9	

2	0	0	0	356	0,0	0,1	0,2	-5,2	7,1	-17,2	-0,8	
37	0	1	1	*90*	*0,4*	*0,0*	*0,7*	*1,4*	*13,7*	*3,3*	1,6	-0,9
SO	1	0	0-10%	0	3,1	16,8	-12,0	-1173,0	209,9	-46,7	3,0	
2	0	0	0	419	-0,5	0,2	0,8	6,3	-2,3	-2,3	-0,1	
38	0	1	1	*92*	*0,1*	*0,2*	*0,1*	*4,7*	*23,9*	*9,9*	0,3	0,1
SO	1	0	33-100%	0	35,7	-5,2	-105,0	-8,2	1675,8	-22,2	4,1	
2	0	0	0	272	0,2	-0,4	-0,1	-13,0	-20,1	29,0	-0,2	
39	0	1	1	*85*	*0,0*	*0,2*	*1,0*	*7,8*	*0,6*	*12,6*	1,9	0,4
SO	1	0	33-100%	0	3,7	28,5	-17,2	-1743,8	298,1	-82,1	3,3	
2	0	0	0	316	0,9	0,8	-0,4	7,3	-23,9	-176,2	1,1	
40	0	1	1	*93*	*0,2*	*0,2*	*1,0*	*6,4*	*19,9*	*5,3*	1,3	0,5
SO	1	0	33-100%	0	2,1	-10,1	-115,4	480,3	159,3	48,2	4,1	
2	1	0										
41	1	0										
PS	1	0		0	40,6	-3,4	-47,0	989,5	5293,3	3926,2	4,3	
2	1	0										
42	1	0										
PS	1	0		0	-36,5	11,6	80,3	540,9	1727,2	-4223,3	4,2	
2	1	0										
43	1	0										
PS	1	0		0	28,9	-24,0	-88,2	-246,6	-564,7	-3807,9	4,1	
2	1	0										
44	1	0										
PS	1	0		0	11,4	-498,1	111,4	10481,0	3455,7	2800,4	5,5	
2	1	1										
45	1	0										
PP	1	0		0	-25,2	30,0	84,5	261,3	330,0	-11836,5	4,7	
2	1	1										
46	1	0										
PP	1	0		0	15,9	-13,8	99,5	-46,9	-384,1	25466,6	5,4	
2	1	1										
47	1	0										
PP	1	0		0	95,6	22,8	87,6	971,4	3296,8	-14330,1	5,0	
2	1	1										
48	1	0										
PP	1	0		0	-0,7	14,3	43,6	-1037,0	-635,3	1378,4	3,5	
2	1	-1										
49	1	0										
PM	1	0		0	7,5	1,3	-27,1	224,2	-82,9	791,6	3,0	
2	1	-1										
50	1	0										
PM	1	0		0	-1,3	6,2	-20,8	498,2	370,2	-858,1	2,9	
2	1	-1										
51	1	0										
PM	1	0		0	21,1	-0,3	-20,8	-48,0	-537,5	-81,7	3,0	
2	1	-1										
52	1	0										
PM	1	0		0	7,6	-0,5	-55,0	-5,0	36,4	-116,5	3,5	
2	0	0	0	28	18,4	30,7	27,8	-1339,5	571,6	-331,8	3,4	
53	0	0	0	*93*	*1,4*	*1,9*	*7,1*	*564,9*	*52,5*	*65,8*	3,0	7,4
NH	0	1	33-100%	0	1,1	8,8	-14,0	110,9	-200,5	-337,2	2,5	
2	0	0	0	295	30,0	14,0	-40,2	-1845,4	2195,8	498,9	3,7	
54	0	0	0	*96*	*29,0*	*2,8*	*23,7*	*551,3*	*1705,4*	*188,5*	4,1	-9,1
NH	0	1	33-100%	0	0,0	0,1	0,0	-0,4	2,5	-28,6	-0,5	

2	0	0	0	426	36,3	-0,1	-16,1	-824,7	1777,1	112,8	3,5	
55	0	0	0	*93*	*1,5*	*2,6*	*3,7*	*112,4*	*118,3*	*34,7*	3,1	-6,4
NH	0	1	33-100%	0	-15,7	-2,8	-44,4	252,1	464,1	123,5	3,4	
2	0	0	0	535	-40,0	2,8	36,5	-403,6	78,9	-22,3	3,5	
56	0	0	0	*94*	*26,3*	*3,5*	*15,0*	*224,4*	*1137,4*	*29,9*	4,1	-6,4
NH	0	1	33-100%	0	-1,9	1,0	-1,2	82,3	164,1	-47,6	1,3	
2	0	0	1	344	1,7	0,2	-1,2	-36,7	142,8	2,6	1,1	
57	0	0	1	*100*	*0,1*	*0,0*	*0,1*	*4,9*	*8,6*	*5,4*	1,1	0,8
NO	0	0	33-100%	0	1,1	0,8	-0,1	21,9	153,9	1,2	1,0	
2	0	0	0	254	-2,7	-0,6	2,8	-14,4	36,7	27,1	1,2	
58	0	0	0	*95*	*0,2*	*0,2*	*0,8*	*12,0*	*11,5*	*27,4*	0,9	1,0
NO	0	0	33-100%	0	6,3	12,6	-6,8	-495,4	-47,8	-47,7	2,5	
2	0	0	0	375	0,0	11,5	-10,6	-972,6	101,8	22,2	2,7	
59	0	0	0	*91*	*0,4*	*1,4*	*2,4*	*85,4*	*33,1*	*31,4*	2,9	-3,8
NO	0	0	33-100%	0	-1,3	-13,7	-22,1	437,5	125,9	-78,7	2,9	
2	0	0	0	318	-0,5	0,5	1,0	15,0	29,1	-3,8	0,3	
60	0	1	0	*90*	*0,1*	*0,5*	*0,9*	*33,9*	*4,1*	*3,2*	1,3	0,7
SO	1	0	33-100%	0	-9,8	13,5	-122,0	-657,1	-1060,3	147,9	4,2	
2	0	0	0	250	-0,2	-0,3	0,5	-52,3	8,4	-52,0	0,4	
61	0	1	0	*95*	*0,1*	*0,2*	*0,6*	*26,9*	*10,4*	*2,6*	0,4	0,8
SO	1	0	33-100%	0	-109,2	-4,8	-122,2	-35,5	-4776,3	-330,2	4,5	
2	0	0	0	361	0,8	-0,5	-0,2	14,0	-2,1	-19,1	0,0	
62	0	1	1	*92*	*0,4*	*0,1*	*0,1*	*3,9*	*17,1*	*0,4*	0,1	-0,1
SO	1	0	33-100%	0	18,5	22,7	-123,0	-1123,4	660,1	34,4	4,2	
2	0	0	0	986	0,0	0,0	0,0	0,0	0,0	0,0	0,0	
65	0	1	0	*70*								
SH	1	1	33-100%	0	-3,1	-7,9	-8,8	1314,9	-1004,4	800,3	3,1	
2	0	0	0	749	49,4	48,6	-26,1	-3787,8	2337,4	-176,7	4,1	
66	0	0	0	*69*	*13,8*	*21,9*	*1,3*	*872,4*	*553,9*	*110,5*	3,7	-5,8
NH	0	1	33-100%	0	2,7	-11,8	-18,5	553,2	129,9	-47,1	2,8	
2	0	0	1	555	-0,8	-0,5	0,6	-13,9	49,0	100,0	0,7	
67	0	1	1	*73*	*0,0*	*0,1*	*0,0*	*0,3*	*1,7*	*2,9*	0,7	0,0
SH	1	1	10-33%	0	-93,2	40,6	-54,2	-1509,0	-3983,7	-127,9	4,3	
2	0	0	0	398	0,4	1,6	1,5	3,7	-25,1	9,6	0,7	
68	0	1	0	*79*	*0,5*	*0,3*	*0,8*	*32,5*	*10,5*	*3,0*	0,3	-0,3
SH	1	1	33-100%	0	14,8	-8,8	-24,6	1057,0	254,4	-1747,2	3,4	
2	0	0	0	429	43,6	21,0	-32,4	-1235,4	2383,3	-194,1	3,8	
69	0	0	0	*68*	*0,5*	*3,2*	*3,8*	*156,0*	*40,0*	*101,6*	3,3	-6,7
NH	0	1	33-100%	0	7,2	-1,1	-2,8	-100,0	-224,5	-502,9	2,2	
2	0	0	0	294	-1,6	-0,6	-1,2	-38,3	13,9	-49,7	0,7	
70	0	1	1	*72*	*0,1*	*0,1*	*1,3*	*1,6*	*11,6*	*3,8*	1,1	-0,4
SH	1	1	33-100%	0	9,0	-26,9	128,2	-172,9	-766,0	4319,0	4,4	
2	0	0	0	336	57,5	37,6	-43,2	-3172,1	3055,7	301,9	4,1	
71	0	0	0	*71*	*7,3*	*10,3*	*13,0*	*209,5*	*67,8*	*91,4*	3,0	-9,0
NH	0	1	10-33%	0	-4,1	-1,5	-16,6	37,9	11,9	161,2	2,5	
2	0	0	0	399	-0,4	-0,9	-0,2	-68,4	44,4	-32,3	0,6	
72	0	1	1	*68*	*0,0*	*0,1*	*0,0*	*10,4*	*13,3*	*6,4*	-0,8	0,1
SH	1	1	10-33%	0	-3,8	-4,7	-27,2	-650,6	30,0	-2717,5	3,5	
2	0	0	0	248	34,3	4,3	-30,7	-326,7	2104,2	42,4	3,6	
73	0	0	0	*67*	*6,5*	*0,5*	*1,5*	*25,5*	*88,0*	*2,5*	2,9	-7,5
NH	0	1	10-33%	0	6,0	4,0	-4,8	44,0	117,0	66,9	1,9	
2	0	0	0	312	-0,8	-0,4	0,4	-14,7	25,3	48,1	0,3	
74	0	1	1	*63*	*0,1*	*0,1*	*0,1*	*5,9*	*1,3*	*2,5*	0,3	-0,1
SH	1	1	33-100%	0	-4,3	340,7	-240,1	-12605,0	2906,6	-1049,7	5,4	

2	0	0	0	286	45,2	3,2	-35,5	-784,0	2549,5	41,8	3,7	
75	0	0	0	*64*	*12,8*	*0,6*	*7,9*	*270,3*	*676,4*	*7,1*	3,8	-7,7
NH	0	1	33-100%	0	7,7	-2,7	-21,4	-80,7	416,9	-239,6	2,8	
2	0	0	0	285	-1,1	-0,3	-0,3	-32,6	40,5	-56,8	0,5	
76	0	1	1	*66*	*0,5*	*0,2*	*0,4*	*6,6*	*35,6*	*0,7*	0,6	0,1
SH	1	1	33-100%	0	144,8	47,8	181,9	-1773,8	2687,6	-5745,6	4,8	
2	0	0	0	142	45,5	14,2	-3,7	-873,9	1335,0	-117,4	3,5	
77	0	0	0	*65*	*2,4*	*0,1*	*4,7*	*10,7*	*158,3*	*49,7*	2,6	-2,9
NH	0	1	33-100%	0	5,1	1,5	-7,3	115,8	317,7	-315,0	2,2	
2	0	0	0	249	-1,0	0,0	-0,9	20,8	-18,9	20,2	0,3	
78	0	1	1	*64*	*0,2*	*0,2*	*1,3*	*6,1*	*21,0*	*2,7*	0,7	-0,4
SH	1	1	33-100%	0	-43,4	98,5	233,5	990,4	3231,0	-2874,7	4,8	
2	0	0	0	15	21,5	30,0	26,6	1963,3	1154,5	429,6	3,6	
79	0	0	0	*60*	*1,1*	*6,9*	*1,6*	*505,6*	*111,1*	*60,2*	2,9	8,4
NH	0	1	10-33%	0	-6,8	5,6	-2,7	-22,5	-156,3	739,5	2,4	
2	0	0	0	149	-0,4	-0,6	2,1	-46,8	21,1	4,6	0,8	
80	0	1	0	*67*	*0,1*	*0,4*	*1,2*	*15,8*	*5,9*	*0,5*	0,8	-0,3
SH	1	1	33-100%	0	-14,3	-18,3	6,7	692,9	40,2	328,0	2,9	
2	0	0	0	158	33,7	23,4	-19,8	-300,1	2282,4	-227,7	3,6	
81	0	0	0	*67*	*10,9*	*7,0*	*4,0*	*196,1*	*622,9*	*126,3*	3,9	-4,6
NH	0	1	33-100%	0	4,6	5,0	4,6	1,0	219,7	-1472,2	2,9	
2	0	0	0	9	0,0	0,0	0,0	0,0	0,0	0,0	0,0	
82	0	1	0	*63*								
SH	1	1	33-100%	0	28,1	-5,9	77,2	595,1	-686,6	18035,9	5,1	
2	0	0	0	23	4,9	1,3	-5,6	-57,6	344,4	-180,7	2,0	
83	0	0	0	*62*	*0,1*	*0,1*	*0,3*	*0,9*	*15,9*	*75,4*	2,0	
NH	0	1	0-10%	1	4,9	1,4	-5,6	-61,4	355,5	-236,6	2,1	
2	0	0	1	169	-0,6	-0,2	0,1	-8,9	29,0	-9,8	-0,1	
84	0	1	1	*73*	*0,1*	*0,2*	*0,1*	*6,1*	*2,1*	*5,9*	-0,1	0,0
SH	1	1	33-100%	0	5,6	29,0	19,8	-961,1	-33,9	-2124,2	3,5	
2	0	0	0	285	41,7	37,6	-37,7	-127,8	2936,0	-221,1	3,9	
85	0	0	0	*67*	*2,6*	*0,7*	*0,1*	*254,5*	*45,7*	*98,2*	3,1	-7,3
NH	0	1	33-100%	0	-3,9	-2,2	1,3	33,9	-482,3	-84,5	2,0	
2	0	0	1	310	-0,1	0,0	0,0	5,7	5,0	13,8	-1,0	
86	0	1	1	*67*	*0,1*	*0,2*	*0,1*	*2,6*	*1,9*	*5,0*	-1,3	0,0
SH	1	1	33-100%	0	8,7	-7,4	-14,2	-506,0	-637,7	334,6	2,8	
2	0	0	0	170	49,3	26,2	-39,6	-318,5	3127,1	-179,0	3,9	
87	0	0	0	*63*	*3,3*	*0,3*	*3,8*	*48,0*	*139,6*	*96,2*	3,4	-8,6
NH	0	1	33-100%	0	-3,4	-3,0	-2,9	114,9	-616,0	-236,6	2,3	
2	0	0	0	243	-0,4	0,0	0,2	-0,1	27,6	-26,4	-0,2	
88	0	1	0	*74*	*0,2*	*0,3*	*0,4*	*2,5*	*3,9*	*9,8*	0,1	0,0
SH	1	1	33-100%	0	4,9	5,5	-17,1	-256,6	145,8	63,9	2,6	
2	0	0	0	189	13,0	2,9	-11,2	-112,2	967,1	-20,6	2,8	
89	0	0	0	*68*	*1,7*	*0,3*	*1,3*	*10,1*	*53,8*	*23,6*	2,8	-2,5
NH	0	1	10-33%	0	2,6	-0,4	-16,6	266,2	474,7	-226,1	2,6	
2	0	0	0	306	-0,6	-0,6	-1,7	32,6	48,2	16,9	0,7	
90	0	1	0	*69*	*0,1*	*0,2*	*0,5*	*2,8*	*4,8*	*11,9*	0,8	-0,5
SH	1	1	33-100%	1	5,5	-46,2	20,7	-156,5	153,5	-1416,5	3,5	
2	0	0	0	258	39,3	37,4	-26,7	-1252,2	3305,0	-214,0	3,9	
91	0	0	0	*65*	*10,0*	*5,1*	*17,0*	*309,3*	*943,7*	*73,2*	3,2	-8,7
NH	0	1	33-100%	0	-10,6	-1,7	4,1	64,0	237,4	-117,3	2,2	
2	0	0	0	79	0,4	0,2	3,8	-13,4	-28,9	-9,5	1,2	
92	0	1	1	*68*	*0,1*	*0,2*	*0,6*	*1,8*	*2,3*	*7,0*	0,0	0,5
SH	1	1	10-33%	1	125,7	-41,6	-94,6	4449,4	1853,6	-22296,3	5,3	

2	0	0	0	299	25,6	-29,9	-27,5	1308,6	1985,5	-1128,7	3,7	
93	0	0	0	*71*	*12,4*	*36,2*	*11,9*	*982,6*	*798,1*	*158,7*	3,9	-8,8
NH	0	1	33-100%	0	-261,0	45,3	-143,9	5661,0	-11735,0	1639,8	5,2	
2	0	0	0	249	0,6	-0,3	-1,6	-8,7	49,7	-19,4	0,6	
94	0	1	1	*70*	*0,1*	*0,1*	*0,2*	*3,3*	*5,8*	*2,9*	0,4	0,1
SH	1	1	33-100%	0	-18,1	-106,7	-73,8	5072,0	39,6	315,2	4,4	
2	0	0	0	196	40,2	-3,5	-28,1	-1129,0	2597,3	196,6	3,7	
95	0	0	0	*76*	*3,4*	*0,6*	*2,0*	*104,8*	*22,1*	*24,3*	2,5	-7,8
NH	0	1	10-33%	0	3,0	-0,7	-4,2	163,8	446,9	631,3	2,4	
2	0	0	0	193	0,0	-0,2	0,0	56,4	-15,9	76,6	0,5	
96	0	1	1	*70*	*0,0*	*0,1*	*0,1*	*4,8*	*3,2*	*2,7*	0,5	0,1
SH	1	1	33-100%	0	-54,5	7,6	12,3	125,9	-3171,4	-1564,8	3,9	
2	0	0	0	18	1,4	4,9	15,5	-764,2	436,6	-361,6	2,8	
97	0	0	0	*72*	*2,6*	*0,2*	*4,6*	*107,9*	*110,0*	*14,9*	2,2	4,8
NH	0	1	33-100%	0	3,9	-0,6	-2,6	-117,0	-49,5	-315,2	1,8	
2	0	0	1	97	-0,3	-0,1	0,3	4,7	14,4	4,4	-0,5	
98	0	1	1	*69*	*0,0*	*0,1*	*0,1*	*2,0*	*3,0*	*1,0*	-0,6	0,1
SH	1	1	10-33%	0	-64,1	86,9	180,3	-3573,4	-4900,6	-949,5	4,7	
2	0	0	0	172	30,8	3,7	1,1	-227,5	1390,7	494,0	3,2	
99	0	0	0	*68*	*4,3*	*0,1*	*2,4*	*64,3*	*1311,4*	*87,4*	3,4	-0,7
NH	0	1	33-100%	0	-24,3	1,8	-15,5	-175,6	-378,7	966,4	3,1	
2	0	0	1	82	-0,2	-0,1	0,1	1,5	9,7	-0,5	-1,0	
100	0	1	1	*74*	*0,1*	*0,0*	*0,0*	*0,5*	*7,0*	*0,6*	-0,6	0,1
SH	1	1	33-100%	0	-446,9	1,2	-176,4	616,6	-1531,7	-692,4	5,3	
2	0	0	0	134	-2,8	22,7	-22,3	-1629,0	177,3	-4,0	3,3	
101	0	0	0	*66*	*1,4*	*1,9*	*0,5*	*74,8*	*107,6*	*5,3*	2,6	-8,2
NH	0	1	33-100%	0	0,4	1,9	-4,2	-510,5	75,8	230,2	2,1	
2	0	0	0	239	0,2	-0,1	2,8	-10,4	199,3	-13,0	1,3	
102	0	1	0	*67*	*0,3*	*0,1*	*0,5*	*3,2*	*47,7*	*18,7*	1,5	0,5
SH	1	1	33-100%	0	23,7	28,3	40,9	-1044,9	-2459,3	-8433,8	4,5	
2	0	0	0	13	-0,2	-20,5	1,2	1028,2	-83,1	-327,3	2,9	
103	0	0	0	*61*	*0,5*	*0,3*	*1,0*	*13,6*	*12,5*	*3,0*	2,9	-1,8
NH	0	1	33-100%	1	11,8	-0,1	20,2	129,3	-439,4	-30,5	2,8	
2	0	0	1	161	-3,9	0,6	-0,2	28,4	153,1	-28,6	1,4	
104	0	1	1	*63*	*0,1*	*0,1*	*0,2*	*0,1*	*2,5*	*2,4*	1,3	-0,1
SH	1	1	10-33%	0	-24,2	-420,6	-219,3	21003,2	1323,1	-2710,0	5,6	
2	0	0	0	178	60,2	13,3	-14,5	-65,5	2250,7	-244,7	3,7	
105	0	0	0	*61*	*6,2*	*1,7*	*3,4*	*13,0*	*316,3*	*120,4*	3,3	-3,1
NH	0	1	33-100%	0	-0,9	0,6	3,8	107,0	-71,8	-847,9	2,4	
2	0	0	0	172	-1,5	-0,2	4,1	-28,8	64,4	-10,6	1,3	
106	0	1	0	*58*	*0,0*	*0,1*	*2,2*	*3,2*	*5,6*	*9,9*	1,7	0,7
SH	1	1	33-100%	0	-3,4	-1,6	-13,6	93,2	229,5	-54,4	2,3	
2	0	0	0	18	0,7	-53,9	17,1	643,4	238,2	-1137,3	3,6	
107	0	0	0	*57*	*1,9*	*22,7*	*0,5*	*341,4*	*116,4*	*114,5*	4,0	-3,7
NH	0	1	33-100%	0	111,5	71,4	-101,6	4668,2	-1654,5	3397,5	4,6	
2	0	0	0	14	0,0	0,0	0,0	0,0	0,0	0,0	0,0	
108	0	1	0	*60*								
SH	1	1	33-100%	0	7,1	9,2	16,7	-632,9	-564,4	-234,7	2,8	
2	0	0	0	251	11,4	55,4	-18,4	-2001,3	905,2	-167,9	3,7	
109	0	0	0	*64*	*5,8*	*27,1*	*2,1*	*996,4*	*448,5*	*90,5*	4,1	-4,5
NH	0	1	33-100%	0	-7,8	7,2	1,4	-460,5	320,3	-1284,3	2,9	
2	0	0	0	98	-0,3	-1,2	-0,6	61,7	-20,2	-18,1	0,5	
110	0	1	1	*88*	*0,0*	*0,2*	*0,1*	*11,8*	*3,5*	*6,7*	-0,6	-0,3
SH	1	1	10-33%	1	-400,4	5,6	157,2	-4656,4	6593,3	-10052,4	5,4	

Acronyms and common terms

In this work acronyms are frequently used, as well as some expressions and terms adopted in order to summarize important definitions and concepts. Each of them is defined in the text when adopted for the first time; however, the following list should help the reader.

Acronyms

- *CVM*. Abbreviation for *Caging and Vent Mechanism*.
- *DOF*. Abbreviation for *Degree of Freedom* (also plural).
- *LISA*. Abbreviation for *Laser Interferometer Space Antenna*.
- *GPRM*. Abbreviation for *Grabbing Positioning and Release Mechanism*.
- *GRS*. Abbreviation for *Gravitational Reference Sensor*.
- *TM*. Abbreviation for *Test Mass*. In this book, it can be referred either to the Test Mass of LISA Pathfinder or to the test mass of the ground testing.
- *TMMF*. Abbreviation for *Transferred Momentum Measurement Facility*.

Common terms

- *compliant test*. In LISA Pathfinder, release test with compliant (pin or plunger) release velocity, i.e. with velocity inside the requirements of LISA Pathfinder.
- *copuling surface*. In LISA Pathfinder, surfaces of the TM indentation designed for a geometrical coupling with the shaped ends of the plungers, in order to make the plungers grab the TM.
- *fast pin release*. In LISA Pathfinder, release strategy with the pins retracting with maximum velocity (response of the piezo to an inverse step of voltage). The nominal release is for instance a fast pin release. In the in-flight release

campaign, the fast pin releases are composed of N tests (nominal releases) and R tests (reduced pin releases).

- *force profile.* Used for "force time history".
- *free flight velocity.* In LISA Pathfinder, constant velocity of the TM after the release, when it is injected into free fall. In the on-ground testing, constant velocity of the TM barycentre after the pin release and the detachment from the needles.
- *hammering.* In LISA Pathfinder, operation performed sometimes before the in-flight release: after the handover to pins, the pins are retracted and the plungers extracted in order to adjust the TM ϕ rotation through the impact between the pyramidal shape of the Z- plunger and the TM; the operation is then inverted (pin extraction and plunger retraction as in the handover to pins). Alternating these two operations allows to investigate the TM-plunger contact or to adjust the ϕ rotation of the TM.
- *handover to pins.* In LISA Pathfinder, the transition between the configuration with the TM grabbed by the plungers to the configuration with the TM held firmly by the two opposite pins.
- *handover to plungers.* In LISA Pathfinder, the transition between the configuration with the TM caged by the CVM to the configuration with the TM grabbed by the plungers.
- *in-flight.* Referred to the in-flight mechanism or to the in-flight release tests of LISA Pathfinder.
- *insert.* In the on-ground testing, cylindrical body at the centre of the test mass that reproduces the material properties of the landing area of the in-flight TM.
- *landing area.* In LISA Pathfinder, surface of the TM indentation (orthogonal to the axis of the release z) designed for the contact between each pin and the TM.
- *needles.* In LISA Pathfinder, they are three fingers positioned on the opposite side of the TM w.r.t. the GPRM, in order to block the TM and apply the preload.
- *nominal configuration.* In LISA Pathfinder, configuration of the release mechanism at the release: the TM is in contact only with the pins, the release system is aligned w.r.t. z axis, the TM lies in the zero position and is not rotated w.r.t. the housing.
- *nominal release.* In LISA Pathfinder, desired behaviour of the system at the release, with a preload of 0.3 N, the pins retracting quickly and symmetrically in order to produce the rupture of the adhesive bonds, the TM moving only along z direction (mono-dimensional motion) with velocity in the requirement, such that the plungers retract before any contact with the TM.

- *on-ground*. Referred to the on-ground tests of the space mechanism, and especially to the TMMF.
- *pin*. Release tip of the GPRM, hosted inside the plunger.
- *pin release*. In LISA Pathfinder, release in the nominal situation: retraction of the pins in order to detach the TM from the GPRM and allow the free fall of the TM. In the in-flight release, it is followed by the retraction of the plungers.
- *pin release velocity*. In LISA Pathfinder, velocity of the TM after the pin release and before the retraction of the plungers.
- *plunger*. Grabbing finger of the GPRM, designed for grabbing and positioning the TM.
- *plunger release*. In LISA Pathfinder, special group of (non-nominal) release tests performed uniquely by retracting the plungers, starting from a configuration with the TM grabbed by the plungers on the coupling surfaces (i.e. without pin extraction). Also called P tests. Do not confuse with *plunger release velocity* (which, in a nominal test performed with pin release, is the release velocity after the retraction of the plungers).
- *plunger release velocity*. In LISA Pathfinder, velocity of the TM after the retraction of the plungers, defined for all the release strategies. Do not confuse with *plunger release* (which is a particular release strategy performed through the retraction of the plungers).
- *release signal*. General term that defines the measurement of the TM linear and/or angular displacement at the release.
- *reliability test*. In LISA Pathfinder, test of hypothesis for the detection of the reliability in a release test.
- *reliable test*. In LISA Pathfinder, release test for which it is possible to detect three samples that lie on a straight line, i.e. three consecutive samples corresponding to a motion of the TM with constant velocity.
- *requirement*. Maximum (translational or rotational) release velocity of the TM allowed in LISA Pathfinder (corresponding to a maximum momentum). In general, it is referred to the plunger release velocity, since the capacitive control is activated after the retraction of the plungers.
- *slow pin release*. In LISA Pathfinder, release strategy with a slow retraction of the pins. Also called S test.

Original contributions of the author

The goal of the research was twofold: estimating the effect of adhesion in LISA Pathfinder, by means of the on-ground testing of a copy of the GPRM; and analysing the data of the in-flight release campaign, in order to describe the release dynamics.

The research activity was part of the collaboration between the University of Trento and the LISA Pathfinder mission, and was financed by many institutions (as reported in the acknowledgements) in order to achieve the established goals. For this reason, the operations and the analyses discussed in this thesis are oriented to problem-specific solutions rather than applications of new general scientific methods.

Nevertheless, the research allowed to develop some original contributions. I report them in the following list with reference to the chapter of the thesis and related publications.

- the TMMF (described in chapter 2) is an innovative setup for the measurement of small adhesive impulses (see the references of section 1.2). The main structure of the TMMF was however already given at the beginning of my PhD; my task was the substitution of the previous release mechanism with a copy of the GPRM, and the testing of the mechanism. This took several months since many electrical circuits, softwares (LabView VIs) and alignment procedures had to be re-designed in order to adapt to the new component. In particular, due to the very quick dynamics of the mechanism, I have dealt with the problem of the synchronization between event and measurement (of interferometer and camera). With respect to the previous setup (whose main results are reported in [24]), the different dynamics of the new system (with the quick initial adhesive pull, not detectable by a differentiation of the signal) led to a conservative estimation of the contribution of adhesion to the in-flight release velocity, based on statistical considerations. This method represents an original contribution w.r.t. the previous TMMF tests, due to the possibility of predicting a conservative difference of impulses which is independent of the magnitude of the impulses and on the systematic effect of other constraint forces (which dominates the motion). The approach was presented in [51] and [65].

- the analysis of chapter 3 was aimed at the precise estimation of the adhesive impulse (and not simply the conservative estimation of the difference). The mode-base estimation described in the chapter allows to estimate magnitude and duration of the adhesive impulse. In the literature many works deal with the estimation of impulses and small forces (see the survey of section 1.2.1), and some works are dedicated to the estimation of the properties of the impulses (like magnitude and location) through the analysis of the excited modes of a plate (see the references of section 3.4). Compared to these works, a novelty of the method presented in this thesis consists in the possibility of estimating the impulse properties by means of a single measurement (differently than other methods that adopt several strain gauges). Moreover, the method is applied to a moving plate (compared to other works where the vibrating plate is pinned or clamped) and the estimation is independent of additional forces that dominate the 1 DOF dynamics of the plate and that are affected by some uncertainty. Compared to other works, main limits of the method are the hypotheses needed, i.e. some basic knowledge of the force profiles acting on the plate (which are however based on experimental observations of the TMMF properties and on previous analyses of the adhesive forces), and the missing information about modes with higher frequencies. A consequence of these limitations is the high uncertainty of the estimation (which is accepted thanks to the purposes of the on-ground testing). The method, which has been proposed to a journal (see the page "PhD activity" at the end of the thesis), can be further improved (as proposed in section 4.9.4).

- the analyses of the in-flight releases of chapter 4 are very case-specific; they can constitute an original contribution as the result of the novelty of the mechanism and of its release procedure (see the survey of [56]). Due to the specificity of the mechanism, the in-flight data have been analysed by taking into account the properties of the mechanism and the release procedure. In particular, the separated analysis of *pin release velocities* and *plunger release velocities* is an innovative contribution w.r.t. the observations of ESOC, which took into account only the plunger release velocities [112]. The analysis of the velocity at the pin release allowed to determine the influence of the first operation (pin retraction) on the final TM momentum that the capacitive control must face after the retraction of the plungers. Moreover, the analysis of the impulses at the pin release, although based on a simple model, allowed to observe the prevailing influence of the TM-plunger contact. As commented, the work is preliminary and must be completed with the analysis of the geometry of the system (some recent highlights are reported in section 4.9.1) and with detailed dynamical simulations. Part of the analyses of this chapter have been presented in [120] and discussed with ESA.

Acknowledgements

This work has been realized thanks to the support of many researchers and institutions.

I am grateful to my tutor, Prof. Daniele Bortoluzzi, for his constant assistance during my PhD activity and for giving me the possibility of participating the LISA Pathinder collaboration. I appreciated his ability in focusing on many problems of different kind (both theoretical and practical) by highlighting the most important information and logical deductions, as well as his high care and precision in the research activity. The credit of many things I learned during my research goes to Daniele, and he had a key role in all the steps of my research. I would like to thank him also for the chance of contributing to the teaching activity of the Department, which was for me a great experience.

The TMMF in its latest configuration (chapter 2) has been assembled thanks to the fundamental collaboration of Carlo Zanoni, Luca Gambini, Blondo Seutchat and Andrea Virzì. Thanks to Hans Rozemeijer for his supervision of the ground release procedure. I would also like to thank Massimo Gennara and the Electronic Laboratory of the Department of Physics for the realization of important electronical devices of the ground testing.

In the analysis of the data of the TMMF releases (3), Nicolangelo Favia had a fundamental role. Starting from preliminary analyses on the results of the TMMF experiments that Daniele and I performed, in his master degree thesis (of which I was co-advisor) Nicolangelo analyzed in details the problem of the threshold (section 3.2.2) and the FEM modelation of the test mass (section 3.3.2), providing important data and algorithms for the prosecution of the work. I would like to thank Nicolangelo for his work and for the collaboration he gave me also after his master degree. I am also grateful to Michelangelo Marini for his collaboration in a FEM simulation performed during the review of the thesis.

The same can be said for the PhD student Davide Vignotto regarding the analysis of the in-flight data (chapter 4). Davide and I analyzed together the rough data of the in-flight release campaign in order to save and classify each test separately, identifying the main parameters for each release test. When I focused on the measured velocities at the release (reported in this work), the support of Davide has been very important, thanks also to his analyses of the capacitive

effects and of the configuration of the mechanism at the release (by taking into account constructive properties, tolerances and the results of technical notes), like for instance the plunger bistability (section 4.2.3). Davide is currently prosecuting the research on the behaviour of the GPRM at the release, by means of a new TMMF experimental campaign.

I would like to thank Jose Mendes (ESOC) for his assistance during the analysis of the release data. Some comments of the first part of chapter 4, regarding the motivations of the in-flight release campaign and additional tests (like the adhesion test and the performance of the capacitive actuation), are based on data and analyses provided by Jose. The in-flight release test campaign was planned by Jose Mendes and ESOC together with Daniele Bortoluzzi, Carlo Zanoni, Mance Davor and Hans Rozemeijer, on the basis of the first in-flight releases and of the on-ground predictions.

Thanks to ESA and Paul McNamara for the possibility of publishing the satellite data.

I would like to thank the TIFPA group of the Department of Physics of the University of Trento (and in particular Stefano Vitale, William Weber, Mauro Hueller, Rita Dolesi, Paolo Pivato, Ferran Gibert) for the constant assistance and for giving me the possibility of collaborating with the LISA Pathfinder mission. Thanks to William Weber for the help in the interpretation of the in-flight measurements.

This work was possible thanks to the support of all the people that collaborated with me during my PhD activities.

I am grateful to my PhD colleagues of the Mechatronic group: Andrea Bisoffi, Marco Bolignari, Mirko Brentari, Matteo Cocetti, Luca De Pascali, Riccardo Donà, Mattia Duranti, Andrea Ficorella, Fatemeh Kharaman, Alessandro Mazzalai, Giacomo Moretti, Edoardo Pagot, Matteo Perini, Matteo Ragni, Gastone Rosati Papini, Blondo Seutchat, Kateryna Skrypka, Sultan, Gianmarco Valenti. A special thank to Carlo Zanoni, which worked on my same research topic and gave me an important support and precious suggestions.

Finally, I would like to thank all the professors (in particular Luca Zaccarian, with whom I collaborated in the first months of my PhD), the researchers, the students and the employees of the Department of Industrial Engineering. A special mention goes to Sara Di Salvo (Department of Industrial Engineering) for its fundamental assistance during the PhD course.

The on-ground testing (discussed in chapters 2 and 3) has been funded by ESA (European Space Agency), ASI (Agenzia Spaziale Italiana), INFN (Istituto Nazionale di Fisica Nucleare), TIFPA (Trento Institute for Fundamental Physics Applications), Airbus Defence and Space.

The in-flight data of the LISA Pathfinder mission (discussed in chapter 4) are courtesy of ESA, ESOC (European Space Operations Centre) and TIFPA.

PhD activities

Scientific Production

I have been co-author of the following works:

- D. Bortoluzzi et al. *Injection of a body into a geodesic: lessons learnt from the LISA Pathfinder case.* Aerospace Mechanisms Symposium (AMS), Santa Clara (US), May 4-6, 2016.
- D. Bortoluzzi et al. *Testing the LISA Pathfinder test mass uncaging and injection into a geodesic.* European Conference on Spacecraft Structures, Materials and Environmental Testing (ECSSMET), Toulouse (France), September 27-30, 2016.
- D. Bortoluzzi, D. Vignotto, A. Zambotti. *Analysis of the in-flight injection of the LISA Pathfinder test-mass into a geodesic.* 18th European Space Mechanisms and Tribology Symposium (ESAMTS), 18th-20th September 2019.
- M. Brentari et al. *Position and speed control of a low-cost two-wheeled, self-balancing inverted pendulum vehicle.* 2015 IEEE International Conference on Mechatronics (ICM). IEEE, 2015.

and of the following works as a member of the LISA Pathfinder collaboration:

- M. Armano et al. *Sub-femto-g free fall for space-based graviational wave observatiories: LISA Pathfinder results.* Physical Review Letters, Vol. 116, Iss. 23 - 10 June 2016.
- M. Armano et al. *Capacitive sensing of test mass motion with nanometer precision over millimeter-wide sensing gaps for space-borne gravitational reference sensors.* Physical Review D, Vol. 96, Iss. 6 - 15 September 2017.
- M. Armano et al. *Characteristics and Energy Dependence of Recurrent Galactic Cosmic-Ray Flux Depressions and of a Forbush Decrease with LISA Pathfinder.* The Astrophysical Journal, Vol. 854, n.2 (2018), p. 113.

while the following work has been recently submitted to the journal "Mechanical Systems and Signal Processing" (August 2019):

- D. Bortoluzzi, A. Zambotti, N. Favia. *A vibration mode-based adhesion impulse characterization technique.*

Participation to Congresses, Schools and Workshops

- participation to the course *LabView Core 1.* Lecturer: Claudio Cupini, I.R.S.. Padova (Italy), January 26-28, 2015.
- participation to the *European Conference on Spacecraft Structures, Materials and Environmental Testing* (ECSSMET). Organizing institutions: CNES, ESA, DLR. Toulouse (France), September 27-30, 2016. Presentation of the paper: *Testing the LISA Pathfinder test mass uncaging and injection into a geodesic.*
- participation to the summer school *Stability and Bifurcation of Dynamical Systems. Theoretical Aspects and Applications.* Organizing institutions: GaDeS group (AIMETA), University of Genova. Savona (Italy), July 3-7, 2017.

PhD Courses

I have attended the following courses organized by the Department of Industrial Engineering of the University of Trento (in the list, I report name of the course and lecturer):

- *Microscopy Techniques* (David Maniglio)
- *Nonlinear Hybrid Dynamical Systems* (Luca Zaccarian)
- *Technical English* (Felicity Hope)
- *Numerical Optimization* (Enrico Bertolazzi)
- *Design of Experiments* (Paolo Bosetti)
- *Nonlinear Vibrations* (Daniele Bortoluzzi)
- *Object Oriented Modeling* (Francesco Biral)

Teaching and Tutoring Activity

During my PhD I have been for three years (2015-2017) teaching assistant of the course *Mechanical Vibrations* (lecturer: Daniele Bortoluzzi) of the Master Degree in Mechatronic Engineering of the University of Trento.

I have been co-advisor of the following Master Theses in Mechatronic Engineering:

- *Controllo non lineare di carichi sospesi* (2016). Student: Mattia Zandonà. Advisor: Luca Zaccarian.
- *Verifica sperimentale della velocità di rilascio della massa di prova della missione Lisa Pathfinder* (2017). Student: Nicolangelo Favia. Advisor: Daniele Bortoluzzi.

- *Analisi dei dati di telemetria del satellite LISA Pathfinder: dinamica del rilascio delle masse di prova* (2017). Student: Davide Vignotto. Advisor: Daniele Bortoluzzi. Co-advisor: William Weber.

Bibliography

[1] J. B. Hartle. *Gravity: An introduction to Einstein's general relativity*. 2003.

[2] A. Einstein. *Die Grundlagen der allgemeinen Relativitätstheorie*. Annalen der Physik, XLIX, 1916, pp. 769-822.

[3] ESA, LISA Pathfinder. *First steps to observing gravitational waves from space*. ESA Brochure, BR-323 (2015): 1-16.

[4] J. M. Weisberg, J. H. Taylor, and L. A. Fowler. *Gravitational waves from an orbiting pulsar*. Scientific American 245.4 (1981): 74-83.

[5] J. Cervantes-Cota, S. Galindo-Uribarri, and G. Smoot. *A brief history of gravitational waves*. Universe 2.3 (2016): 22.

[6] B. P. Abbott et al. *Observation of gravitational waves from a binary black hole merger*. Physical review letters 116.6 (2016): 061102.

[7] K. Danzmann and the LISA Study Team. *Laser Interferometer Space Antenna: A Cornerstone Mission for the Observation of Gravitational Waves*. ESA System and Technology Study Report No. ESA-SCI (2000).

[8] Danzmann, Karsten, et al. *LISA: Unveiling a hidden Universe*. Assessment Study Report ESA/SRE 3.2 (2011).

[9] F. Antonucci et al. *The LISA Pathfinder mission*. Classical Quantum Gravity, vol. 29, no. 12, pp. 124014.1-124014.11, 2012.

[10] M. Armano et al. *The LISA Pathfinder Mission*. Journal of Physics: Conference Series Volume 610, Issue 1, 11 May 2015, Article number 012005.

[11] M. Armano et al. *Sub-femto-g free fall for space-based gravitational wave observatories: LISA pathfinder results*. Physical review letters 116.23 (2016): 231101.

[12] P. McNamara et al. *LISA Pathfinder*. Classical and Quantum Gravity 25.11 (2008): 114034.

[13] M. Armano et al. *LISA Pathfinder: First steps to observing gravitational waves from space*. 11th International LISA Symposium. IOP Publishing, 2017.

[14] M. Armano, et al. *Beyond the Required LISA Free-Fall Performance: New LISA Pathfinder Results down to 20 μHz.* Physical review letters 120.6 (2018): 061101.

[15] M. Armano et al. *Capacitive sensing of test mass motion with nanometer precision over millimeter-wide sensing gaps for space-borne gravitational reference sensors.* Physical Review D 96.6 (2017): 062004.

[16] M. Armano et al. *Characteristics and energy dependence of recurrent galactic cosmic-ray flux depressions and of a forbush decrease with LISA Pathfinder.* The Astrophysical Journal 854.2 (2018): 113.

[17] M. Armano et al. *Precision charge control for isolated free-falling test masses: LISA pathfinder results.* Physical Review D 98.6 (2018): 062001.

[18] Armano, Michele, et al. *Charge-induced force noise on free-falling test masses: results from LISA Pathfinder.* Physical review letters 118.17 (2017): 171101.

[19] N. Brandt and W. Fichter. *Revised electrostatic model of the LISA Pathfinder inertial sensor.* Journal of Physics: Conference Series. Vol. 154. No. 1. IOP Publishing, 2009.

[20] Ke-Xun Sun et al. *LISA gravitational reference sensors.* Journal of Physics: Conference Series. Vol. 60. No. 1. IOP Publishing, 2007.

[21] S. Anza et al. *The LTP experiment on the LISA Pathfinder mission.* Classical and Quantum Gravity 22.10 (2005): S125.

[22] H. M. Araújo et al. *Detailed calculation of test-mass charging in the LISA mission.* Astroparticle Physics 22.5-6 (2005): 451-469.

[23] A. Neukom. *LISA Caging Mechanism Requirements Specification for GPRM.* ESA internal document S2-HTS-RS-3001, ESA (2005).

[24] C. Zanoni and D. Bortoluzzi. *Experimental-Analytical Qualification of a Piezoelectric Mechanism for a Critical Space Application.* IEEE/ASME Transactions on Mechatronics 20.1 (2015): 427-437.

[25] M. Armano et al. *LISA Pathfinder: the experiment and the route to LISA.* Classical and Quantum Gravity 26.9 (2009): 094001.

[26] D. Bortoluzzi, J. W. Conklin, and C. Zanoni. *Prediction of the LISA Pathfinder release mechanism in-flight performance.* Advances in Space Research 51.7 (2013): 1145-1156.

[27] J. M. Smit. *Inertial Sensor Actuation model for LISA Pathfinder End-to-end Simulator.* Technical note of the Netherlands Institute for Space Research, S2-SRO-TN-2001 (2005).

[28] B. Zahnd, M. M. Zimmermann, and R. Spörri. *LISA Pathfinder cage and vent mechanism. Development and qualification.* Proceedings 15th European Space Mechanism and Tribology Symposium (ESMATS). 2013.

[29] M. Biserni et al. *Hydraulic actuator for the LISA Pathfinder Caging Mechanism: technological challenges*. Proc 12th European Space Mechanism and Tribology Symposium ESMATS SP-653. 2007.

[30] P. Mäusli et al. *GPRM. Design description*. ESA internal document S2-HTS-DDD-3001, ESA (2007).

[31] I. Koeker et al. *Alignment and Testing of the GPRM as Part of the LTP Caging Mechanism*. 15th European Space Mechanisms and Tribology Symposium. Vol. 718. 2013.

[32] D. Bortoluzzi et al. *Object injection in geodesic conditions: In-flight and on-ground testing issues*. Advances in Space Research 45.11 (2010): 1358-1379.

[33] S. Durrant, 2005. *LISA-pathfinder test mass release task group report*. ESA internal document S2-EST-RP-3019, ESA.

[34] F. Antonucci et al. *LISA Pathfinder: mission and status*. Classical and Quantum Gravity 28.9 (2011): 094001.

[35] C. Zanoni et al. *Testing the injection of the LISA Pathfinder test mass into geodesic conditions*. Proc. 15th Eur. Space Mech. Tribology Symp. 2013.

[36] D. Bortoluzzi et al. *Measurement of momentum transfer due to adhesive forces: On-ground testing of in-space body injection into geodesic motion*. Review of Scientific Instruments 82.12 (2011): 125107.

[37] Zhou, Yu, and B. J. Nelson. *The effect of material properties and gripping force on micrograsping*. Proceedings 2000 ICRA. Millennium Conference. IEEE International Conference on Robotics and Automation. Symposia Proceedings (Cat. No. 00CH37065). Vol. 2. IEEE, 2000.

[38] P. Fortescue, J. Stark. *Spacecraft Systems Engineering*. John Wiley & Sons Ltd., New York, 2001.

[39] P. M. Winslow and D. V. McIntyre. *Adhesion of metals in the space environment*. Journal of Vacuum Science and Technology 3.2 (1966): 54-61.

[40] A. Merstallinger, et al. *Assessment of cold welding between separable contact surfaces due to impact and fretting under vacuum*. ESA Scientific & Technical Memoranda 279 (2009): 57.

[41] Benedetti, M., et al. *The Role of Adhesion and Sub-Newton Pull-Off Forces on the Test Mass Release for the LISA Experiment*. World Tribology Congress III. American Society of Mechanical Engineers, 2005.

[42] D. Bortoluzzi et al. *LISA Pathfinder test mass injection in geodesic motion: status of the on-ground testing*. Classical and Quantum Gravity 26.9 (2009): 094011.

[43] D. Bortoluzzi, M. Benedetti, and J. W. Conklin. *Indirect measurement of metallic adhesion force as a function of elongation under dynamic conditions*. Mechanical Systems and Signal Processing 38.2 (2013): 384-398.

[44] A. Neukom et al., 2005. *Grabbing and pass-over analysis.* ESA internal document S2-HTS-RP-3013, ESA.

[45] Neukom, Andreas, Romeo Romano, and Philipp M. Nellen. *Testing and lessons learnt of LISA GPRM.* Proc. 13th Eur. Space Mechanism Tribology Symposium, 2009.

[46] A. Neukom. *LISA Caging Mechanism GPRM. Design changes for FMs.* ESA internal document S2-HTS-TN-3013, ESA (2002).

[47] P. A. Mausli. *LISA Caging Mechanism GPRM. Mechanical analysis report.* ESA internal document S2-HTS-RP-3002, ESA (2007).

[48] P. Nellen. *LISA Caging Mechanism GPRM. Retraction measurements.* ESA internal document S2-HTS-TR-3011, ESA (2007).

[49] P. A. Mausli, P. Nellen. *LISA caging mechanism GPRM. Release tip interferometer tests.* ESA internal document S2-HTS-TR-3024, ESA (2008).

[50] C. Zanoni et al. *Summary of the results of the LISA-Pathfinder Test Mass release.* Journal of Physics: Conference Series. Vol. 610. No. 1. IOP Publishing, 2015.

[51] D. Bortoluzzi et al. *Injection of a Body into a Geodesic: Lessons Learnt from the LISA Pathfinder Case.* Aerospace Mechanism Symposium 2016, NASA/CP-2016-219090.

[52] R. Romano et al. *Request for Waiver LISA GPRM TM positioning accuracies.* ESA internal document S2-HTS-RFW-3007, ESA (2008).

[53] A. Neukom. *LISA Caging Mechanism GPRM. Functional Test Report QM1.* ESA internal document S2-HTS-TR-3022, ESA (2008).

[54] A. Neukom. *LISA Caging Mechanism GPRM. Functional Test Report QM2.* ESA internal document S2-HTS-TR-3023, ESA (2008).

[55] A. Neukom. *GPRM: Grabbing finger rotation measurement.* ESA internal document S2-HTS-TR-3028.

[56] Zanoni, Carlo. *Drag-free Spacecraft Technologies: criticalities in the initialization of geodesic motion.* arXiv preprint arXiv:1602.00268 (2016).

[57] C. Oram. *LISA Caging Mechanism GPRM. Structural Analysis Report.* ESA internal document S2-HTS-RP-3001, ESA (2006).

[58] L. Kogut and Izhak Etsion. *Adhesion in elastic-plastic spherical microcontact.* Journal of Colloid and Interface Science 261.2 (2003): 372-378.

[59] K. L. Johnson, K. Kendall, A. D. Roberts. *Surface energy and the contact of elastic solids.* Proceedings of the royal society of London. A. mathematical and physical sciences 324.1558 (1971): 301-313.

[60] Boris V. Derjaguin, Vladimir M. Muller, and Yu P. Toporov. *Effect of contact deformations on the adhesion of particles.* Journal of Colloid and interface science 53.2 (1975): 314-326.

[61] Jacob N. Israelachvili. *Intermolecular and surface forces.* Academic press, 2011.

[62] Fuller, K. N. G., and David Tabor. *The effect of surface roughness on the adhesion of elastic solids.* Proceedings of the Royal Society of London. A. Mathematical and Physical Sciences 345.1642 (1975): 327-342.

[63] C. Zanoni, D. Bortoluzzi, and J. W. Conklin. *Simulation of a critical task of the LISA release mechanism: the Injection of the Test Mass into Geodesic.* 9th LISA Symposium. Vol. 467. 2013.

[64] M. Benedetti, D. Bortoluzzi, and S. Vitale. *A momentum transfer measurement technique between contacting free-falling bodies in the presence of adhesion.* J. Appl. Mech., vol. 75, no. 1, p. 011016, 2008.

[65] D Bortoluzzi, A. Zambotti, et al. *Testing the LISA Pathfinder Test Mass uncaging and injection into a geodesic.* ECSSMET 2016, 2016.

[66] ESA internal document S2-HTS-RP-3003, Issue 1, ESA (2006).

[67] Benedetti, M., et al. *A Momentum Transfer Measurement Experiment Between Contacting Bodies in the Presence of Adhesion Under Near-Zero Gravity Conditions.* Experimental Analysis of Nano and Engineering Materials and Structures (2007): 433-434.

[68] Hey, Franz Georg, et al. *Development of a Highly Precise Micronewton Thrust Balance.* IEEE Transactions on Plasma Science 43.1 (2015): 234-239.

[69] Hey, Franz Georg, et al. *Development of a Micro-Thruster Test Facility which fulfils the LISA requirements.* Journal of Physics: Conference Series. Vol. 610. No. 1. IOP Publishing, 2015.

[70] Trezzolani, F., et al. *Development of a counterbalanced pendulum thrust stand for electric propulsion.* Measurement 122 (2018): 494-501.

[71] Sanchez, J., and H. Benaroya. *Review of force reconstruction techniques.* Journal of Sound and Vibration 333.14 (2014): 2999-3018.

[72] Draper, J. W., S. W. Lee, and E. C. Marineau. *Numerical construction of impulse response functions and input signal reconstruction.* Journal of Sound and Vibration 432 (2018): 259-271.

[73] Jacquelin, E., A. Bennani, and P. Hamelin. *Force reconstruction: analysis and regularization of a deconvolution problem.* Journal of sound and vibration 265.1 (2003): 81-107.

[74] Polk, James E., et al. *Recommended practices in thrust measurements.* No. IEPC-2013-440. California Institute of Technology (Pasadena,) Jet Propulsion Lab, 2013.

[75] Polzin, Kurt A., et al. *Thrust stand for electric propulsion performance evaluation.* Review of Scientific Instruments 77.10 (2006): 105108.

[76] Rocca, Simone. *ONERA micronewton thrust balance: Analytical modelling and parametric analysis.* Aerospace Science and Technology 15.2 (2011): 148-154.

[77] Haag, Thomas W. *Thrust stand for high-power electric propulsion devices.* Review of Scientific Instruments 62.5 (1991): 1186-1191.

[78] Lun, J., and C. Law. *Direct thrust measurement stand with improved operation and force calibration technique for performance testing of pulsed microthrusters.* Measurement Science and Technology 25.9 (2014): 095009.

[79] D'Souza, Brian C., and Andrew D. Ketsdever. *Investigation of time-dependent forces on a nano-Newton-second impulse balance.* Review of Scientific Instruments 76.1 (2005): 015105.

[80] Cubbin, E. A., et al. *Pulsed thrust measurements using laser interferometry.* Review of Scientific Instruments 68.6 (1997): 2339-2346.

[81] Bortoluzzi, D., et al. *Dynamic measurements of impulses generated by the separation of adhered bodies under near-zero gravity conditions.* Experimental mechanics 48.6 (2008): 777-787.

[82] Koizumi, Hiroyuki, Kimiya Komurasaki, and Yoshihiro Arakawa. *Development of thrust stand for low impulse measurement from microthrusters.* Review of scientific instruments 75.10 (2004): 3185-3190.

[83] Benedetti, M., et al. *Dynamic adhesion measurement for the verification of the grabbing positioning and release mechanism for the LISA Pathfinder Test Mass release.* 12th European Space Mechanism & Tribology Symposium, 2007.

[84] Benedetti, M., D. Bortoluzzi, and C. Zanoni. *Non-linear Mechanical Behaviour of Metallic Micro-wires under Dynamic Axial Loads.* Experimental mechanics 52.3 (2012): 215-228.

[85] Gane, N., P. F. Pfaelzer, and David Tabor. *Adhesion between clean surfaces at light loads.* Proceedings of the Royal Society of London. A. Mathematical and Physical Sciences 340.1623 (1974): 495-517.

[86] Savkoor, Arvin R. *Models of friction based on contact and fracture mechanics.* Fundamentals of friction: macroscopic and microscopic processes. Springer, Dordrecht, 1992. 111-133.

[87] Bortoluzzi, D., et al. *Investigation of Dynamic Failure of Metallic Adhesion: A Space-Technology Related Case of Study.* Dynamic Behavior of Materials, Volume 1. Springer, Cham, 2014. 201-208.

[88] Bortoluzzi, D., et al. *A new perspective in adhesion science and technology: testing dynamic failure of adhesive junctions for space applications.* Experimental mechanics 50.8 (2010): 1213-1223.

[89] Bortoluzzi, D., et al. *Ground-based verification of mechanisms for inorbit objects release*. Proceedings of the 12th IFToMM World Congress, Besançon (France). 2007.

[90] D. Bortoluzzi, P. A. Mäusli, R. Antonello, and P. M. Nellen. *Modeling and identification of an electro-mechanical system: The LISA grabbing positioning and release mechanism case*. Adv. Space Res., vol. 47, no. 3, pp. 453-465, 2011.

[91] D. Bortoluzzi et al. *Test Mass release testing. GPRM release test results*. ESA internal document S2-UTN-TN-3116, Issue 1.1, ESA (2016).

[92] Meier, Lukas. *Statistical and Numerical Methods for Chemical Engineers*. Lecture Notes of W. Stahel (ETH Zürich) and A. Ruckstuhl (ZHAW), 2012.

[93] Nicolangelo Favia. *Verifica sperimentale delle velocità di rilascio della massa di prova della missione LISA Pathfinder*. Master Thesis in Mechatronic Engineering. Advisor Daniele Bortoluzzi, Co-Advisor Andrea Zambotti. University of Trento, 2017.

[94] Hu, Pengcheng, et al. *Compensation for the variable cyclic error in homodyne laser interferometers*. Sensors 15.2 (2015): 3090-3106.

[95] Halverson, Peter G,, et al. *Techniques for the Reduction of Cyclic Errors in Laser Metrology Gauges for the Space Interferometry Mission*. American Society for Precision Engineering ASPE's 16th Annual Meeting, Nov. 10-15, 2001.

[96] Rao, Singiresu S., and Fook Fah Yap. *Mechanical Vibrations*. Vol. 4. Upper Saddle River: Prentice Hall, 2011.

[97] Meirovitch, Leonard. *Fundamentals of vibrations*. Waveland Press, 2010.

[98] Leissa, Arthur W. *Vibration of plates*. Ohio State University, Columbus, 1969.

[99] Yen, Ching-Shih, and Enboa Wu. *On the inverse problem of rectangular plates subjected to elastic impact, Part I: Method development and numerical verification*. Journal of applied Mechanics 62.3 (1995): 692-698., ASME Journal of Applied Mechanics 62 (1995) 692?698.

[100] Jiang, X. Q., and H. Y. Hu. *Reconstruction of distributed dynamic loads on an Euler beam via mode-selection and consistent spatial expression*. Journal of Sound and Vibration 316.1-5 (2008): 122-136.

[101] Vyas, N. S., and A. L. Wicks. *Reconstruction of turbine blade forces from response data*. Mechanism and machine theory 36.2 (2001): 177-188.

[102] Wang, Bor-Tsuen, and Chun-Hsien Chiu. *Determination of unknown impact force acting on a simply supported beam*. Mechanical systems and signal processing 17.3 (2003): 683-704.

[103] J.M. Smit. *Inertial sensor actuation model for LISA Pathfinder*. Technical note of the Netherlands Institute for Space Research, 2005.

[104] Carlo Zanoni. *DFACS Performance and Plunger Disturbance*. Technical Note of Astrium, 2009.

[105] Davide Vignotto. *Analisi dei dati di telemetria del satellite LISA Pathfinder: dinamica del rilascio delle masse di prova*. Master Thesis in Mechatronic Engineering. Advisor Daniele Bortoluzzi, Co-Advisors William Weber and Andrea Zambotti. University of Trento, 2017.

[106] Bai, Yan-zheng, et al. *Capacitive position measurement for high-precision space inertial sensor*. Frontiers of Physics in China 4.2 (2009): 205.

[107] Hannen, V. M., et al. *End-to-end simulations for the LISA Technology Package*. Classical and Quantum Gravity 20.10 (2003): S261.

[108] Conklin, John, and Anh N. Nguyen. *Drag-free Control and Drag Force Recovery of Small Satellites*. (2017).

[109] Bortoluzzi, Dolesi, Hueller, Vitale e Weber. *Electrode configuration tradeoff*. 2002.

[110] J.M. Smit. *Notes on Capacitive Sensing for LISA/SMART2*. 2003.

[111] Brandt, Nico, and Walter Fichter. *Revised electrostatic model of the LISA Pathfinder inertial sensor*. Journal of Physics: Conference Series. Vol. 154. No. 1. IOP Publishing, 2009.

[112] Jose Mendes. *TM Release Experiments*. ESA internal document, 2017.

[113] Stefano Siboni. *Dispense per il corso di Meccanica Razionale 1*. Lecture notes, http://www.ing.unitn.it/ siboni/dispenseA2MR/, 2010.

[114] D. Bortoluzzi, D. Vignotto, A. Zambotti. *Status of the analysis of the in-flight and on-ground testing of the LPF GPRM and the TM release*. Technical note LISA UTN INST TN 009 (2019). .

[115] Kay, Steven M. *Fundamentals of statistical signal processing*. Prentice Hall PTR, 1993.

[116] S. Vitale. *Signal and noise*. Lecture notes, University of California at Berkeley, L.N.L. - I.N.F.N. (REP) 71/92.

[117] Wiener, Norbert. *Extrapolation, interpolation and smoothing of stationary time series-with engineering applications*. MIT Press, (1949).

[118] Sheil, J., and I. O'Muircheartaigh. *Algorithm AS 106: The distribution of non-negative quadratic forms in normal variables*. Journal of the Royal Statistical Society. Series C (Applied Statistics) 26.1 (1977): 92-98.

[119] J. Bausch. *On the Efficient Calculation of a Linear Combination of Chi-Square Random Variables with an Application in Counting String Vacua.* Journal of Physics A: Mathematical and Theoretical, Volume 46, Number 50.

[120] D. Bortoluzzi, D. Vignotto, A. Zambotti. *Analysis of the in-flight injection of the LISA Pathfinder test-mass into a geodesic.* 18th European Space Mechanisms and Tribology Symposium (ESAMTS), 18th-20th September 2019.